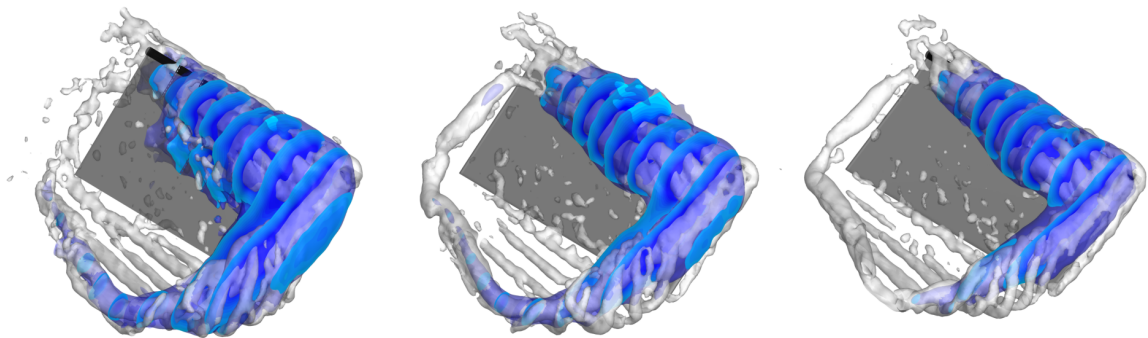


MASTER OF SCIENCE THESIS



Three-dimensional flow and load characteristics of flexible revolving wings at low Reynolds number

Remco van de Meerendonk

20th June, 2016

Three-dimensional flow and load characteristics of flexible revolving wings at low Reynolds number

MASTER OF SCIENCE THESIS

For obtaining the degree of Master of Science in Aerospace Engineering
at Delft University of Technology

Remco van de Meerendonk

20th June, 2016



Delft University of Technology

Copyright © Aerospace Engineering, Delft University of Technology
All rights reserved.

DELFT UNIVERSITY OF TECHNOLOGY
DEPARTMENT OF AERODYNAMICS

The undersigned hereby certify that they have read and recommend to the Faculty of Aerospace Engineering for acceptance the thesis entitled “**Three-dimensional flow and load characteristics of flexible revolving wings at low Reynolds number**” by **Remco van de Meerendonk** in fulfillment of the requirements for the degree of **Master of Science**.

Dated: 20th June, 2016

Supervisors:

Dr. ir. B.W. van Oudheusden

Dr. M. Percin

Dr. D. Ragni

Dr. ir. G.E. Elsinga

Preface

This M.Sc. thesis concludes the Aerodynamics and Wind Energy master program at Delft University of Technology: faculty of Aerospace Engineering, and summarizes the research work that has been done during the thesis project. During the thesis I have been able to follow my interest for applied experimental aerodynamics and I would to thank my supervisors dr. Mustafa Percin and dr. ir. Bas van Oudheusden for giving me this opportunity. I am grateful for the excellent guidance throughout the project, all the discussions which have been very motivating to me and for giving me the opportunity to present my work at the 18th Lisbon Symposia.

I would like to thank my family for having supported me during my studies in Delft to become an engineer. Also I would like to thank all my friends for making my time in Delft very enjoyable. Thanks for all the great memories!

A subset of the results related to the investigation of the spatial-temporal evolution of the flow field with the associated vortical structures and the temporal evolution of forces on a flat rectangular revolving wing for the different degree of chordwise flexibility of this M.Sc. thesis project have been presented at the 18th International Symposia on Applications of Laser and Imaging Techniques to Fluid Mechanics *van de Meerendonk et al. (2016)*.

Remco van de Meerendonk
Delft, The Netherlands
20th June, 2016

Abstract

This study explores the flow field and fluid-dynamic loads generated by revolving low-aspect-ratio flat plate wings undergoing a revolving motion starting from rest. Three wings with different degree of chordwise flexural stiffness (i.e., rigid, moderate flexibility and high flexibility) have been tested in order to investigate the influence of wing flexibility. The wings have an angle of attack of 45 deg in their undeformed condition. The measurements have been performed in a water tank at a Reynolds number of 10,000 based on the chord length and terminal velocity at the 75% span position, and a Rossby number of 1.93. The experimental campaign consisted of phase-locked tomographic particle image velocimetry (PIV) measurements complemented with simultaneous force measurements. The three-dimensional velocity fields are captured in three measurement volumes positioned side-by-side along the span of the wing for different phases of the revolving motion, generating a time-resolved volumetric velocity field data set. Subsequently, the pressure field and the loads acting on the wing are reconstructed from the velocity data.

The force measurements reveal that the lift generation of the rigid and moderately flexible wings is comparable while it is slightly reduced for the highly flexible wing. The drag shows a monotonic decrease with decreasing flexural stiffness. Consequently, the lift-to-drag ratio is increased significantly with decreasing flexural stiffness and is found to correlate well with the geometric angle of attack of the deformed wing. Additionally, it is shown that the rigid wing with a geometric angle of attack identical to that of the deformed wing generated similar lift and drag. This suggests that the geometric angle of attack at steady-state conditions is dominant for the lift and drag generated by chordwise flexible wings.

The PIV measurements reveal a vortex system consisting of a leading edge vortex (LEV), a trailing edge vortex (TEV), a tip vortex (TV) and a root vortex (RV) that forms at the onset of the motion. For decreasing flexural stiffness, the coherency of this vortex system and spanwise transport of vorticity in the LEV that is driven by a negative spanwise pressure gradient is increased, which contributes to the stability and retention of the LEV. Furthermore, the TV and LEV are confined to a smaller region within the flow field for increased wing flexibility. At greater phases of the revolving motion, near midspan, the core of the LEV structure is lifted off and expanded into a substantial bubble-like structure that extends towards the tip, which is indicative of vortex breakdown. The onset of vortex breakdown correlates well with the formation of a positive spanwise pressure gradient region near midspan at the leading edge on the suction side of the wing. The vortex system structures encompass a low pressure region.

As the low pressure region accompanying the LEV becomes smaller with increasing flexibility, the total force acting on the wing is reduced, but it is also tilted more towards the lift direction due to the wing deformation. As a consequence, the lift component remains relatively high, also because the suction peak is located closer to the wing surface. Simultaneously, the drag is significantly suppressed for increasing flexibility, which is also reflected in the smaller size of the wake. While the sectional lift along the full span is comparable for the different wings, the sectional drag is significantly reduced at the outboard wing locations for increasing flexibility. The corresponding spanwise centroids of lift and drag are located at approximately 70% of the span for all wings throughout the complete revolving motion.

This study improves the understanding of the effect of wing flexibility on the aerodynamic performance of flapping-wing flight. The dominance of the geometric angle of attack on the resultant lift and drag, and the constant spanwise centroid of the lift and drag for chordwise flexible revolving wings may significantly simplify the modeling of flexible flapping-wing flight.

Contents

Preface	v
Abstract	vii
Nomenclature	xiii
1 Introduction	1
2 Flapping-wing aerodynamics	5
2.1 Terms and definitions	5
2.2 Flapping wings: Important phenomena	7
2.3 Revolving wings	9
2.3.1 Rigid revolving wings	10
2.3.2 Flexible wings	15
2.4 Summary	18
3 Pressure & load reconstruction from PIV measurements	21
3.1 Pressure reconstruction	21
3.2 Load reconstruction	23
3.3 Pressure & load reconstruction on a rigid flapping revolving wing	25
3.4 Summary	26

4	Experimental Methods	27
4.1	Experimental Setup & Model description	27
4.2	Kinematics	28
4.3	Wing Flexibility	29
4.4	Force Measurements	30
4.5	Volumetric flow imaging by tomographic PIV	31
4.5.1	Experimental setup & Experimentation	31
4.5.2	Data processing	35
4.5.3	Wing reconstruction	37
4.6	System integration & Measurement procedure	38
5	Numerical Methods	41
5.1	Pressure reconstruction	41
5.1.1	Flow field in rotating reference frame	42
5.1.2	Pressure gradient	42
5.1.3	Integration of pressure gradients	44
5.2	Load reconstruction	48
5.3	Discussion on the pressure & load reconstruction	50
5.3.1	Material derivative of velocity: Eulerian - Lagrangian	50
5.3.2	Mask convergence	51
5.3.3	Dirichlet boundary condition	52
5.3.4	Euler effect	54
5.3.5	Divergence free flow	56
5.4	Verification	56
5.4.1	Verification of the pressure reconstruction algorithm with analytic test problems	57
5.4.2	Verification of the pressure and load reconstruction methods with a numerical simulation	58

6	Results: Wing reconstruction & Force measurements	63
6.1	Wing reconstruction	63
6.1.1	Reconstruction quality	64
6.1.2	Deformation characteristics	64
6.2	Force measurements	68
6.2.1	Measurement uncertainty in the reported steady-state value	68
6.2.2	Lift, drag and performance characteristics	69
6.2.3	Spanwise and chordwise location of the center of pressure	73
6.2.4	Comparison with literature	74
6.3	Conclusion	77
7	Results: Flow field	79
7.1	Definitions	79
7.2	Flow structures	82
7.2.1	Experimental uncertainty of the flow field	82
7.2.2	Coherent structures	83
7.2.3	Flow field characteristics	86
7.3	Spanwise characteristics	93
7.3.1	Total circulation	93
7.3.2	LEV circulation	97
7.3.3	Circulation: Total - LEV - TEV	103
7.3.4	LEV centroid	105
7.3.5	Spanwise vorticity flux of the LEV	110
7.4	Conclusion	112
8	Results: Pressure & Load reconstruction	115
8.1	Pressure field	115
8.1.1	Spanwise distribution	116
8.1.2	Comparison with coherent flow structures	118

8.1.3	LEV pressure centroid	121
8.1.4	Pressure gradient	124
8.2	Loads	130
8.2.1	Lift & drag coefficient	130
8.2.2	Lift & drag force contributions	131
8.2.3	Sectional lift & drag coefficients	134
8.3	Summary of the spanwise characteristics in terms of the LEV properties and sectional force coefficients for $\delta^* = 1, 1.5$ and 4	145
8.4	Conclusion	147
9	Conclusions & Recommendations	149
9.1	Conclusions	149
9.2	Recommendations for future work	151
A	Time-series animation of flow structures	159
A.1	Q-criterion isosurfaces	160
A.2	Q-criterion colored with helical density	161
A.3	Spanwise vorticity	162
A.4	Spanwise velocity	163
A.5	Spanwise vorticity flux density	164
A.6	Pressure distribution	165
A.7	Vortical structures and pressure distribution	166
A.8	Spanwise pressure gradient	167
A.9	Pressure gradient in x -direction	168

Nomenclature

Abbreviations

3D3C	Three-dimensional three-component
AoA	Angle of attack
AR	Aspect ratio
CFD	Computational Fluid Dynamics
FOV	Field of View
IR	Image resolution
LE	Leading edge
LEV	Leading edge vortex
PIV	Particle Image Velocimetry
PPP	Particles per pixel
RV	Root vortex
SR	Spatial resolution
TE	Trailing edge
TEV	Trailing edge vortex
TR	Temporal resolution
TV	Tip vortex

Coefficients

C_d, C_D	Sectional drag, total drag coefficient
C_l, C_L	Sectional lift, total lift coefficient

Greek Symbols

α	Angle of attack	[deg]
γ_1, γ_2	Two-dimensional vortex location, size detection criterion	[–]
Γ	Circulation	[m ² /s]
δ^*	Chord lengths traveled at reference length ($r/R = 0.75$)	[–]
θ	Rotation angle	[deg]
μ	Dynamic viscosity	[kg/m ³]
Π_1	Effective stiffness	[–]

ρ	Density	$[kg/m^3]$
ω	Vorticity	$[1/s]$
Ω	Angular velocity	$[rad/s]$
$d\Omega/dt$	Angular acceleration	$[rad/s^2]$

Latin Symbols

A^*	Dimensionless stroke amplitude for revolving wings	$[-]$
c	Chord length	$[m]$
d/D	Sectional drag, total drag	$[N/m], [N]$
E	Young's modulus	$[N/m^2]$
EI	Flexural stiffness	$[Nm^2]$
h	Thickness	$[m]$
I	Area moment of inertia	$[m^4]$
k	Reduced frequency	$[-]$
l/l	Sectional lift, total lift	$[N/m], [N]$
N	Vector offset	$[vec]$
p	Pressure (relative to ambient pressure)	$[Pa]$
r'	Spanwise distance from the rotation axis	$[m]$
r, R	Position along span, span length	$[m]$
R_g	Radius of gyration	$[m]$
R_{ref}	Spanwise reference length at $r/R = 0.75$ measured from rotation axis	$[m]$
RA	Spanwise length from rotation axis to wing root	$[m]$
Re	Reynolds number	$[-]$
Ro	Rossby number	$[-]$
S	Wing area	$[m^2]$
s	Distance to wing surface	$[m]$
t	Time	$[s]$
V_t	Terminal velocity, defined at the 75% span position	$[m/s]$
x'	Distance along the chord	$[m]$
x'_{geo}	Distance along the line that connects the LE and TE	$[m]$
x, y, z	Direction along the x, y, z axis	$[m]$
Q-criterion	Three-dimensional vortex identification criterion	$[1/s^2]$

Superscripts

*	Dimensionless
---	---------------

Subscripts

f	Fluid
---	-------

Chapter 1

Introduction

Its easy to explain how a rocket works, but explaining how a wing works takes a rocket scientist

Philippe Spalart

Increasing interest in micro air vehicles (MAVs) has stimulated the investigation of the aerodynamic phenomena that occur in small scale natural flyers. In this low Reynolds number regime, the aerodynamic performance (stability, maneuverability, and efficiency) of existing MAVs lacks that of such biological flyers (Pines & Bohorquez, 2006). Therefore, associated studies are often inspired by the study of natural flyers such as birds, bats and insects. The maximum lift coefficient reported in literature for different experiments as a function of Reynolds number is given in Figure 1.1.

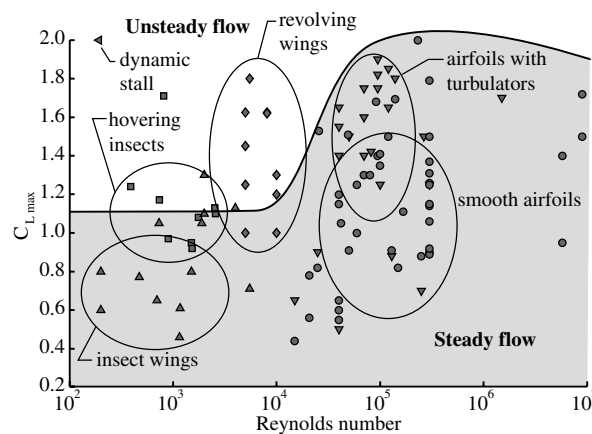


Figure 1.1: Maximum lift coefficient as a function of Reynolds number. Shaded data represents experiments in a steady flow and non-shaded data represents unsteady or three-dimensional experiments. (Jones & Babinsky, 2010).

A step decline in steady flow based airfoil performance is observed in the Reynolds number range of 10^4 to 10^5 , marking the boundary between steady and unsteady lift-generating

mechanisms. While flapping-wing flight benefits from unsteady aerodynamic effects which enhance the aerodynamic performance, other means of force generation (i.e., fixed-wing and rotary-wing mechanisms) suffer from deteriorated aerodynamic performance when operating at low Reynolds numbers. Therefore, one of the fundamental challenges is to achieve a better understanding of the aerodynamic phenomena associated with flapping-wing flight.

The unsteady mechanisms inherent for flapping-wing aerodynamics are: Wagner effect, clap and fling effect, Kramer effect, added mass effect, wake capture effect, and a stable leading edge vortex (LEV). The formation of a stable LEV is one of the most prominent mechanisms responsible for the enhanced aerodynamic forces sustaining flapping flight (Sane, 2003). At high angles of attack the flow separates at the leading edge and a LEV is formed which is accompanied by a low pressure region at the suction side of the airfoil. The suction forces that act normal to the wing surface are dominant for the net forces acting on the wing (Usherwood & Ellington, 2002). While for translating wings under a high angle of attack the flow separates and a well known von Kármán street is formed, a stable LEV is observed for revolving wings (Sane, 2003; Lentink & Dickinson, 2009). The LEV phenomenon in the context of flapping-wing aerodynamics has been subject to a number of studies in the last three decades, particularly to achieve a better understanding of its formation and the mechanisms responsible for its stability. It has been hypothesized that spanwise pressure gradients and the associated vorticity transport (Ellington et al., 1996), and the apparent rotational accelerations which are characterized by the Rossby number (Lentink & Dickinson, 2009; Jardin & David, 2014, 2015) play an important role in this respect. The sweeping (translational) aspect of the full flapping-wing motion can be represented by a revolving wing model, in which these rotational inertial mechanisms and spanwise gradients are also present. This simplified arrangement is important because flapping wings start approximately from rest at the beginning of each half-stroke of the full flapping motion. In nature not only natural flyers benefit from the enhanced aerodynamic performance associated by a stable LEV. For instance LEVs also elevate the lift of autorotating plant seeds such that the descent is prolonged and the seeds can be dispersed over greater distances by the wind (Lentink et al., 2009).

One characteristic aspect of biological flapping-wing flight that is not commonly taken into account in mechanical simulations is the influence of wing flexibility. The wing size is the dominant factor in flexural stiffness scaling and the spanwise flexural stiffness is 1-2 orders of magnitude higher than the chordwise flexural stiffness. Different studies have indicated the possible benefits of flexibility on the aerodynamic performance (Shyy et al., 2010). However, so far, the study of revolving flexible wings has been largely based on force measurement and qualitative (dye) visualization. Further quantitative information regarding the flow field development and its connection to the force generation will be instrumental in improving the understanding of the effect of wing flexibility on the aerodynamic performance of revolving wings.

In the field of fluid dynamics and engineering the pressure field is often of great interest. The pressure gradient is a relevant physical quantity and is expressed as the force per unit volume. By evaluating a time-resolved flow field, the instantaneous pressure field reconstruction can be reconstructed under the assumption of incompressible flow, employing the Navier-Stokes equations (van Oudheusden, 2013). Subsequently, the loads can be reconstructed by eval-

uating the integral momentum balance obtained by integrating the Navier-Stokes equation within a control volume (Anderson, 2011). Traditional instantaneous static pressure measurements in the flow field typically rely on pressure probes, which is an intrusive measurement technique and has a poor spatial resolution. Integral loads are traditionally obtained using balance measurements. However, for low Reynolds numbers, the signal-to-noise ratio of the measurements with this system decreases (Mohebbian & Rival, 2012). Also for applications where the model instrumentation is problematic or impossible to set up such as for observing freely flying birds, a balance system can often not be used. Particle image velocimetry (PIV) is a non-intrusive measurement technique allowing to obtain time-resolved flow field velocity data. Moreover, this technique is adaptable to moving objects and keeps its sensitivity for low Reynolds numbers in comparison to traditional pressure measurement techniques.

Recent advancements in volumetric imaging capabilities, notably tomographic PIV (Elsinga et al., 2006; Scarano, 2013) have motivated the current experimental investigation to further investigate the effects of wing flexibility in the context of flapping-wing aerodynamics in more detail. By incorporating the pressure field in the analyses, a complete description of the incompressible flow field is given, and the link between the temporal evolution of the vortical structures and the associated pressure forces can be obtained properly.

Experimental studies focusing on the volumetric measurements of flow fields around revolving wings are scarce. Furthermore, the majority of the studies are limited to rigid wings and often do not accompany analyses with reconstructed pressure fields and loads. The aim of the current study is to investigate the spatial-temporal evolution of the flow field of revolving low-aspect-ratio wings, and to connect the associated vortical structures and pressure fields to the temporal evolution of the fluid-dynamic forces acting on the wing. Wings with different degree of chordwise flexibility are considered, to study the influence of wing deformation on the aerodynamics of the wings. For this purpose, phase-locked tomographic PIV measurements were performed in three volumes along the wing span for different phases of the revolving motion in order to obtain time-resolved three-dimensional three-component (3D3C) flow field data sets around the wing. Simultaneous force measurements were carried out by means of a six-component water submersible force sensor to obtain the temporal variation of the forces during the revolving motion. Pressure fields are reconstructed from the PIV data, which also enables the calculation of forces acting on the wing from the flow fields by use of a control-volume approach.

This document is divided into 3 parts. In the first part, comprising chapter 2 and 3, an overview of the literature and the research that has been carried out is given. Chapter 2 focuses on the flapping-wing aerodynamics, while chapter 3 is focused on the reconstruction of pressure field data and loads from flow field data. In the second part, consisting of chapter 4 and 5, the methodology that is used in this study is given. Chapter 4 covers the experimental methodology and chapter 5 explains the numerical and data processing methods. In the third part, comprising chapter 6, 7 and 8, the results of this study are presented and discussed. In chapter 6 details about the wing deformation are given and the force measurements results are presented. In chapter 7 the flow field results are analyzed and in chapter 8 the pressure and load reconstruction results are discussed. Finally in chapter 9 the main conclusions of this thesis are given and recommendations for further studies are summarized.

Chapter 2

Flapping-wing aerodynamics

In this chapter the aerodynamic phenomena that characterize flapping-wing aerodynamics are summarized. Specifically the aerodynamic phenomena that occur during the sweeping/flapping translation, which can be represented by a revolving-surgling wing model, are addressed in more detail. Finally more insights into flexible wings are given.

The first section describes some terms and definitions that are used throughout this document.

2.1 Terms and definitions

This section describes some terms and definitions that are used throughout this document and are based on those frequently encountered in literature. The most common non-dimensional numbers that are used in the context of flapping-wing aerodynamics are:

- **Reynolds number** (Re) Defined in terms of a reference velocity scale (U_{ref}) and a reference length scale (L_{ref}),

$$Re = \frac{\rho U_{ref} L_{ref}}{\mu} \quad (2.1)$$

In the context of revolving wings U_{ref} is usually defined as the velocity at the midspan, 75% span, wingtip or at the radius of gyration. L_{ref} is usually defined as the chord length. The Reynolds number characterizes the flow conditions over a body immersed in fluid and states the relative importance of inertial/viscous forces. More precisely: *"The Reynolds number determines how 'fast', relative to the flow velocity, momentum will be diffused in the cross-stream direction by viscosity or turbulence and thus how thick the boundary layer will grow relative to the dimensions of the body"* (McLean, 2012).

- **Aspect ratio (AR)** Defined in terms of the span length (R) and the mean chord length (c) for a single wing planform,

$$AR = \frac{R}{c} \quad (2.2)$$

In the context of revolving flight the aspect ratio is defined based on the single wing planform, excluding the length scale of the wing root to the revolving axis. The distance from the root of the wing until the axis of revolving is taken into account in the definition of the Rossby number.

- **Rossby number (Ro)** for revolving wings. Defined in terms of the radius of gyration length scale (R_g) and a mean chord length scale (c),

$$Ro = \frac{R_g}{c} \quad (2.3)$$

For revolving flight the apparent centrifugal and Coriolis accelerations are inversely proportional to the Rossby number. Furthermore, for revolving flight, the LEV is stabilized by the centrifugal and Coriolis apparent accelerations that are present at low Rossby numbers (Lentink & Dickinson, 2009).

- **Radius of gyration (R_g)** For revolving flight the approximate radius of gyration is defined in terms of the area moment of inertia (I) of the wing area about the axis of forward motion, and the wing area (S),

$$R_g = \sqrt{\frac{I}{S}} \quad (2.4)$$

where the wing area is approximated by the span length and mean chord length ($S = R \cdot c$). For a uniform mass distribution the radius of gyration for a revolving wing describes the radial distance from the revolving axis of forward motion at which the mass of a body can be concentrated without altering the rotational inertia of the wing about that axis.

- **Reduced frequency (k)** For hovering flight the reduced frequency, based on the wingtip velocity, is expressed in terms of the stroke amplitude (ϕ_0 [rad]) and the aspect ratio (AR) as (Shyy et al., 2010),

$$k = \frac{\pi}{\phi_0 AR} \quad (2.5)$$

The reduced frequency expresses the unsteadiness of the flow associated with a flapping-wing flight. The dimensionless stroke amplitude (A^*) is expressed as Lentink & Dickinson (2009),

$$A^* = \phi_0 AR = \phi_0 R/c \quad (2.6)$$

where the dimensionless stroke amplitude (A^*) expresses the amplitude as the number of chord lengths traveled. For revolving flight the apparent Euler acceleration is inversely proportional to the dimensionless stroke amplitude .

- **Effective stiffness** (Π_1) The effective stiffness for rectangular chordwise flexible wings is approximated with a beam model instead of a plate model by neglecting the Poisson's ratio of the specific material (Kang et al., 2011). Defined in terms of Young's modulus (E), thickness ratio ($h^* = h/c$), fluid density (ρ_f) and a reference velocity (U_{ref}) as,

$$\Pi_1 = \frac{Eh^{*3}}{(12\rho_f U_{ref}^2)} \quad (2.7)$$

For a revolving chordwise flexible wing the effective stiffness parameter expresses the ratio of elastic bending forces over fluid dynamic forces. Note that for a plate model an additional factor of $(1 - \nu^2)$ is present within the denominator, where ν is the Poisson's ratio. For most PET type materials ν is about 0.35 resulting in an additional factor of about 0.9. To simplify the general comparison of the effective stiffness parameter Π_1 between wings with slightly different materials, the beam model is used by neglecting the Poisson's ratio.

2.2 Flapping wings: Important phenomena

Natural flyers often encompass a flapping-wing motion to stay airborne. Flapping-wing aerodynamics is characterized by unsteady three-dimensional effects that occur at low Reynolds numbers which are responsible for the enhanced aerodynamic forces sustaining flapping-flight. The basic flapping-wing motion kinematics are given in Figure 2.1.

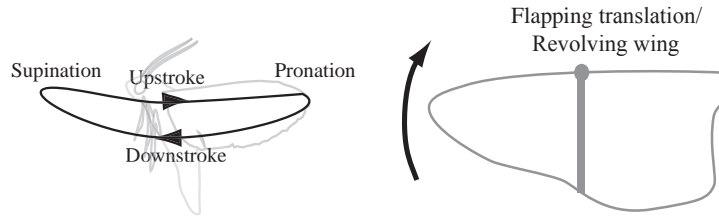


Figure 2.1: Basic flapping-wing motion. Modified from (Sane, 2003).

At the supination and pronation the wing will rotate around a chordwise axis to change its angle of attack. During the flapping-wing translation the wing sweeps and undergoes a revolving wing motion around a central axis. The main unsteady mechanisms for flapping-wing aerodynamics include (Sane, 2003; Lehmann, 2004):

- **Wagner effect** The Wagner effect introduces a delay in the build-up of circulation for an impulsively inclined starting wing before reaching steady state values. This delay may result of two phenomena: First, viscous latency results in a finite time before the Kutta condition is established. Second, the starting vortex induces a velocity field counteracting the growth of the circulation bound to the wing.
- **Wing-wing interaction, the 'clap and fling'** The clap and fling motion is a wing-wing interference effect and is illustrated in Figure 2.2. During the clap phase low

vorticity is shed. As a result the starting vortex is decreased in strength at the start of the fling phase allowing a more rapid build-up of circulation. On top of that a jet of air is given an extra push. During the fling phase a low pressure zone is created allowing a rapid build-up of circulation and attached vorticity.

- Delayed stall and LEV** At high angles of attack the flow separates at the leading edge and a LEV is formed which is remarkably stable. For a flapping-wing a spanwise flow gradient is present. As the flapping-wing translates, a spanwise velocity gradient interacts with the LEV causing the spanwise flow to spiral towards the tip. One of the hypothesis to explain LEV stability is that spanwise flow redirects momentum transfer from the chordwise direction into the spanwise direction causing the LEV to remain smaller. This spanwise advection of vorticity balances the production of vorticity at the leading edge such that the LEV remains stable throughout the flight. This redirection of momentum is illustrated in Figure 2.2. More details about the stability mechanisms are given in subsection 2.3.1.

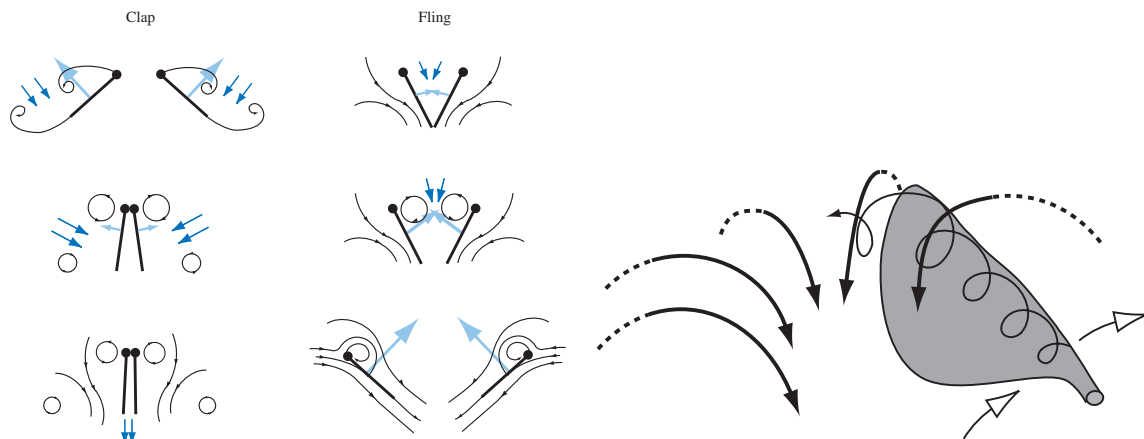


Figure 2.2: *Left:* Clap and Fling. *Right:* LEV for flapping-wing. (Sane, 2003).

At Reynolds number of $O(10^4)$ or lower the LEV is a common flow phenomenon in flapping-wing aerodynamics (Shyy et al., 2010).

- Kramer effect** During stroke reversal the wing rapidly rotates around its spanwise axis. During this rotation the flow is deviating from the Kutta condition and moving away from the trailing edge (TE) causing a sharp velocity gradient leading to shear. Fluid particles resist shear and additional circulation is built to reestablish the Kutta condition. Summarized, the wing generates circulation to counteract the rotational effects. Viscosity has a latency and the actual Kutta condition may be never seen, but still this circulation will be built during the rotation and affects the net force generation.
- Added Mass** "Added mass" is also often called "added mass inertia", "acceleration reaction" or "virtual mass" and is an unsteady effect. When an object is accelerating in a fluid region it encounters a reaction force due to the accelerated fluid.
- Wing-wake interference, wake capture** During stroke reversal the wing potentially interacts with its shed vortices. These vortices induce a strong flow field. When the wing reverses direction, it encounters the enhanced velocity and acceleration fields. This

allows the wing to extract energy from the shed wake which lead to higher forces as illustrated in Figure 2.3.

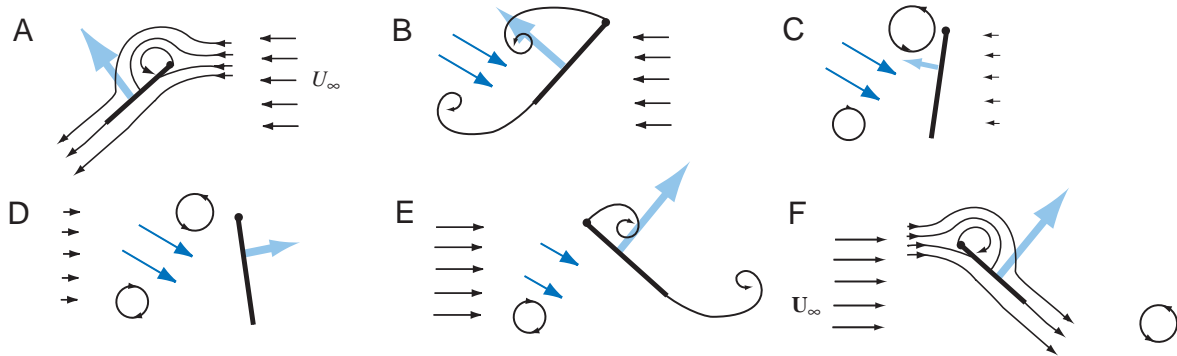


Figure 2.3: Wake capture. A to F indicate the time sequence (Sane, 2003).

This wake capture phenomena can lead to enhanced lift production and increased flight efficiency. By changing the stroke frequency and the stroke amplitude, the fluid speed and accelerated mass can be adjusted influencing the kinetic energy available in the momentum jet available in the wake.

2.3 Revolving wings

At high angles of attack the flow separates at the leading edge and a LEV is formed of which its suction forces acting normal to the wing surface are dominant for the net forces acting on the wing (Usherwood & Ellington, 2002). The stable LEV with its associated low pressure region is one of the most prominent mechanisms responsible for the enhanced aerodynamic forces sustaining flapping flight, and is driven by a revolving wing motion (Sane, 2003). The sweeping (translational) aspect of the full flapping-wing motion can be represented by a revolving wing model. This simplified arrangement approximates each half-stroke (upstroke, downstroke as illustrated in Figure 2.1). A revolving-surging wing represents the revolving motion of a wing at a constant angle of attack. While for translating wings under a high angle of attack the flow separates and a well known von Kármán street is formed, for revolving wings a stable LEV is observed (Sane, 2003; Lentink & Dickinson, 2009; Garmann et al., 2013). Usherwood & Ellington (2002) studied revolving and translating hawkmoth wings at a Reynolds number of 8,000. While for an unsteady revolving wing motion the maximum lift coefficient is 1.75, the lift coefficient was only 0.71 for the translating wing indicating the key role of the rotational inertial mechanisms that are responsible for the enhanced aerodynamic force generation.

Several studies have investigated the fundamental flow phenomena associated with revolving wings in more detail. Although natural flyers have flexible wings and several studies have indicated the possible beneficial effects of flexibility on the aerodynamic performance (Shyy et al., 2010), the majority of the studies have investigated rigid revolving wings. First, more insights are given into rigid revolving wings, after which more details about flexible wings are presented.

2.3.1 Rigid revolving wings

LEV For a revolving wing, the LEV separates at the leading edge (LE) of which its suction forces acting normal to the wing surface are dominant for the net forces acting on the wing. As a result the net force vector for a rigid wing acts normal to the wing surface (Usherwood & Ellington, 2002). Birch et al. (2004) experimentally studied a steady-revolving wing at a Reynolds number of 120 and 1,400. It was shown that for both a Reynolds number of 120 and 1,400 the angle of the net force vector is normal to the wing at an angle of attack of 40 deg onwards indicating that the pressure forces are dominant for both low and high Reynolds number as illustrated in Figure 2.4.

Garmann & Visbal (2014) numerically studied revolving rectangular wings at an angle of attack of 60 deg and a Reynolds number of 1,000 for an aspect ratio of 1,2 and 4. For a revolving wing the LEV is located close to the surface of the wing and provides a suction force throughout the motion. Towards the tip the LEV lifts off as an arch-like structure and reorients itself along the chord through its connection with the tip vortex (TV). Downstream of the TE vorticity is shed and a trailing edge vortex (TEV) is formed. In Figure 2.4 the vortex system structure for a rectangular revolving rigid wing is illustrated. It was shown that the LEV grows along the span of the wing such that its chordwise extent eventually became constrained by the TE with increasing aspect ratio, leading to a saturation of the aerodynamic loads. As a result there is no advantage of increasing the aspect ratio once the LEV occupies the entire chord of the wing, which happens around an aspect ratio of 2.

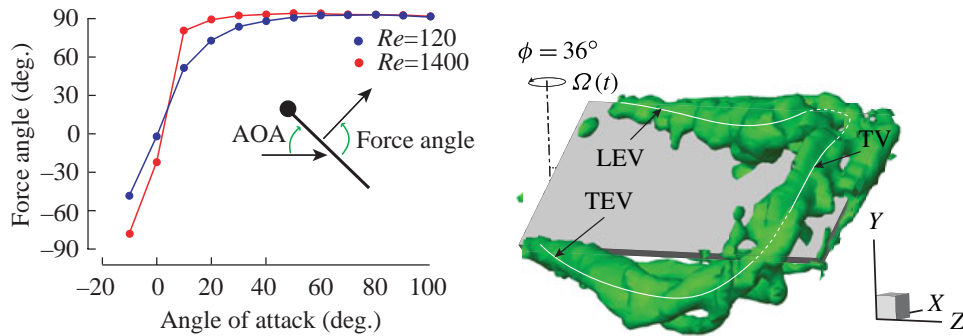


Figure 2.4: Left: Net force angle as a function of angle of attack (Birch et al., 2004). Right: Rectangular revolving rigid wing vortex system overview (Carr et al., 2015).

Stability mechanisms of LEV Different hypotheses have been proposed to explain the stability of the LEV during revolving flight, such as the spanwise advection of vorticity (Ellington et al., 1996), the downward induced flow from the tip, limiting the growth of the LEV (Birch & Dickinson, 2001) or the apparent rotational (Coriolis and centrifugal) accelerations that are characterized by a low Rossby number (Lentink & Dickinson, 2009). In this respect (Jardin & David, 2014, 2015) showed that although LEV attachment can be obtained by the spanwise advection of vorticity, the high aerodynamic performance is ensured by the apparent Coriolis effect.

Birch & Dickinson (2001) experimentally studied a flapping wing at an angle of attack of 45 deg and a Reynolds number of 160. Fences at 40% and 60% span position were placed to study the effect of spanwise flow on the stability of the LEV. For both with and without fences an attached LEV was observed. Compared to higher Reynolds numbers the pressure gradient in the vortex core might be too small to drive substantial axial flow. It was hypothesized that for low Reynolds number flows the downward induced flow from the tip reduces the effective angle of attack, limiting the growth of the LEV. In (Birch et al., 2004) flow visualization indicated an intense narrow region of spanwise flow within the core of the LEV for a Reynolds number of 1,400 that is in accordance with the hypothesis of spanwise advection of vorticity that balances the production at the LE. However, this feature of intense spanwise flow is not observed for a Reynolds number of 120. It was suggested that the transport of vorticity from the LE to the wake, that permits prolonged vortex attachment, takes different forms at different Reynolds numbers.

Jardin & David (2014) numerically studied the influence of spanwise gradients to stabilize the LEV on a rectangular revolving wing at an aspect ratio of 4 and an angle of attack of 45 deg at a Reynolds number of 500. In Figure 2.5 the spanwise vorticity and lift coefficient are given for three test cases with different spanwise gradient profiles.

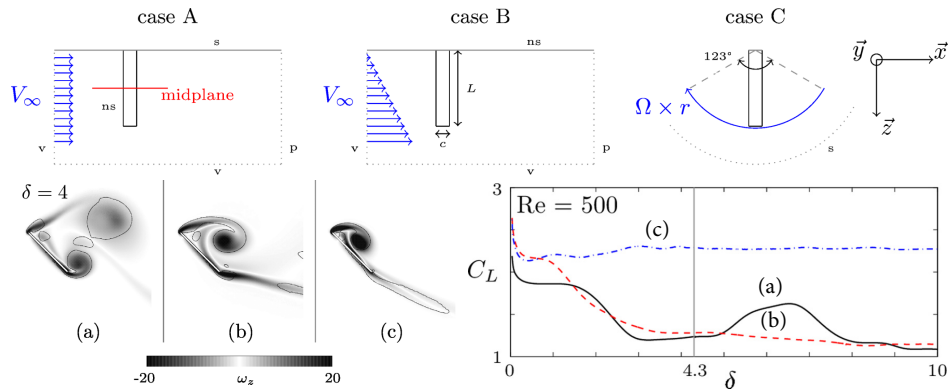


Figure 2.5: Spanwise vorticity (ω_z) at a travel length of $\delta = 4$ and lift coefficient (C_L) for different travel lengths. For case C, 1δ corresponds to a rotation angle of approximately 28.6 deg. (Jardin & David, 2014).

Although the spanwise gradient in case B and C promote a stable LEV, the rotational effects play a key role in the high lift generation for revolving wings. Jardin & David (2015) continued this study and studied the influence of the centrifugal and Coriolis term. By neglecting terms in the Navier-Stokes equations the effects on the flow structures and lift coefficients are analyzed. In Figure 2.6 the flow structures and the lift coefficients are given for combinations of including/excluding the apparent rotational effects. The Coriolis effect causes the LEV to stay close to the wing surface, such that the low pressure region associated with the LEV is located close to the wing surface resulting in high lift coefficients. Furthermore, the Coriolis effects stabilize the rotational flow, limiting global burst and concentrate the burst near the tip. It was concluded that the Coriolis effect is the main mechanism for the enhanced lift generation for revolving wings.

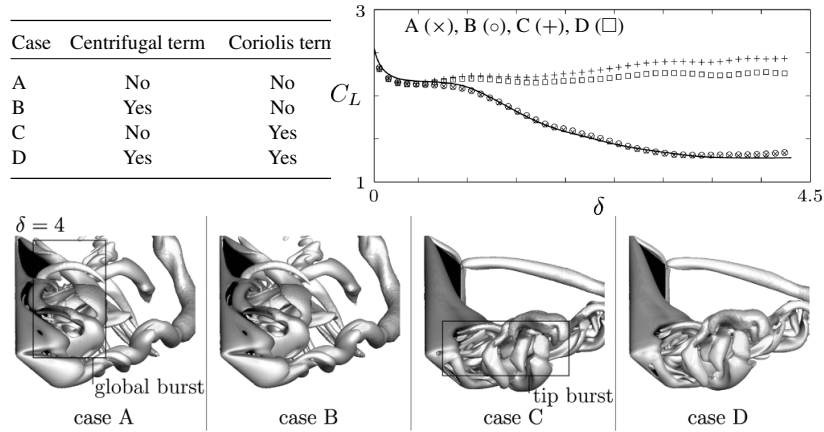


Figure 2.6: Effect of centrifugal and Coriolis term in Navier-Stokes equations on the flow structures for a travel length of $\delta = 4$ and the lift coefficient as a function of δ (Jardin & David, 2015).

Lentink & Dickinson (2009) experimentally studied the dynamic scaling parameters of revolving wings that are responsible for the enhanced LEV. For hovering flight, expressed in a rotating reference frame, the centrifugal and Coriolis apparent acceleration are inversely proportional to the Rossby number Ro . The apparent angular acceleration (Euler effect) is inversely proportional to $A^* = \phi_0 R/c$, where ϕ_0 is the stroke amplitude. By varying Ro force augmentation decreased with increasing Ro , which is consistent with the general prediction that the LEV is stabilized at low Ro . In Figure 2.7 the basic flow visualizations are summarized to indicate the basic flow structure for different values of A^* , Ro and Re , as well as the Rossby numbers that are present in natural flyers. Although the Reynolds number

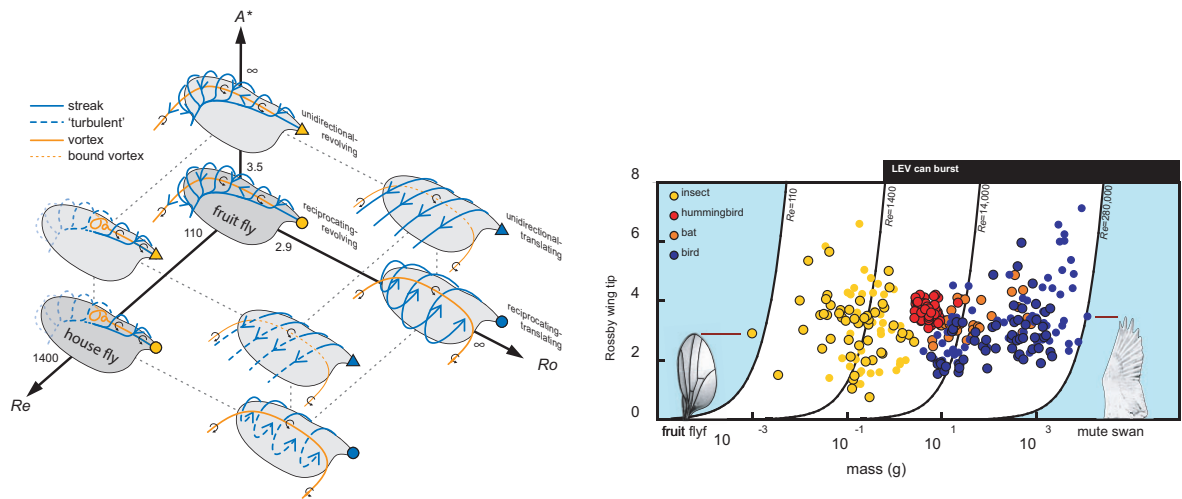


Figure 2.7: Left: Cartoon of basic flow structures for different values of A^* , Ro and Re . Right: Rossby number based on wing tip radius for natural flyers (Lentink & Dickinson, 2009)

varies significantly for different natural flyers, the Rossby number that is based on the wing tip radius is confined in a small range around $Ro_{\text{wing tip}} = 3$.

Volumetric imaging capabilities Experimental studies focusing on the volumetric measurements of flow fields around flapping wings are scarce. Percin & van Oudheusden (2015b) acquired 3D3C flow fields around revolving-surging and revolving-pitching rigid flat-plate wings for an angle of attack of 45 deg and a Reynolds number of 10,000 by means of tomographic PIV. It was shown that the revolving-pitching wing produces much higher aerodynamic forces compared to the revolving-surging case and affects the force histories until approximately 6 chord lengths. Carr et al. (2013) studied a rigid rectangular revolving flat-plate wing for an angle of attack of 45 deg and a Reynolds number of 5,000 using phase-locked and phase-averaged stereoscopic PIV for different chord planes to reconstruct phase-averaged spanwise 2D3C velocity data sets. Detailed analyses were made for wings of aspect ratio 2 and 4. For an aspect ratio of 2 the overall LEV-TV structure remains more coherent and is located closer to the wing surface. The vortical structure breaks down at a higher travel distance compared to the wing with an aspect ratio of 4. Carr et al. (2015) continued the study about the effect of aspect ratio on rotating wings from (Carr et al., 2013) in more detail. Additionally it was shown that the aft tilt of the LEV is larger for an aspect ratio of 4 compared to 2. The aft LEV tilt reduces the spanwise LEV circulation due to the conversion of spanwise vorticity to chordwise vorticity. Wolfinger & Rockwell (2014) studied a rigid rectangular revolving flat-plate wing at an angle of attack of 45 deg and a Reynolds number of 1,400 for different Rossby numbers using a similar experimental setup. An increased coherency of the vortex system was observed for lower Rossby numbers and it was suggested that the stability or retention of the LEV is coupled with the interior structure of the tip and root vortices.

Effect of Reynolds number In (Lentink & Dickinson, 2009) it was shown that the mechanisms responsible for LEV stability are insensitive for a Reynolds number range of $100 < Re < 14,000$. Jones & Babinsky (2011) experimentally studied a rectangular revolving flat-plate wing with an aspect ratio of 4 across a range of Reynolds numbers from 10,000 to 60,000. The force levels and flow structures were not observed to change significantly over the range of Reynolds numbers. Garmann et al. (2013) numerically studied a revolving rectangular wing at an angle of attack of 60 deg with an aspect ratio of one and a Rossby number of 1.02. The overall vortex structure was mostly insensitive for a Reynolds number range of 200 to 60,000. For a Reynolds number higher than 2,000 the feeding sheets of the vortex system became susceptible to instabilities and formed shear layer substructures. Subsequently, the formation of these substructures agree well with the breakdown of the LEV. Increasing Reynolds number was observed to slightly augment the average lift and drag coefficients. Percin & van Oudheusden (2015a) experimentally studied a rectangular flat-plate wing with an aspect ratio of 2 and a Rossby number of $R_g/c = 1.8$ undergoing a revolving acceleration from rest until a predefined terminal velocity. For an angle of attack of 45 deg and a Reynolds number range of 5,000 to 25,000 the force and vorticity generation increase slightly with Reynolds number. The general behavior of the flow structures were not greatly influenced by the Reynolds number.

Effect of angle of attack Ozen & Rockwell (2012) experimentally studied a rectangular revolving flat-plate wing with an aspect ratio of 1 and a Rossby number of $R_g/c = 1.02$ for

a range of Reynolds numbers from 3,600 to 14,500. A stable LEV was observed for angles of attack between 30 deg and 75 deg. In (Percin & van Oudheusden, 2015a) it was shown that for a range of angles of attack from 15 deg to 75 deg the behavior of the vortical structures was found to be similar, however their morphology is altered by the promoted separation at higher angles of attack. For an angle of attack of 45 deg the lift coefficient reaches a maximum (Usherwood & Ellington, 2002; Garmann et al., 2013; Percin & van Oudheusden, 2015a).

LEV breakdown Although LEV breakdown may not significantly affect the force generation, it often does mark the end of the ability to characterize and model it (Jones et al., 2016; Lentink & Dickinson, 2009; Percin & van Oudheusden, 2015b; Garmann et al., 2013). In Garmann & Visbal (2014) it was shown that vortex breakdown occurs around midspan for each aspect ratio and showed a strong dependence on the spanwise pressure gradient established between the root and the tip. Between the midspan and the wing tip a substantial bubble-like structure is formed. The LEV bubble-like structure grows with span until about 75% of the span at which the LEV is lifted-off the surface (Carr et al., 2013; Garmann & Visbal, 2014). Jones et al. (2016) experimentally studied a rectangular revolving wing with a Reynolds number of 2,500 and an aspect ratio of two at an angle of attack of 45 deg. Vortex breakdown was found to occur at midspan and is characterized by axial flow reversal, entrainment of opposite-sign vorticity and a rapid expansion of the vortex structure into a bubble like-structure. A proper orthogonal decomposition and the location of the centroid of a vortex were concluded to be most useful in identifying the phase angle at which vortex breakdown occurs.

Spanwise characteristics Poelma et al. (2006) experimentally studied an impulsive revolving wing at an angle of attack of 50 deg with a Reynolds number of 256. The wing planform is based on a *Drosophila* wing. In Figure 2.8 the spanwise circulation as function of formation number is given. The spanwise component of the LEV grows proportional to the formation (traveled distance / chord) number (FN). The peak for different spanwise sections is observed at a similar formation number of 2. At the TE the circulation peak builds up at roughly the same rate. However, at the TE-base, significant circulation is shed early in the revolving motion. The peak circulation at the tip is higher than at the base.

Birch et al. (2004) studied a steady revolving rigid wing that is based on a *Drosophila* wing planform at an angle of attack of 45 deg for a Reynolds number of 120 and 1,400. The sectional lift coefficient that is based on the Kutta-Joukowski theorem is given in Figure 2.9. For decreasing Reynolds number less circulation is built up due to the influence of viscosity. For a Reynolds number of 1,400 the sectional lift distribution is increased along the span of the wing until approximately $0.65r/R$ at which the sectional lift reached a maximum, after which it decreases towards the tip. Garmann & Visbal (2014) calculated the sectional lift coefficient for steady-state conditions, i.e. a rotation angle of 270 deg as given in Figure 2.9. For an aspect ratio of two, the sectional lift distribution is increased along the span of the wing until approximately 70% at which the sectional lift reached a maximum, after which it decreases to zero at the tip.

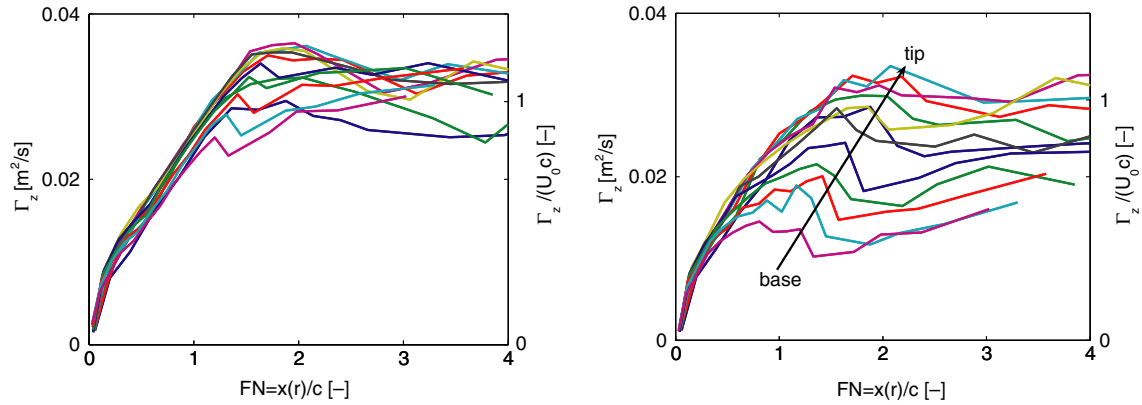


Figure 2.8: Spanwise circulation Γ_z as a function of formation number FN (Poelma et al., 2006). *Left:* Leading edge. *Right:* Trailing edge.

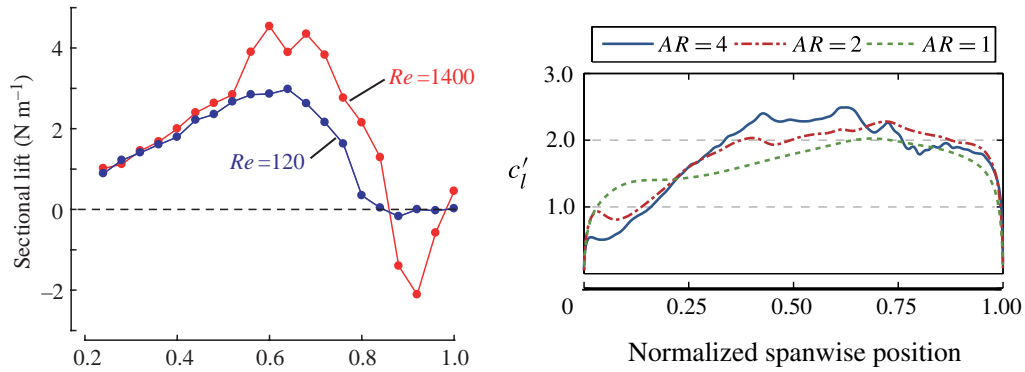


Figure 2.9: *Left:* Sectional lift coefficient based on the Kutta-Joukowski theorem as a function of spanwise position (Birch et al., 2004). *Right:* Sectional lift coefficient as a function of spanwise position (Garmann & Visbal, 2014).

Wing planform shape In (Usherwood & Ellington, 2002) it was found that quite radical changes for different leading edge shapes did not significantly influence the aerodynamic forces. Kruyt et al. (2015) experimentally studied the revolving flat-plate wings with different aspect ratios. It was found that the lift and drag values of the rectangular flat-plate wing models fall in the range of the lift and drag values generated by the wings of 12 hummingbird species.

2.3.2 Flexible wings

Natural flyers typically have flexible wings which are challenging to model because of the complex fluid-structure interference effects. This can be simplified as follows: The fluid flow creates pressure and viscous stresses which deform the wing. As a result, the wing changes shape which affects the fluid flow again. This results in a moving boundary problem under the effect of the fluid flow around the boundary.

Flexural stiffness Flexural stiffness is expressed as EI , where E is the Young's modulus and I is the area moment of inertia of a cross sectional area. Combes (2003) found that for natural flyers the wing size is the dominant factor in flexural stiffness scaling and that the spanwise flexural stiffness is 1-2 orders of magnitude higher than the chordwise flexural stiffness. This anisotropy is bigger for larger wing sizes.

Effective stiffness The ratio of elastic bending forces over fluid-dynamic forces for a rigid chordwise flexible wing is approximated using the effective stiffness parameter Π_1 . Combes (2003) report that if the wing flexural stiffness is a functional scaling parameter, elastic similarity should be maintained. Elastic similarity holds that the angular wing deflection should remain constant: $\delta/L = \text{cons}$ (McMahon, 1973).

Wing shape: Wing inertial, elastic and fluid forces In general the passive pitch motion of flapping wings are balanced by the wing inertial, elastic and fluid forces. In Figure 2.10 an illustration is given of the relative importance of the inertia-elastic, and the fluid dynamic vortex force and added mass contribution as function of the reduced frequency (k), and the density ratio (ρ^*) times thickness ratio (h_s^*).

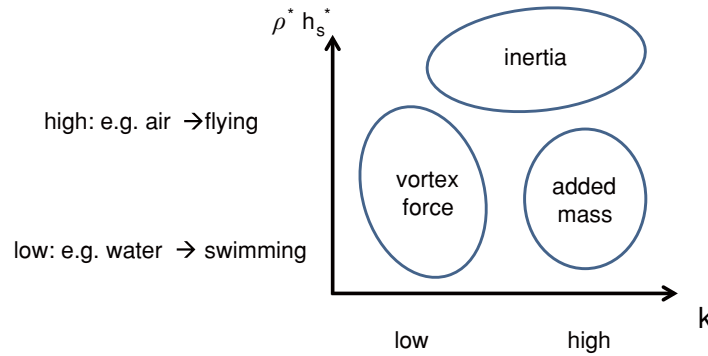


Figure 2.10: Dominant mechanisms for force generation that is responsible for the wing deformation as function of the reduced frequency (k), and the density ratio (ρ^*) times thickness ratio (h_s^*). Inertia force is the inertial-elastic force acting on the wing due to the wing acceleration relative to the imposed motion at the wing root. (Shyy et al., 2013).

where the density ratio is defined as $\rho^* = \rho_s/\rho_f$, ρ_s is the density of the wing structure and ρ_f is the fluid density. The thickness ratio is defined as $h^* = h/c$ where h is the wing thickness and c is the mean chord. At low density ratios the fluid-dynamic vortex force, indicating the interaction of the vortices with the wing and the added mass force, is of higher relative importance compared to high density ratios in the formation of the wing shape.

For water the density ratio is of the order ($O(1)$) and the forces that are responsible for the wing deformation are dominated by the fluid-dynamic vortex or added mass forces. For air the density ratio (ρ^*) is of the order $O(10^3)$ and the forces that are responsible for the wing deformation are dominated by the inertial-elastic forces. As a result, for high density ratios that are dominated by inertial-elastic forces, it may be possible to decouple the fluid-structure problem (Daniel, 2002). A simplified model structural model (i.e. linear beam theory or

finite element method) can be used to compute the instantaneous spatial bending pattern. Subsequently, this wing design can be used within the fluid-dynamic model to determine the fluid forces acting on the model.

For a constant angular velocity wing inertia is negligible and the forces can be attributed to fluid dynamic phenomena (Dickson, 2004). Subsequently, for a unidirectional steady-state chordwise flexible revolving wings the TE deflection can be expressed in terms of the fluid-dynamic normal force coefficient C_N and the effective stiffness Π_1 (see Equation 2.7) by means of the steady Euler-Bernoulli beam equation as,

$$\delta_{TE}/c = \frac{C_N}{16\Pi_1} \quad (2.8)$$

Flexible revolving wings Although several studies have indicated the possible beneficial effects of flexibility on the aerodynamic performance (Shyy et al., 2010), experimental studies investigating flexible revolving wings remain scarce. Zhao et al. (2009) studied chordwise flexible wings with different degree of chordwise flexibility for different angles of attack at a Reynolds number of 2,000 for a steady-state revolving motion. The flexural stiffness was changed using different materials and sheet thicknesses over a range measured for insects (Combes, 2003). In Figure 2.11 the force coefficients are given as a function of angle of attack for different flexural stiffness values. It was observed that the lift-to-drag ratio is

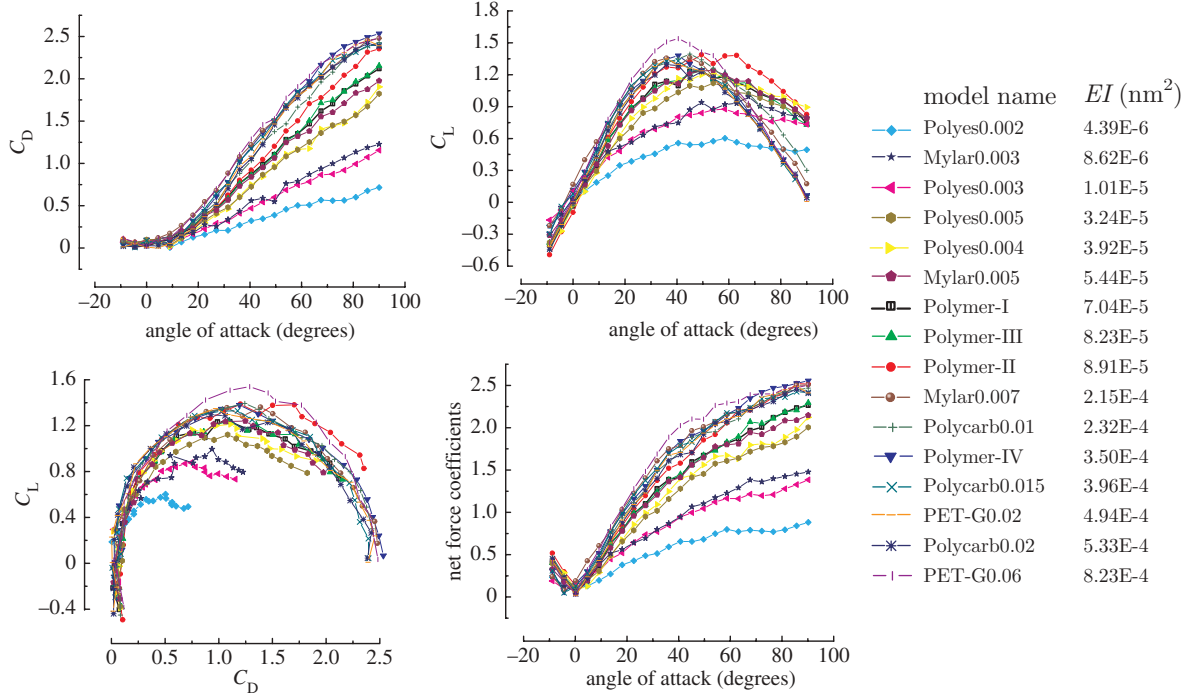


Figure 2.11: Force coefficients as a function of angle of attack for different flexural stiffness values (Zhao et al., 2009).

relatively insensitive to wing flexibility for angles of attack from 20 deg to 60 deg, while the ability to generate both lift and drag decreased. For $\alpha < 45$ deg the lift decreases with

decreasing flexural stiffness. However for $\alpha > 45$ deg low flexural stiffness wings reach a plateau while high flexural stiffness wings show a decrease in lift. For a rigid wing (high flexural stiffness) the maximum lift is observed at $\alpha = 45$ deg, however for flexible wings the maximum lift is dependent on the flexural stiffness. The aerodynamic force generation reduced monotonically for decreasing flexural stiffness. (Zhao et al., 2011) found that flexibility does not fundamentally change the aerodynamic flow structures, but the LEV is smaller for lower flexural stiffness and correlates with the aerodynamic forces. Beals & Jones (2015) studied a passive chordwise flexible revolving wing for Reynolds numbers from 10,000 to 25,000. For the flexible wing the lift was measured to be consistently lower than that of the rigid wing throughout the revolving motion, however, passive wing deformation mitigated the lift losses when a wake was encountered, i.e. for rotation angles larger than 360 degrees.

Besides from the possible beneficial effects of wing flexibility related to revolving wings, wing flexibility is also thought to be important in enhancing aerodynamic forces during rapid stroke reversals (Mountcastle & Daniel, 2009; Eldredge et al., 2010; Beals & Jones, 2015).

2.4 Summary

Natural flyers benefit from unsteady aerodynamic effects which enhance the aerodynamic performance. The unsteady mechanisms inherent for flapping-wing aerodynamics are: Wagner effect, clap and fling effect, Kramer effect, added mass effect, wake capture effect, and delayed stall and LEV. The stable LEV is one of the most prominent mechanisms sustaining flapping flight and is driven by a revolving wing motion.

Revolving wings translate around a central axis and approximate the sweeping (translational) aspect of a full flapping-wing motion. The sustained LEV occurring in a revolving motion is accompanied by a low pressure region at the suction side of the airfoil. The suction forces that act normal to the wing surface are dominant throughout the motion. The LEV lifts off as an arch-like structure and reorients itself along the chord through its connection with the TV. Different hypotheses have been proposed to explain the stability of the LEV during revolving flight, such as the spanwise advection of vorticity (Ellington et al., 1996), the downward induced flow from the tip, limiting the growth of the LEV (Birch & Dickinson, 2001) or the apparent rotational (Coriolis and centrifugal) accelerations that are characterized by a low Rossby number (Lentink & Dickinson, 2009). In this respect (Jardin & David, 2014, 2015) showed that although LEV attachment can be obtained by the spanwise advection of vorticity, the high aerodynamic performance is ensured by the apparent Coriolis effect. The Coriolis effect causes the LEV to stay close to the wing surface, such that the low pressure region associated with the LEV is located close to the wing surface resulting in high lift coefficients. An increased coherency of the vortex system was observed for a decreased aspect ratio and lower Rossby number, and it was suggested that the stability or retention of the LEV is coupled with the interior structure of the tip and root vortices. The LEV and overall vortex system are relatively insensitive for a significant range of low Reynolds numbers, however, at higher Reynolds numbers the vortex system becomes susceptible to instabilities and small scale structures are formed. A stable LEV was observed for a large range of angles of attack

from 15 deg to 70 deg. The maximum lift coefficient for a rigid revolving wing is found at an angle of attack of 45 deg. LEV breakdown was found to occur near midspan for different aspect ratio, at which a substantial bubble-like structure is formed that extends to the wing tip. The LEV bubble-like structure grows with span until about 75% of the span at which the LEV is lifted-off the surface. The sectional lift distribution is increased along the span of the wing until approximately 70% at which the sectional lift reached a maximum, after which it decreases to zero at the tip.

Although natural flyers have flexible wings and several studies have indicated the possible beneficial effects of flexibility on the aerodynamic performance (Shyy et al., 2010), the majority of the studies have investigated rigid revolving wings. For natural flyers the wing size is the dominant factor in flexural stiffness scaling of which the spanwise flexural stiffness is 1-2 orders of magnitude higher than the chordwise flexural stiffness. The lift-to-drag ratio is relatively insensitive to wing flexibility for angles of attack from 20 deg to 60 deg, while the ability to generate both lift and drag decreased. Flexibility does not fundamentally change the aerodynamic flow structures, but the LEV is smaller for lower flexural stiffness and correlates with the aerodynamic forces. For the flexible wing the lift was measured to be consistently lower than that of the rigid wing throughout the revolving motion, however, passive wing deformation mitigated the lift losses when a wake was encountered, i.e. for rotation angles larger than 360 degrees.

Chapter 3

Pressure & load reconstruction from PIV measurements

In this chapter the different methods available for the pressure and load reconstruction from PIV measurements are explained. The numerical methods for the reconstruction of the pressure field and loads that are used in this study are addressed in more detail in [chapter 5](#). First, the pressure reconstruction is addressed, after which more findings about the load reconstruction are given. An overview is given of the image and spatial resolution that have been used in literature for the reconstruction of pressures and loads from flow field data. Finally, findings about the pressure and load reconstruction for a rigid revolving wing are given.

3.1 Pressure reconstruction

Pressure fields contributions corresponding to a set of velocity data can be derived using:

- Navier-Stokes equations under incompressible flow conditions ([van Oudheusden, 2013](#))
- Coupling with Computational Fluid Dynamics (CFD) ([Jaw et al., 2009](#))
- Analytically eliminate the surface pressure integral from the Navier-Stokes equations in integrals of pure kinematic flow characteristics (velocity and vorticity) ([Noca et al., 1999](#))

By assuming incompressible flow the pressure reconstruction from velocity field data by means of the Navier-Stokes equations involves 2 steps,

- Computation of pressure gradients

- Integration of pressure gradients

Pressure gradient Assuming incompressible flow ($\rho = \text{cons}$; $\nabla \cdot \mathbf{u} = 0$) and a constant viscosity ($\mu = \text{cons}$) in the absence of gravity, the pressure gradient in an inertial reference can be obtained using the momentum equation as (van Oudheusden, 2013),

$$\nabla p = -\rho \frac{D\mathbf{u}}{Dt} + \mu \nabla^2 \mathbf{u} \quad (3.1)$$

where p is the pressure, \mathbf{u} is the velocity, ρ is fluid density and μ is the dynamic fluid viscosity.

For instantaneous pressure information of an unsteady flow phenomena, time information data is needed irrespectively of the integration technique chosen. For instance, for divergence free flow ($\nabla \cdot \mathbf{u} = 0$) there is no time information needed in the Poisson formulation, but to prescribe the Neumann condition (pressure gradient) time information is still required. In theory the formulation of the different pressure gradients (based on Eulerian, Lagrangian, or Poisson) are essentially equivalent. However, the different methods are used in discrete form and the type of implementation implies the propagation of the velocity error and the sensitivity to the spatial and temporal discretization. To get accurate spatial and temporal derivatives the velocities need to be accurately measured which puts additional constraints on the PIV experiment settings.

For the determination of the pressure field the most important sources of error are,

- Truncation error: Error by numerical discretization to estimate the acceleration
- Precision error: Error by propagation of the uncertainty of the individual velocity data

In the evaluation of the material derivative of the velocity ($\frac{D\mathbf{u}}{Dt}$), the Eulerian approach is expected to be more sensitive to advective motion, while the Lagrangian is more sensitive to rotation dominated flows because this complicates the flow path reconstruction (de Kat & van Oudheusden, 2012).

Integration of pressure gradient The integration of the pressure gradients can be performed using,

- Direct integration
 - Space-marching integration (Baur & Kongeter, 1999)
 - OMNI-directional integration (Liu & Katz, 2006)
 - * Median polling (Dabiri et al., 2014)
- Poisson equation
- Coupling with CFD

For external incompressible PIV flow measurements setting up a Poisson problem to integrate the pressure gradients is expected to perform best due to its smoothing properties that can suppress the errors present in PIV data (Charonko et al., 2010; Gurka et al., 1999). The Poisson equation is an elliptic linear partial differential equation. Because the equation is elliptic there are no characteristic directions of information propagation, such that boundary conditions are required along the full boundary of the domain of integration.

Phase averaging At low Reynolds numbers the flow is very repeatable for the same kinematic motion and justifies the use of phase-locked measurements (Poelma et al., 2006; Percin & van Oudheusden, 2015b), such that the acceleration information can be derived in the rotating reference frame. For phase-locked measurements the signal-to-noise ratio can be increased by means of ensemble averaging, such that the temporal resolution may be relieved. By assuming a Gaussian distribution of the measurements error its the random error scales with the standard deviation σ and the sample size N as σ/\sqrt{N} .

3.2 Load reconstruction

By evaluating a time-resolved flow and pressure field in a control volume, the loads on an immersed object can be evaluated using a control volume approach (Anderson, 2011).

The Reynolds transport theorem allows to relate the full-spatial-temporal acceleration information as,

$$\int_{V(t)} \frac{\partial \rho \mathbf{u}}{\partial t} dV = \frac{d}{dt} \int_{V(t)} \rho \mathbf{u} dV - \int_{S(t)+S_b(t)} \rho \mathbf{u} (\mathbf{u}_{CV(b)} \cdot \mathbf{n}) dS \quad (3.2)$$

where $V(t)$ is the control volume, $S(t)$ is the external contour of the control volume, and $S_b(t)$ is the internal contour of the control volume (as depicted in Figure 5.4). By assuming a divergence free flow ($\nabla \cdot \mathbf{u} = 0$), the control volume approach can be expressed in pure surface integrals using the "Derivative Moment Transformations" (DMT) (Wu et al., 2005; Mohebbian & Rival, 2012) as,

$$\frac{d}{dt} \int_{V(t)} \rho u_i dV = \frac{d}{dt} \int_{S(t)+S_b(t)} \rho x_i u_j n_j dS \quad (3.3)$$

where x_i is the position vector from any fixed origin in space.

3.2.0.1 Overview of image and spatial resolution for pressure/load reconstruction from flow field data

Based on (Poelma et al., 2006; van Oudheusden et al., 2006, 2007; David et al., 2009; Ragni et al., 2011; Mohebbian & Rival, 2012; Gharali & Johnson, 2014; Tronchin et al., 2015) the spatial resolution (SR) and image resolution (IR) are evaluated that have been used for the

pressure and load reconstruction from flow field data. In Figure 3.1 the SR is plotted against the IR, and the SR and IR with the chord as reference length are plotted against the field of view (FOV) for the studies mentioned above.

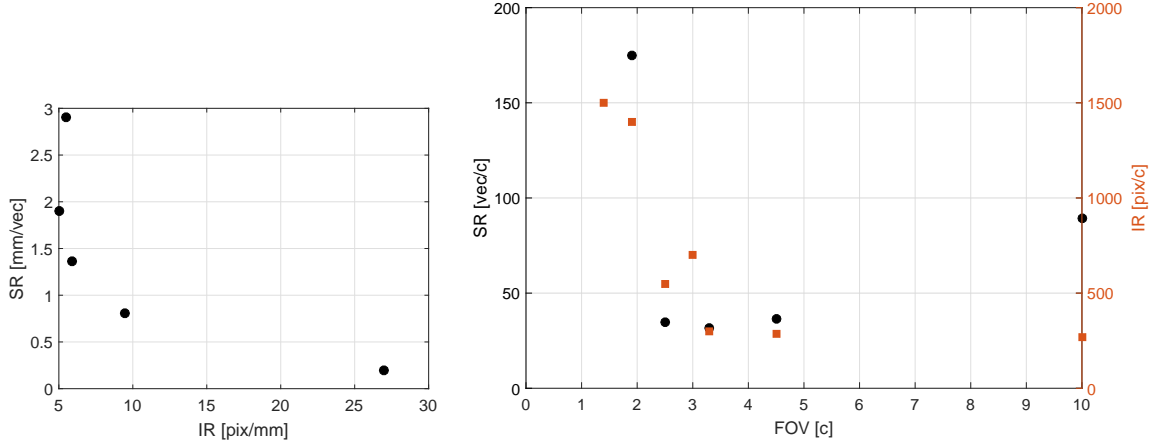


Figure 3.1: *Left:* Spatial- and Image resolution. *Right:* Spatial (\circ)- and Image (\square) resolution as a function of FOV. Resolutions taken in the freestream direction corresponding to the direction of drag.

It can be seen that the SR and IR in the different experimental studies differs significantly. Although no common set of SR and IR are observed, some limits can be identified. An approximate lower limit for the SR of 31 vec/c , and an approximate lower limit for the IR of 285 pix/c can be identified. Moreover, it can be observed that for a smaller FOV often a higher SR and IR are used.

Mohebbian & Rival (2012) numerically studied the unsteady load estimation of a flat-plate with a periodic gust input by means of the DMT method. It was concluded that the loads from velocity field data were determined accurately if the spatial resolution is sufficiently high. A line integration was performed around the control volume boundary to evaluate the pressure term. If wake vortices are present on the control volume boundary large velocity gradients need to be evaluated. With limited spatial and temporal resolution, large errors are introduced within the evaluation of these velocity gradients which mainly affects the drag estimation. Gharali & Johnson (2014) experimentally studied the loads in dynamic stall for a Reynolds number of 40,000 for a reduced frequencies range of $0.05 < k < 0.12$. A line integration was performed to evaluate the pressure term from the PIV measurements. In this study it was concluded that the lift is determined best for a small FOV with a high SR. If vortices are present at the downstream control volume boundary, the drag is determined best if the location of the downstream control volume boundary is placed such that it is not disturbed by the wake vortices and its large velocity gradients.

Ragni et al. (2011) experimentally studied the loads of a propeller blade at a Reynolds number of 310,000 and a Mach number of 0.6. Phase-locked stereoscopic measurements were performed. The pressure field data was reconstructed from the flow field data with of a Poisson integration scheme. A comparison of the pressure field with CFD computations shows a

reasonable agreement, with a maximum mismatch on the order of 10%, in the entire measurable PIV region. The PIV-based lift coefficient was comparable to the CFD computations, while the drag coefficient is predicted less accurately, showing differences in the order of 20%.

3.3 Pressure & load reconstruction on a rigid flapping revolving wing

Tronchin et al. (2015) experimentally studied the loads and pressure field for a flapping revolving wing at a Reynolds number of 1,000 using 3D3C velocity data obtained from phase-averaged cross-correlated stereo-PIV planes. The pressure was evaluated using an iterative direct integration technique with alternating directions of the integration paths to limit the directional dependency of error propagation. The acceleration information is determined in an inertial frame by acquiring, per phase angle, 5 volumetric images with small time shifts and subsequently calculating the acceleration from the velocity fields furthest separated in time, with a corresponding temporal resolution of 150 ms. The reconstructed force coefficients, based on an integral momentum approach as well as an integral of the pressure field on the surface of the wing, are compared with DNS simulations as illustrated in Figure 3.2.

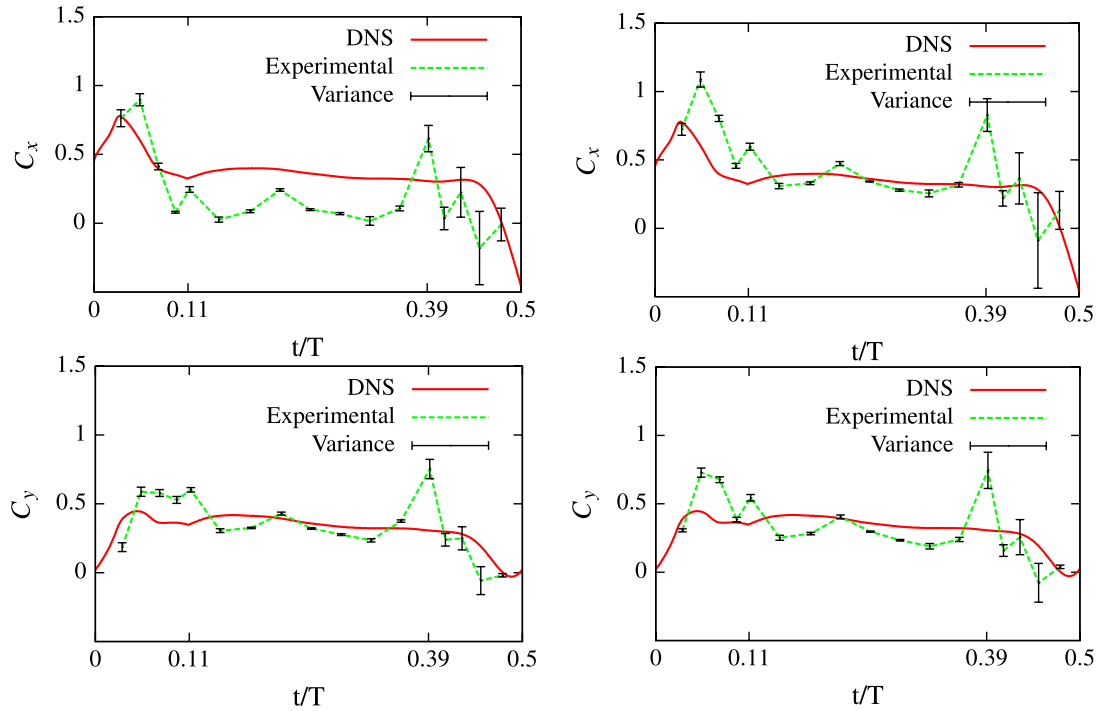


Figure 3.2: Force coefficients as a function of time over plunging period (Tronchin et al., 2015). x, y indicate the forces in respectively the drag, lift direction. *Left:* Integral momentum equation. *Right:* Integral at the surface of the wing

The results of the integral momentum equation approach are similar to those obtained by directly evaluating the pressure field on the surface of the wing. The low level of variance for both the integral momentum equation and the integral at the surface of the wing suggests

an homogeneous evolution of loads over different periods of motion, excepted during the deceleration phase. This study suggests that the calculated pressure field is obtained with sufficient accuracy for a global analysis of the topology of the flow field and the evaluation of loads acting on an immersed object.

3.4 Summary

For an incompressible flow the instantaneous pressure field can be calculated from a time-resolved velocity field. Pressure gradients are obtained from the Navier-Stokes momentum equation and the pressure field is calculated by the integration of the pressure gradients. At low Reynolds numbers the flow is very repeatable for the same kinematic motion and justifies the use of phase-locked measurements (Poelma et al., 2006; Percin & van Oudheusden, 2015b), such that the acceleration information can be derived in the rotating reference frame. In the evaluation of the material derivative the Eulerian approach is expected to be more sensitive to advective motion, while the Lagrangian is more sensitive to rotation dominated flows because this complicates the flow path reconstruction (de Kat & van Oudheusden, 2012). For external incompressible PIV flow measurements, setting up a Poisson problem to integrate the pressure gradients is expected to perform best due to its smoothing properties that can suppress the errors present in PIV data (Charonko et al., 2010; Gurka et al., 1999). Tronchin et al. (2015) experimentally studied the loads and pressure field for a flapping revolving wing at a Reynolds number of 1,000 using 3D3C velocity data obtained from phase-averaged cross-correlated stereo-PIV planes. This study suggests that the calculated pressure field is obtained with sufficient accuracy for a global analysis of the topology of the flow field and the evaluation of loads acting on an immersed object. The spatial resolution and the FOV that have been used in PIV measurement campaigns show a large variation in the literature. For the PIV imaging settings it is expected that when a wake contains many vortices, it is beneficial to have a smaller FOV with a higher spatial resolution to accurately evaluate the relative high velocity gradients in a vortex. Based on literature a lower limit for the spatial resolution of approximately $31 \text{ vec}/c$ is found for the reconstruction of pressure and load information from flow field data.

Chapter 4

Experimental Methods

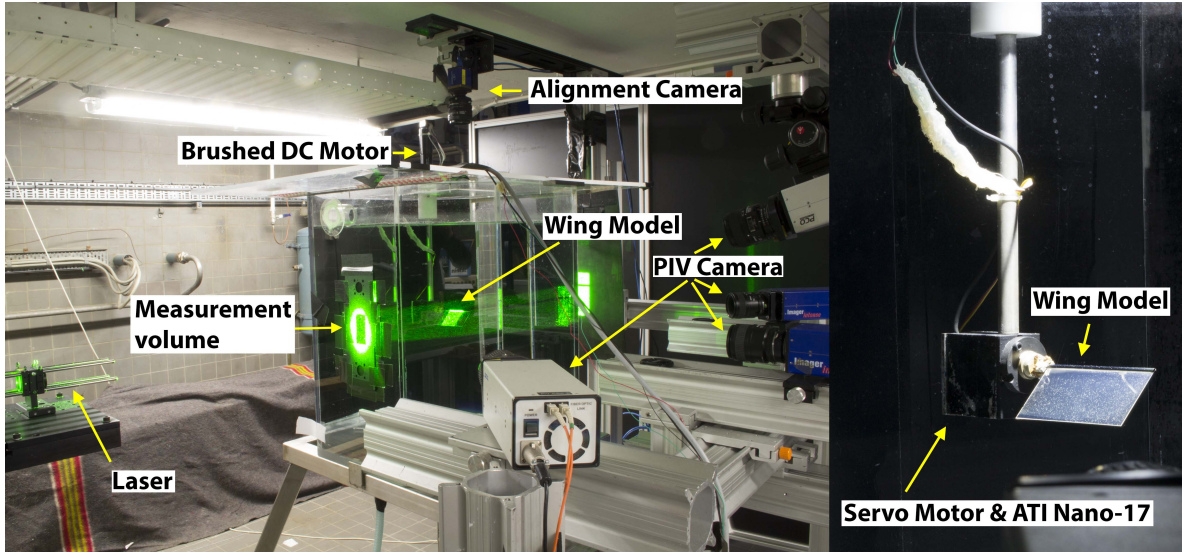
Phase-locked tomographic PIV measurements were performed in three volumes along the wing span for different phases of the revolving motion in order to obtain time resolved 3D3C flow field data sets around the wing. Simultaneous direct force and moment measurements were carried out by means of a six component water submergible force sensor.

4.1 Experimental Setup & Model description

The experiments were conducted in a water tank (Figure 4.1) at the Aerodynamic Laboratory of Delft University of Technology (TU Delft). The octagonal tank (600 mm in diameter and 600 mm in height) is made of Plexiglas walls allowing full optical access for illumination and imaging (Figure 4.1). The main axis of the driving system is mounted vertically in the water tank. The revolving motion of the model is controlled by a brushed DC motor and a gearbox (gear ratio of 132:1). A submerged servo motor connected to the wing is used to control the angle of attack, which is set to 45 deg in the present experiments. The model consists of a flat plate with a chord length (c) of 50 mm and a span length (R) of 100 mm, resulting in a wing aspect ratio of 2. At the leading edge 1.5 mm radius halfround carbon fiber rods are glued on the upper and lower side of the wing to provide spanwise rigidity. This leading edge structure extends at the wing root at which it is clamped in the mount. The offset between the mount and the wing root is 1 mm. An overview of the wing planform parameters can be found in Table 4.1.

Table 4.1: Wing planform parameters (Carbon fiber properties: vDijk Pultrusion Products).

Property	Value
Chord (c)	50 mm
Span (R)	100 mm
Aspect ratio (AR)	2
LE carbon fiber rod radius	1.5 mm

**Figure 4.1:** Experimental setup; *Left:* Overview. *Right:* Close-up of the wing model.

4.2 Kinematics

The three-quarter (75%) span length of the wing model is taken as the reference position to characterize the motion kinematics. The non-dimensional parameters describing the motion kinematics are: convective time ($t^* = t \cdot V_t / c$, where t is time in seconds and V_t is the constant terminal velocity established after the acceleration phase) and chords traveled ($\delta^* = \delta / c$, where δ is the distance traveled by the wing at the reference spanwise position). The revolving wing motion starts from rest and is subjected to by a constant acceleration to reach a predefined V_t of 0.2 m/s over a time interval corresponding to a displacement of one chord length (i.e. $0 < \delta^* < 1$), after which the wing continues to revolve at a constant velocity (i.e. for $\delta^* > 1$).

The distance between the root and the rotation axis is 42 mm, giving a reference revolving length $R_{ref} = 117$ mm. This gives a terminal angular velocity Ω_t of 1.7094 rad/s and a constant angular acceleration $d\Omega/dt$ of 3.4188 rad/s². The chords traveled (δ^*) in the constant acceleration phase is described by $\delta^* = \frac{1}{4}t^{*2}$ and in the constant velocity phase by $\delta^* = t^*$. One chord length of travel ($1\delta^*$) corresponds to a rotation angle of $\theta = 24.49$ deg. The prescribed wing kinematics for the phase angles of the PIV measurements is illustrated in Figure 4.2.

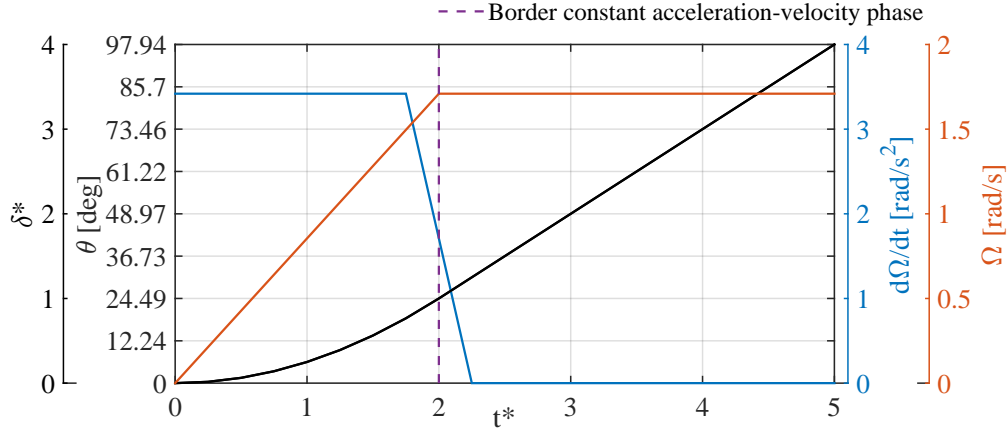


Figure 4.2: Wing kinematics for all phase angles: chord traveled (δ^*), rotation angle (θ), angular velocity (Ω) and angular acceleration ($d\Omega/dt$) as a function of convective time (t^*).

Based on the chord length and the terminal velocity defined at the reference position, the Reynolds number is 10,000 (see Equation 2.1). The approximate radius of gyration R_g around the revolving axis is calculated as,

$$R_g = \sqrt{I_{xx}/S} \quad (4.1)$$

where I_{xx} is the area moment of inertia of the wing area about the axis of forward motion (x -axis, see Figure 4.4) and S is approximately the wing area ($S = R \cdot c$). Based on the distance between the root and rotation axis, the radius gyration is $R_g = 96.4$ mm ($0.54r/R$) and the Rossby number is approximately $Ro = 1.93$ (see Equation 2.3).

An overview of the kinematics parameters is given in Table 4.2.

Table 4.2: Kinematics parameters based on 75% span position.

Property	Value
Constant acceleration phase	$0 < \delta^* < 1$
Constant velocity phase	$\delta^* > 1$
Rotation angle	$1\delta^* = 24.49$ deg
Terminal velocity V_t	0.2 m/s
Reynolds number Re	10,000
Rossby number Ro	1.93

4.3 Wing Flexibility

The chordwise flexural stiffness is approximated by using EI , where E is the Youngs modulus and $I = Rh^3/12$ is the area moment of inertia of the wings cross section along the chord, h being the thickness (variable). The effective stiffness, which represents the ratio of elastic

bending forces over fluid dynamic forces, is approximated using Π_1 , see Equation 2.7. Three models with different flexural stiffness have been studied by changing the material and plate thickness as given in Table 4.3.

Table 4.3: Wing model parameters for $c = 50$ [mm], $U_{ref} = V_t = 0.2$ [m/s], $AR=2$ and $\rho_f = 1000$ [kg/m³]. (PET properties: Hostaphan GN, Mitsubishi polyester film GmbH.)

Material	Young's modulus E [Nm ⁻²]	Thickness h [mm]	Flexural stiffness EI [Nm ²]	Π_1	Description
Plexiglas	$\approx 3300 \cdot 10^6$	1	$2.75 \cdot 10^{-2}$	55	1 [mm] Rigid
PET	$\approx 4350 \cdot 10^6$	0.175	$1.94 \cdot 10^{-4}$	0.389	175 [μ m] Moderate flexibility
	$\approx 4500 \cdot 10^6$	0.125	$7.32 \cdot 10^{-5}$	0.147	125 [μ m] High flexibility

The flexible wing thicknesses were selected based on preliminary balance measurements. The 175 [μ m] flexible wing was selected because the drag was lower while the lift had a similar magnitude compared to the 1 [mm] rigid wing. The 125 [μ m] flexible wing was selected because the lift decreased while the relative decrease in drag was still higher compared to the 175 [μ m] flexible wing.

The refractive index of the Plexiglas, PET and water is approximately 1.49, 1.57 and 1.33 respectively. Because the thicknesses are small the light distortions are limited.

4.4 Force Measurements

The force measurements are performed for an extended time interval of $0 < \delta^* < 14$.

Experimental setup The forces and moments exerted on the wing were measured with a water-submersible ATI Nano17/IP68 force sensor. The sensor is calibrated to have a maximum sensing value of 25 N in x , y and 35 N in z -direction with a resolution of 1/160 N, and a torque capacity of 250 N·mm with a resolution 1/32 N·mm. The force and moment data were acquired at 2 kHz acquisition frequency via an in-house developed LabVIEW code.

Signal processing For ensemble averaging of the force signals about 260 data records were used for the rigid wing and 200 for the flexible wings. These data records are based on the total number of force measurements. In Figure 4.3 the mean Power Spectral Density (PSD), based on an ensemble average size of 200, for both lift and drag force signals is given. From the 3 wing models, the test-rig for the rigid wing was observed to have the lowest natural frequency, which is 10 Hz. To eliminate electronic noise, effects of mechanical vibrations from the driving system and resonance of the test-rig, the ensemble averaged force data is filtered with a Chebyshev II low-pass filter that has a cut-off frequency of 8 Hz with a stopband attenuation of 80 dB. A forward-backward filtering technique is applied to prevent a time-shift of the data. Lift and drag coefficients are defined with respect to the reference velocity, which is the terminal wing velocity at the 75% span reference plane, see Equation 5.17.

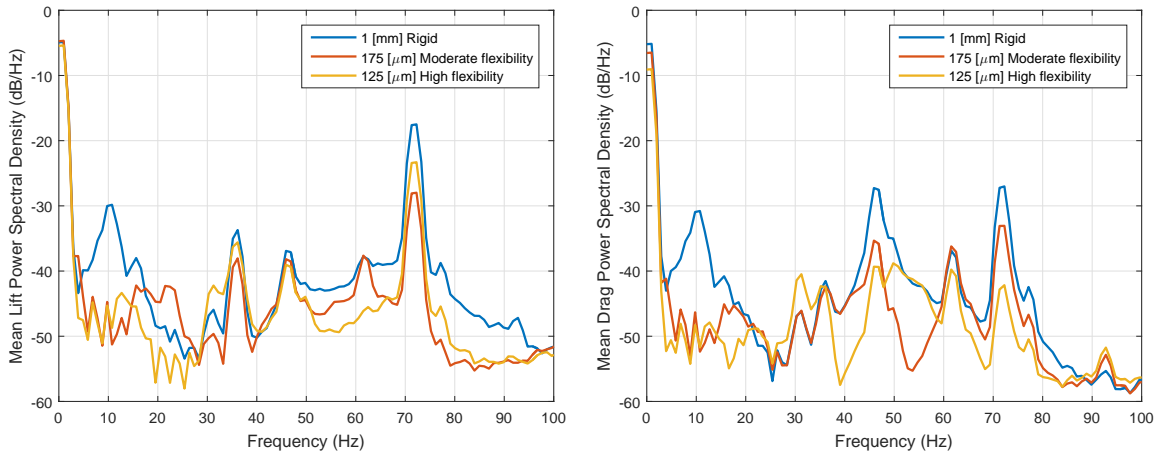


Figure 4.3: Mean Power Spectral Density based on an ensemble size of 200. *Left:* Lift. *Right:* Drag.

4.5 Volumetric flow imaging by tomographic PIV

4.5.1 Experimental setup & Experimentation

Imaging Figure 4.4 *left* shows a schematic top view of the tomographic PIV setup. Four 12 bit PCO Sensicam CCD cameras were used to record the particle images. Camera 1, 3 and 4 have a resolution of 1376×1040 pixels and a pixel pitch of $6.45 \mu\text{m}$ and are arranged on the same horizontal $x - z$ -plane with an aperture angle of 90 deg . Camera 2 has a resolution of 1280×1024 pixels and a pixel pitch of $6.7 \mu\text{m}$ and is located above camera 3 with an aperture angle of 20 deg with respect to the horizontal plane. Double frame images were taken at the moment in the motion when the wing is oriented normal to camera 3 and data for different revolving phases are obtained by appropriately changing the starting position of the wing revolution. Each camera was equipped with a Nikon 60 mm focal objective with numerical aperture $f_{\#} = 16$. Scheimpflug adapters were used on the three off-axis cameras to align the mid-plane of the measurement volume with the focal plane.

Illumination The volume was illuminated by a Quantel CFR 200 mJ double-pulsed Nd:Yag laser at a wavelength of 532 nm . Knife edges filters were used to constrain the illuminated volume.

Field of view The full flow field around the wing was captured by combining three tomographic measurement volumes, each measuring $100 \times 75 \times 45 \text{ mm}^3$ ($2c \times 1.5c \times 0.9c$) in the x, y, z -direction, respectively, as shown in Figure 4.4. The corresponding magnification factor is approximately 0.09. The volumes are symmetric with respect to the mid-span plane of the wing and have an overlap of 5 mm . The illumination volume was kept at a fixed position in the water tank, which corresponds to measurement volume 2 as indicated in Figure 4.4

left. To change the measurement volume the complete driving system was translated along the z -direction corresponding to the viewing direction of camera 3. The IR is approximately 13.76 pixels/mm (≈ 688 pixels/c). The particle images were interrogated using windows with a final size of $48 \times 48 \times 48$ voxels with an overlap factor of 75% giving an approximate spatial resolution of 0.87 mm/vector (≈ 57 vectors/c).

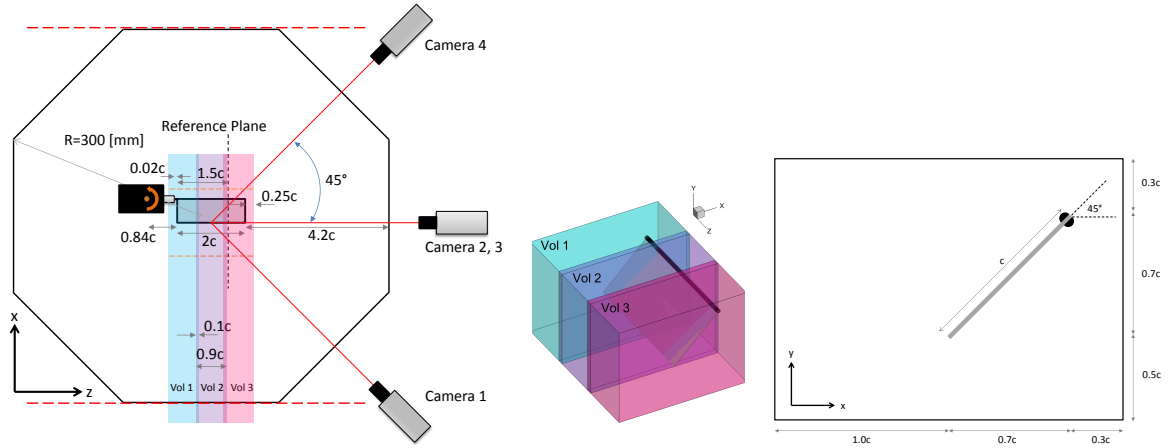


Figure 4.4: *Left:* Schematic top view and experimental setup. *Middle:* Schematic of the measurement volumes. *Right:* Schematic representation of the chordwise field of view. Schematics illustrated with a rigid wing.

Alignment of the Wing model - Field of view The wing model was connected to the brushed DC motor which was fixed to the top plate of the water tank. The top plate of the water tank can be translated in one direction. To align the wing chord normal to the viewing direction camera 3 for all three volumes, an additional alignment camera was used, see Figure 4.1. Finally the following conditions have to be met:

- The wing chord should be aligned normal to viewing direction of camera 3. This is manually checked with camera 3.
- The wing translation should be aligned with the top part translation. This is manually checked with the alignment camera. The top part can translate along the side edges of the water tank as indicated by the red dotted lines in Figure 4.4. When translating the top part of the water tank the wing model LE carbon fiber rod should only translate along its longitudinal direction.

Finally, to measure volume 2 the top plate was fixed with screws. To measure volume 1 & 3, the top part was translated over a predefined distance of 40 mm such that there is a 5 mm overlap between volumes.

Seeding Polyamide spherical particles of 56 μm diameter were used as tracer particles. They have a sufficiently small slip velocity with respect to water, remain suspended in the water for a long time and have good scattering properties due to its relatively large size.

Furthermore they have shown to be good tracer particles in similar tomographic PIV experiments (Percin & van Oudheusden, 2015b). The seeding concentration, expressed in particles per pixel (ppp), is approximately 0.035-0.04. The corresponding source density (N_s) is approximately 0.35-0.4.

Flow conditions After each measurement there is a pause of 3 minutes in order to let the water in the tank reach quiescent conditions. The waiting period of 3 minutes between consecutive measurements was tested by means of reconstructing the velocity fields for the first phase angle ($\delta^* = 0.0625$). It was confirmed that the flow is undisturbed in the domain upstream of the wing.

Image acquisition Because the flow is repeatable at low Reynolds numbers for the same kinematic motion a time resolved velocity field can be created from phase-locked measurements (Poelma et al., 2006; Percin & van Oudheusden, 2015b). An ensemble averaging size of 5 is used to further increase the signal to noise ratio of the velocity field data. The PIV measurements were taken for the interval $0.0625 < \delta^* < 4$. For the rigid case a temporal resolution (TR) is set to 62.5 ms for the entire interval, which corresponds to a non-dimensional temporal resolution ($TR^* = TR \cdot V_t / c$) of 0.25, generating 19 revolving phases. For the flexible wings, the $TR^* = 0.25$ for $0.0625 < \delta^* < 1.5$ and $TR^* = 0.5$ for $1.5 < \delta^* < 4$, generating a total of 14 revolving phases. The three-dimensional flow fields were ensemble averaged with a sample size of 5 obtained by repeating the measurements for each phase. This gives a total number of 705 measurements. The average time required for each measurement was approximately 6 minutes. In Table 4.4 an overview is given of all the measured phase angles for the rigid and flexible wings.

Table 4.4: Overview measured phase angles in terms of δ^* .

δ^*	0.0625	0.140625	0.25	0.390625	0.5625	0.765625	1	1.25	1.5	
1 [mm] Rigid	✓	✓	✓	✓	✓	✓	✓	✓	✓	
175 [μm] Moderate flexibility	✓	✓	✓	✓	✓	✓	✓	✓	✓	
125 [μm] High flexibility	✓	✓	✓	✓	✓	✓	✓	✓	✓	
δ^*	1.75	2	2.25	2.5	2.75	3	3.25	3.5	3.75	4
1 [mm] Rigid	✓	✓	✓	✓	✓	✓	✓	✓	✓	✓
175 [μm] Moderate flexibility		✓		✓		✓		✓		✓
125 [μm] High flexibility		✓		✓		✓		✓		✓

The lower number of measurements for the flexible wings was a compromise to limit the total measurement time. Because the exact temporal requirements for a good pressure reconstruction were not known beforehand the rigid wing had a high temporal resolution for all phases. For the flexible cases a high temporal resolution was taken in the initial acceleration and velocity phase up to $\delta^* = 1.5$.

The time separation between the double frame exposures is set such that the maximum particle displacement is about 10 pixel. An approximate time separation Δt between exposures

is approximated in terms of the kinematics, camera properties and field of view as,

$$\Delta t = \frac{10 \cdot \frac{1}{TR}}{\Omega \cdot R_{\max}} \quad (4.2)$$

where R_{\max} is the spanwise distance between the revolving axis and the tip part of each volume.

Table 4.5: Summary of experimental settings for tomographic PIV measurements.

Tomographic PIV	Phase-locked double frame images Time resolved velocity field
Imaging	4 × PCO Sensicam CCD camera Resolution Camera 1,3,4: 1376×1040; pixel pitch: 6.45 μm Resolution Camera 2: 1280×1024; pixel pitch: 6.7 μm 4 × Nikon 60 mm objective, $f_{\#} = 16$
Field of view	3 volumes of 100×75×45 mm ³ (2c×1.5c×0.9c) in the x, y, z -direction Image resolution: 13.76 pixels/mm (≈ 688 pixels/c) Spatial resolution: 0.87 mm/vector (≈ 57 vectors/c)
Illumination	Quantel CFR 200 mJ double-pulsed Nd:Yag laser Wavelength: 532 nm
Seeding	Polyamide spherical particles Mean diameter: 56 μm Concentration: ppp \approx 0.035-0.04 Source density: $N_s \approx 0.35$ -0.4
Flow conditions	Time between consecutive measurements: 3 minutes
Image acquisition	Rigid: TR*=0.25 Flexible: TR* = 0.25 for $0.0625 < \delta^* < 1.5$ and TR* = 0.5 for $1.5 < \delta^* < 4$ Ensemble average size: 5 Maximum particle displacement: 10 pixels

Discussion on the limitations of the experimental setup & experimentation Due to the strong scattering behavior of the particles a numerical aperture of $f_{\#} = 16$ could be used ensuring that the focal depth spanned the 45 mm field of view in the z -direction. To ensure the relative high spatial resolution of 0.9 mm/vector for a field of view of 100×75 mm² in the respective x, y -direction (see in Figure 4.4 *right*), the particles were interrogated with a window box size of 48×48×48 and an overlap factor of 75%. To perform a robust cross-correlation 5-10 particles in an interrogation box are required (Scarano, 2013). To cover the complete model in spanwise direction (z -direction) with 3 volumes of 45 mm and an interrogation window of 48×48×48, an approximate minimum of ppp= 0.03 is required. The high ppp and corresponding high source density was a compromise in order to span the model with only 3 volumes. Because the seeding concentration drops over time an $0.035 < \text{ppp} < 0.04$ was used when new seeding was applied. The reconstruction quality was additionally monitored by an intensity z -profile as given in Figure 4.5. The edge of the measurement

volumes drop quickly which indicates that only particles inside the volume are illuminated. The signal-to-noise ratio is approximately $14/8$ counts ≈ 1.75 , with a corresponding ghost level of approximately $8/(14 - 8)$ counts $\cdot 100\% \approx 130\%$. Although this ghost level is relatively high, the correlation for the vector calculation is quite robust. Therefore, it is expected that the reconstructed velocity vectors are representative for the true flow field vectors. To increase the signal to noise ratio of the velocity data an ensemble averaging sample size of 5 for each phase is used. Ensemble sizes of 3, 5 and 8 were tested. The ensemble size of 5 was selected as it is a compromise between the incremental improvement of the velocity field data and the measurement time.

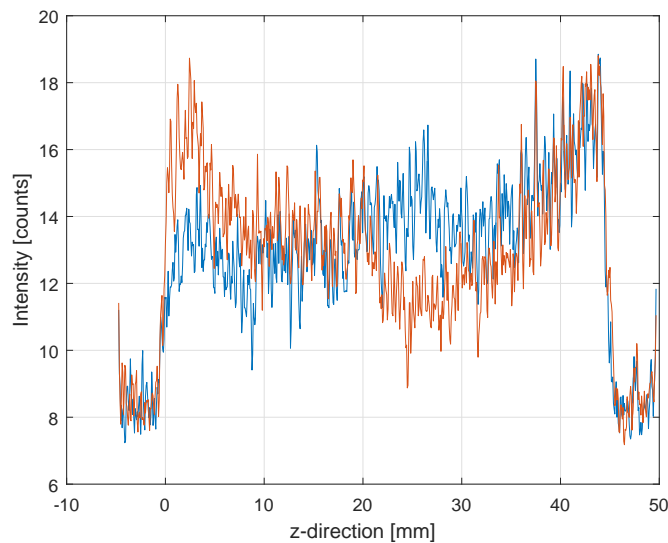


Figure 4.5: Intensity z -profile 1 [mm] Rigid wing, $\delta^*=0.0625$, Volume 3. Red and blue lines indicate the 2 double frame image laser pulses

4.5.2 Data processing

In the following section the data processing is explained. The commercial software package DaVis version 8.1.6. from LaVision GmbH is used for all the data processing.

4.5.2.1 Calibration

All tomographic PIV measurements are calibrated using a single geometric calibration to ensure that the coordinate system is fixed in inertial space for all measurements. For geometric calibrations a type-10 3D calibration plate from LaVision GmbH is used. The geometric calibration is based on a third order polynomial fit of 4 equidistant images that span from 0 to 45 mm in z -direction. The 0 and 45 mm plate calibration planes are aligned with the illumination volume (Figure 4.4 *left*). The residual of the curve fitting the calibration data is approximately 0.2 [pix]. To ensure an accuracy of 0.1 [pix] in misalignment error, volume self calibrations are performed once every 2 revolving phase measurement series. The volume self calibration is based on 100 images of particles moving in the measurement volume in absence

of the wing. The obtained misalignment error, after volume self calibration, is reduced to approximately 0.01 [pix].

4.5.2.2 Image pre-processing

All images are pre-processed first by subtracting a sliding minimum of 7×7 pixels in order to remove the background noise and eliminating most of the reflections of the model. Second, the images are normalized to the first exposure of camera 1 based on a local average. The size of the local normalization filter is 51 pixels and is applied for each image separately.

4.5.2.3 Vector calculations

After 2 consecutive phase angles new volume self-calibrations were performed. Because the volume self-calibrations needed to be performed manually only 2 phase angles per measurement day were processed per data processing day. This allowed for a higher number of iteration and search window related settings for the vector calculations than necessary without increasing the total time required for the data processing. As a result a high convergence was reached for the resultant vector calculations.

Volume reconstruction The reconstructed volume is based on the common volume seen by all cameras to increase the quality of the volume reconstruction. The particle volume is reconstructed using the fast MART algorithm with a MinLOS initialization, 13 CSMART iterations and 12 Smooth iterations.

Volume correlation (direct correlation) The cross correlation was performed with 4 steps. All steps have a spherical window shape with Gaussian weighting to decrease the number of outliers. All steps have an overlap of 75% to allow for a more accurate detection of the small flow structures.

The correlation window size is lowered within 4 steps from 128×128 - 96×96 - 64×64 - 48×48 voxels. The principle of multiple steps is that the rough particle shift (predictor) is detected in the initial step. Next, the volumes for the next step are deformed by the estimated shift (predictor) and the remaining particle shift is calculated (corrector), and added to the predictor.

In step 1,2 and 3 volume binning is used to detect the rough shift. This approach allows to decrease the computation time. In the final step no volume binning is applied to resolve the remaining detected sub pixel changes as the final corrector.

The maximum peak search radius in the step 1 is 24×24 voxels in order to find the maximum particle shift in the flow field. Next, the peak search radius is lowered in order to decrease the computation time.

In Table 4.6 an overview is given of the vector calculation parameters.

Table 4.6: Overview parameters vector calculation.

Step	Size [voxel]	Shape	Overlap %	Peak search radius [voxel]	Volume Binning	Passes
1	128	Spherical-Gaussian	75	24	8×8×8	2
2	96	Spherical-Gaussian	75	8	4×4×4	2
3	64	Spherical-Gaussian	75	2	2×2×2	2
4	48	Spherical-Gaussian	75	1	no	4

Between the different passes within a step spurious vectors that are present after cross correlation are detected and replaced using the universal outlier detection algorithm (Westerweel & Scarano, 2005). The parameters for the universal outlier detection are based on 2x remove & insert with an epsilon value of 0.1 pixels. The remove threshold is 2, the insert threshold is 3, the number of neighbors used for the calculation is 5×5×5 and the filter is only applied to vectors when the number of neighbors is above 6. Missing vectors are recursively replaced by the average of its direct neighbor vectors. Finally the vector field is smoothed twice using a Gaussian kernel of 3×3×3. For step 1, 2 and 3 two passes are used, while for the final step four passes are used in order to ensure the convergence.

4.5.2.4 Vector post-processing & Ensemble averaging

After the volume correlation again the universal outlier detection algorithm is applied. The parameters are the same as the one applied between the different passes, however the final vector field is only smoothed once.

Finally the 5 images per phase angle are ensemble averaged, giving the resultant vector field.

4.5.3 Wing reconstruction

The wing is reconstructed by use of a number of tracer points along the wing model. By visually identifying these points in all camera images and using the imaging calibration information, these points can be reconstructed in 3D space. At the leading edge, the angle of attack (AoA) is set to 45 deg by the servo motor at the beginning of the experiment. The deflection of the rigid wing is negligible and the flexible wings deform during the revolving motion under the effect of hydrodynamic loads.

For the rigid wing the tip-LE is reconstructed in volume 3. Next, tip-TE edge is reconstructed based on an angle of attack of 45 deg. Finally, the wing profile at the tip is extruded with $2c$ in the negative z -direction.

The flexible wings deflect and twist during the revolving motion. The chordwise deflection at the tip is reconstructed by defining equidistant points between the leading and trailing edge points in all images and further triangulation of these points (note that the leading edge point is defined on the wing surface after the carbon fiber rod). Subsequently, the twist angle is obtained by measuring the geometric angle of attack at 4 spanwise positions,

1. At the wing tip in volume 3
2. At the edges of measurement volume 2 by use of light reflection on the wing planform (see Figure 4.6 *right*).
3. At the wing root in volume 1.

A second degree polynomial is fitted to the acquired data point to represent the spanwise variation of the geometric angle of attack. The full wing is reconstructed based on the chordwise deflection information at the wing tip and the geometric angle information along the span. The wing reconstruction has a resolution of 60 points along the chord and 121 points along the span. The wing is spanned with $2c$ in z -direction from the identified tip region. In Figure 4.6 the images with reconstruction points for camera 1 are given by use of which the 125 [μm] High flexible wing is reconstructed at $\delta^* = 4$.

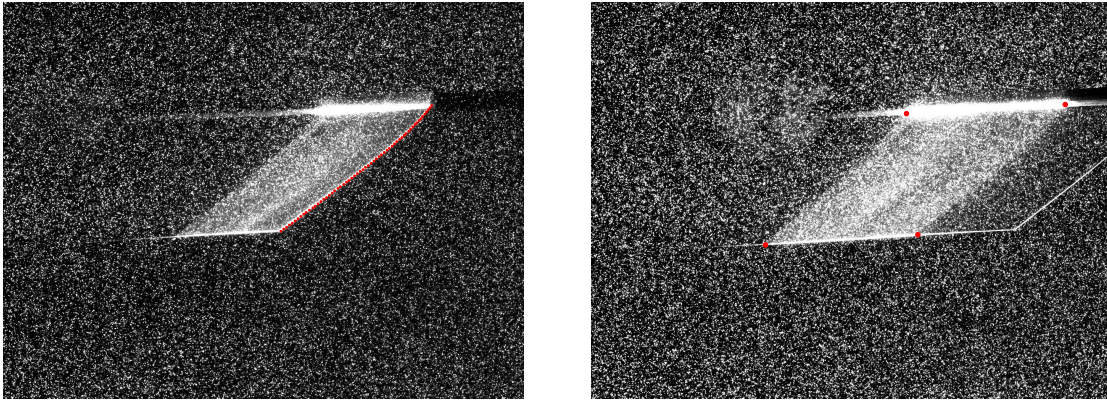


Figure 4.6: 125 [μm] High flexible wing reconstruction seen by camera 1 for $\delta^* = 4$. *Left:* Tip region - volume 3. *Right:* Middle region - volume 2

4.6 System integration & Measurement procedure

The full data acquisition setup is given in Figure 4.7. Three groups of equipment can be identified:

- Motion control and Force acquisition (Blue)
- PIV image acquisition (Orange)
- Synchronization (Green)

Blue The *blue* system controls the kinematics and acquires the forces. The setup contains a computer (PC 2), a data acquisition system, a balance which measures the forces and moments, a servo which controls the angle of attack and a brushed DC motor which controls the revolving motion. On PC 2 the LabView software is installed.

Orange The *orange* system acquires the PIV images. The setup contains a computer (PC 1), a Programmable Timing Unit, a laser and cameras. On PC 1 the DaVis software is installed.

Green The *green* system contains a digital pulse generator which can be set at a certain frequency.

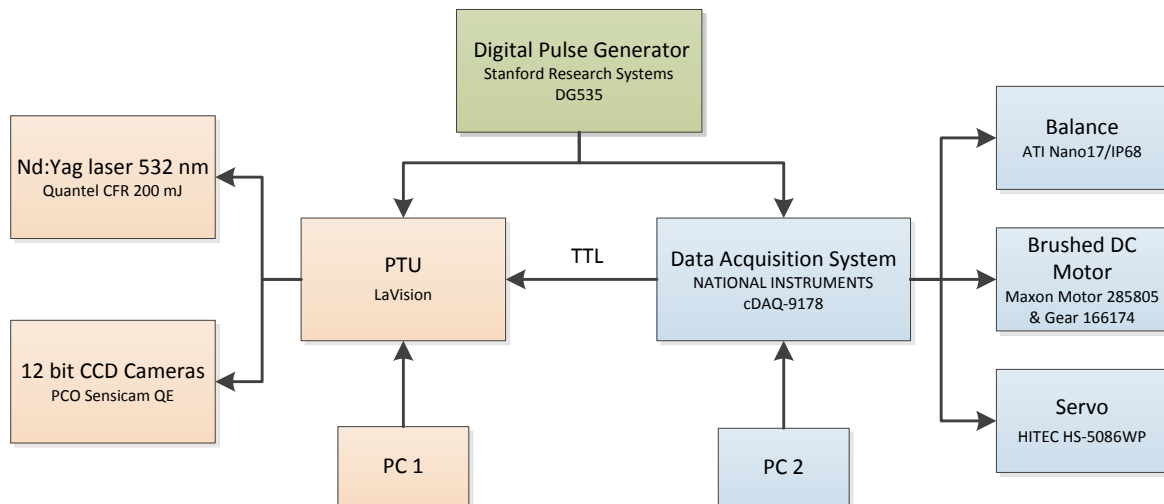


Figure 4.7: Data acquisition setup.

Blue-Orange-Green integration The digital pulse generator provides a reference signal for both the *blue* and *orange* system. An in-house developed LabView code controls the servo and brushed DC motors, and synchronizes the wing motion with the force data acquisition and the PIV measurements. This is accomplished by externally triggering the PTU by a TTL trigger signal which is generated by the LabView script. The image acquisition starts with the rising edge of the TTL trigger signal. Within the LabView script a time delay between the start of the revolving motion and the TTL trigger signal is introduced such that the 2 double frame images are taken symmetric with respect to the normal position of the wing, i.e. when the wing chord is aligned normal to viewing direction camera 3 (see Figure 4.4).

Measurement procedure The daily measurement procedure is given below. The sub items indicate the steps for each phase angle measurement.

- *Morning*
- The water tank is filled.
- Plate calibration images are taken.
- Seeding is applied.

- Volume self calibration images are taken.
 - Once every 2 phase angles the wing is cleaned, the seeding is checked and images for the volume self calibration are taken.
 - The phase angle is set in LabView.
 - The time separation between the double frame exposures is set such that the maximum particle displacement is about 10 pixels.
 - The time delay within LabView to generate the TTL trigger signal is set such that the double frame images are taken symmetric with respect to the aligned normal position of the wing chord in the viewing direction of camera 3.
 - A waiting period of 3 minutes is applied to reach quiescent flow conditions in the water tank.
 - Measurements are taken.
- The water tank is drained.
- *Evening*

Chapter 5

Numerical Methods

From the phase-locked tomographic PIV measurements 3D3C flow fields are obtained. In this chapter the methodology, which is followed to reconstruct pressure fields and loads from the 3D3C velocity data, is explained in detail. The calculations of the pressure fields and the loads are performed for each measurement volume individually. Additionally the pressure field is scaled between the volumes and expressed with respect to a reference pressure value.

The experiments are performed in water with the following approximate reference values,

Table 5.1: Fluid reference values based on water.

Property	Value
Density (ρ_f)	1,000 kg/m ³
Dynamic viscosity (μ_f)	$1 \cdot 10^{-3}$ N s/m ²

In the remainder of this chapter the fluid subscript f is omitted unless stated otherwise.

5.1 Pressure reconstruction

The pressure field reconstruction is carried out under the assumption of incompressible flow, employing the Navier-Stokes equations (van Oudheusden, 2013). Pressure gradients are obtained from the momentum equation and the pressure field is calculated by the integration of the pressure gradients.

At low Reynolds numbers the flow is very repeatable for the same kinematic motion, which justifies the use of phase-locked measurements (Poelma et al., 2006; Percin & van Oudheusden, 2015b). In view of this phase-locked measurement procedure, the pressure reconstruction is most conveniently set up in the rotating reference frame aligned with the revolving wing, regarding the evaluation of the temporal derivatives from the phase-locked flow field data

sets. The flow fields obtained in the PIV measurements are given in the inertial ‘laboratory’ reference frame. First, the conversion of the flow field from the inertial to the rotating reference frame is explained. Second, the pressure gradients are calculated in the moving reference frame. Third, the pressure gradients are integrated.

Note that, as the pressure is a scalar quantity, the reconstructed surfaces of constant pressure are independent of the reference frame (inertial or moving) that is used (Vanyo, 2015).

5.1.1 Flow field in rotating reference frame

The velocity field data is converted from the inertial reference frame to the rotating reference frame as,

$$\mathbf{u}_{\text{rotating}} = \mathbf{u}_{\text{inertial}} - \boldsymbol{\Omega} \times \mathbf{r}_{\text{pv}} \quad (5.1)$$

where \mathbf{u} is the velocity vector, $\boldsymbol{\Omega}$ the angular velocity of the wing (see Figure 4.2) and \mathbf{r}_{pv} the position vector measured from the rotation axis. The distance between the root of the wing and the rotation axis is 42 mm (0.84c, see Figure 4.4 *left*). From the rigid wing reconstruction the x, y, z -coordinates of the root-LE are approximated with respect to volume 1 as 29.9 [mm], 13.9 [mm], 11 [mm]. Consequently the position vector for each data point in the flow fields is calculated.

In the remainder of this section the considered velocity is the apparent velocity in the rotating reference frame unless specified otherwise.

5.1.2 Pressure gradient

Assuming incompressible flow ($\rho = \text{cons}$; $\nabla \cdot \mathbf{u} = 0$), a constant viscosity ($\mu = \text{cons}$) and discarding gravity, the pressure gradient in a rotating reference frame is given as (Vanyo, 2015),

$$\frac{1}{\rho} \nabla p = -\frac{D\mathbf{u}}{Dt} - \underbrace{\boldsymbol{\Omega} \times (\boldsymbol{\Omega} \times \mathbf{r}_{\text{pv}})}_{\text{Centrifugal}} - \underbrace{2 \boldsymbol{\Omega} \times \mathbf{u}}_{\text{Coriolis}} - \underbrace{\frac{d\boldsymbol{\Omega}}{dt} \times \mathbf{r}_{\text{pv}}}_{\text{Euler}} + \nu \nabla^2 \mathbf{u} \quad (5.2)$$

where p is the pressure and ν is the kinematic viscosity. Where for a Newtonian fluid and incompressible flow the shear stress τ_{ij} can be approximated as (White, 2006),

$$\tau_{ij} = \mu \left\{ \frac{\partial u_i}{\partial x_j} + \frac{\partial u_j}{\partial x_i} \right\} + \delta_{ij} \lambda \frac{\partial u_j}{\partial x_j} \left(\begin{array}{c} \frac{\partial u_j}{\partial x_j} = 0 \\ = \end{array} \right) \mu \left\{ \frac{\partial u_i}{\partial x_j} + \frac{\partial u_j}{\partial x_i} \right\} \quad (5.3)$$

and,

$$\begin{aligned} \frac{\partial}{\partial x_j} \tau_{ij} &= \frac{\partial}{\partial x_j} \left[\mu \left\{ \frac{\partial u_i}{\partial x_j} + \frac{\partial u_j}{\partial x_i} \right\} \right] \stackrel{\langle \mu = \text{cons} \rangle}{=} \mu \frac{\partial}{\partial x_j} \left\{ \frac{\partial u_i}{\partial x_j} + \frac{\partial u_j}{\partial x_i} \right\} \\ &\stackrel{\left(\frac{\partial u_j}{\partial x_j} = 0 \right)}{=} \mu \frac{\partial^2 u_i}{\partial x_j^2} = \mu \nabla^2 \mathbf{u} \end{aligned} \quad (5.4)$$

Newton's laws of motion are valid in an inertial reference system. The centrifugal, Coriolis and Euler effects introduce apparent forces due to working in a non-inertial reference frame. The centrifugal effect is independent of the fluid motion relative to the rotating reference frame and can be represented by a radial pressure distribution. The centrifugal effect, seen as a radial pressure distribution, can be calculated as the gradient of a scalar function as $\boldsymbol{\Omega} \times (\boldsymbol{\Omega} \times \mathbf{r}_{pv}) = -\frac{1}{2} \nabla [(\boldsymbol{\Omega} \times \mathbf{r}_{pv}) \cdot (\boldsymbol{\Omega} \times \mathbf{r}_{pv})]$ (Vanyo, 2015). The Coriolis effect is dependent on the velocity of the fluid relative to the rotating reference frame and therefore less straightforward to interpret when dealing with complex flows. The Coriolis effect is significant at low Rossby numbers. Its significance can be interpreted as the time required for a particle to complete its translational motion while having rotated a significant angle (Vanyo, 2015). The Euler effect is independent of the fluid motion relative to the rotating reference frame, and scales with the rotational angular acceleration of the rotating reference frame and the position vector. Note that the Euler effect only has a contribution in the acceleration phase (up to $1\delta^*$). Because the rotating reference frame is rotating purely about the y -axis the centrifugal, Coriolis and Euler effect do not contribute in the direction of lift (y -axis).

The material derivative ($\frac{D\mathbf{u}}{Dt}$), i.e. the acceleration of a fluid particle followed from a Lagrangian perspective, is calculated by means of an Eulerian or an iterative pseudo-Lagrangian description. For the Eulerian approach the material derivative is calculated by separately evaluating the local time-derivative and convective terms as,

$$\frac{D\mathbf{u}}{Dt} = \underbrace{\frac{\partial \mathbf{u}}{\partial t}}_{\text{local}} + \underbrace{(\mathbf{u} \cdot \nabla) \mathbf{u}}_{\text{convective}} \quad (5.5)$$

The iterative pseudo-Lagrangian approach is given as (de Kat & van Oudheusden, 2012),

$$\mathbf{x}_p^k(t, \tau) = \mathbf{x} + \mathbf{u}(\mathbf{x}, t)\tau + \frac{1}{2} \frac{D\mathbf{u}^k}{Dt}(\mathbf{x}, t)\tau^2 \quad (5.6)$$

$$\frac{D\mathbf{u}^{k+1}}{Dt}(\mathbf{x}, t) = \frac{\mathbf{u}(\mathbf{x}_p^k(t, \Delta t), t + \Delta t) - \mathbf{u}(\mathbf{x}_p^k(t, -\Delta t), t - \Delta t)}{2\Delta t} \quad (5.7)$$

where τ is taken as the temporal spacing of the measured flow fields (Δt). Predicted particle positions $\mathbf{x}_p^k(t, \tau)$ outside the domain are not extrapolated to prevent associated errors. Instead, at these locations the material derivative is calculated based on the Eulerian approach. This algorithm is iterated until convergence is obtained/reached. Decreasing τ and finding more predicted particles positions inside the domain, such that a larger part of the domain is calculated with the pseudo-Lagrangian approach, was found to marginally effect the reconstructed pressures so that it is not considered in the present study to decrease the amount of computation time.

An Eulerian based material derivative is found to perform best in order to evaluate the material derivative and is used for the remainder of this study, see subsection 5.3.1.

5.1.3 Integration of pressure gradients

The pressure field is integrated by setting up a Poisson problem as,

$$\nabla^2 p = \nabla \cdot (\nabla p) \quad (5.8)$$

Coordinate system The flow field data obtained from the PIV measurements is given on an ordered grid that is equally spaced with Δx , Δy and Δz in the x , y , z -direction respectively. The coordinate system and grid that are used for the pressure reconstruction are identical to the velocity measurements and are given in Figure 5.1.

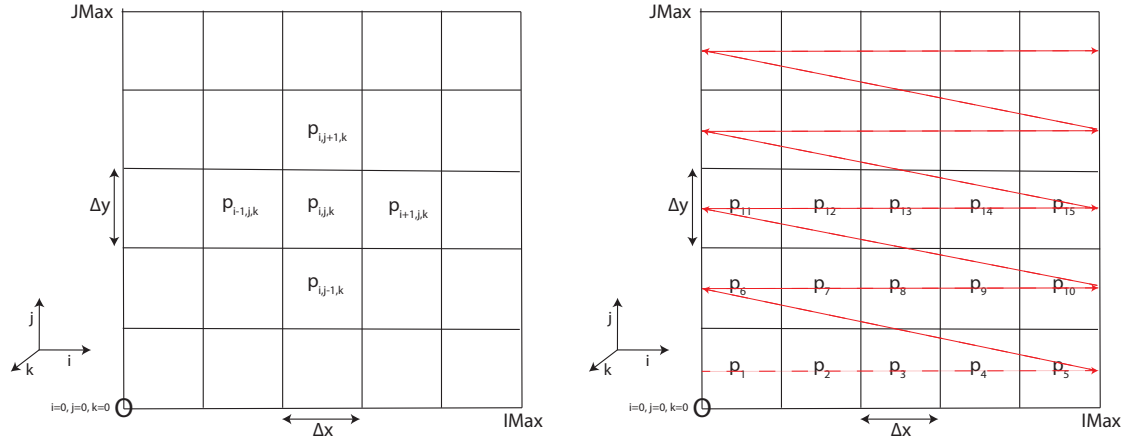


Figure 5.1: Coordinate system; *Left:* General matrix format. *Right:* Global node index.

The x -direction is aligned with the i -direction with a vector size of $IMax$. The y -direction is aligned with the j -direction with a vector size of $JMax$. The z -direction is aligned with the k -direction with a vector size of $KMax$. The global node index (NI) coordinate system is illustrated by the red arrows and given as,

$$NI = i + (j - 1) \cdot IMax + (k - 1) \cdot IMax \cdot JMax \quad (5.9)$$

Discretization The 3D Poisson problem discretization is set up using finite second-order-accurate central-difference schemes as,

$$\begin{aligned} \frac{\partial^2 p_{i,j,k}}{\partial x^2} &= \frac{p_{i+1,j,k} - 2p_{i,j,k} + p_{i-1,j,k}}{\Delta x^2} ; & \frac{\partial^2 p_{i,j,k}}{\partial y^2} &= \frac{p_{i,j+1,k} - 2p_{i,j,k} + p_{i,j-1,k}}{\Delta y^2} ; \\ \frac{\partial^2 p_{i,j,k}}{\partial z^2} &= \frac{p_{i,j,k+1} - 2p_{i,j,k} + p_{i,j,k-1}}{\Delta z^2} \end{aligned} \quad (5.10)$$

with,

$$\nabla^2 p_{i,j,k} = \frac{\partial^2 p_{i,j,k}}{\partial x^2} + \frac{\partial^2 p_{i,j,k}}{\partial y^2} + \frac{\partial^2 p_{i,j,k}}{\partial z^2} \quad (5.11)$$

Consequently, a 7-point stencil is created.

System of equations A system of equations is generated based on the global NI coordinate system. The final system of equations is given as: $[B][p_{NI}] = [S]$. $[B]$ is a sparse matrix containing the discretized Poisson problem (LHS of Equation 5.8). $[B]$ is built using a triplet format. This format allows incorporating all types of boundary conditions with ease and it is computationally cheap. $[S]$ is the solution vector (RHS of Equation 5.8). The pressure vector $[p_{NI}]$ is obtained by numerically solving the system of equations using the ‘mldivide,’ operator of Matlab 2015a[®].

Boundary conditions At the boundaries of the integration domain Neumann boundary conditions (spatial gradient of pressure) normal to the boundary are imposed. The Neumann boundary conditions are set up using a second-order-accurate central-difference scheme by introducing ghost points outside of the calculation domain. To insert a Neumann boundary condition at a specific node point the following strategy is applied:

1. Create a new ghost point in the outward normal direction of the node face at which the Neumann boundary condition is imposed
2. Set up the standard 7-point stencil with this additional ghost point
3. Use the ghost point to set up a new equation in the sparse matrix which evaluates the Neumann boundary condition. The discretization of the pressure gradient is based on the second-order-accurate central-difference scheme as:

$$\begin{aligned} \frac{\partial p_{i,j,k}}{\partial x} &= \frac{p_{i+1,j,k} - p_{i-1,j,k}}{2\Delta x} ; & \frac{\partial p_{i,j,k}}{\partial y} &= \frac{p_{i,j+1,k} - p_{i,j-1,k}}{2\Delta y} ; \\ \frac{\partial p_{i,j,k}}{\partial z} &= \frac{p_{i,j,k+1} - p_{i,j,k-1}}{2\Delta z} \end{aligned} \quad (5.12)$$

For instance if the problem is set up in 1D along the x -axis based on Figure 5.1, the contribution of node 1 at which a Neumann boundary condition is imposed towards the left (outward normal direction) is evaluated as,

$$\begin{bmatrix} -2/\Delta x^2 & 1/\Delta x^2 & 0 & 0 & 0 & 1/\Delta x^2 \\ \dots & \dots & \dots & \dots & \dots & \dots \\ \dots & \dots & \dots & \dots & \dots & \dots \\ \dots & \dots & \dots & \dots & \dots & \dots \\ \dots & \dots & \dots & \dots & \dots & \dots \\ 0 & 1/(2\Delta x) & 0 & 0 & 0 & -1/(2\Delta x) \end{bmatrix} \begin{bmatrix} p_1 \\ p_2 \\ p_3 \\ p_4 \\ p_5 \\ p_{ghost} \end{bmatrix} = \begin{bmatrix} S_1 \\ S_2 \\ S_3 \\ S_4 \\ S_5 \\ \frac{\partial p_1}{\partial x} \end{bmatrix} \quad (5.13)$$

This strategy allows to apply the Neumann boundary condition in 3D space by adding more ghost points. This approach was verified by directly substituting Equation 5.12 in the standard 7-point stencil and thereby eliminating the ghost points.

Applying Neumann boundary conditions on the entire boundary of the domain leads to a pressure defined up to an arbitrary constant.

Note, when applying only Neumann boundary conditions the reconstructed pressure values is generally not be equal to the reference pressure because the pressure is defined up to an arbitrary constant.

Mask implementation Based on the position information obtained from the wing reconstruction a mask around the wing is created at which Neumann boundary conditions are imposed. The mask has an equal offset of 7 vectors from the wing surface in the x, y -directions extending over the full span of the wing (see subsection 5.3.2 for the mask convergence study). The masked region in the field of view is illustrated in Figure 5.2.

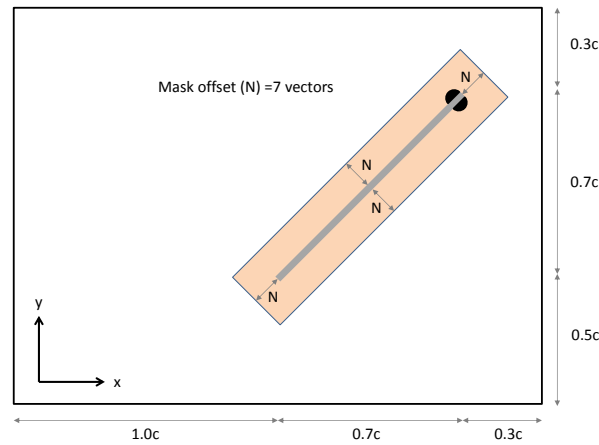


Figure 5.2: Mask implementation.

For a fixed mask over time, the matrix $[B]$ is constant. This allows to benefit from factorizing

[B] before solving the system of equations for varying [S] (flow fields) over time which decreases the computational time.

Pressure field scaling After the pressure fields are obtained for each volume individually, they are scaled with respect to volume 2 at the mid-planes of the overlap regions from volume 1-2 and volume 3-2 (as depicted in Figure 4.4) to obtain a smooth transition between volumes. Subsequently, the complete pressure field is expressed with respect to a reference pressure of 0 Pa.

In the lower right corner of the flow field (maximum x -location, minimum y -location) the flow is assumed to be undisturbed. Accordingly, the pressure at this location is taken as $p_{\text{ref}} = 0$ Pa. A box of $5 \times 5 \times KMax$ (x, y, z -direction) vectors in the lower right corner is referred as the "scale box". In Figure 5.3 the "scale box" for volumes 1, 2 & 3 are given in orange and the midplane of the overlap regions is given in dark blue.

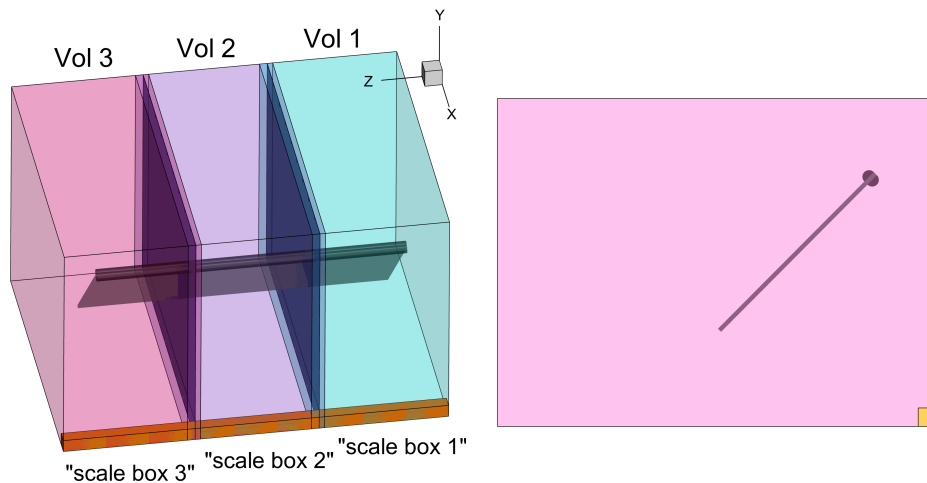


Figure 5.3: Pressure scaling.

The pressure fields are scaled between the volumes and the reference pressure as follows:

- Subtract the mean pressure of "scale box 1" from the pressure field of volume 1. Subtract the mean pressure of "scale box 2" from the pressure field of volume 2. Subtract the mean pressure of "scale box 3" from the pressure field of volume 3.
- Subtract the mean pressure of the midplane of the overlapping region of volume 1 with respect to volume 2 from the pressure field of volume 1. Subtract the mean pressure of the midplane of the overlapping region of volume 3 with respect to volume 2 from the pressure field of volume 3.
- Subtract the mean pressure of "scale box 1, 2 & 3" from the pressure fields of volume 1, 2 & 3.

5.2 Load reconstruction

The fluid-dynamic loads are reconstructed by evaluating the integral momentum balance obtained by integrating the Navier-Stokes equation within a control volume (Anderson, 2011). The general control volume matches the field of view with volume $V(t)$, is bounded by an external contour $S(t)$, and an internal contour $S_b(t)$, which is the outer surface of the wing. \mathbf{n} is the outward normal on both inner and outer contours.

The general control volume configuration can be found in Figure 5.4.

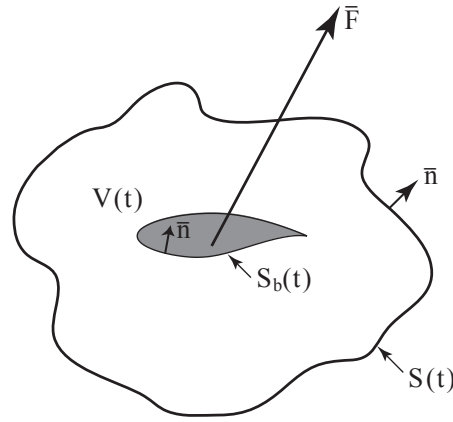


Figure 5.4: General control volume configuration.

In the absence of gravity the instantaneous force \mathbf{F} is given as,

$$\begin{aligned}
 \mathbf{F}(t) = & \underbrace{- \int_{V(t)} \frac{\partial \rho \mathbf{u}}{\partial t} dV}_{\text{I}} - \underbrace{\int_{S(t)+S_b(t)} \rho \mathbf{u} (\mathbf{u} \cdot \mathbf{n}) dS}_{\text{II}} + \underbrace{\int_{S(t)} (-p \mathbf{n} + \boldsymbol{\tau} \cdot \mathbf{n}) dS}_{\text{III}} \\
 & - \underbrace{\int_{V(t)} \rho \boldsymbol{\Omega} \times (\boldsymbol{\Omega} \times \mathbf{r}_{pv}) dV}_{\text{IV}} - \underbrace{\int_{V(t)} 2\rho \boldsymbol{\Omega} \times \mathbf{u} dV}_{\text{V}} - \underbrace{\int_{V(t)} \rho \frac{d\boldsymbol{\Omega}}{dt} \times \mathbf{r}_{pv} dV}_{\text{VI}}
 \end{aligned} \tag{5.14}$$

with,

$$\mathbf{F}(t) = \int_{S_b(t)} (-p \mathbf{n} + \boldsymbol{\tau} \cdot \mathbf{n}) dS \tag{5.15}$$

where,

I volume integral of the time rate of change of momentum

II surface integral on the external and internal contours, which accounts for the momentum flux through the control volume boundaries

III surface integral on external contour accounting for the pressure and viscous stress contributions

IV,V & VI volume integral of respectively the centrifugal, Coriolis and Euler acceleration contributions

The shear stress $\boldsymbol{\tau}$ is evaluated as given in Equation 5.3. For a steady control volume the Reynolds transport theorem allows to evaluate the temporal derivative outside the integral of term I. This is advantageous because the temporal derivative of the total momentum inside the control volume is less sensitive to measurements errors. For an impermeable solid object the no slip condition applies at the body surface and the fluid will have zero velocity relative to its boundary. As a result the integration region $S_b(t)$ of term II drops out.

Finally, the loads are evaluated as,

$$\begin{aligned}
 F_i = & -\rho \frac{d}{dt} \int_V u_i dV - \rho \int_S u_i u_j n_j dS + \int_S (-pn_i + \mu \left\{ \frac{\partial u_i}{\partial x_j} + \frac{\partial u_j}{\partial x_i} \right\} n_j) dS \\
 & - \rho \int_V \boldsymbol{\Omega} \times (\boldsymbol{\Omega} \times \mathbf{r}_{pv}) dV - \rho \int_V 2 \boldsymbol{\Omega} \times \mathbf{u} dV - \rho \int_V \frac{d\boldsymbol{\Omega}}{dt} \times \mathbf{r}_{pv} dV
 \end{aligned} \tag{5.16}$$

The spatial and temporal derivatives are calculated with a second-order-accurate central-difference scheme, except at the boundaries of the temporal evolution at which a first-order-accurate finite difference scheme is employed.

The lift (C_L) and drag (C_D) coefficients are defined as,

$$C_L = \frac{L}{\frac{1}{2}\rho V_t^2 c R}; \quad C_D = \frac{D}{\frac{1}{2}\rho V_t^2 c R} \tag{5.17}$$

Sectional lift & drag coefficient By evaluating the loads in a thin sectional control volume with dimensions matching the field of view in the x, y -directions and a spanwise thickness of dz in the z -direction that is centered at a given chordwise oriented plane, the sectional lift & drag coefficient for that chordwise oriented plane can be approximated as,

$$C_l = \frac{L'/dz}{\frac{1}{2}\rho V_t^2 c} = \frac{l}{\frac{1}{2}\rho V_t^2 c}; \quad C_d = \frac{D'/dz}{\frac{1}{2}\rho V_t^2 c} = \frac{d}{\frac{1}{2}\rho V_t^2 c} \tag{5.18}$$

where L' , D' is the lift, drag calculated from the sectional control volume.

5.3 Discussion on the pressure & load reconstruction

For the analyses in this study the control volume has an offset of 1 vector from the borders of the flow field domain unless stated otherwise. This allows to calculate the spatial gradients at the CV boundary with a finite second-order-accurate central-difference scheme.

5.3.1 Material derivative of velocity: Eulerian - Lagrangian

The pressure field is obtained by the integration of the pressure gradients. In order to calculate the pressure gradients the material derivative of the velocity needs to be evaluated. In Figure 5.5 the influence of the Eulerian and pseudo-Lagrangian calculation methods for the material derivative of velocity on the reconstructed forces is shown. The presented force coefficients are obtained by summing the reconstructed lift and drag coefficients of each individual volume. The solid line represents the force reconstruction results by use of the data with a high temporal resolution ($TR^* = 0.25$), whereas the calculations with the coarsened data set are depicted by the dashed lines ($TR^* = 0.5$).

With an Eulerian based material derivative, the reconstructed lift and drag coefficients that are based on a temporal coarsened data set (dashed lines) agree well with the high temporal resolution data set (solid lines). However, with a pseudo-Lagrangian based material derivative discrepancies are found between the high and coarsened temporal resolution. It can be observed that the reconstructed lift coefficients match reasonably well, but significant discrepancies are found for the reconstructed drag coefficients.

The Eulerian approach is expected to be more sensitive to advective motions, while the Lagrangian approach is more sensitive to rotation dominated flows because this complicates the flow path reconstruction (de Kat & van Oudheusden, 2012). Within a rotating reference frame the dominance of rotation over advective motion is increased compared to an inertial frame such that the Eulerian approach may be anticipated to perform better for evaluating the material derivative. Not only the loads were found to be comparable for a temporally coarsened data set with an Eulerian based material derivative, but also the pressure field. For the calculation of the pressure fields and loads exerting on the tested wings throughout the revolving motion, the Eulerian based material derivative is used for the remainder of this study.

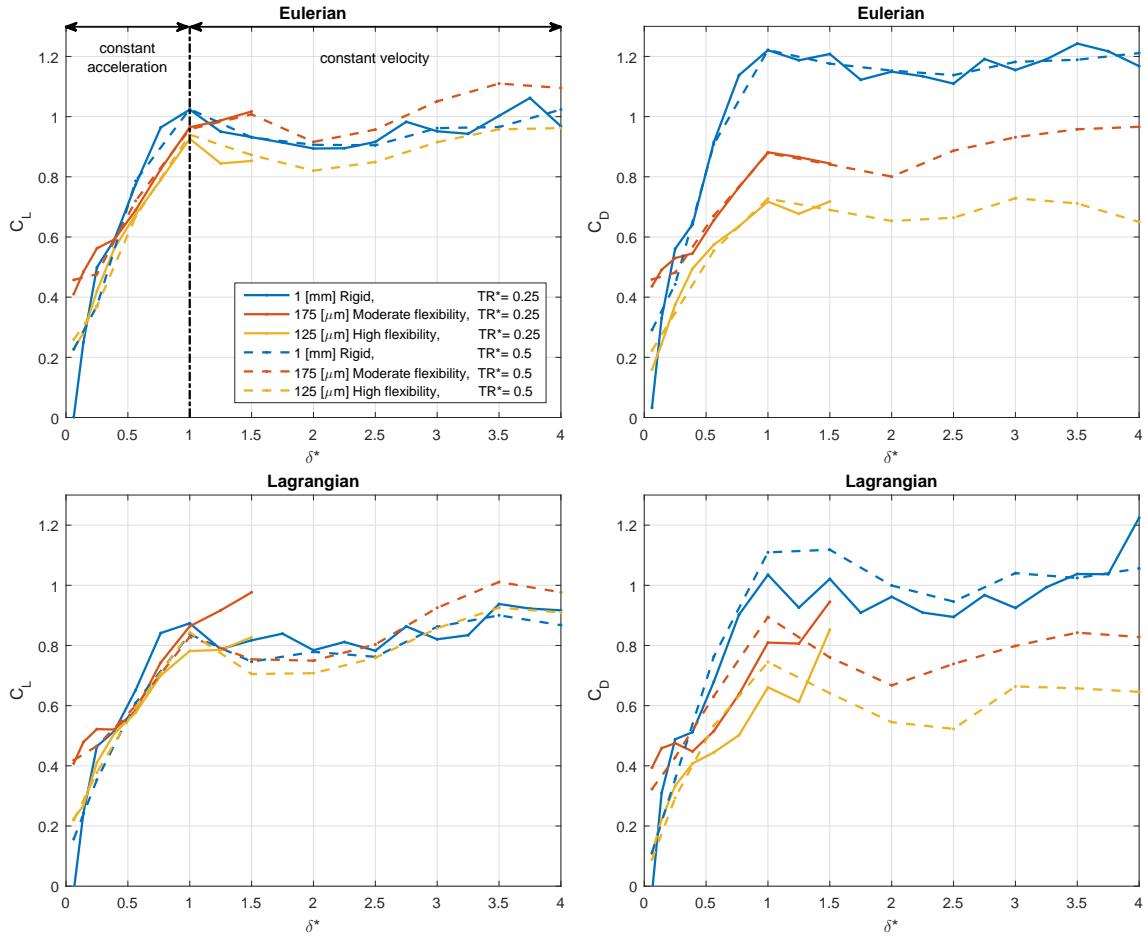


Figure 5.5: Temporal evolution of the reconstructed lift (left column) and drag (right column) coefficient based on the summation of volume 1-3. *Top row:* Eulerian based material derivative of velocity. *Bottom row:* pseudo-Lagrangian based material derivative of velocity. Solid line depicts a high temporal resolution of $TR^* = 0.25$ and the dashed line depicts a coarsened temporal resolution of $TR^* = 0.5$.

5.3.2 Mask convergence

Due to the presence of the wing in the measurement region, the reconstructed velocity vectors at its location and in the close vicinity have a relatively high uncertainty and need to be excluded from the pressure reconstruction. Based on the position information obtained from the wing reconstruction, a mask around the wing is created. The mask convergence study is performed by varying the mask size from no mask $N=0$ to $N=10$, see Figure 5.2. For each different configuration, the corresponding Poisson problem is solved for the calculation of pressure fields and the loads acting on the wing are estimated by means of the aforementioned control volume approach. The optimum mask size is defined as the smallest mask size for converged lift and drag such that the pressure values can be obtained close to the wing surface while estimating the loads accurately. The size of the mask is determined by a lift and drag convergence study for the 1 [mm] Rigid wing as given in Figure 5.6.

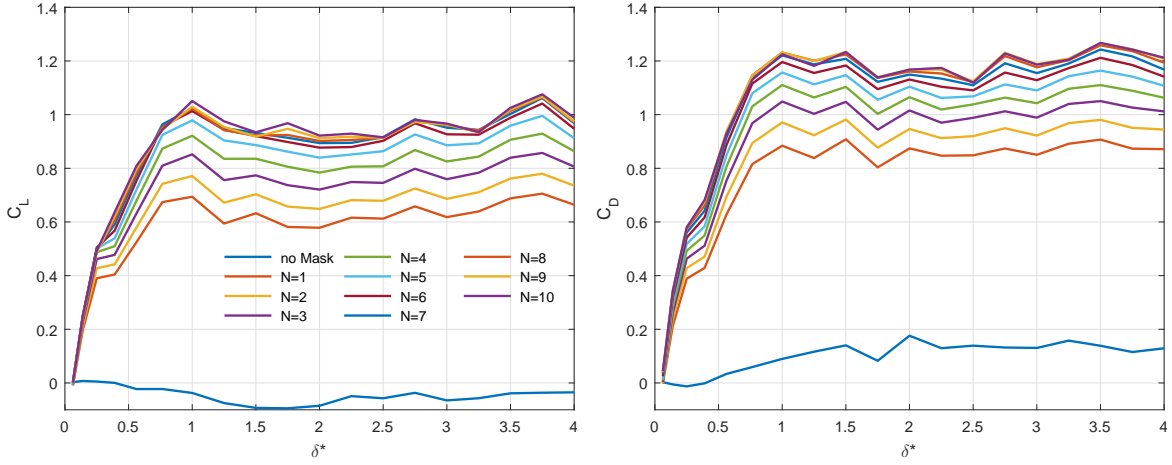


Figure 5.6: Mask convergence study of the 1 [mm] Rigid wing for different mask vector offset values (N) *Left:* Temporal evolution of lift coefficient. *Right:* Temporal evolution of drag coefficient.

It can be observed that in the case of no mask, the pressure fields are calculated such that the resultant forces are found to be close to zero (Figure 5.6). The no-mask case is essentially non-physical since there is a solid body in the field of view and velocity vectors measured at its location and in the close vicinity are generally erroneous. Therefore, this region should be masked and thus the velocity vectors with relatively higher uncertainty should be excluded from the pressure and load calculations. It can be observed that for a vector offset of 7 both lift and drag coefficients are converged. It is assumed that this offset value also gives converged results for the flexible wings. Therefore, for the remainder of the analyses the optimum mask size is determined to have an offset of 7 vectors is used unless stated otherwise.

5.3.3 Dirichlet boundary condition

In this section Dirichlet boundary conditions are compared to Neumann boundary conditions. The errors in this section are based on the difference between the reconstructed pressure gradients and input pressure gradients (Equation 5.2).

Instead of applying Neumann boundary conditions in the undisturbed lower right corner of the flow field, a Dirichlet boundary condition of $p = 0$ Pa can also be applied. Two different Dirichlet boundary condition approaches are tested: a Dirichlet boundary condition at a single single node located at the midplane of each volume or Dirichlet boundary conditions at *KMax* nodes extending over the full spanwise direction as illustrated in Figure 5.7.

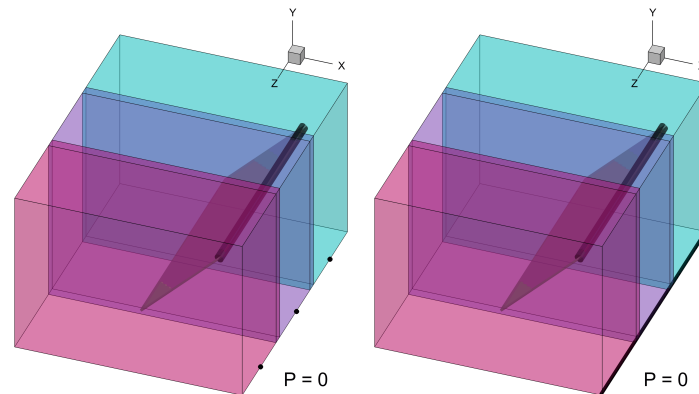


Figure 5.7: Dirichlet boundary condition in the lower right corner of the field of view. *Left:* 1 Dirichlet boundary condition at the midplane of each volume. *Right:* Dirichlet boundary conditions over the full spanwise direction of each volume.

When applying a Dirichlet boundary condition at a point in the midplane or at *KMax* points along the span of the lower right corner; the mean of the error, RMS error and sum of the absolute errors are of similar magnitude compared to those obtained by applying Neumann boundary conditions. In Figure 5.8 the sum of the absolute errors and the RMS error are given for volume 2 of the rigid wing .

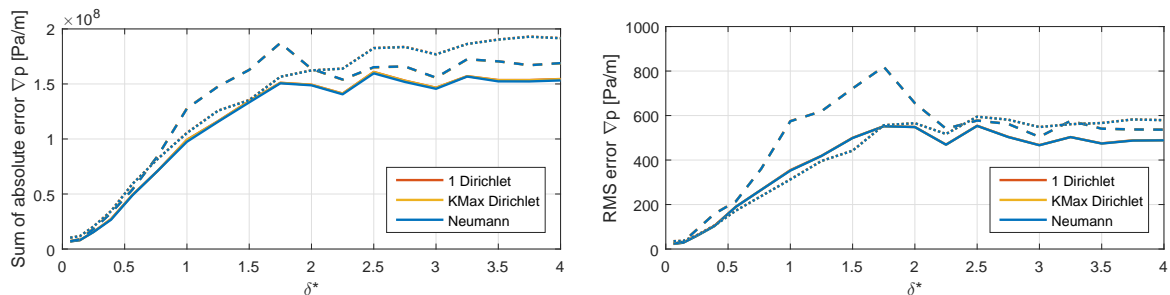


Figure 5.8: 1 [mm] Rigid wing volume 2. Errors based on $dpdx$ indicated by the solid line, $dpdy$ indicated by the dashed line and $dpdz$ indicated by the dotted line. *Left:* Temporal evolution of sum of absolute errors. *Right:* Temporal evolution of RMS error.

The error levels of the different types of boundary conditions are the same. When applying a single or KMax Dirichlet boundary conditions, the transition of the pressure field between volumes was most representative when additionally scaled as described in section 5.1.3. Not only the scaled pressure field was found similar, but also the reconstructed lift and drag. Because the force gradient errors (expressed in terms of pressure gradient errors), scaled pressure fields and reconstructed loads between Neumann and Dirichlet boundary conditions are similar, both approaches are considered to give a representative pressure distribution.

5.3.4 Euler effect

The Euler effect scales with the rotational angular acceleration $\frac{d\Omega}{dt}$. Incorrect modeling of the Euler effect leads to an incorrect pressure field. The acceleration phase of the motion profile is modeled using a step input of full angular acceleration from $0 < \delta^* < 1$. However, at beginning and the end of the acceleration phase ($\delta^*=0$ and 1), the angular acceleration is singular. The actual motion profile is different from this ideal definition and the angular acceleration at $\delta^* = 1$ is calculated as approximately half of the full acceleration by use of the velocity data acquired from the motor encoder. In order to investigate the sensitivity of the pressure calculations to the Euler effect term, the pressure fields of the rigid wing are obtained for three different acceleration values (i.e., zero, half and full angular accelerations) at the end of the acceleration phase as shown in Figure 5.9.

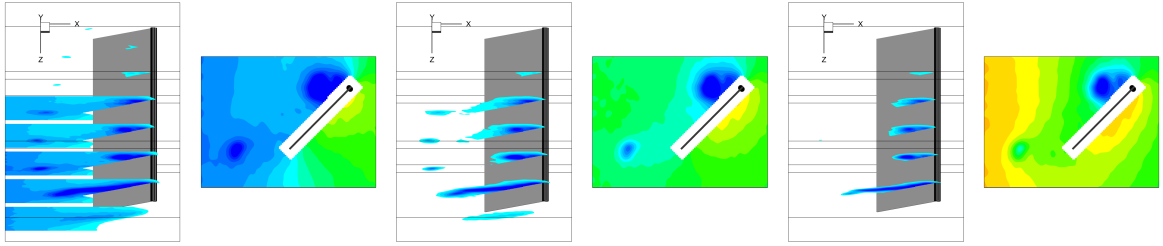


Figure 5.9: 1 [mm] Rigid wing. Influence of Euler effect at $\delta^* = 1$ for chordwise oriented slices and at the 75% span reference plane. *Left:* Zero angular acceleration $\frac{d\Omega}{dt} = 0 \text{ rad/s}^2$. *Middle:* Half of the full angular acceleration $\frac{d\Omega}{dt} = \frac{1}{2} \cdot 3.4188 \text{ rad/s}^2$. *Right:* Full angular acceleration $\frac{d\Omega}{dt} = 3.4188 \text{ rad/s}^2$.

For the zero angular acceleration case at $\delta^* = 1$, high negative pressure levels downstream of the wing model are observed, whereas for the full acceleration case, positive pressure levels are present at the downstream locations. Temporal evolution of the pressure fields shows that neither the full nor zero acceleration case generates pressure fields that are in accordance with the general temporal behavior. On the other hand half of the full acceleration results in a smooth transition from the acceleration phase to the constant phase which is physically more reasonable, see section A.6 for a time-animation of the pressure fields.

In Figure 5.10 the lift and drag contributions are given. The lift and drag coefficients did not change. For the drag contribution a peak in the pressure distribution is found at zero angular acceleration which is due to the absence of Euler effect contribution. This can also be observed at the 75% span reference plane. The pressure gradient difference between zero angular acceleration and half of the full angular acceleration acts in the downstream x -direction (see Figure 5.9) which only influences the pressure contribution in the calculation of the drag coefficient (see Figure 5.10). On the contrary, for the full angular acceleration case a dip is found. Only for half of the full acceleration a smooth transition in the pressure field is present which reflects in a smooth pressure contribution in the calculation of drag. Although the loads acting on the wing are estimated similarly for different Euler term contributions, it is of importance to use correct motion kinematics in the calculation of the pressure fields.

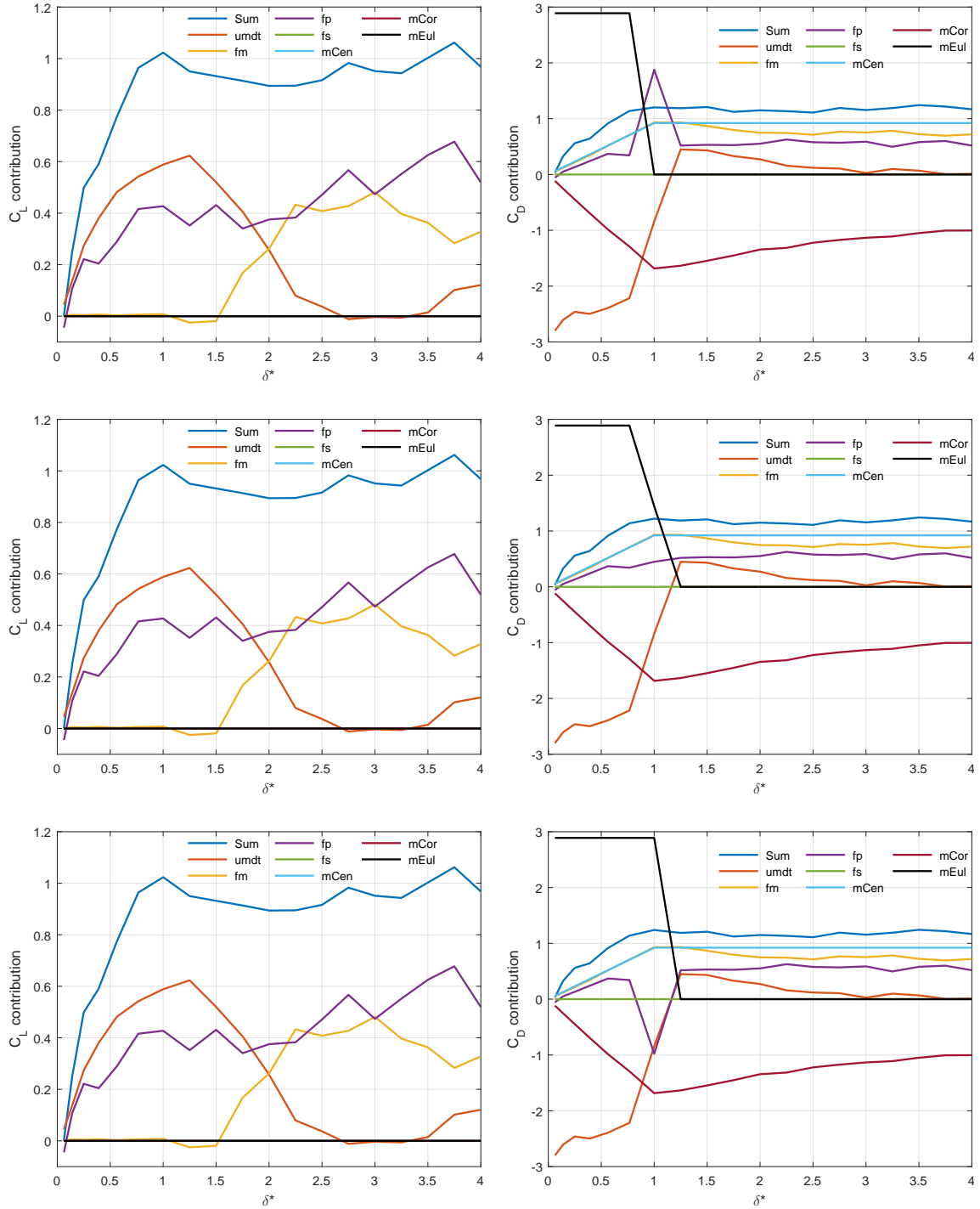


Figure 5.10: Influence of Euler effect of unsteady momentum $umdt$ (I), momentum flux fm (II), pressure fp (III), viscous stress fs (III), centrifugal momentum $mCen$ (IV), Coriolis momentum $mCor$ (V) and Euler momentum $mEul$ (VI) contribution, see Equation 5.14. *Top:* Zero angular acceleration $\frac{d\Omega}{dt} = 0$ rad/s². *Middle:* Half of the full angular acceleration $\frac{d\Omega}{dt} = 0 = \frac{1}{2} \cdot 3.4188$ rad/s². *Bottom:* Full angular acceleration $\frac{d\Omega}{dt} = 3.4188$ rad/s².

5.3.5 Divergence free flow

Although the Mach number is low and the flow can be assumed incompressible and divergence-free, the implementation of this condition leads to erroneous pressure fields.

The Poisson equation for the pressure without rotational effects ($\nabla^2 p'$) can be written as,

$$\nabla^2 p' = \nabla \cdot (\nabla p') = \nabla \cdot \left(-\rho \frac{D\mathbf{u}}{Dt} + \mu \nabla^2 \mathbf{u} \right) = \nabla \cdot \left(-\rho \frac{\partial \mathbf{u}}{\partial t} - \rho (\mathbf{u} \cdot \nabla) \mathbf{u} + \mu \nabla^2 \mathbf{u} \right) \quad (5.19)$$

Assuming incompressible flow ($\rho = \text{const}$; $\nabla \cdot \mathbf{u} = 0$) Equation 5.19 can be written as,

$$\begin{aligned} \nabla^2 p' \stackrel{(\rho = \text{const}; \nabla \cdot \mathbf{u} = 0)}{=} -\rho \nabla \cdot (\mathbf{u} \cdot \nabla) \mathbf{u} &= -\rho \frac{\partial}{\partial x_i} \left(u_j \frac{\partial u_i}{\partial x_j} \right) = -\rho \left\{ \frac{\partial u_j}{\partial x_i} \frac{\partial u_i}{\partial x_j} + u_j \frac{\partial^2 u_i}{\partial x_i \partial x_j} \right\} \\ \stackrel{(\frac{\partial u_i}{\partial x_i} = 0)}{=} -\rho \frac{\partial u_j}{\partial x_i} \frac{\partial u_i}{\partial x_j} & \end{aligned} \quad (5.20)$$

leading to a modified Poisson problem of,

$$\nabla^2 p = \nabla^2 p' + \nabla \cdot \rho \left(-\boldsymbol{\Omega} \times (\boldsymbol{\Omega} \times \mathbf{r}_{pv}) - 2 \boldsymbol{\Omega} \times \mathbf{u} - \frac{d\boldsymbol{\Omega}}{dt} \times \mathbf{r}_{pv} \right) \quad (5.21)$$

Solving this problem gives an incorrect pressure field. Also when plotting the divergence of the velocity field, non-zero values are found. During the PIV measurement and post-processing of the velocity field errors are introduced such that the resultant measured velocity field is not divergence free. It is concluded that for this experimental study the pressure field cannot be reconstructed under the assumption of a divergence free velocity field. To account for a non-divergence free velocity field, Equation 5.8 is used instead.

5.4 Verification

In this section a verification study is presented. First, the pressure reconstruction algorithm is verified using an analytic test problems. Second, the pressure and load reconstruction methods are verified by a numerical simulation.

In this section the material derivative of the velocity is based on the Eulerian approach and only Neumann boundary conditions are imposed unless stated otherwise.

5.4.1 Verification of the pressure reconstruction algorithm with analytic test problems

The pressure reconstruction algorithm is verified using 2 analytic test problems:

- 2D: Taylor green vortex [Green & Taylor \(1937\)](#)
- 3D: Solution from Ethier & Steinman [Ethier & Steinman \(1994\)](#)

When Neumann boundary conditions are applied on all boundaries, the pressure is defined up to a constant. The verification study is based on a C_p value defined such that the range is scaled to $[-1 \ 1]$. This modified C_p allows to compare the distribution of the pressure field. For this verification study ‘PIV’ refers to the reconstructed pressures from the analytical velocity fields.

2D: Taylor green vortex The Taylor green vortex is an unsteady flow of decaying vortex which has an exact closed form solution of the incompressible Navier-Stokes equations. In Figure 5.11 the reconstructed pressures, indicated with PIV, are compared to the numerical results. A 2D diamond shaped mask is added with Neumann boundary conditions on the edges. The spatial resolution is $\Delta x = \Delta y = \pi/150$ mm and the temporal resolution is $\Delta t = 0.1$ s. It can be observed that there is a good agreement between the pressure fields.

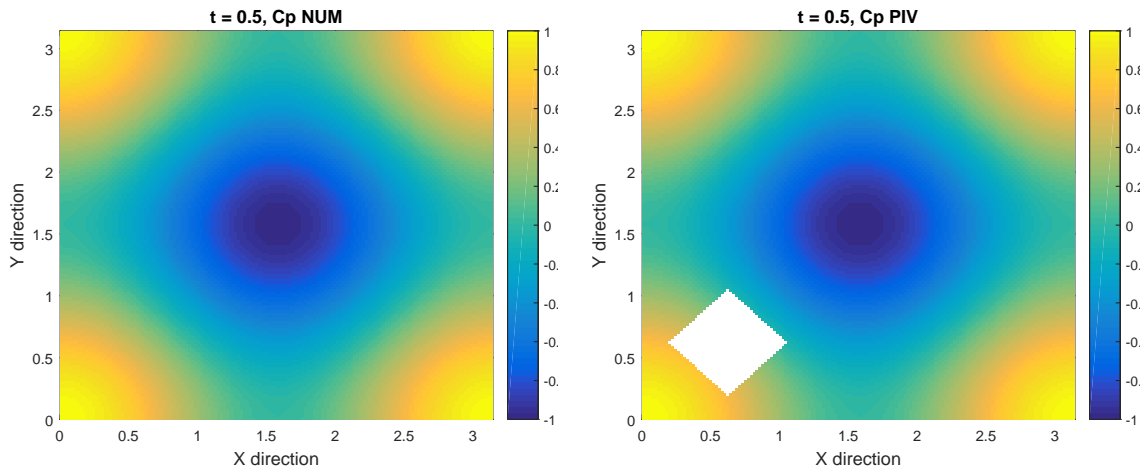


Figure 5.11: Pressure field distribution of Taylor green vortex [Green & Taylor \(1937\)](#). *Left:* Numerical-Analytical. *Right:* PIV all Neumann

3D: Solution from Ethier & Steinman The solution from Ethier & Steinman is a closed form of the incompressible Navier-Stokes equations for the verification of solvers. In Figure 5.12 the reconstructed pressures, indicated with PIV, are compared to the numerical results. A 3D diamond shaped mask is added with Neumann boundary conditions on the edges. The results are compared for the center z -plane. The spatial resolution is $\Delta x = \Delta y =$

0.005 mm and the temporal resolution is $\Delta t = 0.1$ s. It can be observed that the results match and the pressure is calculated quite accurately.

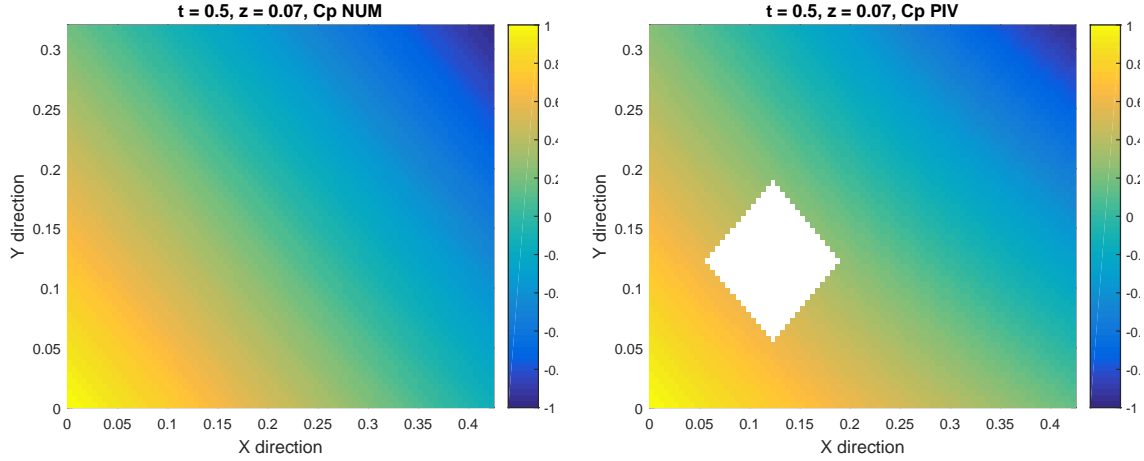


Figure 5.12: Pressure field distribution of Ethier & Steinman solution at midplane with $a = \pi/4$ and $d = \pi/x$ Ethier & Steinman (1994). *Left:* Numerical-Analytical. *Right:* PIV all Neumann.

5.4.2 Verification of the pressure and load reconstruction methods with a numerical simulation

The pressure and load reconstruction results are verified using a numerical data set based on an immersed boundary method¹. The data set contains a plunging NACA 0012 airfoil at a Reynolds number of $Re = 5,000$ and a reduced frequency of $k = 1.2566$ ($k = \frac{\pi f c}{U_{ref}}$), where f is the frequency of the plunging motion. The reference pressure at inflow conditions is zero ($p_{ref} = 0$ Pa). The data is equally spaced with a spatial resolution of $\Delta x = \Delta y = 6$ mm or $0.006c$ and the temporal resolution is $\Delta t = 0.1$ s or $1/25T$ (T is the plunging period).

In Figure 5.13 the flow field and control volume are shown. The control volume has an offset of $0.5c$ from the upper and lower edge of the airfoil, $0.3c$ from the LE and $1c$ from the TE of the airfoil when starting plunging. Note that the control volume is fixed for this study.

¹The numerical data set was provided by TAY Wee-Beng, see (Tay et al., 2013)

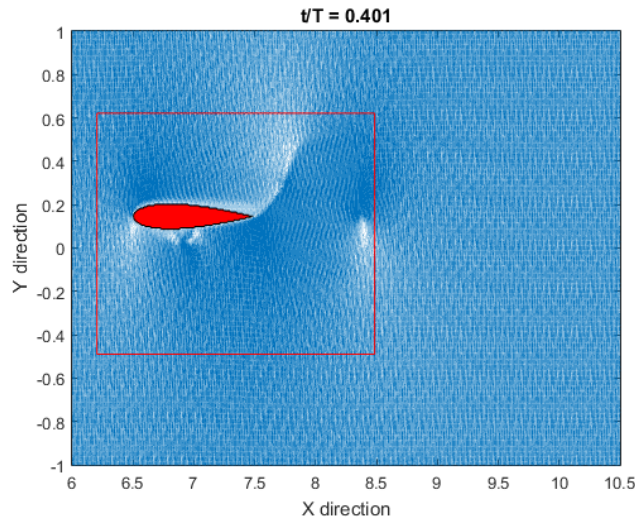


Figure 5.13: Flowfield and control volume (red) of plunging airfoil.

In this section ‘CV’ indicates that the loads are reconstructed based on a control volume analysis.

Verification of load reconstruction The load reconstruction is verified by comparing the reconstructed loads with the numerical simulation. The reconstructed loads are obtained as described in section 5.2 using the control volume approach in which the pressure field from the numerical data is used. The results are given in Figure 5.14.

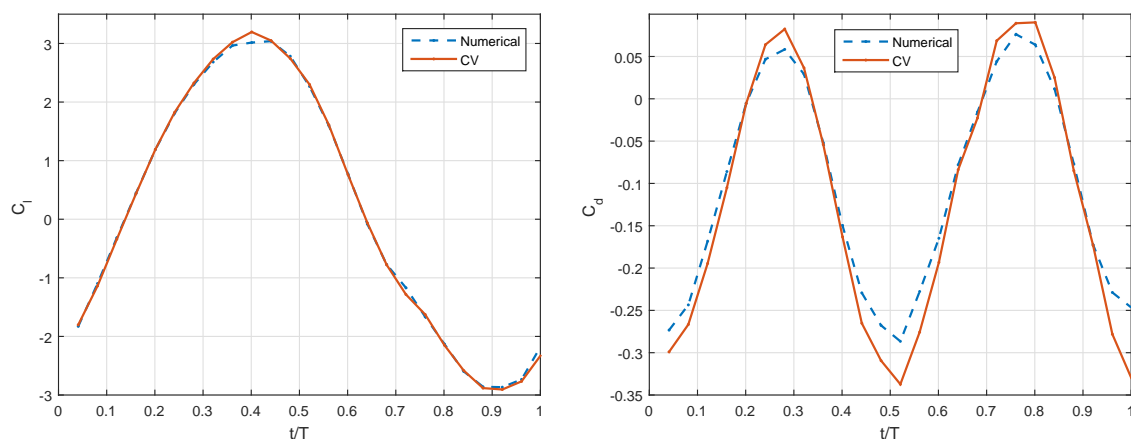


Figure 5.14: Load reconstruction with pressure from numerical data. *Left:* Lift coefficient. *Right:* Drag coefficient.

It can be observed that the reconstructed lift coefficients match very well with the numerical data. For the drag coefficients a slight overshoot is found.

Verification of reconstructed pressure field The reconstructed pressure field is verified by comparing the pressure fields and the reconstructed loads with the numerical simulation. The pressure field is obtained as given in section 5.1, and the reconstructed loads are obtained as described in section 5.2 using a control volume approach in which the reconstructed pressure field is used. For the pressure reconstruction a rectangular mask with an offset of $0.1c$ from the, upper edge, lower edge, LE and TE of the airfoil is used. Neumann conditions are applied on all boundaries unless specified otherwise.

The reconstructed pressure field is scaled to the reference pressure at the uniform inflow conditions ($p_{\text{ref}} = 0$, over the left side of the domain). At $t/T = 0.4$ the reconstructed pressure field is given in Figure 5.15.

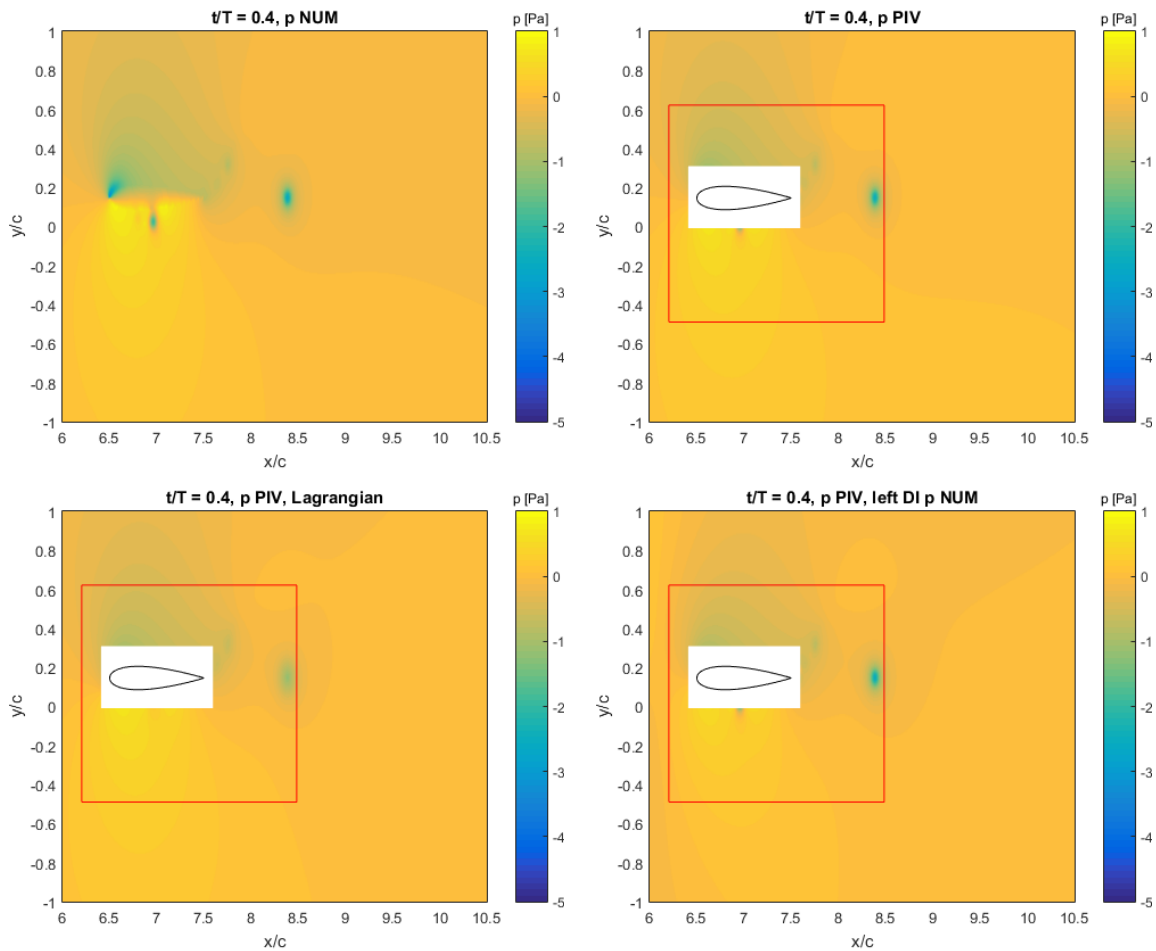


Figure 5.15: Pressure field in Pa. *Top-Left:* Numerical pressure field. *Top-Right:* Reconstructed pressure field form numerical flow field. *Bottom-Left:* Reconstructed pressure field form numerical flow field, material derivative based on pseudo Lagrangian approach. *Bottom-Right:* Reconstructed pressure field form numerical flow field, numerical pressure values are imposed on the inflow boundary in the form of Dirichlet boundary conditions

It can be observed that the distribution of the reconstructed pressure field as well as its magnitude agrees well the numerical pressure field. For the other time steps, the reconstructed pressure fields also match the numerical pressure fields. If the material derivative is based

on the pseudo Lagrangian approach, the high negative peaks in the center of a vortex is not captured as well as the Eulerian approach. This is probably due to the fact that the path reconstruction is more difficult in the vortex center in which large flow field gradients are present. If Dirichlet boundary conditions are prescribed, the pressure values in the vicinity of this boundary are not calculated as accurate as the case in which only Neumann boundary conditions are used.

Next the reconstructed loads by use of the reconstructed pressure fields are given in Figure 5.16.

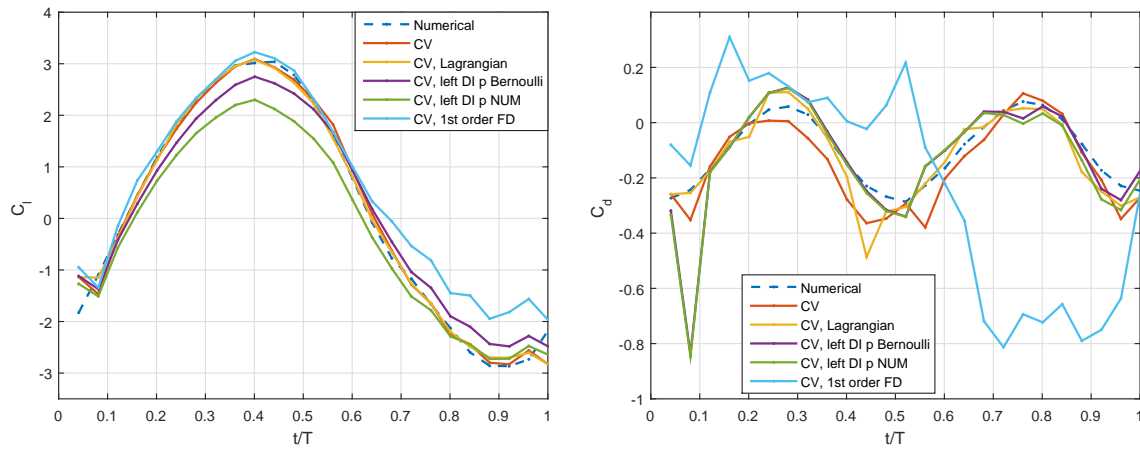


Figure 5.16: Load reconstruction with reconstructed pressure field from numerical flow field. *Left:* Lift coefficient. *Right:* Drag coefficient.

It can be observed that the reconstructed lift coefficients agree well with the numerical data when Neumann boundary conditions are applied on all boundaries. For the drag coefficients a larger overshoot can be observed compared to Figure 5.14 in which the pressure field was taken from the numerical data. This is as expected from literature because the highest uncertainty in the load reconstruction is expected to originate from the reconstructed pressure field. The high discrepancy peaks for the lift and drag coefficients correlate with a vortex moving over the control volume boundary in which large flow field gradients are present. The Lagrangian approach gives very similar reconstructed lift values compared to the Eulerian approach. The reconstructed drag values display an overshoot compared to the numerical data, although the trend is slightly different compared to the Eulerian approach. When imposing both Dirichlet boundary conditions obtained from Bernoulli or directly prescribed from the numerical data on the inflow (left) side of the domain, a higher discrepancy with the numerical load data is found. In this case, also the pressure field has higher discrepancies with the numerical pressure field compared to the Neumann boundary conditions. When setting up a first-order-accurate finite difference scheme (FD) for the Neumann boundary conditions of the Poisson problem, the reconstructed lift is relatively well captured, however the drag shows high discrepancies. This is caused by the relative high errors in the spatial gradients of velocities that arise from the first-order-accurate difference scheme.

Chapter 6

Results: Wing reconstruction & Force measurements

In this chapter the wing reconstruction results are given, after which the force measurement results are presented and discussed. The wing reconstruction methods, based on the volumetric flow imaging measurements, are explained in subsection 4.5.3. The experimental setup and the signal processing methods for the force measurements are given in section 4.4.

6.1 Wing reconstruction

At the leading edge, the angle of attack of the flat plate wings is set to 45 deg by means of the servo motor at the beginning of the experiment. However, the flexible wings deform during the revolving motion under the effect of hydrodynamic loads which changes the geometric angle of attack. For the deformed flexible wings, the geometric angle of attack for a given spanwise location is defined as the angle between the wing motion and the line connecting the reconstructed leading edge and trailing edge points,

$$\alpha_{geo}(z) = \tan^{-1} \left(\frac{Y_{LE}(z) - Y_{TE}(z)}{X_{LE}(z) - X_{TE}(z)} \right) \quad (6.1)$$

where $LE(x, y, z)$ describes the location of the reconstructed LE in x, y -coordinates for a given span (z) location, and $TE(x, y, z)$ describes the location of the reconstructed TE in x, y -coordinates for a given span (z) location.

The local angle of attack is the angle of attack at each chordwise position for a given span (z) location. The variation in the local angle of attack along the chord, which reflects the curvature of the wing, is computed from the gradients between the chordwise reconstructed points. As a result, the local angle of attack calculation is more sensitive wing reconstruction errors

compared to the geometric angle of attack. Therefore, the local angle of attack calculations are performed to attain the general trend of the wing curvature during the revolving motion.

6.1.1 Reconstruction quality

The average uncertainty in the triangulation of the identified points at the tip is approximately 0.3 of the vector spacing, corresponding to an uncertainty of 0.6 deg in the geometric angle of attack.

At the tip the chordwise profile is reconstructed. The mean absolute uncertainty between the reconstructed total length of the tip chord profile and chord (c) over the revolving motion is given in Table 6.1.

Table 6.1: Mean absolute uncertainty between the reconstructed total length of the tip chord profile and chord (c). Uncertainty expressed in terms of vector spacing.

Wing Model	Error [vec]
175 [μm] Moderate flexibility	0.19
125 [μm] High flexibility	0.23

The uncertainty for both flexible wings is low, indicating that the chordwise profile length is reconstructed correctly.

After the chordwise profile is reconstructed, the wing is extruded in z -direction towards the root. The mean absolute uncertainty between the image identified root-TE point and the reconstructed root-TE point over the revolving motion is given in Table 6.2.

Table 6.2: Mean absolute uncertainty between the image identified root-TE point and the reconstructed root-TE point. Uncertainty expressed in terms of vector spacing.

Wing	Error [vec]		
	x	y	z
175 [μm] Moderate flexibility	0.54	1.49	3.58
125 [μm] High flexibility	0.21	1.27	2.81

It can be observed that the highest uncertainty is present in z -direction. This is caused because the wing chord profile is reconstructed at the tip and extruded towards the root over the same z -coordinate. The uncertainty for both x, y -direction are significantly lower and below 2 vectors.

6.1.2 Deformation characteristics

1 [mm] Rigid wing The deflection of the rigid wing is negligible such that it can be assumed to be fully rigid with a fixed geometric and local angle of attack of 45 deg for all phase angles.

175 [μm] Moderate flexible wing In Figure 6.1 the temporal evolution of the geometric and local angle of attack are given for the moderate flexible wing.

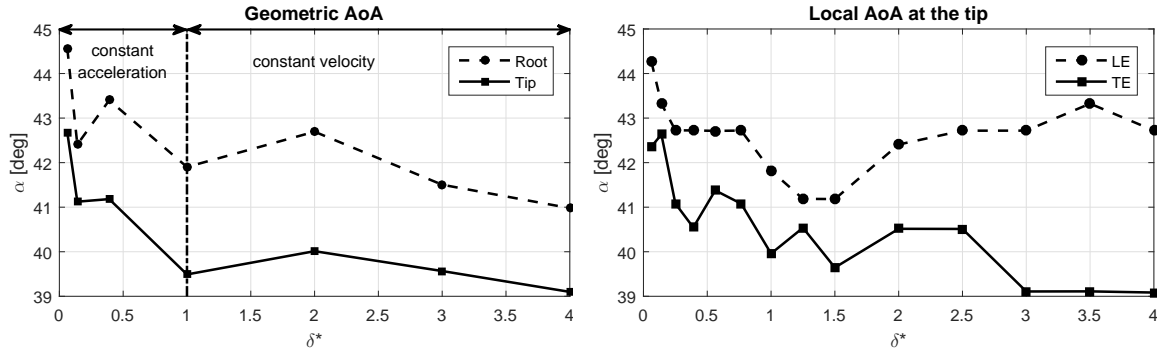


Figure 6.1: 175 [μm] Moderate flexible wing. *Left:* Temporal evolution of geometric angle of attack. *Right:* Temporal evolution of local angle of attack at the tip.

Due to the deflection of the wing the geometric angle of attack decreases as the motion progresses. As expected, at the start of the revolving motion the geometric AoA at the root and tip is close to 45 deg, due to the relatively low fluid forces. The local AoA at the LE is not exactly 45 deg as set by the servo motor. This is because the first detected LE point corresponds to the 1st chord profile point after the LE CF rod. At this chordwise section the wing starts deflecting which results in a local AoA that is slightly lower than 45 deg. The local AoA at the TE is significantly lower than at the LE. When the motion further progresses the wing starts to deflect rapidly until the end of the acceleration phase ($\delta^* = 1$), after which it starts to converge to a final wing shape. At the end of the revolving motion the approximate geometric angle is 41 deg at the root and 39 deg at the tip, resulting in a wing twist angle of 2 deg. The local AoA at the TE of the tip is approximately 39 deg and the difference in local AoA between the LE and TE is approximately 3.5 deg.

In Figure 6.2 the temporal evolution of the root and tip deflection is given.

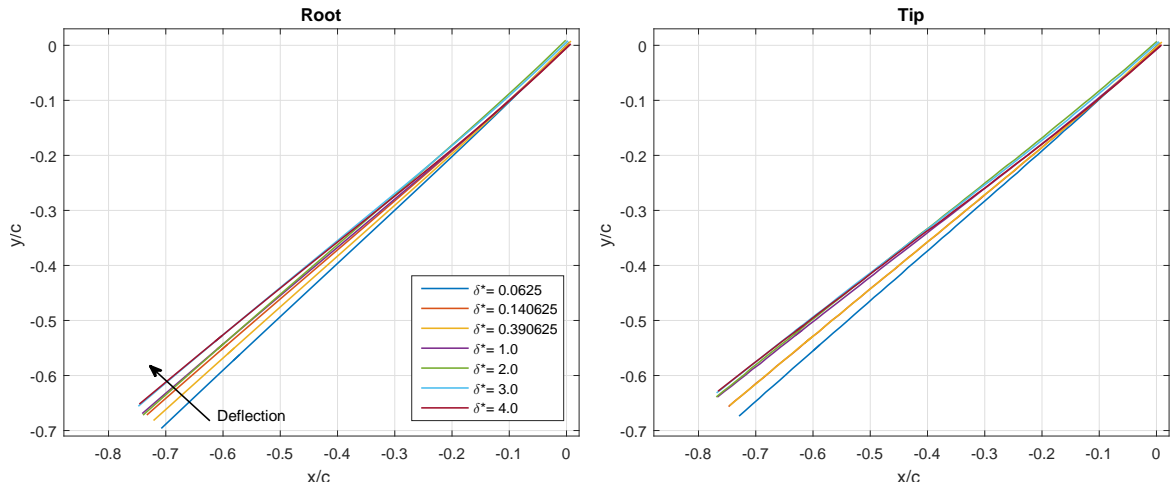


Figure 6.2: 175 [μm] Moderate flexible wing. *Left:* Temporal evolution of root chord profile. *Right:* Temporal evolution of tip chord profile.

It can be observed that the deflection at the tip is higher than at the root for the complete revolving motion. The rate of deflection in chordwise direction is highest close to the LE. This is caused by the increasing moment from TE to LE (zero moment at the TE and maximum moment at the LE). In the later phase of the revolving motion, the wing converges to its final shape in correlation with the forces reaching steady-state values.

125 μm High flexible wing In Figure 6.3 the temporal evolution of the geometric and local angle of attack are given for the high flexible wing.

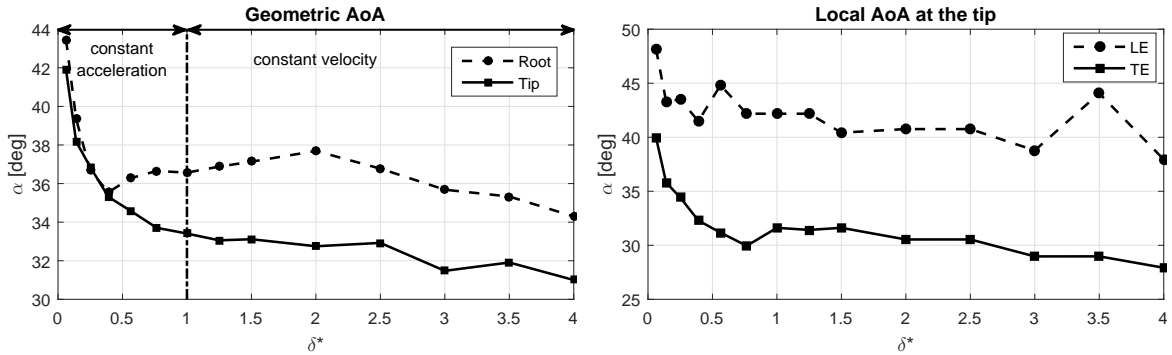


Figure 6.3: 125 μm High flexible wing. *Left:* Temporal evolution of geometric angle of attack. *Right:* Temporal evolution of local angle of attack at the tip.

It can be observed that until $\delta^* = 0.39$ the geometric AoA at the root and tip is approximately equal indicating that the wing deflects evenly along the wing span. Subsequently, the wing deflects more at the outwards spanwise positions which corresponds with a decreased geometric angle of attack. At the end of the revolving motion the approximate geometric angle is 34.5 deg at the root and 31 deg at the tip, resulting in a wing twist angle of 3.5 deg. The local AoA at the TE of the tip is approximately 28 deg and the difference in local AoA between the LE and TE is approximately 10 deg.

In Figure 6.4 the temporal evolution of the root and tip deflection is given. Similar to the 175 μm moderate flexible wing, the deflection at the tip is higher than at the root for greater phases of the revolving motion. Due to the decreased flexural stiffness, the wing deflects more compared to the 175 μm moderate flexible wing which is evident from the stronger deflected chord profiles.

The chordwise variation of the local angle of attack at the tip and the spanwise distribution of the geometric angle of attack at $\delta^* = 4$ are given in Figure 6.5. The geometric angle of attack increases approximately linearly over the span with approximately 3.5 deg indicating torsional deformation of the wing and the formation of wing twist. As can be deduced from the shape of the flexible wings during the revolving motion (see Figure 6.4), the maximum deformation occurs close to the leading edge resulting in a prominent variation of the local angle of attack for the chordwise locations from the leading edge ($x/c = 0$) until approximately $x/c = 0.4$, after which it is mostly constant (see Figure 6.5 right).

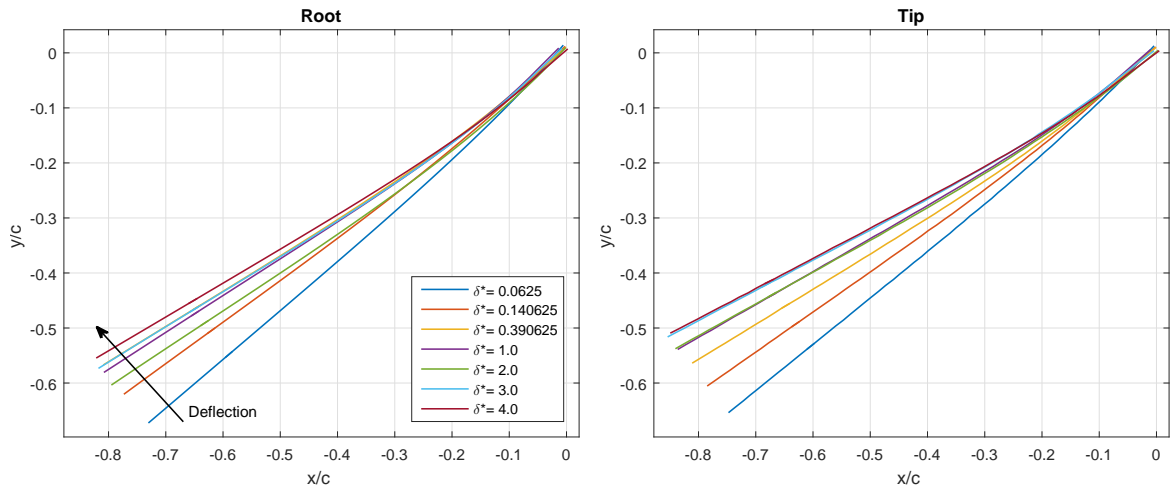


Figure 6.4: 125 [μm] High flexible wing. *Left:* Temporal evolution of root chord profile. *Right:* Temporal evolution of tip chord profile.

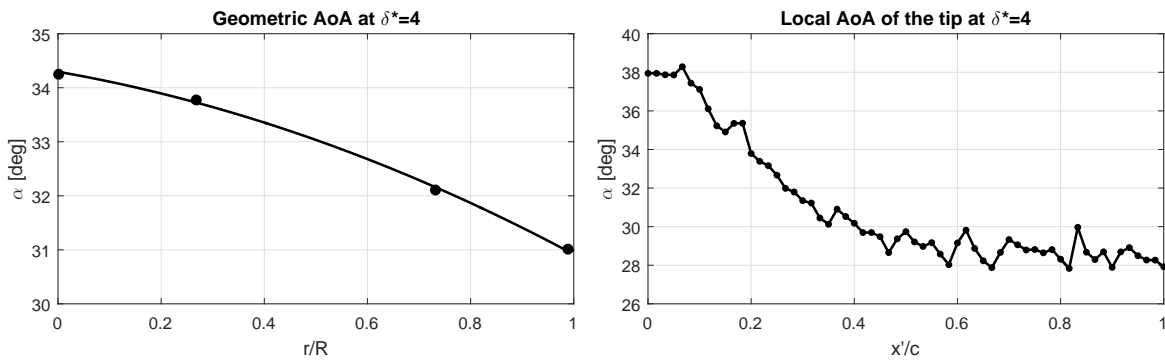


Figure 6.5: 125 [μm] High flexible wing. *Left:* Spanwise evolution of the geometric angle of attack at the end of the revolving motion. *Right:* Chordwise evolution of the local angle of attack of the tip at the end of the revolving motion, x' is the distance along the chord profile.

Chordwise deflection The chordwise deflection is expressed as the distance between the reconstructed TE point of the flexible wing with respect to the rigid wing. In Figure 6.6 the deflection is given for both moderate and high flexible wings.

The chordwise deflection is related to the geometric angle of attack, such that both quantities show a similar temporal variations. At the end of the revolving motion the chordwise deflection at the tip is approximately $0.234c$ for the 125 [μm] high flexible wing and $0.116c$ for the 175 [μm] high flexible wing, and the chordwise deflection at the root is approximately $0.195c$ for the 125 [μm] high flexible wing and $0.088c$ for the 175 [μm] high flexible wing.

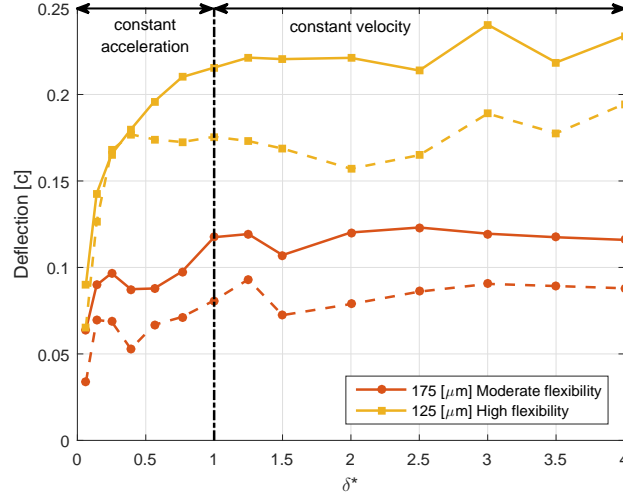


Figure 6.6: Temporal evolution of the chordwise deflection in terms of chord length. The solid line gives the chordwise deflection at the tip and the dashed line gives the chordwise deflection at the root.

6.2 Force measurements

6.2.1 Measurement uncertainty in the reported steady-state value

For greater rotation angles approximate steady-state conditions are expected to occur for uni-directional revolving wings (Percin & van Oudheusden, 2015b,a; Harbig et al., 2013; Jardin & David, 2014, 2015; Beals & Jones, 2015; Jones & Babinsky, 2011). The average measurement uncertainty of the reported lift and drag steady-state value is calculated based on the ensemble averaged and the low-pass filtered data in the steady-state phase ($5 < \delta^* < 10$). The average measurement uncertainty with a 95% confidence level is expressed as twice the standard deviation in percentage of the mean steady-state ensemble averaged data and low pass filtered data are given in Table 6.3.

Table 6.3: Average measurement uncertainty of the reported steady-state lift, drag in percentage of the mean steady-state ($5 < \delta^* < 10$) ensemble averaged data (*left*), and low pass filtered data (*right*) with a 95% confidence interval.

Wing	Average measurement uncertainty [%]			
	Ensemble averaged		Low-pass filtered	
	C_L	C_D	C_L	C_D
1 [mm] Rigid	4.2	4.5	1.1	0.9
175[μm] Moderate flexibility	5.1	4.6	1.6	1.1
125[μm] high flexibility	9.2	4.6	1.5	0.9

The approximate relative average measurement uncertainty for the low-pass filtered steady-state lift and drag are respectively 1.5% and 1%. Because the low-pass filter eliminates the

electrical noise, mechanical vibrations from the driving system and the natural frequency of the test-rig, the measurement uncertainties based on the low-pass filtered data are the most representative for the reported force data.

6.2.2 Lift, drag and performance characteristics

In Figure 6.7, the temporal evolution of the lift and drag characteristics for the different flexible wings considered in this study (i.e. rigid, moderate flexibility and high flexibility) are given.

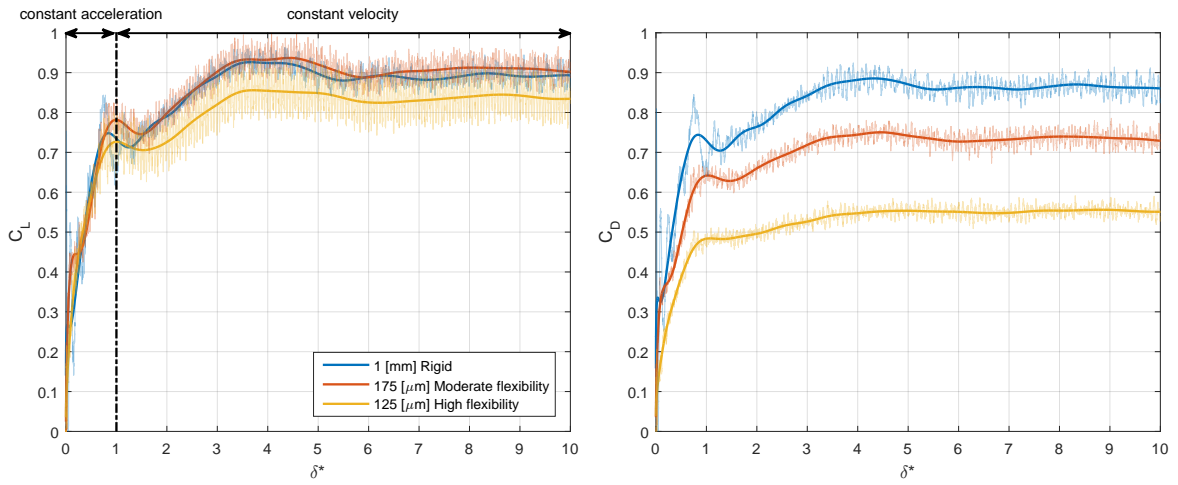


Figure 6.7: *Left:* Temporal evolution of lift coefficient. *Right:* Temporal evolution of drag coefficient. The light background signal is the ensemble average of the raw lift and drag data, and the solid line is the corresponding low-pass filtered data.

The drag and lift for the rigid wing are comparable suggesting that the pressure forces are dominant, so that the net force vector is oriented normal to the wing surface. For all wings, the forces build up rapidly at the start of the motion due to non-circulatory added mass effects. During acceleration the wing encounters an added mass reaction force due to the accelerated fluid, causing an additional force component which is absent after the acceleration phase. For a thin two-dimensional rigid flat plate wing moving in an inviscid fluid the force due to the inertia of the added mass acting normal to the wing surface can be expressed as (Percin & van Oudheusden, 2015b; Ellington, 1984),

$$\mathbf{F} = \rho \frac{\pi}{4} c^2 \frac{d\Omega}{dt} \sin(\alpha) \int_{r'_{root}}^{r'_{tip}} r' dr' \quad (6.2)$$

where r' is the spanwise distance from the revolution axis, α is the angle of attack and $d\Omega/dt$ is the angular acceleration (see Figure 4.2). The added mass reaction force acts normal to the local wing surface and is proportional to the acceleration component in this direction. Therefore, for the rigid wing, its contribution is constant throughout the acceleration phase. However, for the flexible wings, the acceleration component in the wing-normal direction changes since the wings deform (see Figure 6.2 and Figure 6.4) and so does the magnitude of

the added mass force. As the wing deflects, the added mass contribution decreases while its net force vector tilts toward the direction of lift. Summarized, for decreasing flexural stiffness, the net added mass effect is decreased in magnitude and tilted more in the direction of lift. As a result, the build-up of lift during the acceleration phases is comparable for the different wings while the build-up of drag decreases with decreasing flexural stiffness and the associated wing deformation. In addition to the added mass reaction force, circulatory forces associated with the generation of the LEV build up gradually with increasing velocity. For increased flexibility the starting TEV advects quicker downstream (see subsection 7.2.2), such that the velocity field induced by starting TEV counteracting the growth of circulation is attenuated, allowing for a more rapid build up of circulation. At the end of the acceleration phase, there is a slight decrease in the force coefficients as the added mass contribution ceases to contribute. The reduced contribution of the added mass contribution to the drag for the flexible wings is also evident from relatively small decrease of the drag coefficient at the end of acceleration phase when compared to the rigid wing case. After the acceleration phase, the lift and drag continue to increase until a maximum is reached at approximately $\delta^* = 4.5$. Subsequently, the forces decrease slightly until for all wings nearly steady-state conditions are reached at approximately $\delta^* = 5$.

The comparison of the lift data shows that the lift generation of the rigid and the moderate flexible wings are comparable, while smaller lift levels are achieved in the high flexibility case. The drag shows a monotonic decrease with decreasing flexural stiffness. At steady-state conditions, for $\delta^* = 10$, the lift coefficients of the high flexible wing is approximately 7% lower compared to the rigid wing, while the lift coefficient of the moderate flexible wing is approximately 1% higher. The steady-state drag coefficients of the moderate and high flexible wings are respectively 15% and 36% lower compared to the rigid wing

In Figure 6.8, the temporal evolution of the resultant force is given. Due to the monotonic decrease in drag with decreasing flexural stiffness and the decrease in lift for the high flexible wing, the resultant force acting on the model is decreased with decreasing flexural stiffness throughout the revolving motion. For steady-state conditions the resultant forces of the moderate and high flexibility are respectively 6% and 19 % lower compared to the rigid wing.

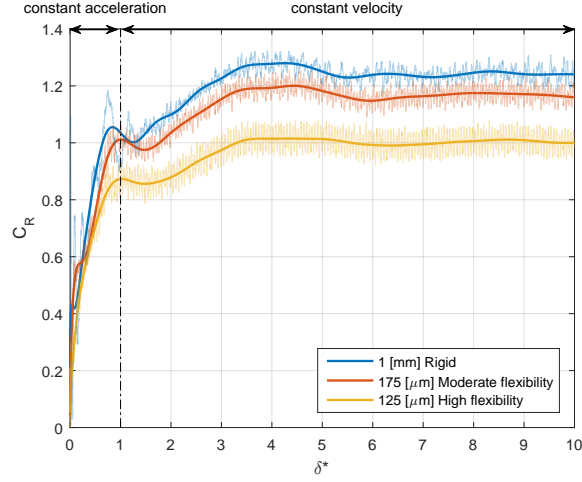


Figure 6.8: Temporal evolution of the resultant force coefficient ($C_R = \sqrt{C_L^2 + C_D^2}$). The light background signal is the ensemble average of the raw lift and drag data, and the solid line is the corresponding low-pass filtered data.

At the leading edge of the wing the flow separates and a LEV is formed which is accompanied by the formation of a low pressure region. The associated suction forces acting normal to the wing surface are the dominant factor determining the net forces acting on the wing (Usherwood & Ellington, 2002). Birch et al. (2004) studied a steady revolving rigid wing for a Reynolds number of 120 and 1,400. At the high Reynolds number of 1,400, for an angle of attack higher than 20 deg, the net force vector is normal to the wing indicating that the pressure forces are dominant (see Figure 2.4). The net force vector for rigid wings acts normal to the wing surface such that,

$$\alpha_{geo} = \tan^{-1} (D/L) \quad (6.3)$$

However, flexible wings deflect which leads to a deviation of the net force vector orientation with respect to the angle of attack that is initially set at the LE (Zhao et al., 2009). Based on Equation 6.3 (i.e., using the ratio of drag to lift) the geometric angles of attack α_{geo} at $\delta^* = 4$ for the rigid, moderate flexible and high flexible wings are calculated as 43.7 deg, 38.6 deg and 32.6 deg, respectively. The geometric angles of attack for these cases are also obtained from the reconstructed wing shapes and a comparison is given in Table 6.4.

Table 6.4: Comparison of the geometric angle of attack α_{geo} based on the wing reconstruction results (section 6.1, Figure 6.1 & Figure 6.3) and the lift-to-drag force relation Equation 6.3. Results apply to $\delta^* = 4$.

Wing	α_{geo} root [deg]	α_{geo} tip [deg]	α_{geo} [deg]
	Wing reconstruction	Wing reconstruction	Force relation
1 [mm] Rigid	45	45	43.7
175[μ m] Moderate flexibility	41	39	38.6
125[μ m] high flexibility	34.5	31	32.6

The spanwise centroid of lift and drag is located at approximately $r/R = 0.7 - 0.75$ for the different wings, see subsection 6.2.3 and subsection 8.2.3. Although the wing reconstruction presented in this section is an approximation of the true wing shape, it can be observed that the reconstructed geometric angles of attack near the tip (or at approximately the spanwise centroid of lift and drag, $r/R = 0.7 - 0.75$) of the wing for $\delta^* = 4$ agree well with the direction of the net forces for the studied wings. This observation suggests that for a chordwise flexible wing the lift-to-drag ratio at steady-state conditions can be estimated based on the geometric angle of attack as illustrated in Figure 6.9.

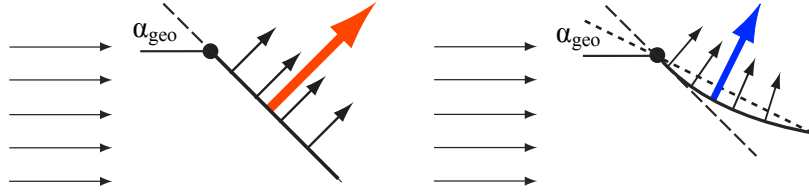


Figure 6.9: Net force angle as a function of geometric angle of attack at steady-state conditions. *Left:* Rigid wing. *Right:* Chordwise flexible wing. Apparent reference flow from left-to-right. Small vectors represent local net forces that act normal to the wing surface, and big vector represent resultant net force that is aligned with respect to the geometric angle of attack.

The approximate aerodynamic efficiency can be estimated using the power factor ($C_L^{1.5}/C_D$) (Wang, 2007). The power factor is a non-dimensional aerodynamic ratio of the mass supported per power. The performance characteristics expressed as the lift-to-drag ratio and the power factor are given in Figure 6.10.

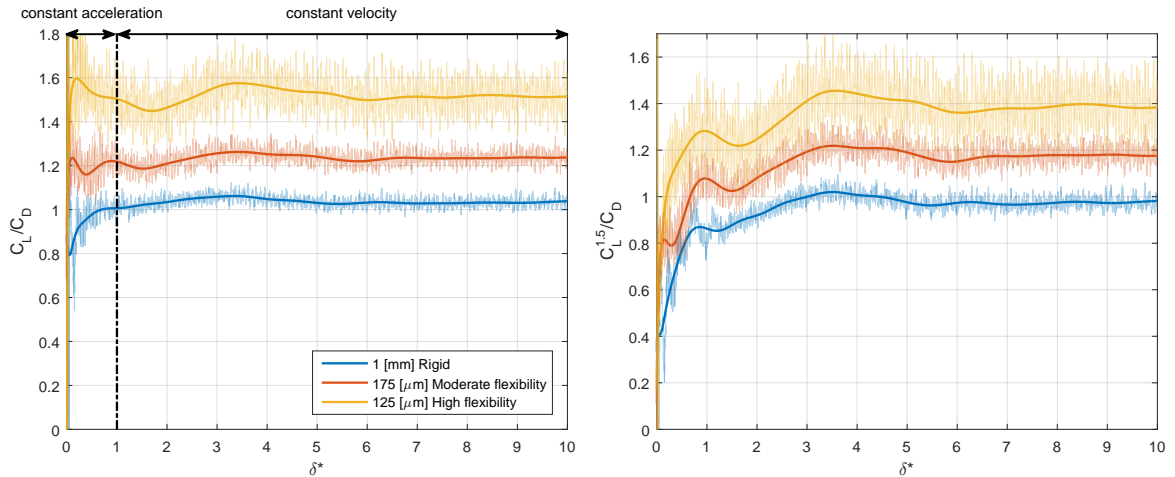


Figure 6.10: *Left:* Temporal evolution of the lift-to-drag ratio C_L/C_D . *Right:* Temporal evolution of power factor expressed as $C_L^{1.5}/C_D$. The light background signal is the ensemble average of the raw data, and the solid line is the corresponding low-pass filtered data.

Due to the relatively higher decrease in drag than lift for decreasing flexural stiffness, both lift-to-drag ratio and power efficiency increase with decreasing flexural stiffness. At the steady-state conditions, for $\delta^* = 10$, the lift-to-drag for the moderate flexible wing and high flexible wing is approximately 18% and 45% higher than for the rigid wing, respectively. The power efficiency for the moderate flexible wing and high flexible wing is approximately 20% and 40%

higher than for the rigid wing at steady-state conditions, respectively.

6.2.3 Spanwise and chordwise location of the center of pressure

The spanwise location of the center of pressure is the location at which the resultant force vector produces the same moment about the root of the wing and is approximated as,

$$\text{Center of pressure, } r = -\frac{M_x}{F_y} - \text{off}_{\text{bal}} \quad (6.4)$$

where r is the spanwise location of the center of pressure. Within the reference frame of the balance, that is rotated with 45 deg (as set by the servo motor) with respect to the flow field data, M_x and F_x are respectively the moment and force vector in x -direction. The term off_{bal} is the offset between the wing root and the balance, of approximately 15 mm. Because the LE is rigid in spanwise direction, the spanwise location of the center of pressure represents the location along the span of the wing. The chordwise location of the center of pressure is the location at which the resultant force vector produces the same moment about the LE of the wing and is approximated as,

$$\text{Center of pressure, } x'_{\text{geo}} = -\frac{M_z}{F_r} \quad ; \quad F_r = \sqrt{F_x^2 + F_y^2} \quad (6.5)$$

where M_z is the moment in z -direction and F_x is the force vector in x -direction within the reference frame of the balance. The lift-to-drag ratio at steady-state conditions agrees well with the geometric angle of attack, see Table 6.4. This implies that the line connecting the LE and TE, which is inclined with the geometric angle of attack, is approximately normal to the force vector F_r , such that the chordwise location of the center of pressure is located on this line as illustrated in Figure 6.11.

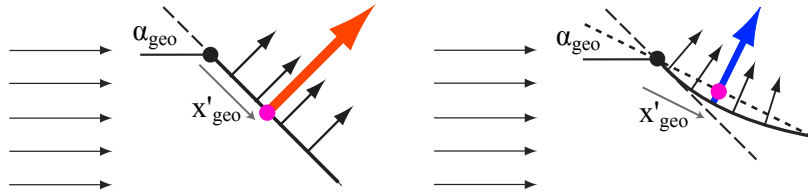


Figure 6.11: Chordwise location, x'_{geo} , of the center of pressure located along the line that connects the LE and TE of the wing (indicated by the magenta dot). *Left:* Rigid wing. *Right:* Chordwise flexible wing. Apparent reference flow from left-to-right.

In Figure 6.12 the spanwise and chordwise location of the center of pressure are given. The spanwise location of the center of pressure is approximately equal for the different wings and decreases slightly during the revolving motion. At steady-state conditions, for $\delta^* = 10$, the center of pressure is located at approximately $0.73 r/R$. The chordwise location of the center of pressure is approximately constant from the end of the acceleration onwards for the different wings. However, for decreasing flexural stiffness the chordwise location of the center of pressure is located closer to the LE of the wing. At $\delta^* = 10$, the chordwise location of the

center of pressure x'_{geo} of the rigid, moderate flexible and high flexible wing is approximately $0.45c$, $0.425c$ and $0.38c$, respectively.

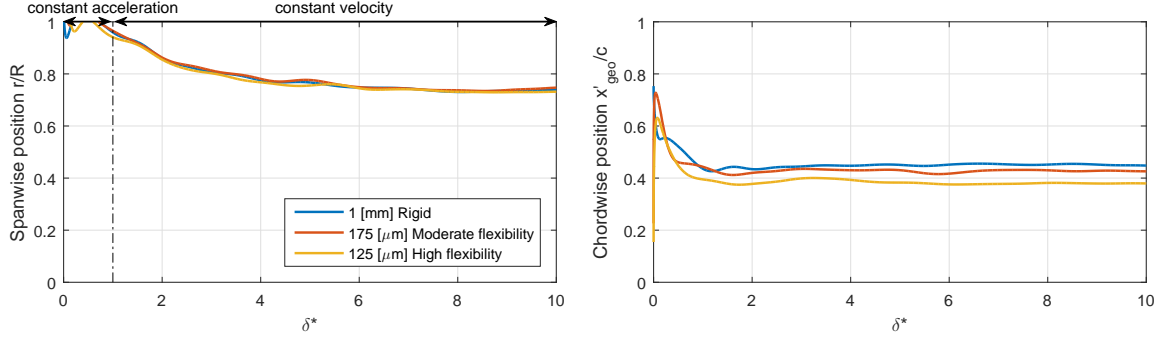


Figure 6.12: Temporal evolution of the location of the center of pressure *Left:* Spanwise location along the span in r/R . *Right:* Chordwise location along the line connecting the LE and TE in x'_{geo}/c (inclined with the geometric angle of attack).

6.2.4 Comparison with literature

Percin & van Oudheusden (2015b) studied a revolving rigid wing at an angle of attack of 45 deg and a Reynolds number of 10,000. The motion kinematics were the same as in this study. The trend in the temporal evolution and magnitude of the lift and drag coefficients are similar compared to the current study. The most pronounced difference between the results is that the magnitude of the drag peak at the end of the acceleration phase is approximately equal to the steady-state value, while in the current study this peak is approximately 13% lower than the steady-state value. The steady-state lift in (Percin & van Oudheusden, 2015b) is approximately 10% higher than the current study. Also in (Percin & van Oudheusden, 2015b) the reported drag closely matches the lift (within approximately 6% at steady-state conditions), which further suggests that the pressure forces are dominant, so that the net force vector is oriented normal to the wing surface. Although the LE structure, clamp position and Rossby number are slightly different in (Percin & van Oudheusden, 2015b), this comparison shows that the steady-state values of the lift and drag are very similar which further validates the current measurements.

Zhao et al. (2009) studied wings with different chordwise stiffness for a large range of angles of attack at a Reynolds number of 2,000 for a steady-state revolving motion. From this study, the force coefficients for varying effective stiffness parameter at an angle of attack of 45 deg are extracted. The effective stiffness parameter Π_1 is calculated based on the flexural stiffness EI , the span ($R = 100$ mm), the mean chord ($c = 33.7$ mm), the fluid density ($\rho_f = 850$ kg/m³) and the reference velocity at 75% span ($U_{ref} = 0.18$ m/s) as,

$$\Pi_1 = \frac{EI}{Rc^3\rho_f U_{ref}^2} \quad (6.6)$$

U_{ref} is approximated by means of the wing planform characteristics and the distance between the root of the wing and the rotation axis ($RA = 127$ mm). The lift and drag coefficient as a function of effective stiffness are given in Figure 6.13.

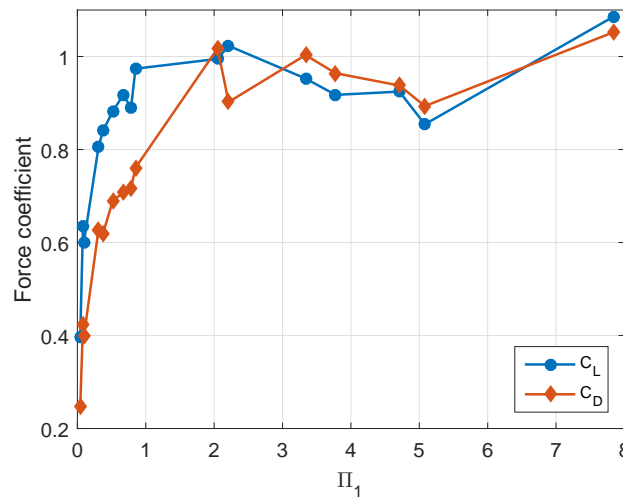


Figure 6.13: Lift and drag coefficient from (Zhao et al., 2009) expressed as function of Π_1 at an angle of attack of 45 deg.

The lift and drag coefficients for a high effective stiffness, corresponding to large Π_1 values, are similar in magnitude to the measured lift and drag coefficients of the rigid wing in this study. Note that the lift and drag coefficients extracted from (Zhao et al., 2009) are corrected to the force coefficient definition as given in Equation 5.17. In the approximate range of $0.8 < \Pi_1 < 2$ the lift is relatively constant, while the drag is already significantly lower. For $\Pi_1 < 0.8$ the lift starts decreasing as well.

Note that Zhao et al. (2009), measured the flexural stiffness EI by means of a custom-built bending apparatus, while in this study EI is approximated based on the wing planform characteristics and material parameters. The approximated Π_1 parameter for the rigid, moderate flexible and high flexible wing are respectively 55, 0.389 and 0.147, see section 4.3. The general trend for the lift and drag coefficient for flexible wings with a decreased Π_1 value is similar. For moderate flexible wings in the range of $0.8 < \Pi_1 < 2$, the lift is similar compared to the rigid wing ($\Pi_1 \gg 1$) while the drag is lower. Moreover, for high flexible wings in the range of $\Pi_1 < 0.8$, a decrease in lift is observed as well as a monotonic decrease in drag. However, from this comparison the force coefficients do not exactly match for the same effective stiffness Π_1 parameters. The differences may be due to the different wing planform and definition of EI . Furthermore the Rossby number in (Zhao et al., 2009) is approximately 5.3, which is significantly higher compared to the a Rossby number of approximately 1.9 in the current study.

M. Percin, R. Vester and B.W. van Oudheusden studied the lift and drag force coefficients for a steady-state revolving rigid wing with Reynolds number of 10,000 for a range of angles of attack ¹. The motion kinematics and the wing planform were the same as in this study. The Rossby number (1.66) is slightly smaller compared to the current study. The steady-state lift and drag coefficients as a function of angle of attack are given in Figure 6.14.

¹Results provided by M. Percin, study not published to date

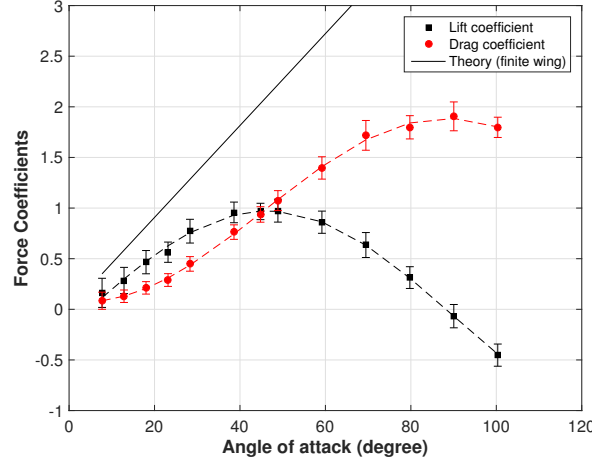


Figure 6.14: Steady-state lift and drag coefficient as function angle of attack.

The steady-state lift and drag coefficients at an angle of attack of 45 deg are approximately 10% higher compared to the current study (as observed in Figure 6.7 for $\delta^* = 10$). However, it should be noted that the steady-state lift and drag coefficients in Figure 6.14 are defined as the average forces in the motion period of $2 < \delta^* < 10$. The empirical relation between the steady-state lift-drag coefficient and the angle of attack is given as,

$$C_L = -0.06 - 0.112 \cos(2.073\alpha) + 1.026 \sin(2.073\alpha) \quad (6.7)$$

$$C_D = 0.978 - 0.903 \cos(2.105\alpha) - 0.098 \sin(2.105\alpha) \quad (6.8)$$

In section 6.2 it is observed that the geometric angle of attack, based on the steady-state lift-to-drag ratio (Equation 6.3), agrees well with the geometric angle of attack near the tip of the wing (Table 6.4). Based on Equation 6.3 the calculated geometric angles of attack α_{geo} at $\delta^* = 10$ for the rigid, moderate flexible and high flexible wings are respectively 44 deg, 39 deg and 33.5 deg. Although the steady-state lift and drag coefficients in Figure 6.14 are higher than in the current study, it is assumed that the relative differences of the lift and drag for different angles of attack are similar. Subsequently, the steady-state lift and drag coefficient found in the current study are compared to the reconstructed steady-state lift and drag coefficient for a rigid wing revolving at the geometric angle of attack for the rigid, moderate flexible and high flexible wing for $\delta^* = 10$ as given in Table 6.5. Note that the reconstructed steady-state lift and drag coefficients are scaled to match the steady-state lift and drag coefficients of the rigid wing in the current study.

It can be observed that the relative decrease in steady-state lift is slightly higher compared to the decrease in drag when revolving a rigid wing at the geometric angle of attack of the moderate and high flexible wings. However the differences are small and the steady-state lift and drag coefficients of the moderate and high flexible revolving wings show a good agreement with a revolving rigid wing at the identical geometric angle of attack of the flexible wing. This suggests that the geometric angle of attack for different degree of chordwise flexibility wings is dominant for the lift and drag acting on the model at steady-state conditions. In Figure 6.15

Table 6.5: Comparison of the steady-state lift and drag coefficient found in the current study and the reconstructed steady-state lift and drag coefficient for a rigid wing revolving at the geometric angle of attack for the rigid, moderate flexible and high flexible wing using the data from Figure 6.14 for $\delta^* = 10$.

Wing	C_L	C_D	α_{geo} [deg]	C_L	C_D
	Figure 6.7	Equation 6.3		Figure 6.14	
1 [mm] Rigid	0.89	0.86	44	0.89	0.86
175[μm] Moderate flexibility	0.9	0.73	39	0.86	0.71
125[μm] high flexibility	0.83	0.55	33.5	0.79	0.54

the suggested net force as a function of geometric angle of attack at steady-state conditions is illustrated.

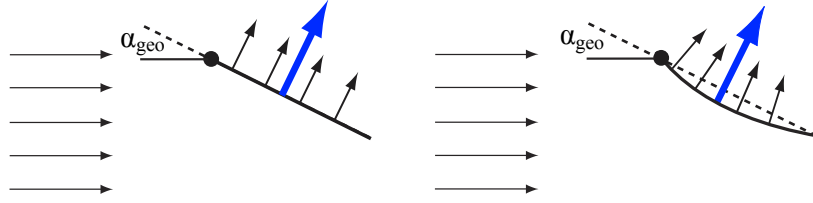


Figure 6.15: Net force as a function of geometric angle of attack at steady-state conditions. *Left:* Rigid wing revolving at the same geometric angle of attack of the flexible wing. *Right:* Chordwise flexible wing. Apparent reference flow from left-to-right. Small vectors represent local net forces that act normal to the wing surface, and big vector represent resultant net force that is similar for a rigid wing revolving at the same geometric angle of attack of the flexible wing.

6.3 Conclusion

Wing reconstruction The 1 [mm] rigid wing has a fixed geometric and local AoA of 45 deg throughout the revolving motion, while the flexible wings deflect significantly during the revolving motion. The 175 [μm] moderate flexible wing deflects and twists along the wing span. Moreover, the deflection and formation of wing twist increase during the revolving motion. At the end of the revolving motion the geometric AoA at the tip is approximately 39 deg at the tip and 41 deg at the tip, resulting in a wing twist angle of 2 deg. The corresponding chordwise deflection at the tip is approximately $0.116c$. The 125 [μm] flexible wing deflects and twists more along the wing span than the 175 [μm] moderate flexible wing. At the end of the revolving motion the geometric AoA at the tip is approximately 31 deg at the tip and 34.5 at the root, resulting in a wing twist angle of 3.5 deg. The corresponding chordwise deflection at the tip is approximately $0.234c$.

The experimental campaign of this study was set up with the focus on the tomographic PIV measurements. Therefore, the wing reconstruction can be considered as an approximation of the true wing shape. For the moderate flexible wing at steady-state conditions, the geometric AoA at the tip is about equal to the local AoA at the tip-TE because the local AoA chordwise

profile at the tip suffers from reconstruction errors. The true local AoA at the tip-TE is expected to be somewhat smaller than 39 deg. The reconstructed wing is used to relate the flow field characteristics to the wing shape and to determine the mask for the pressure reconstruction.

Force measurements During the acceleration phase ($\delta^* < 1$) the build-up of lift is similar for the different wings, while the build-up of drag is significantly lower for decreasing flexural stiffness. At steady state conditions, for $\delta^* = 10$, the lift of the rigid and moderate flexible wing is comparable, while the lift is only slightly (about 7%) smaller for the high flexible wing. The drag shows a monotonic decrease with decreasing flexural stiffness. Moreover, for decreasing flexural stiffness the relative decrease in drag, up to 36% for the most flexible wing, is higher than that for the lift. As a result the lift-to-drag ratio and power efficiency increase significantly with decreasing flexural stiffness. For steady-state conditions the lift-to-drag ratio for the moderate flexible and high flexible wing are approximately 18% and 45% higher than that for the rigid wing, respectively. Furthermore, the power efficiency for the moderate flexible wing and high flexible wing is approximately 40% and 20% higher than that of the rigid wing, respectively.

In the current study a rigid wing and two flexible wings with different degree of chordwise flexibility have been tested. The observations in the current study suggest that the lift-to-drag ratio for chordwise flexible wings at steady-state conditions can be estimated based on the geometric angle of attack near the tip. Moreover, it is shown that a rigid wing with a geometric angle of attack identical to that of the deformed wing generates similar lift and drag. This suggests that the geometric angle of attack at steady-state conditions is dominant for the lift and drag generated by chordwise flexible wings considered in this study. These observations may simplify the modeling of flexible flapping-wing flight, since the aerodynamic forces of chordwise flexible wings may be approximated using an aerodynamic model for a revolving rigid wing at the identical geometric angle of attack of a flexible wing.

At steady-state conditions, for $\delta^* = 10$, the spanwise centroid of pressure is approximately equal for all wings, located at $0.73 r/R$. The chordwise location of the center of pressure is approximately located along the line that connects the TE and LE, and is located closer to the LE with decreasing flexural stiffness. For the rigid, moderate flexible and high flexible wing this location is approximately $0.45c$, $0.425c$ and $0.38c$, respectively.

Chapter 7

Results: Flow field

In this chapter the flow field results are presented and discussed. First, the definitions that are used in the evaluation of the results are given. Second, the major flow structures are presented and discussed. Finally, the spanwise characteristics of the flow field are evaluated and analyzed.

Based on the balance measurements steady-state conditions are reached for $\delta^* > 5$, see section 6.2. However, the imaging measurements are taken up to $\delta^* = 4$, see section 4.5. In this chapter steady-state conditions indicate the imaging measurements for the greatest chord length that has been measured, i.e. $\delta^* = 4$.

7.1 Definitions

Q-criterion (Hunt et al., 1988) Qualitatively a vortex can be interpreted as a connected fluid region with a high concentration of vorticity compared with its surroundings (Wu et al., 2006). Coherent vortex structures in a flow field can be identified using the Q-criterion. The Q-criterion is Galilean-invariant, is based on the symmetric and anti-symmetric components of the velocity gradient tensor ($\nabla\mathbf{u}$), and represents the local balance between shear strain rate and vorticity magnitude (Hunt et al., 1988; Jeong & Hussain, 1995). The Q-criterion is evaluated as,

$$Q = -\frac{1}{2} \frac{\partial u_i}{\partial x_j} \frac{\partial u_j}{\partial x_i} \quad (7.1)$$

Flow regions with a positive value for the Q-criterion are used to identify coherent structures in the flow that are dominated by rotation. Note that the Q-criterion can also be interpreted

as the source term in the Poisson equation for the calculation of the pressure fields. In absence of rotational effects for an incompressible and divergence free flow (see Equation 5.20) the Poisson equation reads,

$$\nabla^2 p' = 2\rho Q \quad (7.2)$$

In this study, similar to other flapping wing studies (see Carr et al. (2013); Garmann et al. (2013); Wolfinger & Rockwell (2014); Bross & Rockwell (2015); Percin & van Oudheusden (2015b)), the Q-criterion is employed because it is useful in the distinction of the shear and rotation dominated regions in a flow field. Furthermore Carr et al. (2013) showed that the Q-criterion produces results are nearly indistinguishable compared to the local structure identification schemes based on the Δ -criterion and λ_2 -criterion which are also based on the velocity gradient tensor, see Jeong & Hussain (1995).

Although the Q-criterion is not rotation invariant, i.e. the components dU_x/dz (spanwise variation of chordwise velocity) and dU_z/dx (chordwise variation of spanwise velocity) are different in the rotating reference frame compared to the inertial reference frame when revolving around the y -axis, the identified Q-criterion isosurfaces are very similar and the differences are negligible. This is because the vorticity is mainly dominated by the chordwise and spanwise vorticity components.

γ_1 & γ_2 (Graftieaux et al., 2001) γ_1 & γ_2 can be used to characterize a vortex. Its definition is based on a non-local scheme and only considers the topology of the flow field. γ_1 is a non-Galilean invariant scalar function that measures the relative rotation about each grid point constrained to a definable interrogation window as,

$$\gamma_1(P) = \frac{1}{N} \sum_M \frac{(\mathbf{R}_{PM} \times \mathbf{U}_M) \cdot \mathbf{z}}{\|\mathbf{R}_{PM}\| \|\mathbf{U}_M\|} = \frac{1}{N} \sum_M \sin(\theta_M) \quad (7.3)$$

where N is the number of grid points M within a bounded square region centered on grid point P , \mathbf{U}_M is the velocity vector, \mathbf{R}_{PM} is the radius vector and θ_M is the angle between the velocity vector \mathbf{U}_M with the radius vector \mathbf{R}_{PM} . The center of a vortex core is identified as the local maximum of $\|\gamma_1\|$.

The vortex core size is identified using $\|\gamma_2\|$ as,

$$\gamma_2(P) = \frac{1}{N} \sum_M \frac{(\mathbf{R}_{PM} \times (\mathbf{U}_M - \mathbf{U}_P)) \cdot \mathbf{z}}{\|\mathbf{R}_{PM}\| \|\mathbf{U}_M - \mathbf{U}_P\|} \quad (7.4)$$

where \mathbf{U}_P is the local advection velocity. Note that in contrast to γ_1 , γ_2 is Galilean invariant. Regions of $\|\gamma_2\| > 2/\pi$ are locally dominated by rotation and therefore represent a vortex core.

Since γ_1 is not Galilean invariant, γ_1 and γ_2 are calculated in the rotating reference frame. For this analysis M is selected as a square region of 15×15 vectors. The detected vortex core size did not change significantly with different sizes of M .

Helical density (Moffatt, 1969) Helical density h or helicity per unit volume indicates the degree to which a flow structure is three dimensional and in what sense, and is also an indicator of vorticity flux along the primary axis of a vortex (Carr et al., 2013). Helical density h is calculated as,

$$h = \mathbf{U} \cdot \boldsymbol{\omega} \quad ; \quad \boldsymbol{\omega} = \nabla \times \mathbf{U} \quad (7.5)$$

where \mathbf{U} is the velocity vector and $\boldsymbol{\omega}$ is the vorticity vector. The helical density is calculated in the inertial reference frame such that the vorticity flux along the primary axis of a vortex is indicative for the spanwise and chordwise advection of vorticity.

Circulation The circulation Γ is calculated as,

$$\Gamma = \int_{S_{xy}} \omega_z dx dy \quad ; \quad \Gamma^* = \frac{\Gamma}{cV_t} \quad (7.6)$$

where S_{xy} is the chordwise oriented integration plane.

Spanwise vorticity flux The spanwise vorticity flux q is calculated as the integration of the spanwise vorticity flux density (third component of helical density) as,

$$q = \int_{S_{xy}} U_z \omega_z dx dy \quad ; \quad q^* = \frac{q}{cV_t^2} \quad (7.7)$$

where S_{xy} is the chordwise oriented integration plane.

Formation number The formation number FN is the distance traveled at each spanwise position $x(r)$ normalized by the chord length as,

$$\text{FN} = x(r)/c = \frac{\delta^*}{0.75 + RA/(2c)} \cdot \{r/R + RA/(2c)\} \quad (7.8)$$

where RA is the distance between the root of the wing and the rotation axis, see section 4.2. r/R is the spanwise coordinate in terms of span length measured from the root. The factor 0.75 is introduced since δ^* is defined at the reference position ($r/R = 0.75$).

7.2 Flow structures

In this section the flow structures for the tested wings are presented. For illustration purposes the two flexible wings are illustrated with a thickness of 0.5 mm. In all figures the left column depicts the 1 [mm] Rigid wing, the middle column depicts the 175 [μm] Moderate flexible wing and the right column depicts the 125 [μm] High flexible wing unless stated otherwise.

7.2.1 Experimental uncertainty of the flow field

For an incompressible flow, a divergence-free flow field is expected. However, due experimental errors the flow field is not divergence-free in complete measurement domain. Furthermore, when assuming a divergence-free flow field in the derivation of the modified Poisson problem, an incorrect pressure field is reconstructed (see subsection 5.3.5).

In Figure 7.1 the temporal evolution of the absolute divergence of the velocity field is given in terms of its mean and rms error value.

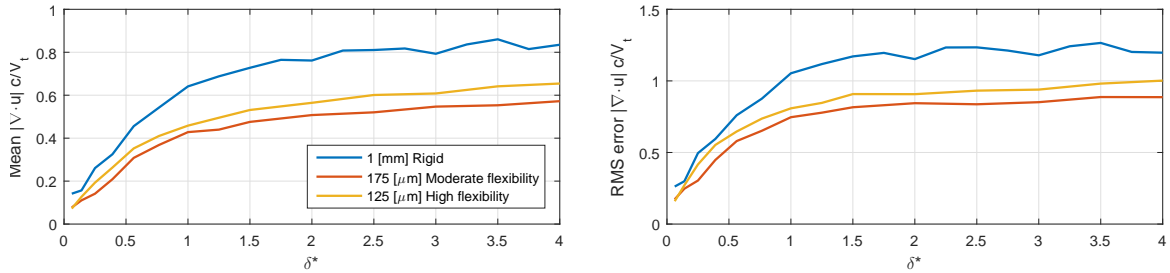


Figure 7.1: Temporal evolution of the experimental uncertainty of the flow field, evaluated by the absolute divergence of the velocity field ($|\nabla \cdot \mathbf{u}c/V_t|$). Based on measurement volumes 1-3. *Left:* Temporal evolution of the mean. *Right:* Temporal evolution of the RMS error.

It is found that the mean and rms error values are significantly lower for the flexible wings compared to the rigid wing. During the acceleration phase the mean and rms error values increase as the revolving motion progresses. Within this phase the vortical structures increase in size and magnitude which are accompanied by increased spatial velocity gradients. Due to reconstruction and discretization errors, errors are introduced within the calculation of these spatial velocity gradients, and subsequently within the reported divergence of the velocity field. At steady-state conditions ($\delta^* = 4$) the mean and rms error values reach a relative constant level.

In Figure 7.2, the spatial distribution of the divergence of the velocity field is given for $\delta^* = 1.5$. It is found that the highest measurement uncertainties agree well with the rotation dominated regions which are accompanied by high spatial velocity gradients. These regions include the LEV, TV, flow regions in close proximity of the wing and the flow regions in the wake of the wing that are located downstream of the TE. Due to the significantly higher thickness of the rigid wing compared to the flexible wings, higher reconstruction errors are introduced, which increases the measurement uncertainty near the wing surface. Moreover, the rigid wing

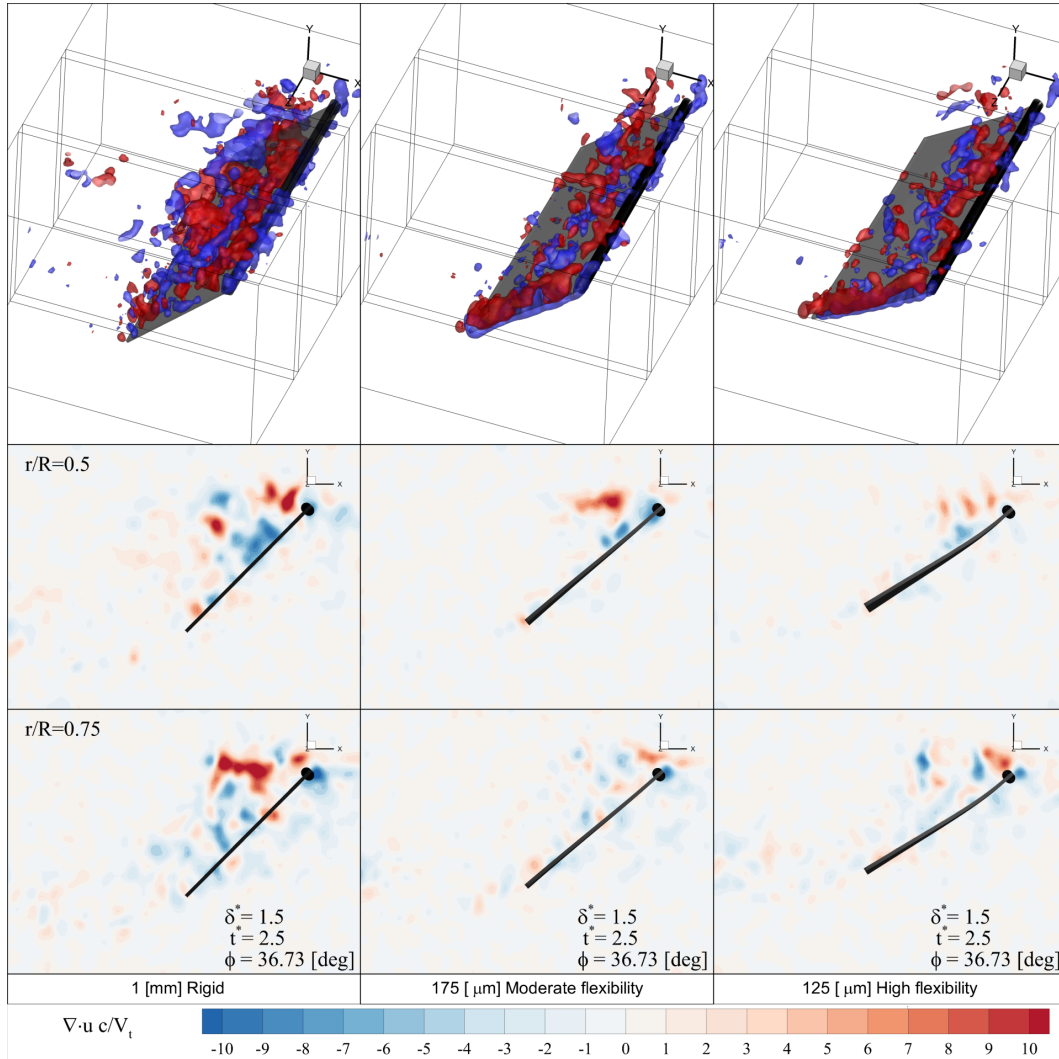


Figure 7.2: Divergence of velocity field ($\nabla \cdot \mathbf{u} c/V_t$) for $\delta^* = 4$. *Top:* isosurface of $\nabla \cdot \mathbf{u} c/V_t$: Blue $\nabla \cdot \mathbf{u} c/V_t = -5$ and Red $\nabla \cdot \mathbf{u} c/V_t = 5$. *Middle:* Divergence of velocity field contour at $r/R = 0.5$. *Bottom:* Divergence of velocity field contour at $r/R = 0.75$.

has the lowest natural frequency (see section 4.4) which also increases the uncertainty of the velocity field in close proximity of the wing.

7.2.2 Coherent structures

Q-criterion isosurfaces In Figure 7.3 the vortical structures are depicted for the three wings at $\delta^* = 1$ and $\delta^* = 1.5$. In section A.1 a time-series animation of vortical structures is given.

The global topology of the vortex system for the three wing models is similar, although the orientation of the structures is clearly affected by the wing deformation. For each wing an

LEV, an initial coherent starting TEV with a number of smaller scale TEVs, a TV and a root vortex (RV) are present. The vortex system for the flexible wings is more coherent with higher Q-criterion values, with the most significant difference occurring for the RV. From the side views the greater tip deflection for the flexible wings compared to the rigid wing can be observed.

Until the acceleration phase $\delta^* = 1$, it can be clearly observed that in relation to the chordwise deflection of the wings, the TV and the starting vortex system is more elongated in the streamwise direction in the flexible cases. For decreasing flexural stiffness, the finger-like swirling vortices that are wrapped circumferentially around the TV are located closer to the center of the TV. These finger-like vortices connect to the secondary small-scale TEVs in all cases. At $\delta^* = 1.5$, a large number of secondary TEVs are present elongating all over the span in the wake. The flexible wings appear to shed a higher ordered and more continuous streak of smaller-scale TEVs compared to the rigid wing. The TEVs move downstream along approximately the local induced angle of attack at the trailing edge of the wing model. For $\delta^* > 2.5$ the vortex formation displays significant chaotic features for all three wings. These results are in accordance with the results reported by [Percin & van Oudheusden \(2015b\)](#), who also performed revolving-surging rigid wing measurements with the same wing planform and kinematics. [Wolfinger & Rockwell \(2014\)](#) observed an increased coherency of the vortex system for lower Rossby numbers and suggested that the stability or retention of the LEV is coupled with the interior structure of the tip and root vortices. The increased coherency of the vortex system for the flexible wings could contribute to the stability or retention of the LEV. The occurrence of vortex breakdown for all wing models is similar. Near the midspan ($r/R = 0.5$) position, the core of the LEV is lifted off and expanded into a substantial bubble-like structure that extends towards to the tip for all three wings which is indicative for the vortex breakdown. This is in accordance with literature for a rigid revolving wing at which the vortex breakdown was also reported to occur near midspan ([Garmann & Visbal, 2014](#); [Jones et al., 2016](#)). The LEV grows in size along the span until about 75% for all three wings. This agrees well with the observations given ([Carr et al., 2013](#)) who studied a rigid revolving wing. For $\delta^* > 1.5$ there is an onset of vortex burst at which the vortex formation starts displaying significant small scale chaotic structures, which appears quite similar for all wings.

The location of the LEV in the x, y -plane is similar for the different flexibilities. However, due to the deflection of the flexible wings the LEV center is located closer to the wing surface. The top part of the LEV-TV is located at approximately the same upward location for all wing models, but the bottom part of the LEV-TV is located closer to the top part of the LEV-TV for decreasing flexural stiffness. As a result the LEV-TV is confined to a smaller region within the flow field, which is most pronounced for greater chord lengths of travel. The reduced size of the LEV is also evident from the spanwise vorticity, see Figure 7.6. Further insights about the LEV properties in terms of its spanwise characteristics are given in subsection 7.2.3.

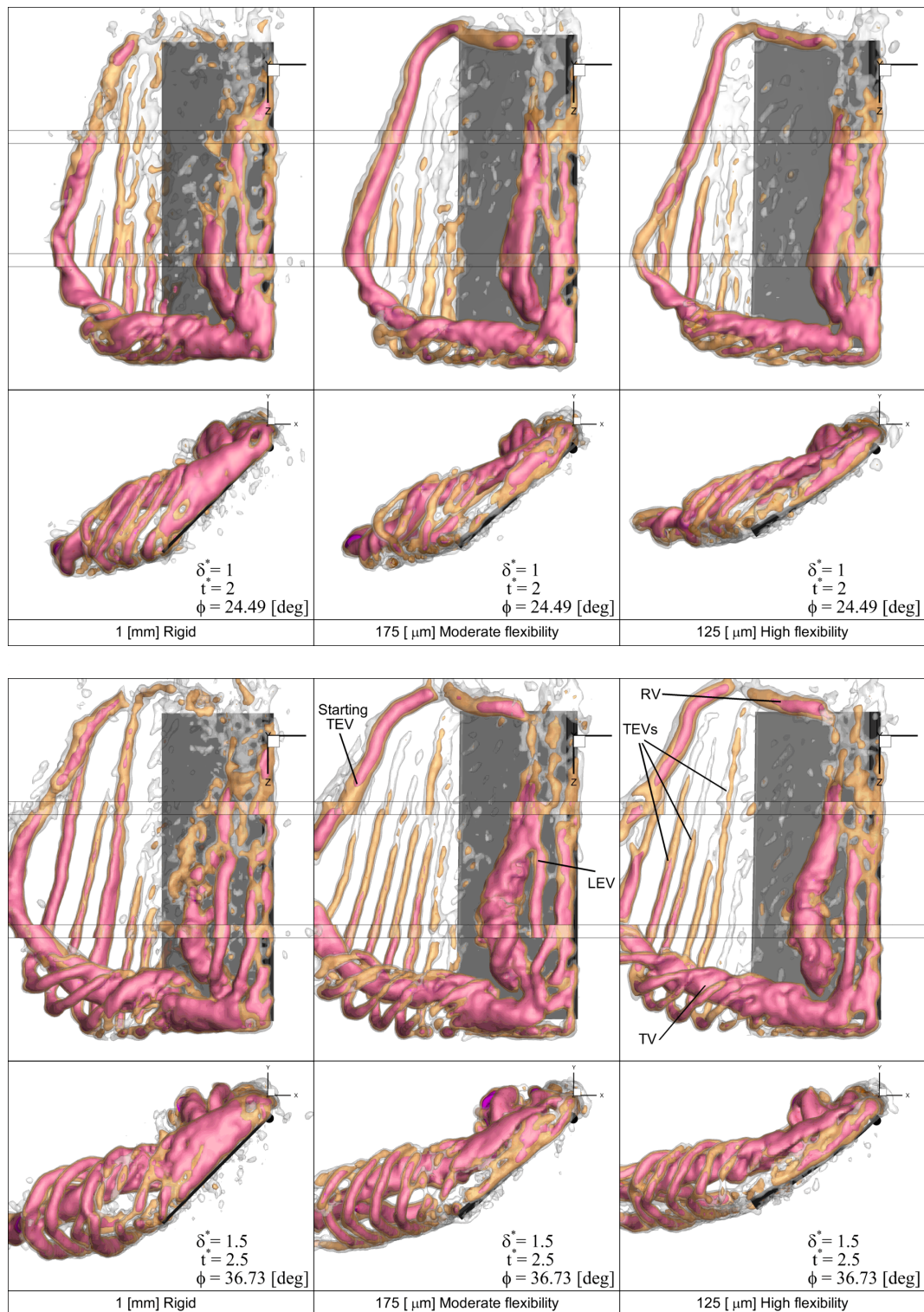


Figure 7.3: Vortical structures for different isosurfaces of Q-criterion: White $Q/(V_t/c)^2 = 3$, Orange $Q/(V_t/c)^2 = 10$ and Pink $Q/(V_t/c)^2 = 30$. *Top:* at the end of the acceleration phase after one chord length of travel ($\delta^* = 1$). *Bottom:* after $\delta^* = 1.5$. The vortex system consists of a starting trailing edge vortex (starting TEV), multiple shed trailing edge vortices (TEVs), a tip vortex (TV), a root vortex (RV) and a leading edge vortex (LEV). *Left:* 1 [mm] Rigid wing. *Middle:* 175 [μm] Moderate flexible wing. *Right:* 125 [μm] High flexible wing.

Q-criterion colored with helical density In Figure 7.4 the vortical structures are identified using the Q-criterion and colored by helical density at $\delta^* = 1.5$. In section A.2 a time-series animation of vortical structures that are colored by helical density is given.

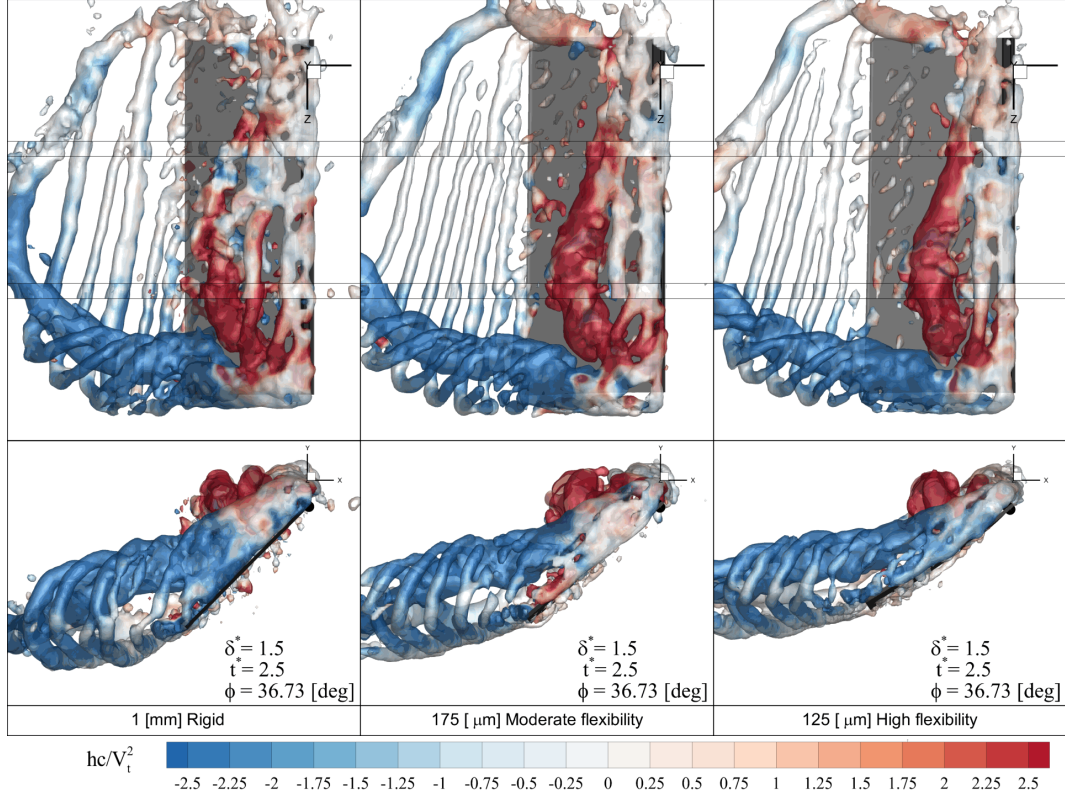


Figure 7.4: Vortical structures for $\delta^* = 1.5$. Isosurfaces of Q-criterion ($Q/(V_t/c)^2=3$) colored by helical density (hc/V_t^2).

The highest positive and negative helical density levels exist in the LEV and TV, respectively. However, the high positive levels are more coherent with decreasing flexural stiffness. These high levels of helical density are indicative of an outboard spanwise vorticity flux along the axis of the LEV which is associated with the spanwise transport of vorticity contributing to the stability of the LEV.

7.2.3 Flow field characteristics

Spanwise vorticity In Figure 7.5 spanwise vorticity contours are given in chordwise oriented planes along the span and at midspan ($r/R = 0.5$) near the onset of the vortex breakdown for $\delta^* = 1.5$ and 2. In section A.3 a time-series animation of the spanwise vorticity contours is given.

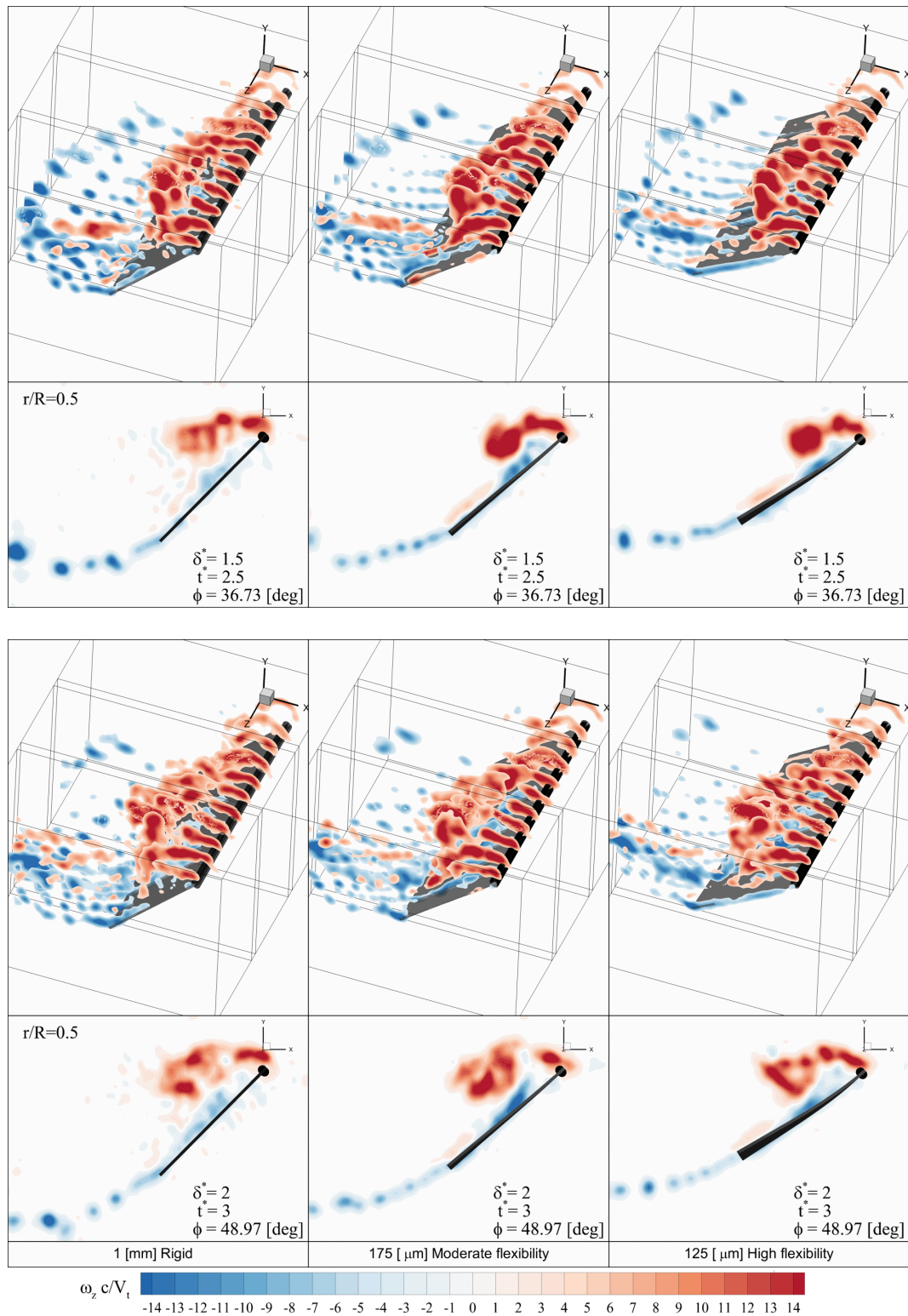


Figure 7.5: Spanwise vorticity contours ($\omega_z c/V_t$). *Top 2 rows:* Vorticity contours along the span and at $r/R = 0.5$ for $\delta^* = 1.5$. *Bottom 2 rows:* Vorticity contours along the span and at $r/R = 0.5$ for $\delta^* = 2$.

At the start of the revolving motion the spanwise vorticity contours display similar two-dimensional characteristics for the different wings. It can be observed that at approximately $\delta^* = 2$ features indicating the onset of LEV breakdown around midspan ($r/R = 0.5$) are present for the different wings. The negative vorticity that is generated between the LEV and the wing interacts with the LEV resulting in formation of discrete pockets of both negative and positive vorticity. Subsequently, the cross-sectional area containing the entrained vorticity starts expanding rapidly. Although for all wings features of the vortex breakdown are present around midspan ($r/R = 0.5$) for greater chord lengths of travel, the flexible wings show a more coherent LEV. In Figure 7.6 vorticity contours are given in chordwise oriented planes along the span, and at the midspan position ($r/R = 0.5$) and reference position ($r/R = 0.75$) at $\delta^* = 4$.

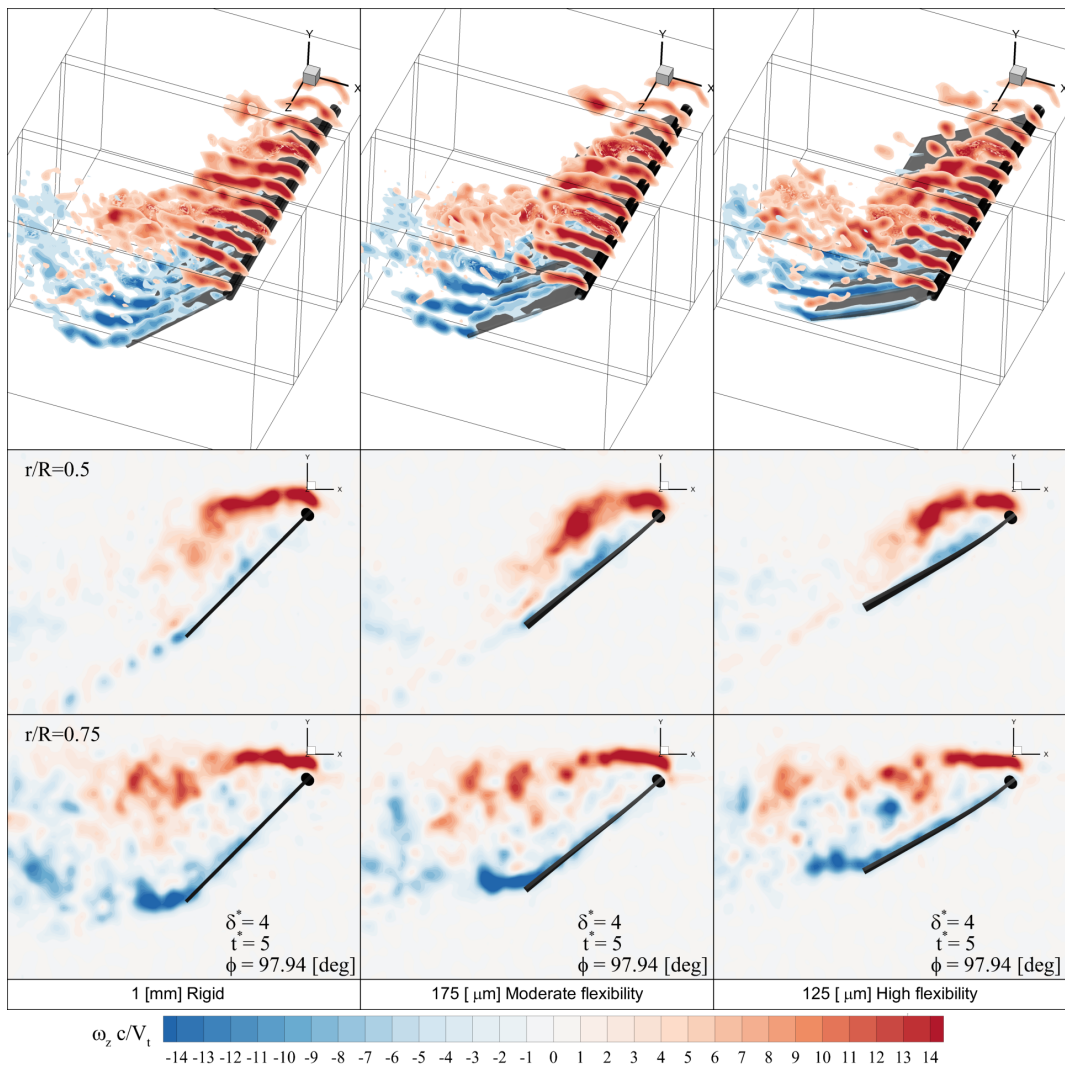


Figure 7.6: Spanwise vorticity contours ($\omega_z c/V_t$) at $\delta^* = 4$. *Top:* Vorticity contours along the span. *Middle:* Spanwise vorticity contour at $r/R = 0.5$. *Bottom:* Spanwise vorticity contour at $r/R = 0.75$.

It can be observed that the vorticity region accompanying the LEV at midspan ($r/R = 0.5$) is more coherent with decreasing flexural stiffness. At the reference position ($r/R = 0.75$) the

LEV region remains more coherent further downstream with decreasing flexural stiffness. At the midspan and reference position it can be clearly seen that the LEV has a similar location for the different wings, however, due to the deflection of the flexible wings the LEV center is located closer to the wing surface. Also it is found that the overall cross-sectional area occupied by the recirculating flow containing the entrained vorticity is significantly smaller with decreasing flexural stiffness. This is especially pronounced within the bubble-like structure ($r/R > 0.5$). These observations are in accordance with the observations made in subsection 7.2.2.

Spanwise Velocity In Figure 7.7 the spanwise velocity is given in chordwise oriented planes along the span and at the midspan position ($r/R = 0.5$), and at a spanwise plane oriented plane (y, z -plane) with an offset of $0.5c$ downstream of the TE in the inertial reference frame for $\delta^* = 1.5$ and 4. In section A.4 a time-series animation of the spanwise velocity contours is given.

For $\delta^* = 1.5$, from the different spanwise velocity contours, an outboard flow at the suction side of the wing can be observed that agrees well with the location of the LEV, see Figure 7.3 and Figure 7.5, respectively. The positive and negative spanwise velocity regions near the tip of the wing correlate with the location of the TV, see Figure 7.3. From the velocity contours at midspan ($r/R = 0.5$), it is found that the highest levels of spanwise velocity correlate well with the regions of high spanwise vorticity flux density, see Figure 7.5. The shear layer emanating from the TE is visible as the interface of spanwise velocity above the shear layer and negligible spanwise velocity below the shear layer. For decreasing flexural stiffness, the interface of the shear layer is smoother which is associated with the more continuous shedding of TEVs, see Figure 7.5. At $0.5c$ downstream of the TE the footprint of the TV is visualized. Due to deflection of the flexible wing the TV is located more upwards with decreasing flexural stiffness, while the spanwise location is approximately maintained. Although, for decreasing flexural stiffness more coherent and slightly higher spanwise velocities near the the LEV are present, lower spanwise velocities in the TV region are found. When progressing further in the revolving motion the region of spanwise flow at the suction side of the wing increases. For $\delta^* = 4$, a large region of spanwise flow can be observed that extends over a significant part of the suction side of the wing. At the midspan ($r/R = 0.5$) position, the region of spanwise flow is distributed over the chord of the wing. For decreasing flexural stiffness the region of spanwise velocity is located more towards the LE. Also, like for $\delta^* = 1.5$, the smoother interface of the shear layer with reduced Kelvin-Helmholtz like instability phenomena can be clearly observed for the more flexible wings. At the reference position ($r/R = 0.75$), a significant part of the spanwise velocity is located near the TE, which is caused due to the interaction of the spanwise velocity with the induced velocities from the TV.

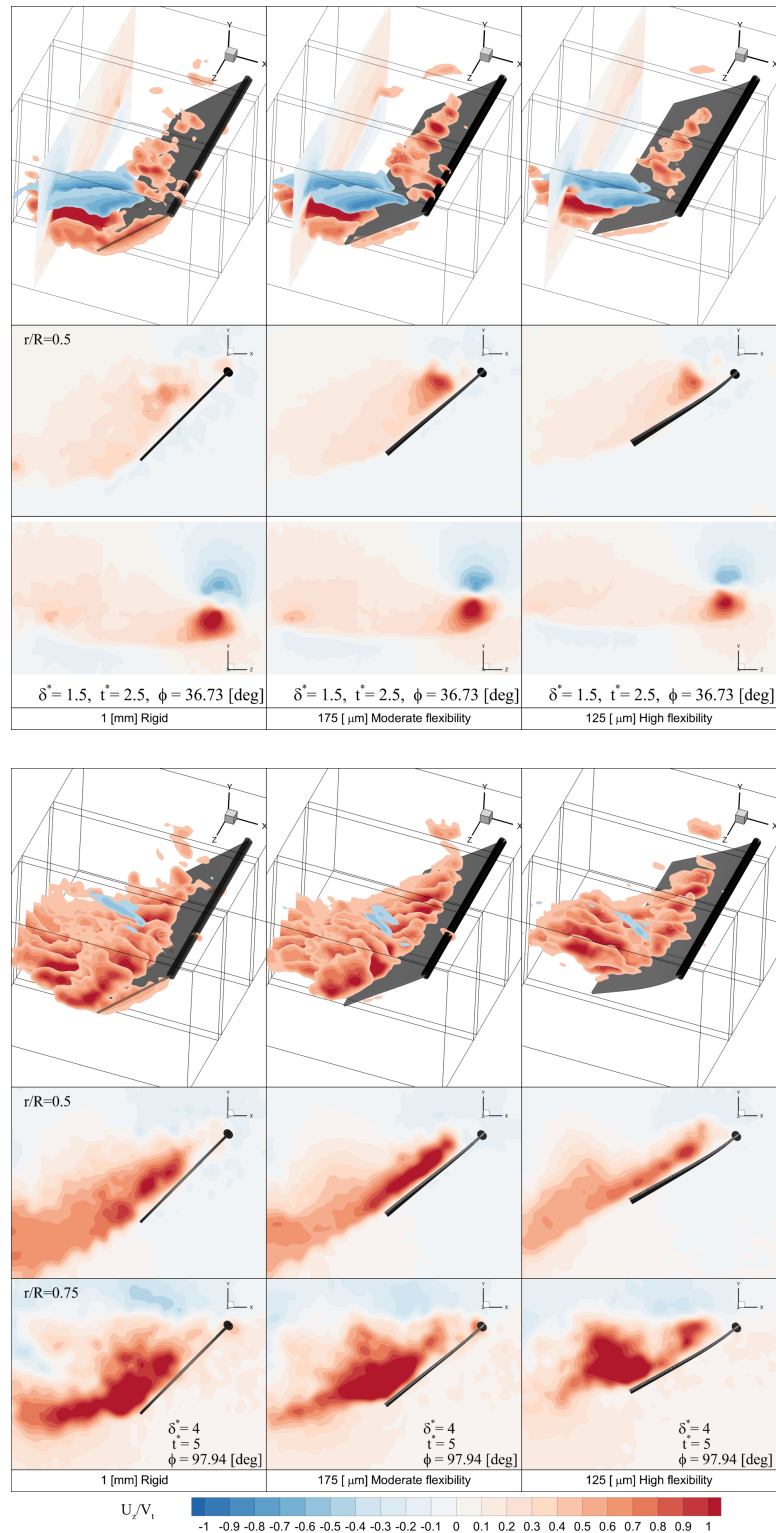


Figure 7.7: Spanwise velocity contours (U_z/V_t) for $\delta^* = 1.5$ and δ^*4 . *Top:* velocity contours along the span and a velocity contour of the wake at an offset of $0.5c$ from the TE. *Middle:* Velocity contour at $r/R = 0.5$. *Bottom:* Velocity contour of the wake at a spanwise oriented plane (y, z -plane) with an offset of $0.5c$ downstream of the TE for $\delta^* = 1.5$, and velocity contour at $r/R = 0.75$ for $\delta^* = 4$.

Spanwise vorticity flux density The spanwise vorticity flux density is the third component of helical density and is indicative for the spanwise advection of vorticity. In Figure 7.8 the spanwise vorticity flux density is given in chordwise oriented planes along the span, at the midspan position ($r/R = 0.5$) and reference position ($r/R = 0.75$) for $\delta^* = 1.5$ and 4. In section A.5 a time-series animation of the spanwise vorticity flux density contours is given.

For $\delta^* = 1.5$, the high positive regions of spanwise vorticity flux density agree well with the location of the LEV core, its high helical density values and the high spanwise velocities, see Figure 7.3, Figure 7.4 and Figure 7.7, respectively. Also the secondary negative vorticity regions just above the suction side of the wing are transported towards the tip as indicated by the negative spanwise vorticity flux density contour levels. For the flexible cases the regions of spanwise vorticity flux density are more coherent compared to the rigid wing. Furthermore the TEVs that are shed from the TEV accompany a more continuous streak of spanwise vorticity flux density. From the different spanwise vorticity contours it can also be observed that the spanwise vorticity flux density of the LEV is more coherent for the flexible wings. These observations agree with the increased helical density values found in Figure 7.4. From the spanwise vorticity flux density contours and the helical density profile it is found that the main spanwise vorticity transport, contributing to the LEV stability, does not occur near the LE of the wing where the shear layers feeds the LEV, but slightly more downstream. Although the spanwise vorticity is high at the LE (see Figure 7.5), the spanwise velocity is low (see Figure 7.7) and as a result the spanwise vorticity flux density is low. At $\delta^* = 4$, it can be observed that the location at which the LEV starts advecting spanwise vorticity from root to tip is located slightly closer to the LE for decreasing flexural stiffness. This observation is most pronounced at the reference position ($r/R = 0.75$) at which the LEV is fully grown within the bubble-like structure. Furthermore, it is found that while the shear layer feeding the LEV mainly had a positive vorticity flux density for $\delta^* = 1.5$, substantial negative values are found for $\delta^* = 4$.

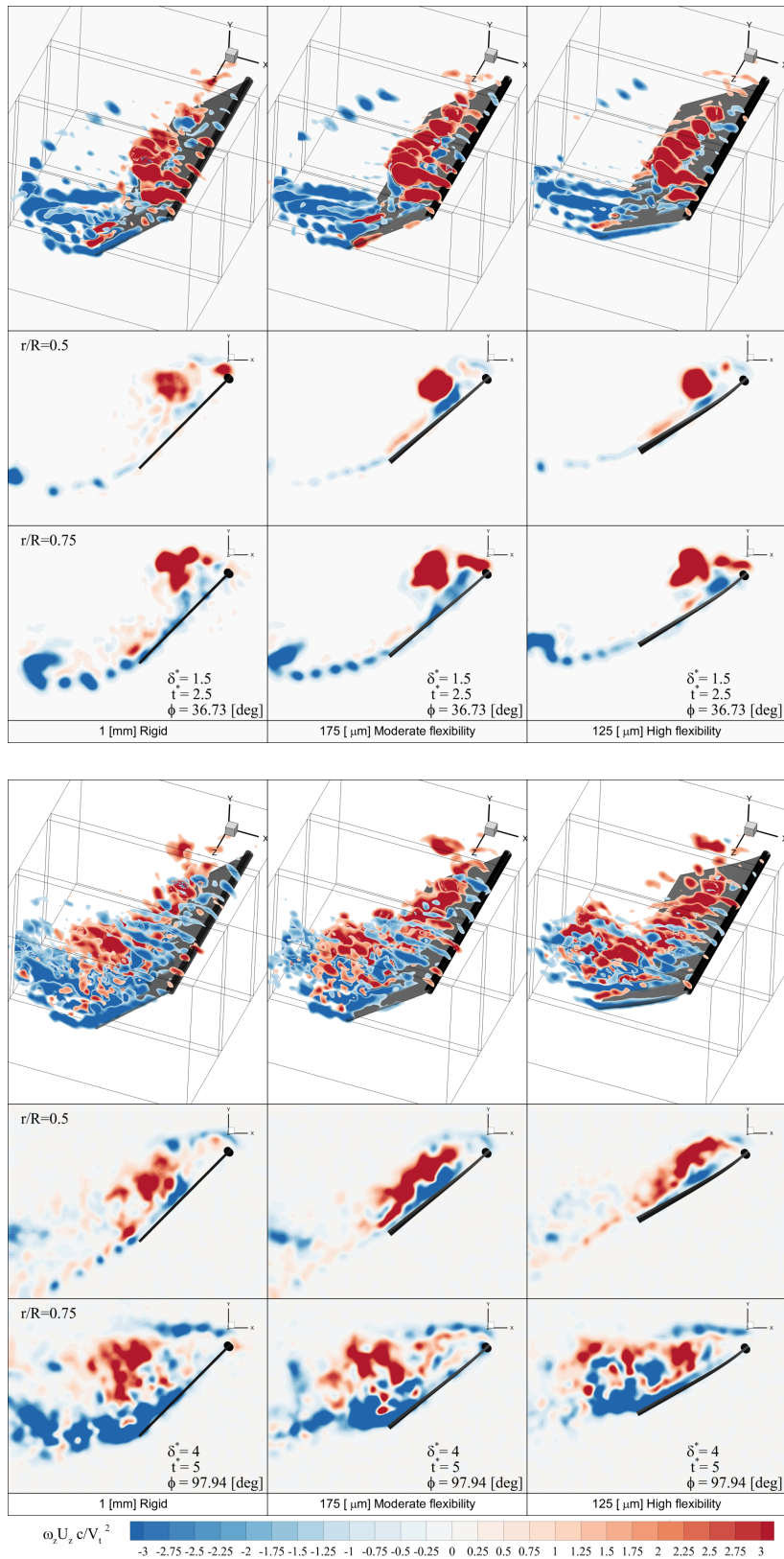


Figure 7.8: Spanwise vorticity flux contours ($\omega_z U_z c / V_t^2$) for $\delta^* = 1.5$ and 4. *Top:* Spanwise vorticity flux contours along the span. *Middle:* Spanwise vorticity flux contour at $r/R = 0.5$. *Bottom:* Spanwise vorticity flux contour at $r/R = 0.75$.

Vorticity in x-direction (ω_x) In Figure 7.9 the vorticity in x-direction (ω_x) is given for $\delta^* = 1.5$ at a spanwise oriented plane (y, z -plane) with an offset of $0.5c$ downstream of the TE, see Figure 7.7 for the location of this plane with respect to the wing.

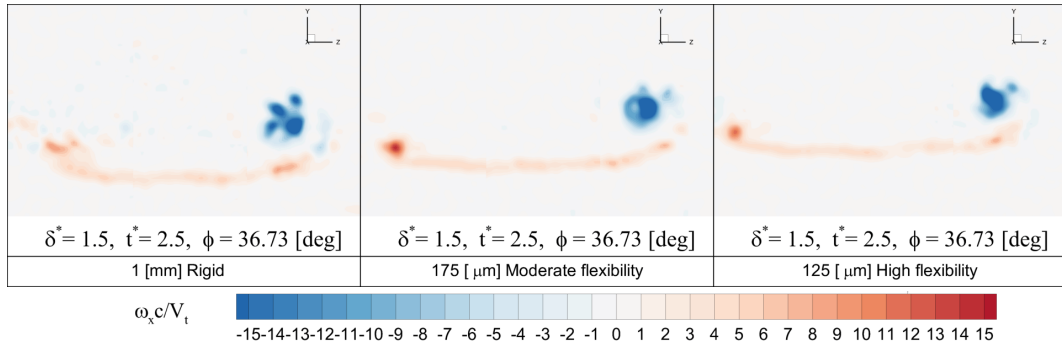


Figure 7.9: Vorticity in x-direction contours ($\omega_x c / V_t$) of the wake for $\delta^* = 1.5$ at a spanwise oriented plane (y, z -plane) with an offset of $0.5c$ downstream of the TE.

The positive ω_x distribution that is shed from the TE over the model is approximately equal for the different wings. The widely distributed positive ω_x levels are in accordance with the observations made in (Kim & Gharib, 2010). In this study it was found that for a translating plate the distribution of ω_x is confined to the counter-rotating tip vortices, while for the rotating plate the positive ω_x levels are widely distributed in the shear layer of the wake. The negative ω_x region corresponds to the TV and is slightly more coherent for the flexible wings. Near the root higher and more coherent ω_x levels are found for the flexible wings compared to the rigid case.

7.3 Spanwise characteristics

7.3.1 Total circulation

The integration region of the total circulation is illustrated in Figure 7.10.

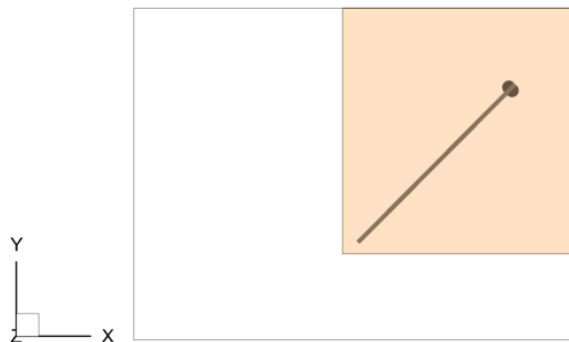


Figure 7.10: Integration region (yellow) within the total field of view (white) for the evaluation of total circulation.

The lower left corner has an offset of approximately $0.05c$ in both x, y -direction from the TE of the rigid wing. For a quiescent flow the total circulation is zero. Due to the close alignment of the downstream integration region with the TE of the wing, the TEV is shed over the boundary early in the revolving motion. Consequently, based on Kelvin's circulation theorem a net circulation is generated within the integration domain. The upper right corner is aligned with the maximum field of view. The total circulation values reported in this chapter were also verified by means of a line integral.

In Figure 7.11 the temporal evolution of the total circulation for different spanwise positions is given. It can be observed that in general the trends in temporal evolution are similar for the

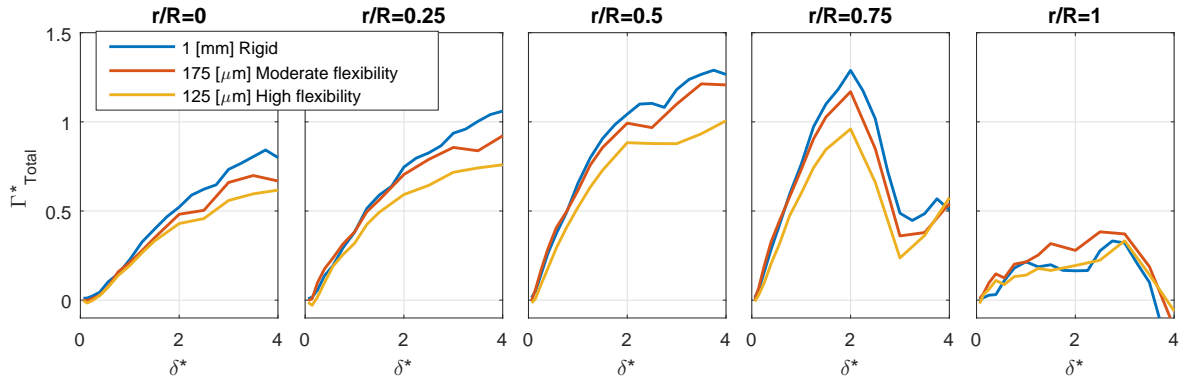


Figure 7.11: Temporal evolution of total circulation (Γ_{Total}^*) for different spanwise positions (r/R).

different wings. The total circulation increases with increasing flexural stiffness. Inboard of midspan ($r/R = 0.5$) the total circulation increases until steady-state conditions are reached, while outboard of midspan features of the vortex breakdown are visible that attenuate the build-up of circulation at midspan, and even significantly decrease the circulation at the reference position ($r/R = 0.75$). At approximately midspan ($r/R = 0.5$) and the reference position ($r/R = 0.75$), for $\delta^* = 2$, a dip can be observed that correlates with the onset of the vortex breakdown. These observations are in accordance with the observations in subsection 7.2.3.

In Figure 7.12 the temporal evolution of the total circulation is given in terms of traveled chord lengths at the reference position and the formation number. It is found that the total circulation has a higher correlation with the formation number than the rotation angle which is related to δ^* . Until a formation number of 1, the different spanwise sections have approximately the same slope for a given wing configuration. The slope is decreased with decreasing flexural stiffness. For the moderate and high flexible wing respectively, $d\Gamma_{Total}^*/dFN$ is approximately 6% and 18% lower compared to the rigid wing.

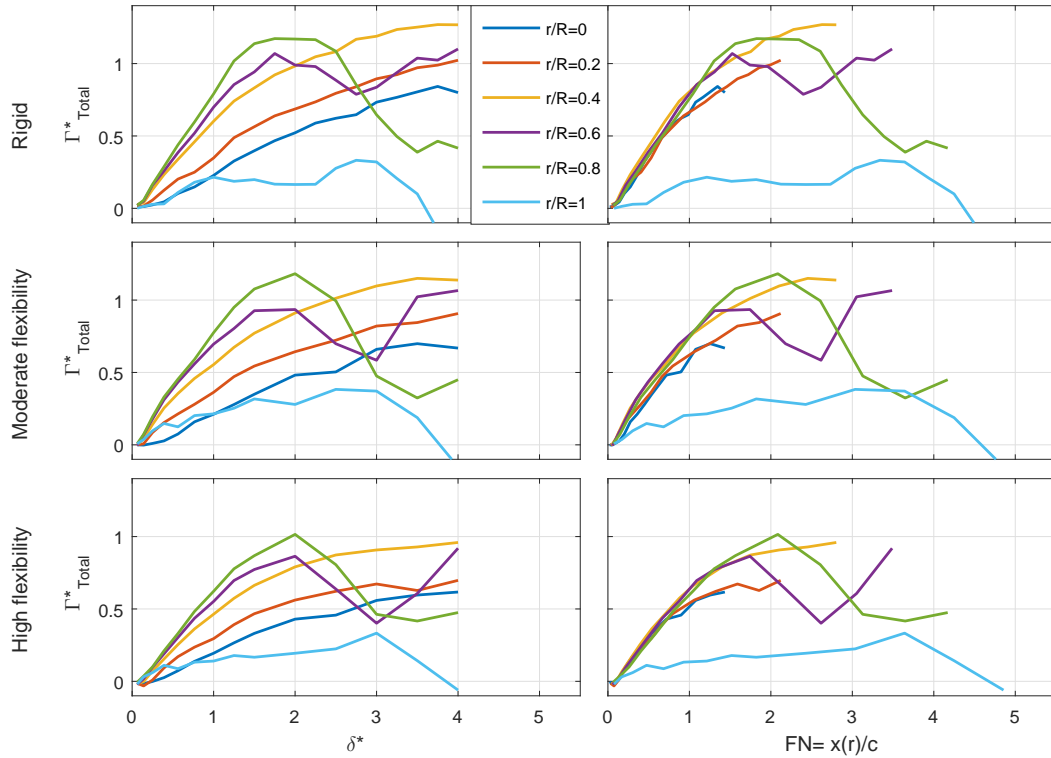


Figure 7.12: Temporal evolution of total circulation (Γ_{Total}^*) for different spanwise positions (r/R). Temporal evolution is expressed in terms of chord traveled (δ^*) and formation number (FN).

In Figure 7.13 the temporal evolution of the spanwise distribution of the total circulation is given. Until the onset of the vortex breakdown ($\delta^* < 2$) there is an approximate linear increase of circulation with spanwise position until ($r/R = 0.9$) which corresponds to the linear increase in rotational velocity. The total circulation is lower for decreasing flexural stiffness except near the tip. At the tip the flexible wings often generate more total circulation. The pronounced dip in total circulation for $2.5 < \delta^* < 3.5$ at approximately ($r/R = 0.7$) correlates with the onset of vortex breakdown that includes significant chaotic features and a rapid expansion of recirculating flow. Due to the rapid expansion, part of the LEV containing positive vorticity is outside the domain of integration. For $\delta^* > 3.5$ the spanwise distribution of total circulation settles to a steady-state distribution. The maximum circulation is slightly shifted outboard with decreasing flexural stiffness.

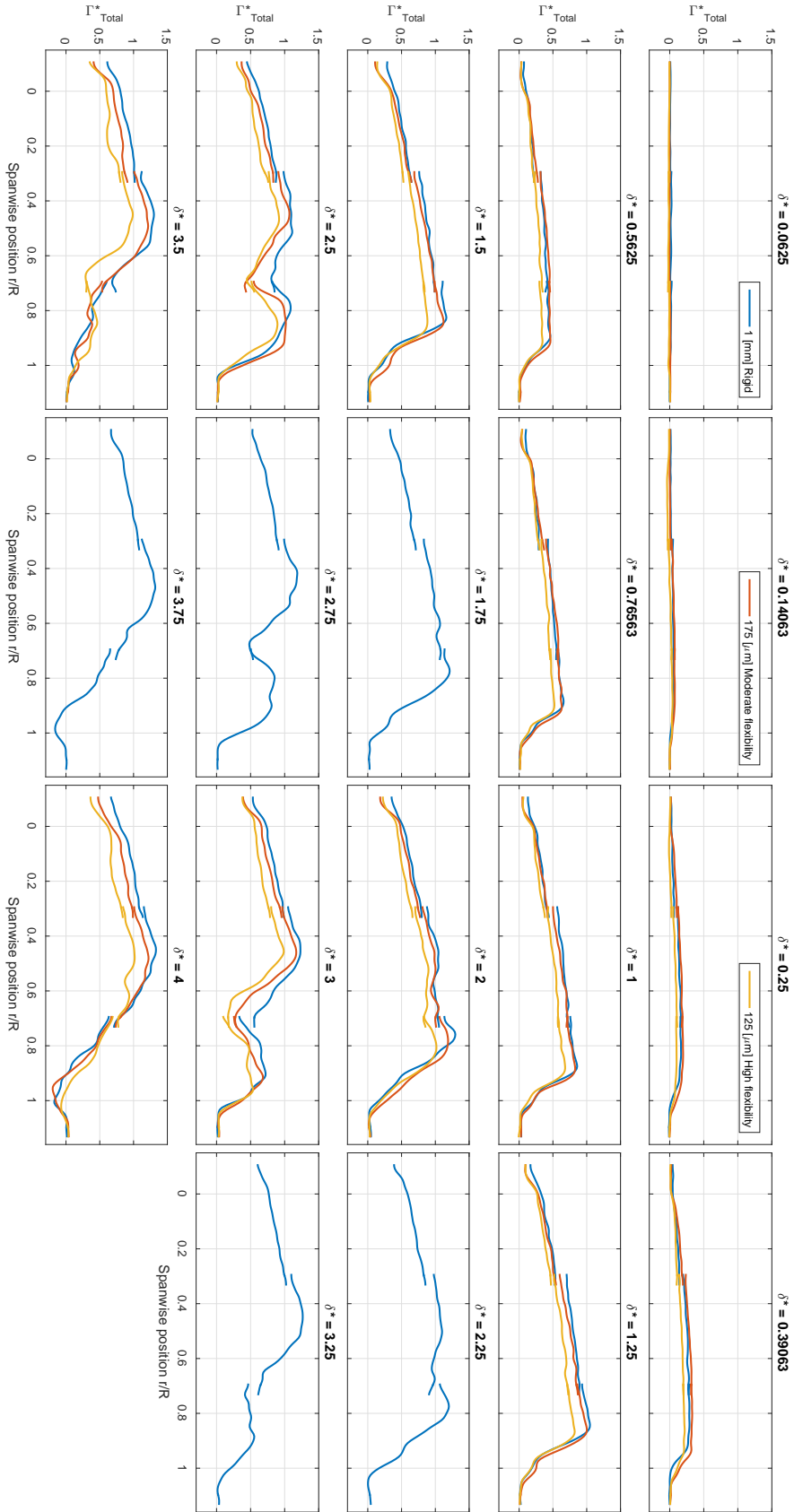


Figure 7.13: Temporal evolution of the spanwise distribution of the total circulation (Γ_{Total}^*).

7.3.2 LEV circulation

Limited domain of integration First, the LEV circulation region is considered as the region for which $\gamma_2 > 2/\pi$ limited to the same integration region that was used in the calculation of the total circulation as illustrated in Figure 7.10. In Figure 7.14 the temporal evolution of the LEV circulation for different spanwise positions is given.

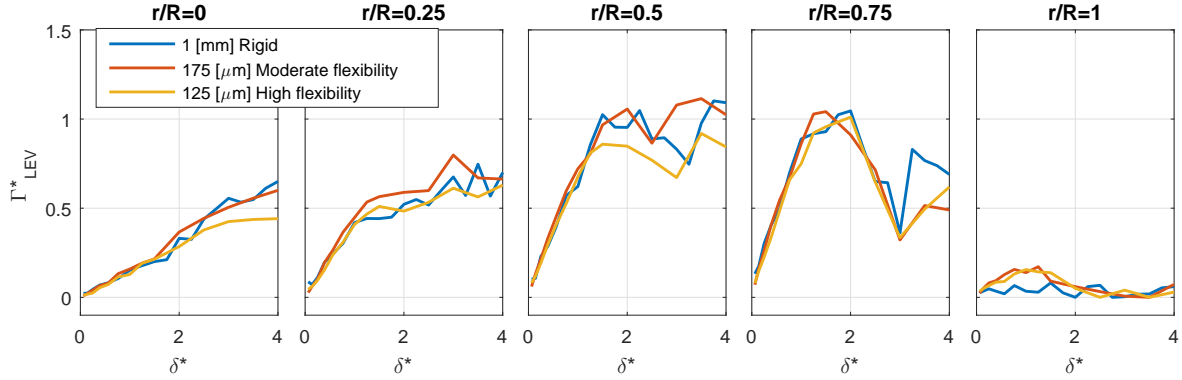


Figure 7.14: Temporal evolution of LEV circulation (Γ_{LEV}^*) for different spanwise positions (r/R).

The LEV circulation does not change significantly with flexural stiffness except at the mid-plane ($r/R = 0.5$). The trend in temporal evolution and magnitude until approximately $\delta^* = 1.5$ are similar compared to the total circulation, see Figure 7.11. This suggests that the bound vorticity (vorticity accumulated in the close vicinity of the wing) is small and most of the vorticity is kept within the LEV. For $\delta^* > 1.5$ the total circulation is higher than the LEV circulation. This is because most of the vorticity within the limited domain of integration is positive which is fully evaluated within the total circulation, while the LEV circulation contains the vorticity for which $\gamma_2 > 2/\pi$. After the onset of vortex breakdown, the LEV is less well-defined, such that the entire region of positive vorticity is not completely captured by $\gamma_2 > 2/\pi$. Moreover, this criterion bounds the LEV to a specific region, while it actually has a smooth transition to its surroundings that encompass some additional positive vorticity.

In Figure 7.15 the temporal evolution of the LEV circulation is given in terms of chord lengths traveled at the reference position and the formation number. Although the correlation of the LEV circulation with formation number is not as strong compared to the total circulation (see Figure 7.12), the correlation is higher with formation number compared to δ^* . Until a formation number of 1, $d\Gamma_{LEV}^*/dFN$ is comparable for the different wings at the same spanwise section. This indicates that the LEV circulation develops comparably in the early phase of the revolving motion with the traveled distance of each spanwise position.

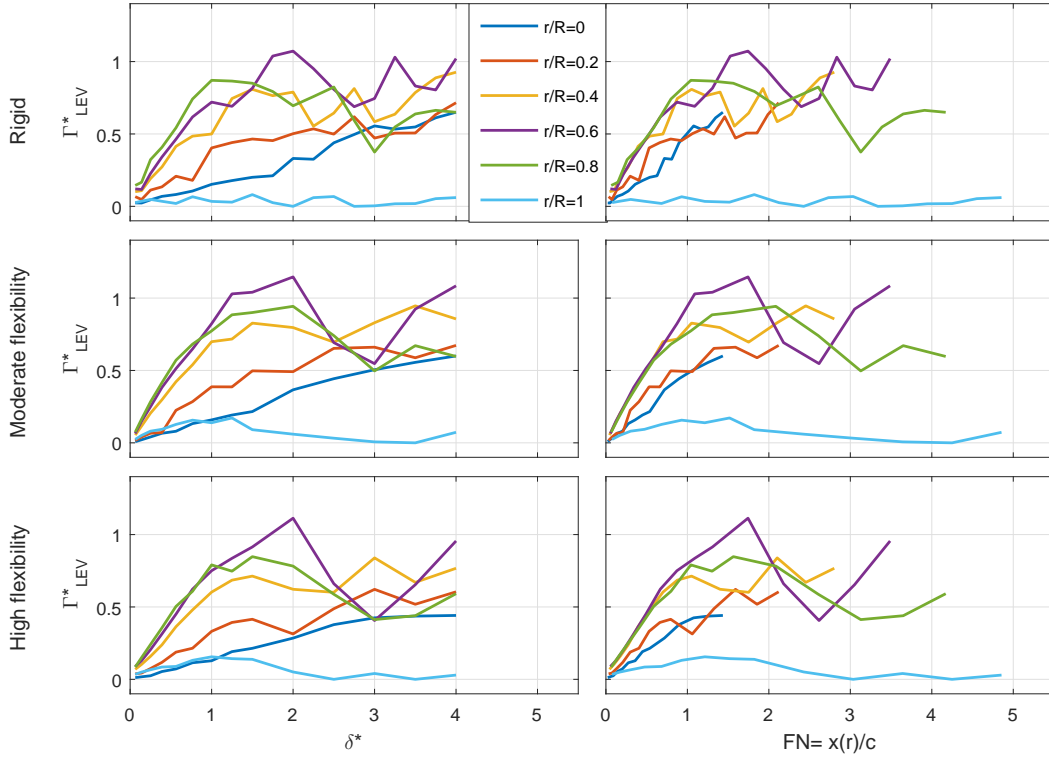


Figure 7.15: Temporal evolution of LEV circulation (Γ_{LEV}^*) for different spanwise positions (r/R). Temporal evolution is expressed in terms of chord traveled (δ^*) and formation number (FN).

In Figure 7.16 the temporal evolution of the spanwise distribution of the LEV circulation is given. Until approximately $\delta^* = 1.5$ the trend and magnitude of the spanwise circulation distribution are similar compared to the total circulation (see Figure 7.13), which indicates that most of the vorticity is kept within the LEV. However, a number of differences are observed. In general the LEV circulation is similar for the different wings, while the total circulation is lower for decreasing flexural stiffness. Also a sharp peak at $r/R = 0.9$ is observed for the total circulation, while a smoother transition is present for the LEV circulation. Furthermore, the dip in total circulation for $2.5 < \delta^* < 3.5$ is less pronounced in the LEV circulation. After the onset of vortex breakdown the vortex formation displays significant chaotic features. Especially within the bubble-structure there is a large cross sectional area of recirculating flow which contains negative vorticity (see Figure 7.6) that could contribute to the strong dip in the total circulation.

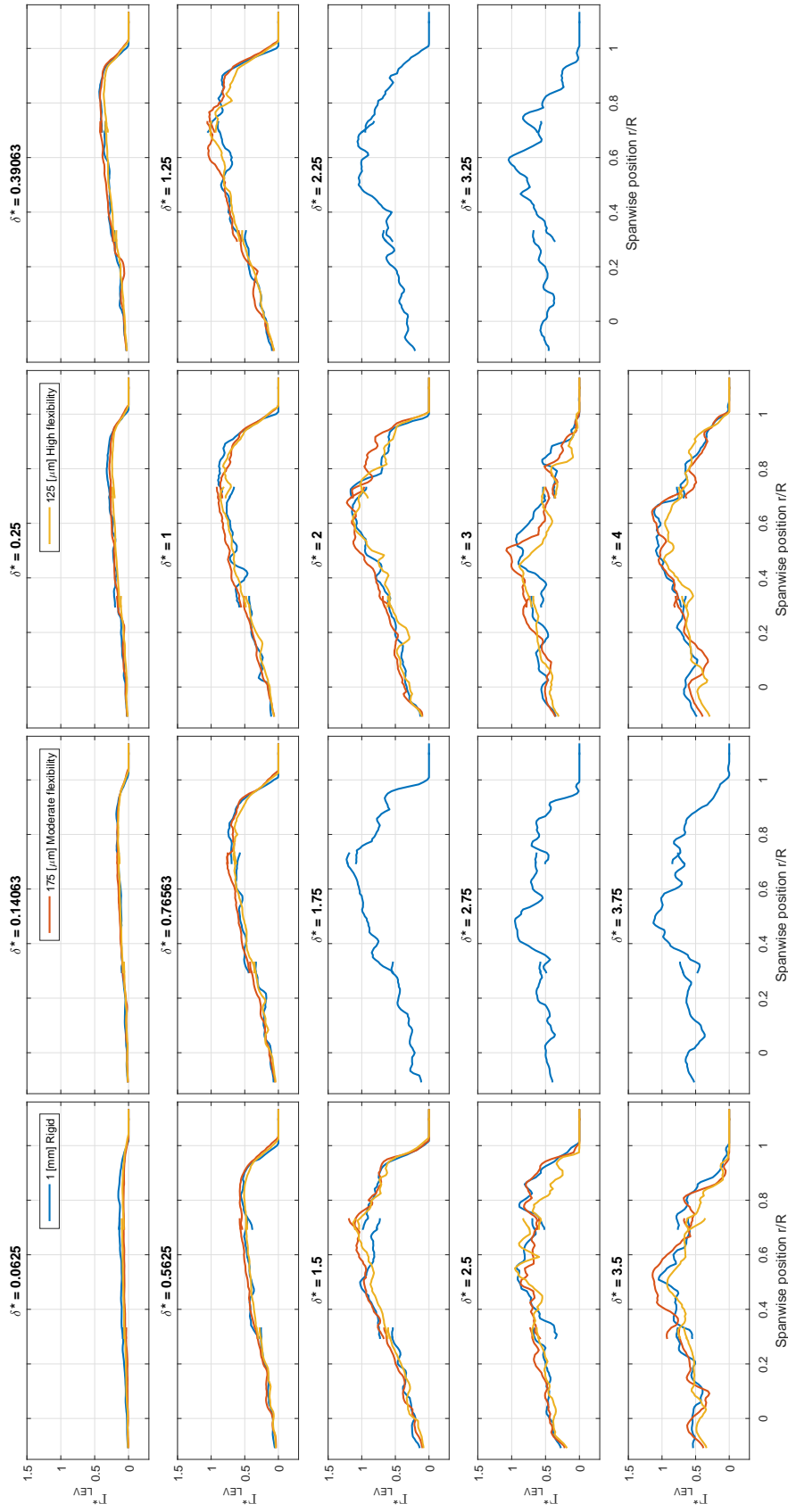


Figure 7.16: Temporal evolution of the spanwise distribution of the LEV circulation (Γ_{LEV}^*).

Complete flow field domain of integration Before vortex breakdown the LEV is relatively close to the wing, see Figure 7.5. At the onset of vortex breakdown a bubble-like structure is formed and the LEV expands beyond the TE. In this section the LEV circulation region is considered as the region for which $\gamma_2 > 2/\pi$ evaluated in the complete flow field to fully capture the LEV. In Figure 7.17 the temporal evolution of the LEV circulation for different spanwise positions is given.

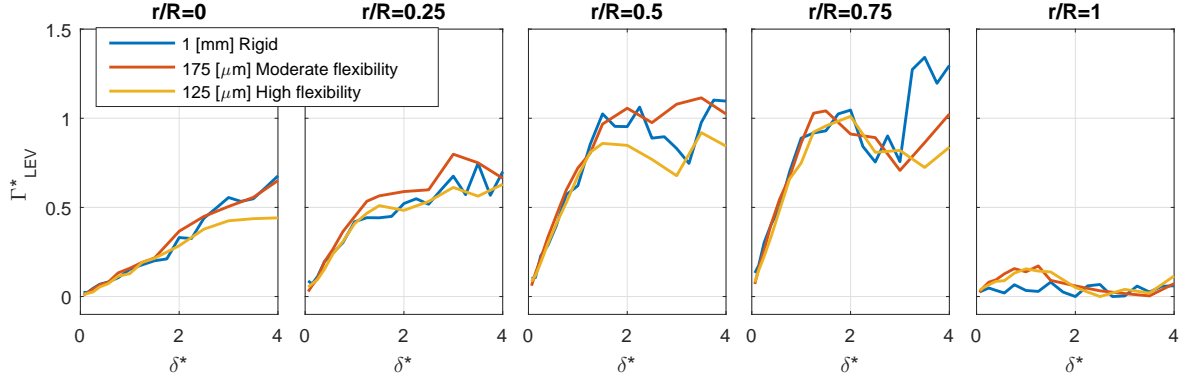


Figure 7.17: Temporal evolution of LEV circulation (Γ_{LEV}^*) for different spanwise positions (r/R).

It can be observed that the dip at the reference position ($r/R = 0.75$) is less pronounced because the entire LEV is captured, while the behavior for the other spanwise positions similar compared to Figure 7.14.

In Figure 7.18 the temporal evolution of the LEV circulation is given in terms of traveled chord lengths at the reference position and the formation number. The dip at ($r/R = 0.6$ and $r/R = 0.8$) are less pronounced which is in accordance with the onset of vortex breakdown, while the behavior for the other spanwise positions is similar compared to Figure 7.15. For all wing cases, the LEV circulation builds up strongly until roughly the same formation number (for approximately $FN > 2$) and a relatively constant level is reached. For greater formation numbers more gradual changes take place.

The increased correlation of the LEV circulation with formation number and the steady-state conditions that occur at greater formation numbers (for $FN > 2$), are in accordance with the observations made in (Poelma et al., 2006) who studied an impulsively-started revolving rigid wing that has a *Drosophila* based wing planform and a Reynolds number of 256.

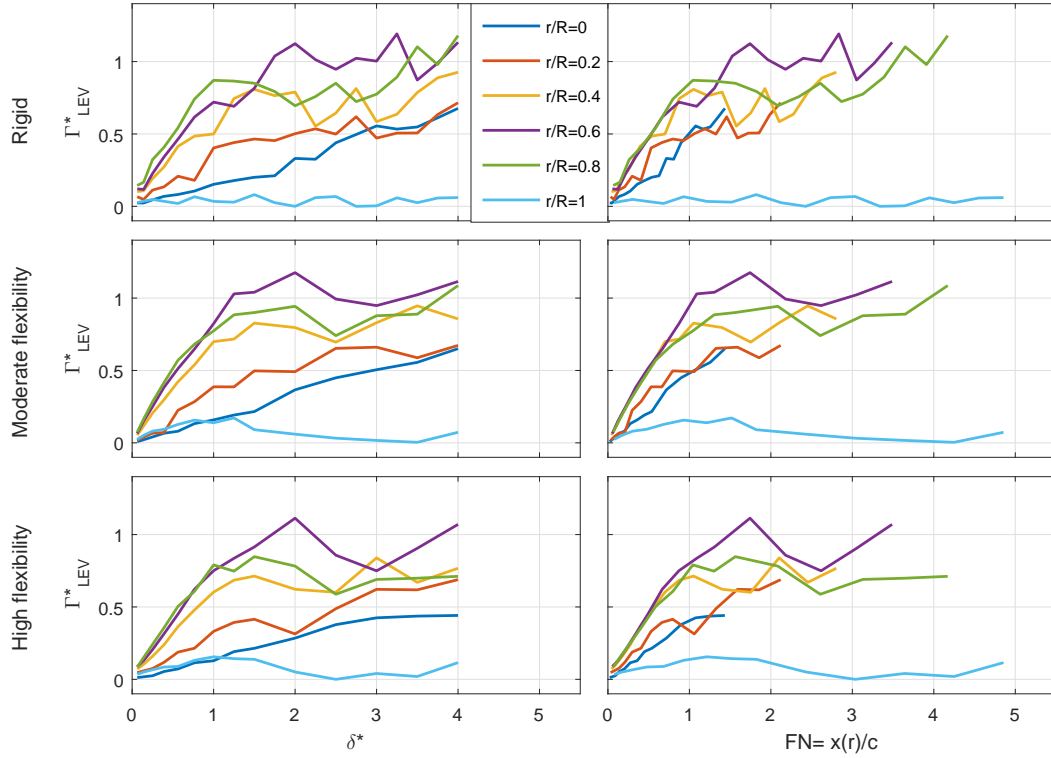


Figure 7.18: Temporal evolution of LEV circulation (Γ_{LEV}^*) for different spanwise positions expressed in terms of chord traveled (δ^*) and formation number (FN).

In Figure 7.19 the temporal evolution of the spanwise distribution of the LEV circulation is given. At steady-state conditions ($\delta^* = 4$), the circulation inboard of midspan ($r/R < 0.5$) is similar for the different wings, while outboard of midspan the circulation decreases significantly with decreasing flexural stiffness. The maximum LEV circulation is found at approximately the reference position ($r/R = 0.75$) at which the expanded LEV bubble-like structure is largest. Subsequently, towards the tip, the spanwise vorticity is tilted into an x -component and transported downstream by the TV.

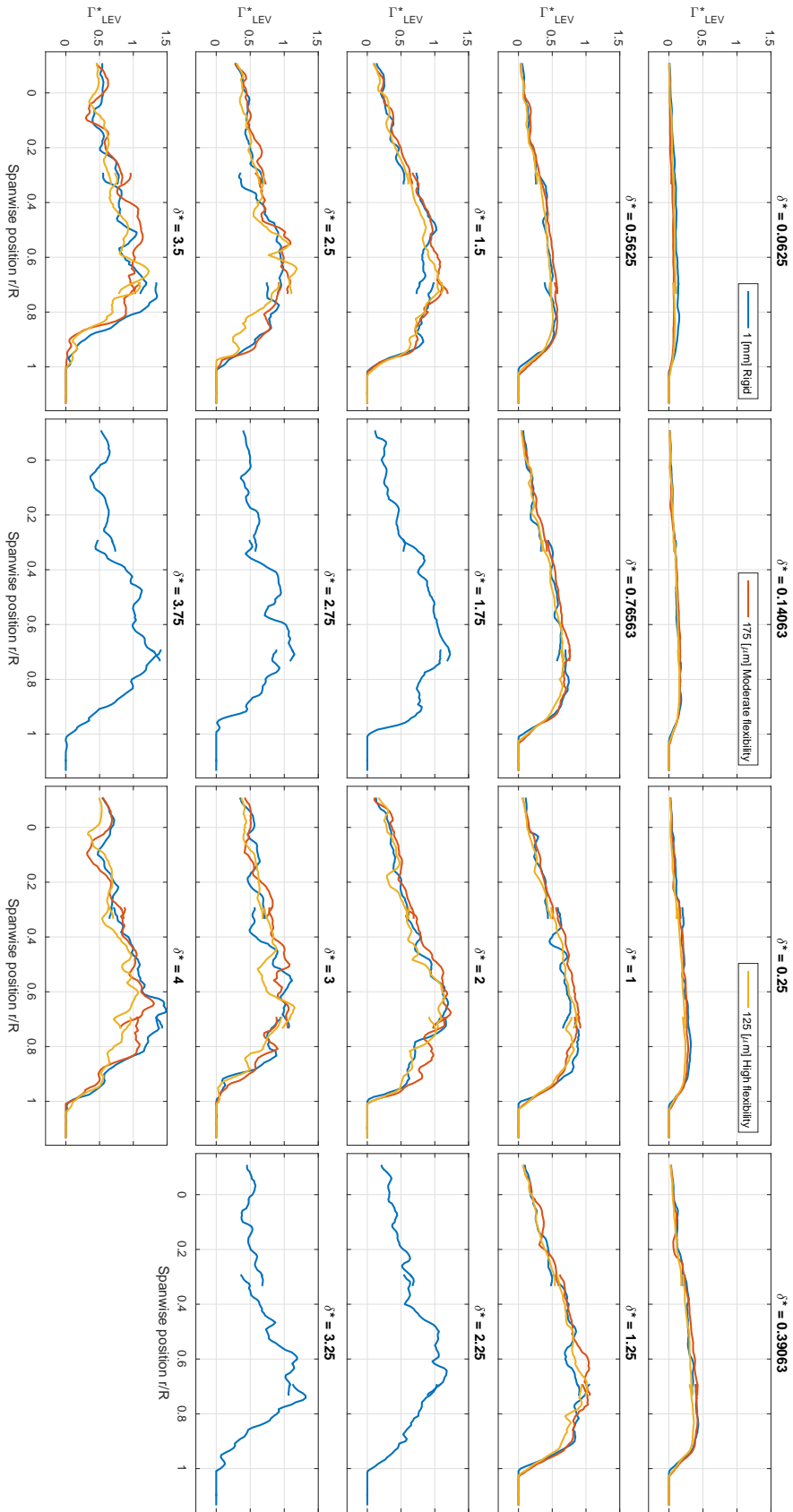


Figure 7.19: Temporal evolution of the spanwise distribution of the LEV circulation (Γ_{LEV}^*).

7.3.3 Circulation: Total - LEV - TEV

The integration of the circulation is evaluated in the complete flow field and the TEV is identified as a region for which $\gamma_2 < -2/\pi$. The spanwise distribution of the total circulation and the total circulation - LEV circulation - TEV circulation are given in Figure 7.20.

Early in revolving motion the flow behaves two-dimensional. According to Kelvin's circulation theorem $D\Gamma/Dt = 0$ which says that the time rate of change of circulation around a closed curve consisting of the same fluid elements is zero (Anderson, 2011). It can be observed that until approximately $\delta^* = 1.25$, the total circulation is zero and all circulation that is created by the wing is present in the field of view. For $\delta^* > 1.25$, the starting TEV is shed over the downstream boundary of the flow field and net positive circulation is created. Also it can be observed that until $\delta^* = 0.5625$ the LEV circulation + TEV circulation is approximately equal to the total circulation. This indicates that the majority of the circulation is kept within the TEV and the LEV and little in the bound circulation (vorticity accumulated in the close vicinity of the wing). For greater revolving phases the TEVs are more difficult to identify compared to the initial coherent starting TEV. A layer of negative vorticity is shed at the TE which is not recognized as a vortex based on the γ_2 criterion such that the bound vorticity cannot be differentiated from the vorticity entrained in the TEV within the present analysis for approximately $\delta^* > 0.5625$.

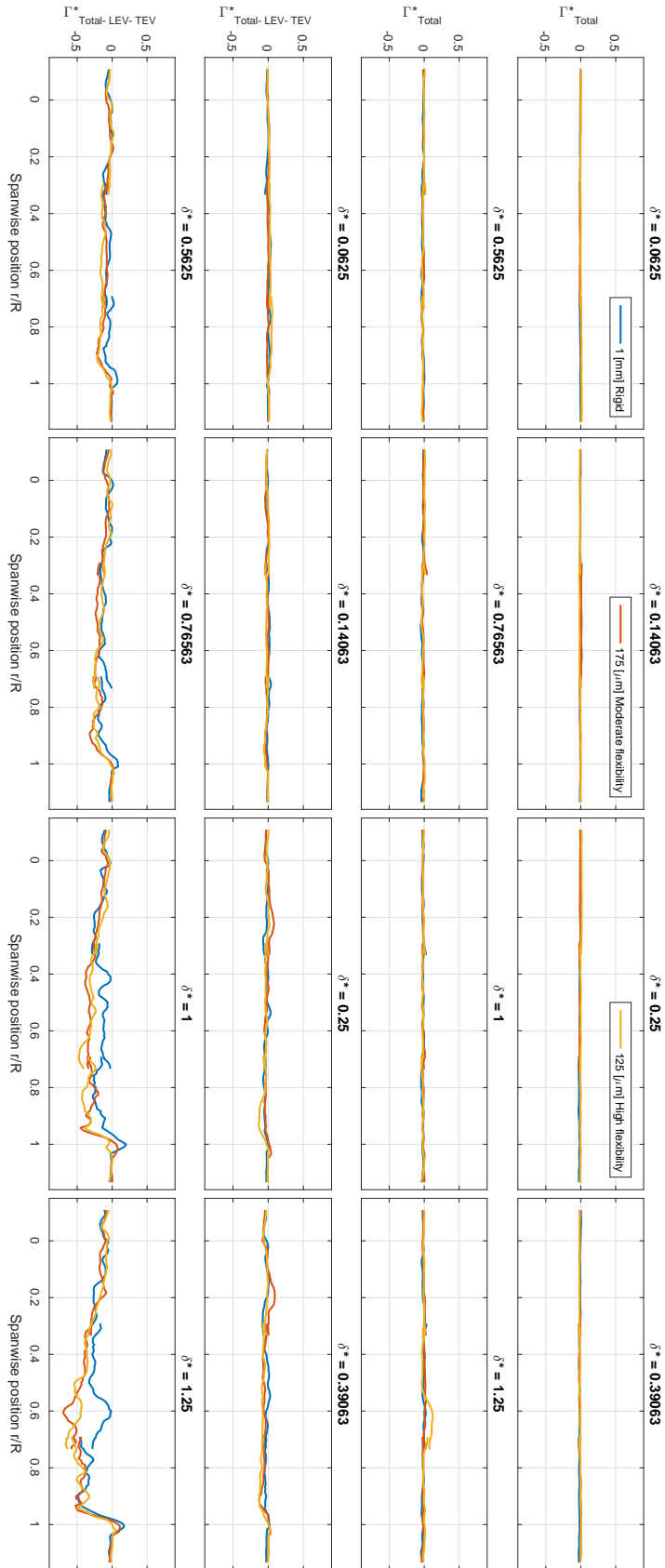


Figure 7.20: Temporal evolution of the spanwise distribution of the circulation. *Top 2 rows:* Total circulation (Γ_{Total}^*). *Bottom 2 rows:* Total circulation - LEV circulation - TEV circulation ($\Gamma_{Total}^* - \Gamma_{LEV}^* - \Gamma_{TEV}^*$).

7.3.4 LEV centroid

The LEV centroid location is calculated as,

$$\bar{\mathbf{x}} = \frac{\int S_{xy} \omega_z \mathbf{x} dx dy}{\int S_{xy} \omega_z dx dy} \quad (7.9)$$

where $\bar{\mathbf{x}}$ is the x, y -coordinate at a chordwise oriented plane measured with respect to the LE of the wing, and S_{xy} is the chordwise oriented LEV circulation integration region that is considered as the region where $\gamma_2 > 2/\pi$ evaluated in the complete flow field. By use of the LEV centroid x, y -coordinates and the wing reconstruction information, the closest distance of the LEV centroid to the wing surface (s) is calculated.

In Figure 7.21 the temporal evolution of the LEV centroid is given for different spanwise positions. It can be observed that the temporal evolution of the LEV centroid x -location is similar for the different wings. For $\delta^* < 2$ the LEV moves downstream for the different spanwise positions. At midspan, for $\delta^* = 2$, the LEV centroid x -location starts moving upstream and the distance of the LEV centroid relative to the wing surface is decreased which correlates with the occurrence of the vortex breakdown. Identifying vortex breakdown by means of the LEV centroid is supported by Jones et al. (2016). It was concluded that the centroid of a vortex and a POD analysis, were found most useful in identifying the phase angle at which the vortex breakdown occurs. At $r/R = 0.9$ a strong dip can be observed at $\delta^* = 3$ which agrees well with the rapid expansion of the bubble-like structure and the downstream movement of the identified LEV in the vicinity of the TV. During this process the LEV centroid is also identified at a more downward location. The approximate similar location of the LEV centroid for all wing cases is in accordance with the observations made in subsection 7.2.2. For approximately $\delta^* > 1.25$, the position of the LEV centroid is located significantly closer to the wing surface with decreasing flexural stiffness.

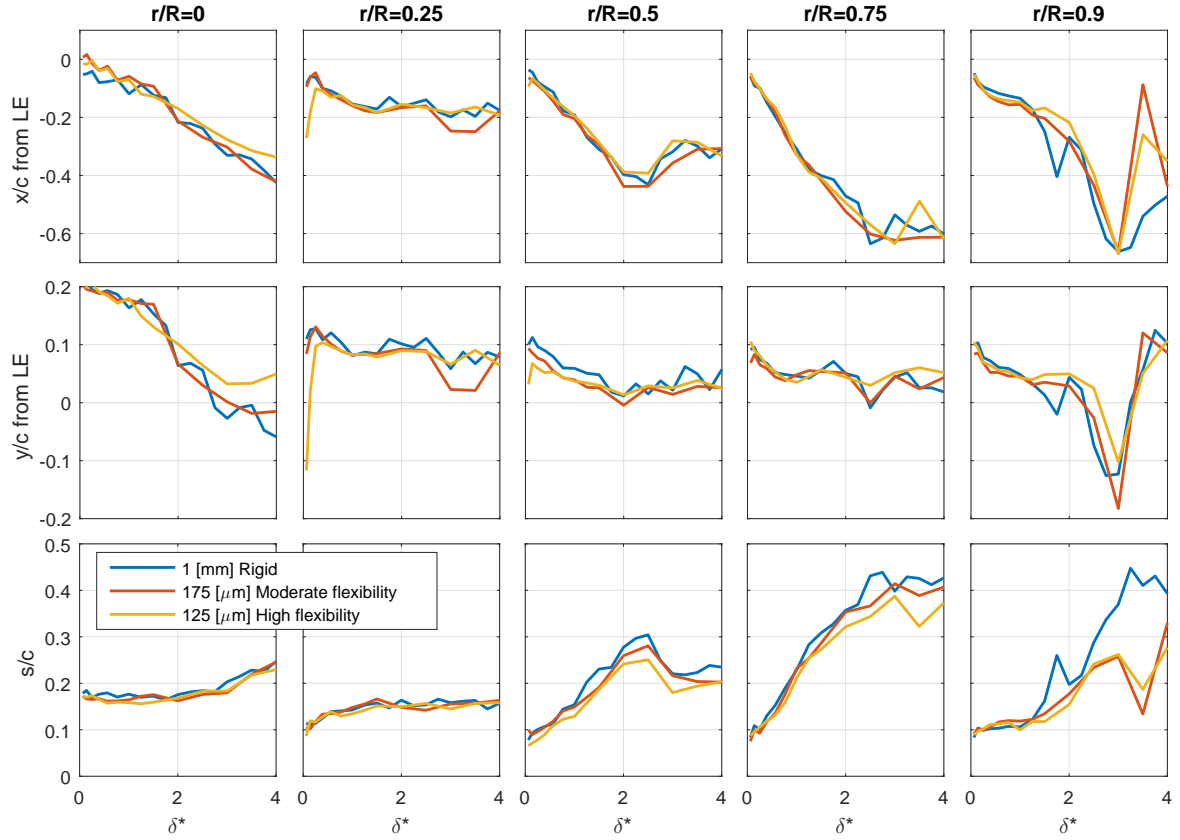


Figure 7.21: Temporal evolution of the LEV centroid for different spanwise positions (r/R). *Top:* Chord distance in x -direction from the LE (x/c). *Middle:* Chord distance in y -direction from the LE (y/c). *Bottom:* Chord distance normal to the wing surface (s/c).

In Figure 7.22 the temporal evolution of the spanwise distribution of the LEV centroid x -location from the LE (x/c) is given. As mentioned above the x -location is similar for the different wings. In the early phases of the revolving motion the LEV centroid is located close to the LE for all spanwise positions, after which the LEV centroid starts to move downstream. Note that the initial peak at $\delta^* = 0.0625$ and 0.14063 for the high flexible wing are incorrect and not representative for the LEV centroid. For $\delta^* > 1.5$, at the onset of vortex breakdown which corresponds to the formation of a significant LEV bubble-like structure, the downstream tilt of the LEV centroid outboard of midspan ($r/R > 0.5$) is significantly higher than inboard of the midspan. The downstream tilt of the LEV converts part of the spanwise vorticity (ω_z) into ω_x , reducing the spanwise circulation. The TE of the rigid wing is located at $\cos(45 \text{ deg}) \approx 0.7 x/c$ downstream from the LE and even further for the flexible wings. Consequently, it is found that the LEV centroid does not move past the TE. These observations are in accordance with (Carr et al., 2015) who studied a revolving rigid wing at an angle of attack of 45 deg and a Reynolds number of $O(10^3 - 10^4)$ depending on the AR. A greater tilt of the LEV outboard of the region in which the LEV is ‘stable’ was observed (in the current study this ‘stable’ LEV might be interpreted as the region inboard of midspan). Furthermore, for an AR= 2 it was observed that the LEV center position does not move past the TE.

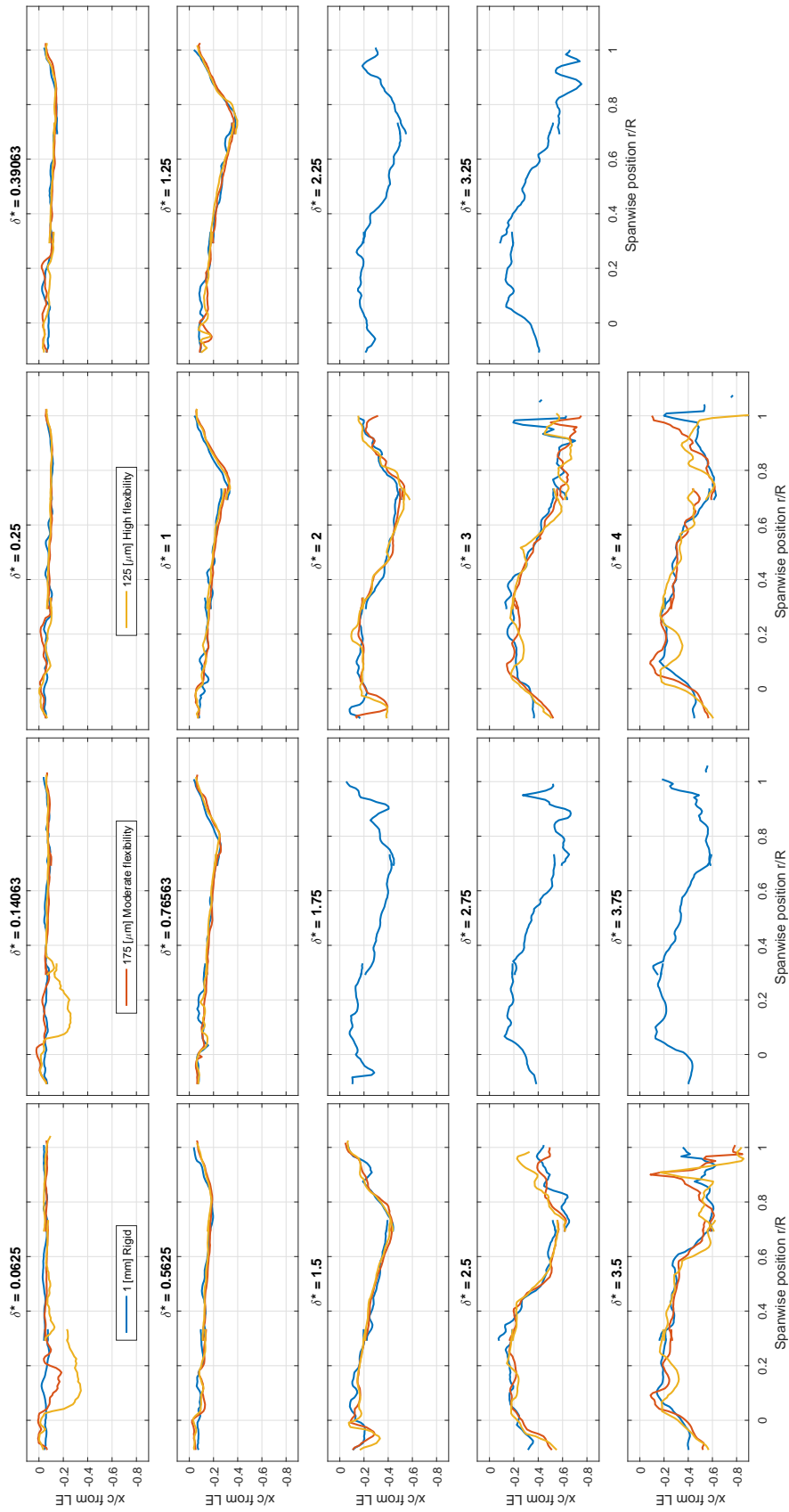


Figure 7.22: Temporal evolution of the spanwise distribution of LEV centroid chord distance in x -direction from the LE (x/c).

In Figure 7.23 the temporal evolution of the spanwise distribution of the distance between the LEV centroid and the wing is given. It can be observed that the LEV centroid is located significantly closer to the wing surface for decreasing flexural stiffness. At approximately the reference plane ($r/R = 0.75$) the LEV has its maximum distance to the wing surface. This spanwise location corresponds with the spanwise location at which the size of the expanded LEV bubble-like structure is largest, see subsection 7.2.2. The TV is located at the tip which constrains the LEV centroid. Inboard of the tip the LEV centroid is located close to the wing surface, while at the tip the LEV centroid is sometimes recognized at the TV and therefore located at infinity (boundary of the field of view). Note that these peaks are not representative for the centroid of the LEV. Especially between the reference position ($r/R = 0.75$) and the TV, the LEV centroid is located significantly closer to the airfoil for the flexible wings. At steady-state conditions ($\delta^* = 4$), it can be observed that inboard of the midspan ($r/R = 0.5$) position the LEV centroid has approximately the same distance to the wing surface for all wing cases. However, outboard of midspan the distance of the LEV centroid to the wing surface is significantly reduced with decreasing flexural stiffness.

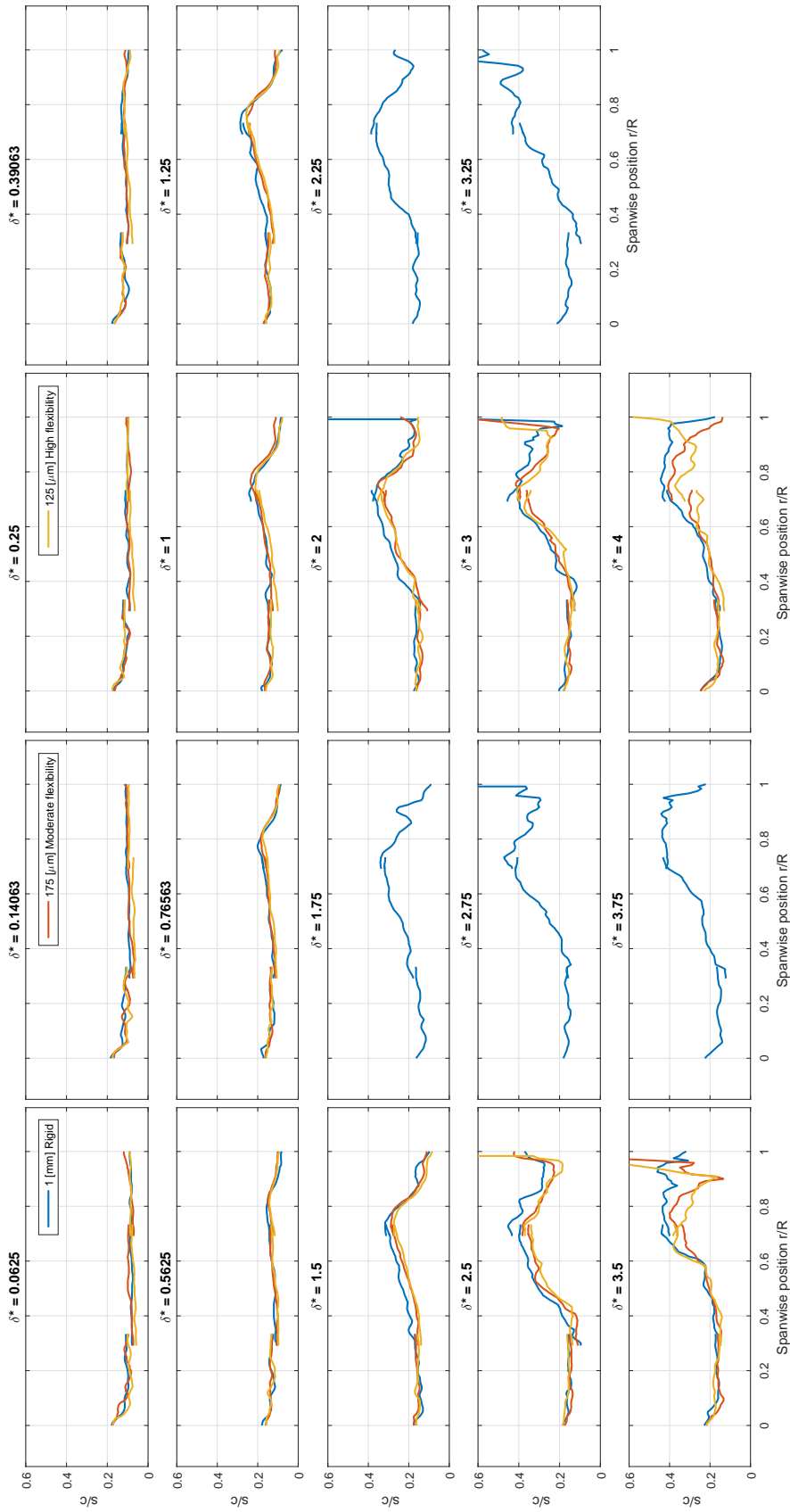


Figure 7.23: Temporal evolution of the spanwise distribution of the LEV centroid chord distance normal to the wing surface (s/c).

7.3.5 Spanwise vorticity flux of the LEV

The integration region for the spanwise vorticity flux of the LEV is considered as the region for which $\gamma_2 > 2/\pi$ evaluated in the complete flow field. In Figure 7.24 the temporal evolution of the spanwise vorticity flux of the LEV for different spanwise positions is given. In general positive values of spanwise vorticity flux are observed which indicate the advection of spanwise vorticity within the LEV from root to tip. At the onset of vortex breakdown at midspan ($r/R = 0.5$) for approximately $\delta^* = 1.5 - 2$ a negative gradient is visible. This negative gradient is an indication that the spanwise transport of vorticity in the LEV is decreased and vorticity is accumulated in that given plane which leads to the grow of the overall cross-sectional area of the LEV bubble-like structure. During this process, spanwise vorticity is tilted into a x -component and in a lesser extent into a y -component generating a strong decrease in the spanwise transport of vorticity in the LEV, see Figure 7.22. Subsequently, when the revolving motion further progresses, this leads to the burst of that vortical structure. For greater chord lengths of travel (δ^*), the vorticity flux approaches steady-state values.

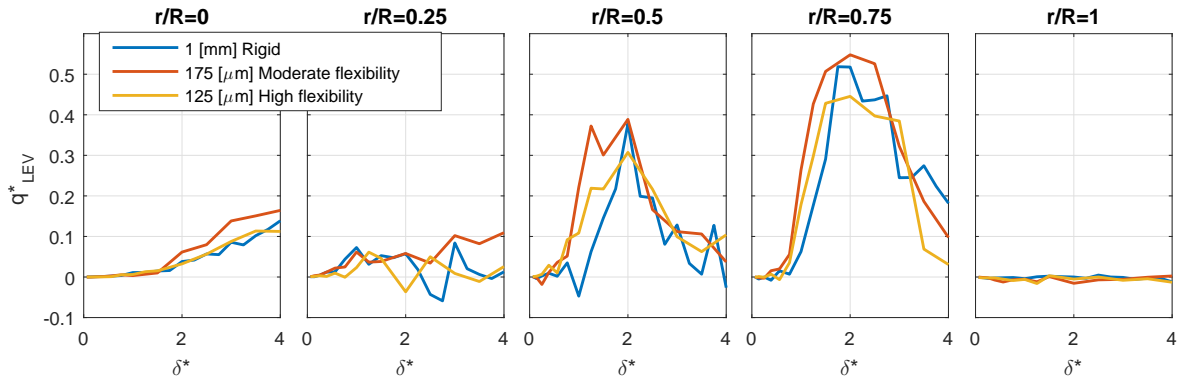


Figure 7.24: Temporal evolution of the spanwise vorticity flux of the LEV (q^*) for different spanwise positions (r/R).

In Figure 7.25 the temporal evolution of the spanwise vorticity flux of the LEV is given. Until approximately the end of the acceleration phase ($\delta^* = 1$) there is little spanwise transport of vorticity within the LEV and the flow behaves two-dimensional. Subsequently, there is a very strong increase of positive spanwise vorticity flux, followed by a transition period that that accompanies the generation of smaller scale chaotic structures in the flow. Finally, at steady-state conditions ($\delta^* = 4$), a constant positive spanwise distribution of spanwise advection of vorticity within the LEV is reached. The oscillations at steady-state conditions are probably caused by the smaller scale chaotic structures in the flow field. These results are in accordance with (Percin & van Oudheusden, 2015b) who also observed a constant spanwise distribution of spanwise advection of vorticity for $\delta^* = 4$. Furthermore it can be noted that the spanwise advection of vorticity within the LEV is stronger for the flexible wings compared to the rigid wing. Until approximately $\delta^* = 2$ the moderate flexibility shows the highest values of vorticity transport, while for $\delta^* > 2$ they have comparable levels of vorticity transport. Finally it can be noted that the advection of vorticity within the LEV is constrained at the tip ($r/R = 1$), where the TV further advects the vorticity downstream.

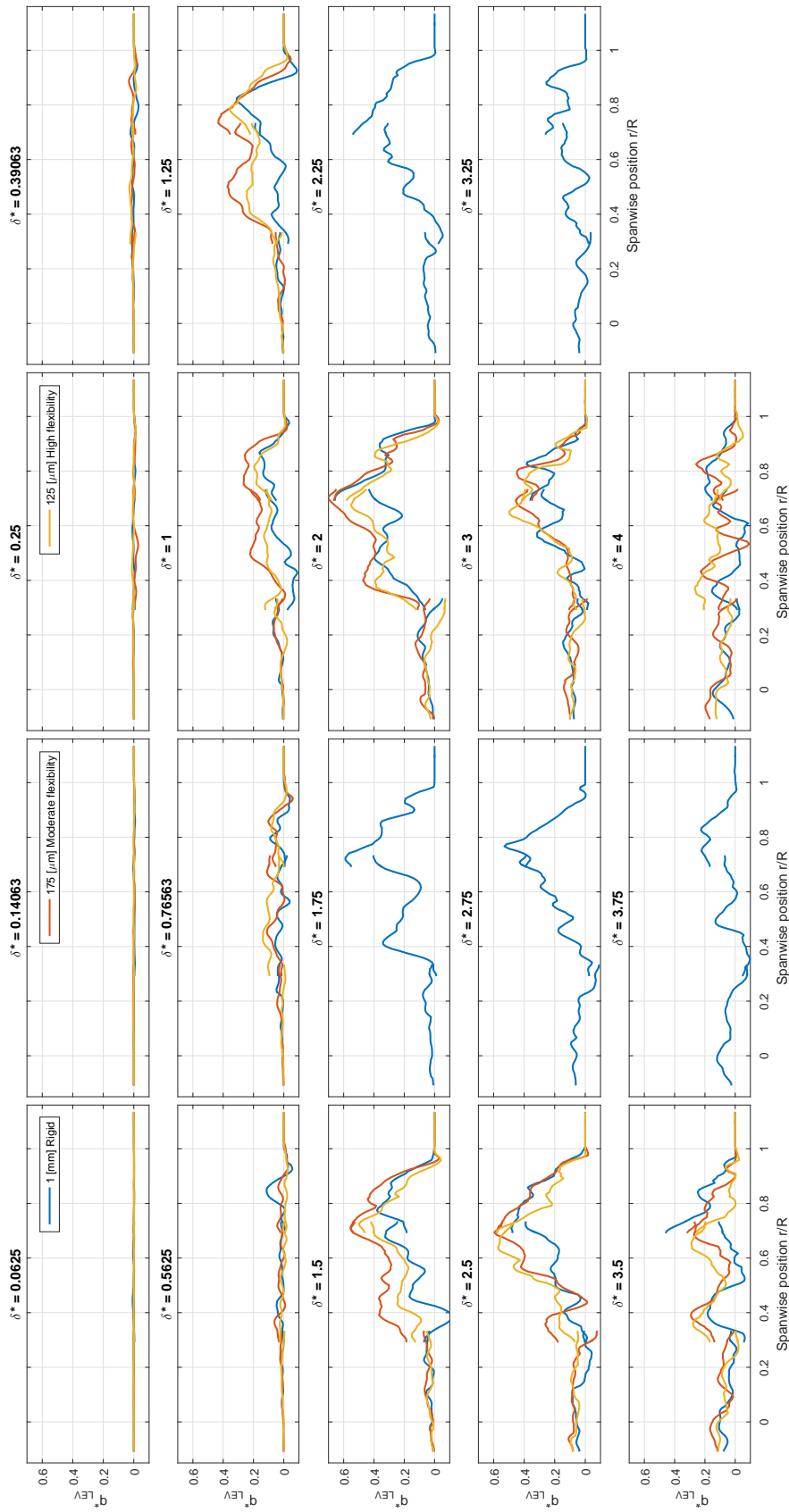


Figure 7.25: Temporal evolution of the spanwise distribution of the spanwise vorticity flux of the LEV (q_{LEV}^*)

7.4 Conclusion

Flow structures A similar vortex system, comprising LEV, TV, RV and starting TEV components, are observed in all cases. For decreasing flexural stiffness, the coherency of this vortex system is increased. Furthermore, the LEV structure of the flexible wings shows higher helical density values compared to the rigid wing. These high levels are indicative for an outboard spanwise vorticity flux along the axis of the LEV which is associated with the spanwise transport of vorticity contributing to the stability and retention of the LEV.

The onset of vortex breakdown is found to occur at approximately midspan ($r/R = 0.5$), for $\delta^* > 1.5$, for all wings. Near midspan, the core of the LEV is lifted off and expanded into a substantial bubble-like structure that extends towards the tip. The LEV grows in size along the span until approximately the reference position ($r/R = 0.75$).

The LEV center is located closer to the wing surface for decreasing flexural stiffness. Also the TV-LEV is confined to a smaller region within the flow field for the flexible wings. The reduced size of the LEV is especially pronounced within the bubble-like structure.

The highest levels of spanwise advection of vorticity correspond with the location of the LEV core. Compared to the rigid wing, a more coherent region of spanwise advection of vorticity along the span is found for the flexible wings. Furthermore, the location at which the LEV starts advecting spanwise vorticity is located slightly closer to the LE for decreasing flexural stiffness.

Due to the increased deflection with decreasing flexural stiffness the TV is located more upward, while the spanwise location is maintained.

Spanwise characteristics Until the end of the acceleration period ($\delta^* = 1$) all wings display similar characteristics in terms of the LEV properties. Subsequently, at about $\delta^* > 1.5$, a transition period appears to occur which correlates with the onset of vortex breakdown. Finally, at approximately $\delta^* = 4$, the spanwise distribution is settled and approximate steady-state conditions are reached.

Early in the revolving motion, until approximately the end of the acceleration period, the LEV circulation is similar for the different wings and shows a linear increase in the spanwise direction until $r/R = 0.9$ which is associated with the increase of the rotational velocity due to the curvilinear nature of the motion, after which it decreases to zero at the tip. Although inboard of midspan ($r/R < 0.5$) the LEV circulation increases until steady-state conditions are reached, outboard of midspan ($r/R > 0.5$) the build-up of circulation is attenuated at the onset of vortex breakdown. At steady-state conditions, the circulation inboard of midspan is similar for the different wings, while outboard of midspan the circulation is decreased significantly with decreasing flexural stiffness. The maximum LEV circulation is found at approximately the reference position ($r/R = 0.75$) at which the expanded LEV bubble-like structure is largest.

The total circulation and LEV circulation have an increased correlation with formation number compared to a rotation angle which is represented by the chord lengths traveled at the reference position (δ^*). Although the slope of total circulation with formation number is decreased for decreasing flexural stiffness, the slope of the LEV circulation with formation number is comparable for the different wings.

The temporal development of the spanwise distribution of the LEV centroid location is comparable for the different wings. The LEV centroid location is similar in absolute sense. However, due to the deflection of the flexible wings, the LEV centroid is located closer to the wing surface. At steady-state conditions, for spanwise locations inboard of midspan, the LEV centroid has approximately the same distance to the wing surface for all wing cases. However, outboard of midspan the distance of the LEV centroid to the wing surface is significantly reduced with decreasing flexural stiffness. Within the bubble-like structure the LEV is tilted significantly aft in the downstream direction, which converts part of the spanwise vorticity (ω_z) into ω_x such that the spanwise circulation is reduced.

Until approximately $\delta^* = 0.5625$ most of the vorticity is kept within the LEV and TEV, and little in the bound circulation. Furthermore, for $\delta^* < 1$ there is little spanwise transport of vorticity within the LEV and the flow behaves rather two-dimensional. At the onset of vortex breakdown ($\delta^* = 1.5$), at the midspan position, a high negative gradient in the spanwise vorticity flux of the LEV is present. This negative gradient is indicative for vorticity accumulation which can eventually lead to the burst of the LEV bubble-like structure. Throughout the revolving motion, the spanwise advection of vorticity within the LEV is higher for the flexible wings compared to the rigid wing. Finally, at steady-state conditions a constant positive spanwise distribution of spanwise advection of vorticity within the LEV is reached.

In section 8.3 a summary of the spanwise characteristics in terms of the LEV properties and sectional force coefficients for $\delta^* = 1, 1.5$ and 4 is given.

Chapter 8

Results: Pressure & Load reconstruction

In this chapter the results of the pressure & load reconstruction for the different wings are presented and discussed. The methods used in the calculation of the pressure fields and loads exerting on the wing are described in chapter 5.

The temporal resolution of the rigid wing is $TR^* = 0.25$ for all phase angles, while the temporal resolution of the flexible wings is $TR^* = 0.25$ for $0.0625 < \delta^* < 1.5$ and $TR^* = 0.5$ for $2 < \delta^* < 4$ (see subsection 4.5.1). In this study a coarsened temporal resolution indicates that $TR^* = 0.5$ instead of $TR^* = 0.25$. To form the coarsened data set from the high-time-resolution data for the rigid wing case, every other phase is selected starting from $\delta^* = 0.0625$ to 4.

For illustration purposes the 2 flexible wings are illustrated with a thickness of 0.5 mm. In all figures the left column depicts the 1 [mm] Rigid wing, the middle column depicts the 175 [μm] Moderate flexible wing and the right column depicts the 125 [μm] High flexible wing unless stated otherwise.

Based on the balance measurements steady-state conditions are reached for $\delta^* > 5$, see section 6.2. However, the imaging measurements are taken up to $\delta^* = 4$, see section 4.5. In this chapter the steady-state conditions indicate the imaging measurements for the greatest chord length that has been measured, i.e. $\delta^* = 4$.

8.1 Pressure field

The pressure fields presented in this section are evaluated by use of the temporally coarsened data with a resolution of $TR^* = 0.5$ such that the different wings can be compared for greater chord lengths up to $\delta^* = 4$.

8.1.1 Spanwise distribution

In Figure 8.1, the pressure contours are given in chordwise oriented planes along the span, and at the midspan position ($r/R = 0.5$) and at the reference position ($r/R = 0.75$) for $\delta^* = 1.5$ and 4.

The low pressure region at the suction side of the wing correlates well with the location of the LEV, as depicted in Figure 7.3 and Figure 7.5. At $\delta^* = 1.5$, a low pressure region is observed downstream of the wing which is associated with the starting TEV. At midspan ($r/R = 0.5$), the location of the low pressure region is similar for the different wings. In section A.6 a time-series animation of the pressure fields is given. After the onset of vortex breakdown, the low pressure region outboard of midspan ($r/R > 0.5$) grows rapidly. At $\delta^* = 4$, the low pressure region accompanied by the LEV reduces in size for decreasing flexural stiffness. Also the high pressure region on the lower side of the wing becomes slightly smaller in size, such that the net pressure difference between the pressure and suction side of the airfoil is significantly decreased with decreasing flexural stiffness, which correlates well with the reduction in the resultant force acting on the wing observed in the balance measurements (see Figure 6.8). Furthermore, it can be observed that the low pressure peak is relatively high, and located closer to the wing surface with decreasing flexural stiffness. These observations are in accordance with the location of the LEV centroid, see Figure 7.21 and Figure 7.22. Furthermore, the low pressure peak is closer to the LE with decreasing flexural stiffness, which is in agreement with the chordwise location of the center of pressure obtained from the balance measurements, see Figure 6.12. Moreover, due to an increased chordwise deflection, the local suction force vectors have an increased alignment with the direction of lift, such that the total net force vector is more inclined in the direction of lift. Although the low pressure region associated with the LEV is reduced in size with decreasing flexural stiffness, resulting in a smaller resultant force on the wing, the corresponding lift generation remains relatively high because of the increased alignment of the force vector in the direction of the lift caused by the wing deformation and the relative high suction peak that is located closer to the wing surface. These observations suggesting a reduction of the total net force and an increase of the lift-to-drag ratio agree well with the balance measurements, as depicted in Figure 6.8 and Figure 6.10.

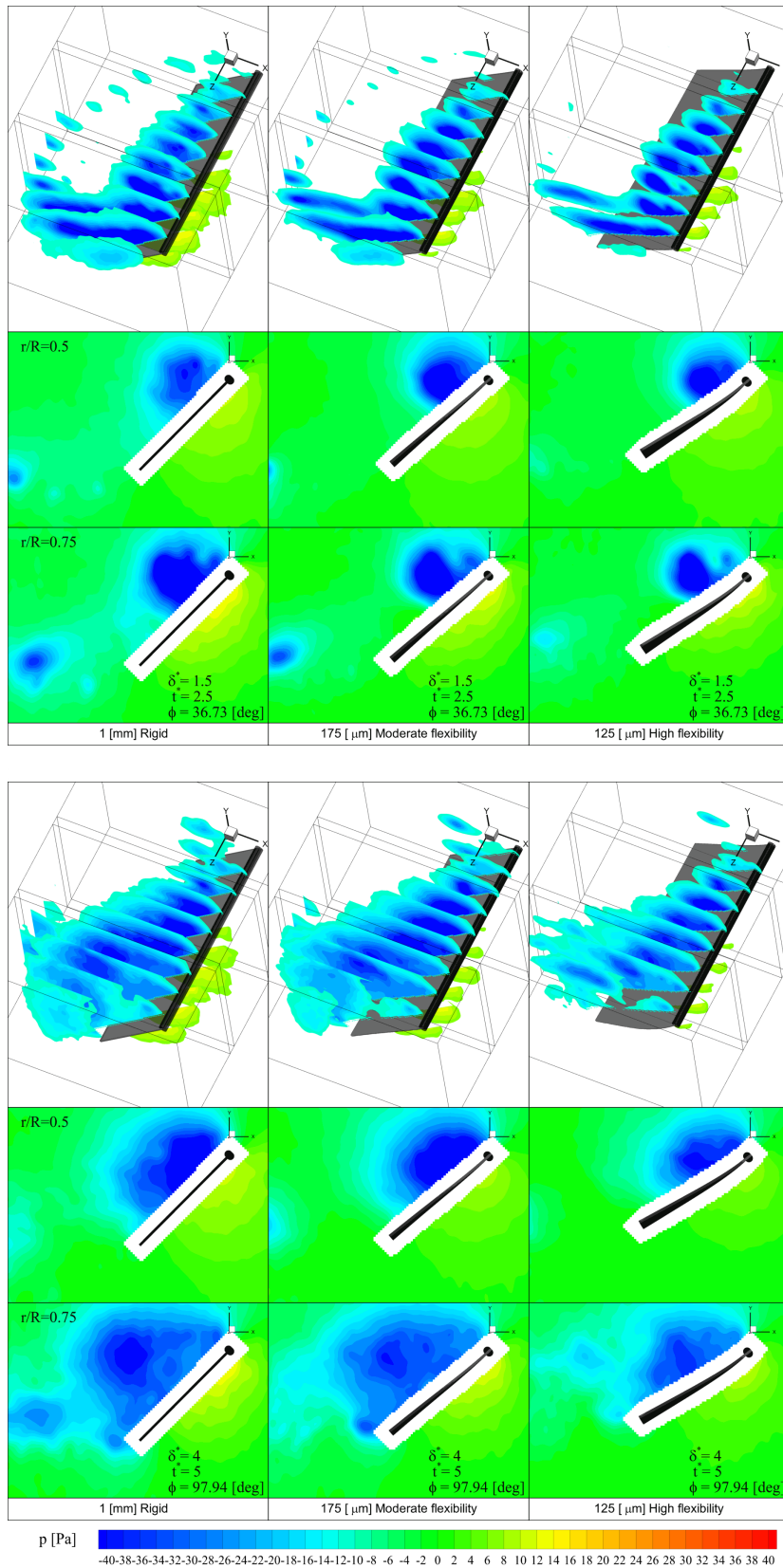


Figure 8.1: Pressure contours (p) for $\delta^* = 1.5$ and 4. *Top:* Pressure contours along the span. *Middle:* Pressure contour at $r/R = 0.5$. *Bottom:* Pressure contour at $r/R = 0.75$.

In Figure 8.2 the footprint of the wake at a spanwise oriented plane (y, z -plane) located at $0.5c$ downstream of the TE is given (see Figure 7.7 for the location of this plane relative to the wing).

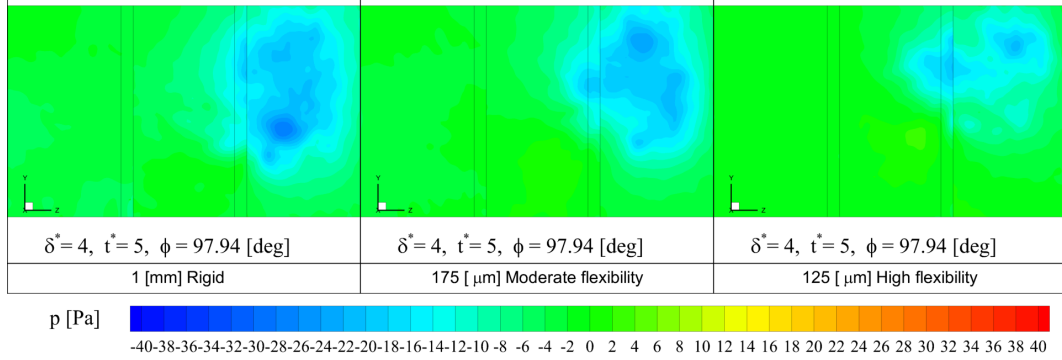


Figure 8.2: Pressure contour (p) of the wake at a spanwise oriented plane (y, z -plane) with an offset of $0.5c$ downstream of the TE for $\delta^* = 4$.

Due to the deflection of a flexible wing, the flow becomes more aligned with the direction of the revolving motion at the trailing edge and a smaller wake is formed which is especially pronounced in the vicinity of the tip vortex. The reduced size and magnitude of the low pressure region in the wake associated with the deflection of the wing, which also results in tilting of the reduced net resultant force vector in the lift direction, accounts for the significant decrease in drag with increasing wing flexibility.

8.1.2 Comparison with coherent flow structures

In Figure 8.3 the low (blue) and high (red) pressure regions are given in conjunction with the vortical structures, which are identified using the Q-criterion, for $\delta^* = 1.5$ and 4. In section A.7 a time-series of the revolving motion is given.

The vortical structures are dominated by rotation in which a low pressure region is created. It can be observed that the transition of the pressure field between the volumes is relatively smooth and that the low pressure regions correlate well with the vortical structures. This high correlation between the pressure regions and the vortical structures is even found after the onset of vortex breakdown when small fragmented chaotic scale structures are formed. Consequently, it can be observed that the vortical structures overlap with the calculated low pressure regions. The regions of decreased pressure corresponding to the small-scale vortical features are not resolved due to the limited spatial resolution and smoothing nature of the Poisson pressure integration scheme. As mentioned earlier the size of the low pressure region is decreasing with decreasing flexural stiffness, which can be observed by the smaller blue isosurface regions for decreasing flexural stiffness. The high pressure region (red) is mainly located outboard of midspan ($r/R > 0.5$) and also decreases in size with decreasing flexural stiffness.

Since the pressure field is independent of the reference frame and the Q-criterion is similar

in both rotating and inertial reference frame for the current case, it is expected that the pressure field is directly related to the Q -criterion because the latter is essentially the source term of the Poisson pressure integration scheme for an incompressible flow in the absence of rotational effects, see Equation 7.2. Although $Q > 0$ does not guarantee the existence of a pressure minimum, in most cases they are equivalent (Jeong & Hussain, 1995). In this study also a high correlation between the low pressure field and Q -criterion is observed.

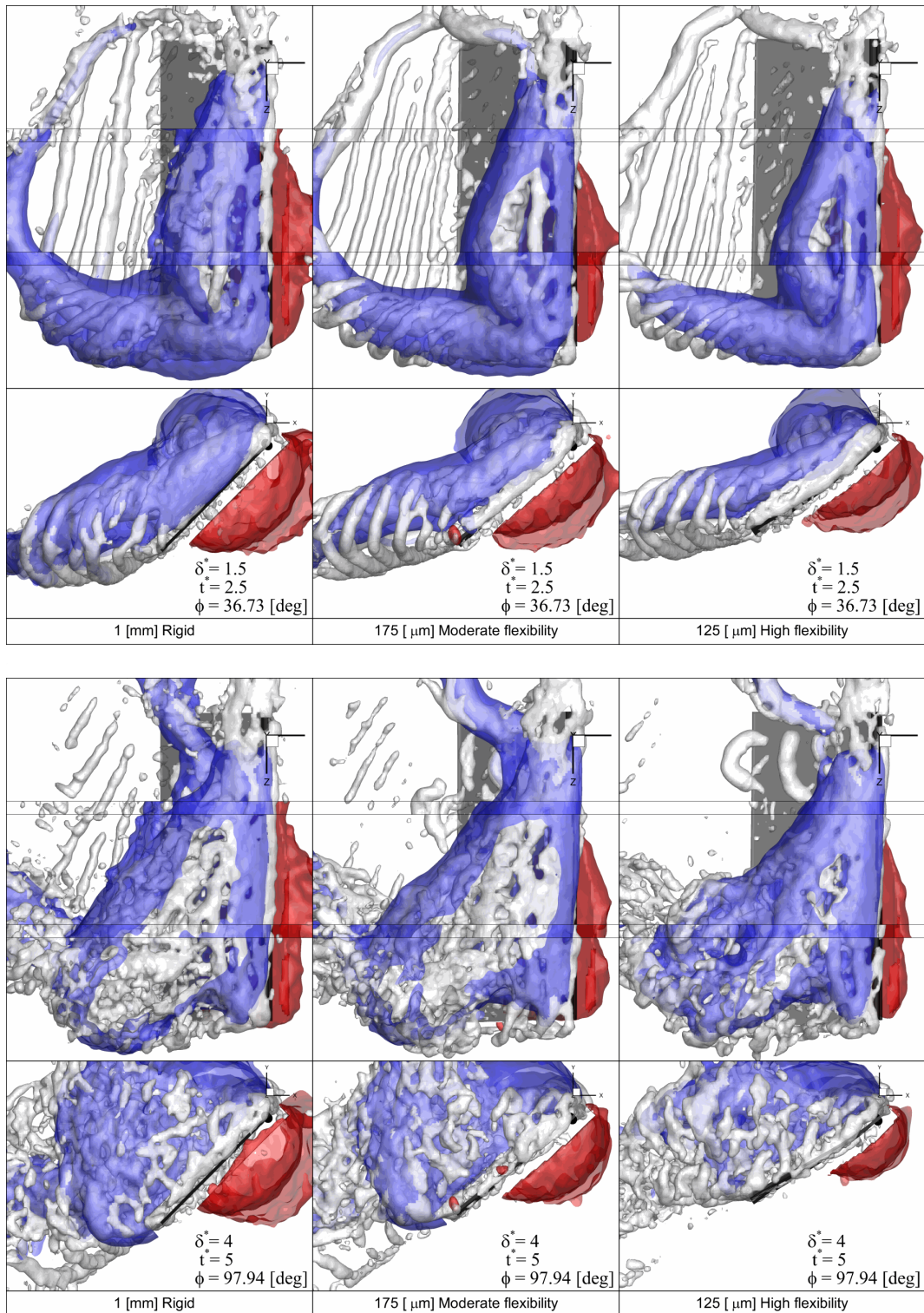


Figure 8.3: Vortical structures and reconstructed pressure fields for $\delta^* = 1.5$ and 4. Isosurfaces of Q-criterion: White $Q/(V_t/c)^2 = 3$. Isosurfaces of reconstructed pressure field: Blue $p = -13$ Pa and Red $p = 6$ Pa.

8.1.3 LEV pressure centroid

The LEV pressure centroid location is calculated as,

$$\bar{\mathbf{x}} = \frac{\int S_{xy} p \mathbf{x} dx dy}{\int S_{xy} p dx dy} \quad (8.1)$$

where \mathbf{x} is the x, y -coordinate at a chordwise oriented plane measured with respect to the LE of the wing, and S_{xy} is the chordwise oriented LEV circulation integration region that is considered as the region for which $\gamma_2 > 2/\pi$ evaluated in the complete flow field, see section 7.1.

In Figure 8.4 the temporal evolution of the spanwise distribution of the LEV pressure centroid x -location is given. The LEV pressure centroid has a high correlation with the LEV centroid location, see Figure 7.22. The greatest differences between the LEV pressure centroid and the LEV centroid location are found near the tip at approximately $r/R = 0.9$ for steady-state conditions. For instance at steady-state conditions LEV pressure centroid of the rigid wing is located more downstream than the LEV centroid.

In Figure 8.5 the temporal evolution of the spanwise distribution of the distance between the LEV pressure centroid and the wing surface (s/c) is given. The distance of the LEV pressure centroid to the wing surface is again in agreement with the distance of the LEV centroid to the wing surface, see Figure 7.23. The greatest differences are, like for the x -location, found at $r/R = 0.9$ for steady-state conditions. For instance, at steady-state conditions, the LEV pressure centroid of the rigid wing has a higher distance to the wing surface. The further downstream location and the higher distance to the wing surface of the LEV pressure centroid, compared to the LEV centroid are likely to stem from the TV. Although the LEV and TV are merged and difficult to differentiate at steady-state conditions, a large region of low pressure can be observed near the wing tip, see Figure 8.3. The LEV-TV accompanies a low pressure region while contains only a low amount spanwise vorticity the near the tip. Because the LEV-TV is maintained far downstream of the LE, the LEV pressure centroid is found further downstream with an increased distance to the wing surface.

In general the LEV pressure centroid has a high correlation with the LEV centroid, such that the LEV center of pressure can be approximated with the LEV center. Consequently, the location of the suction peak within the LEV can be approximated by the LEV center without reconstructing the pressure field from the flow field data.

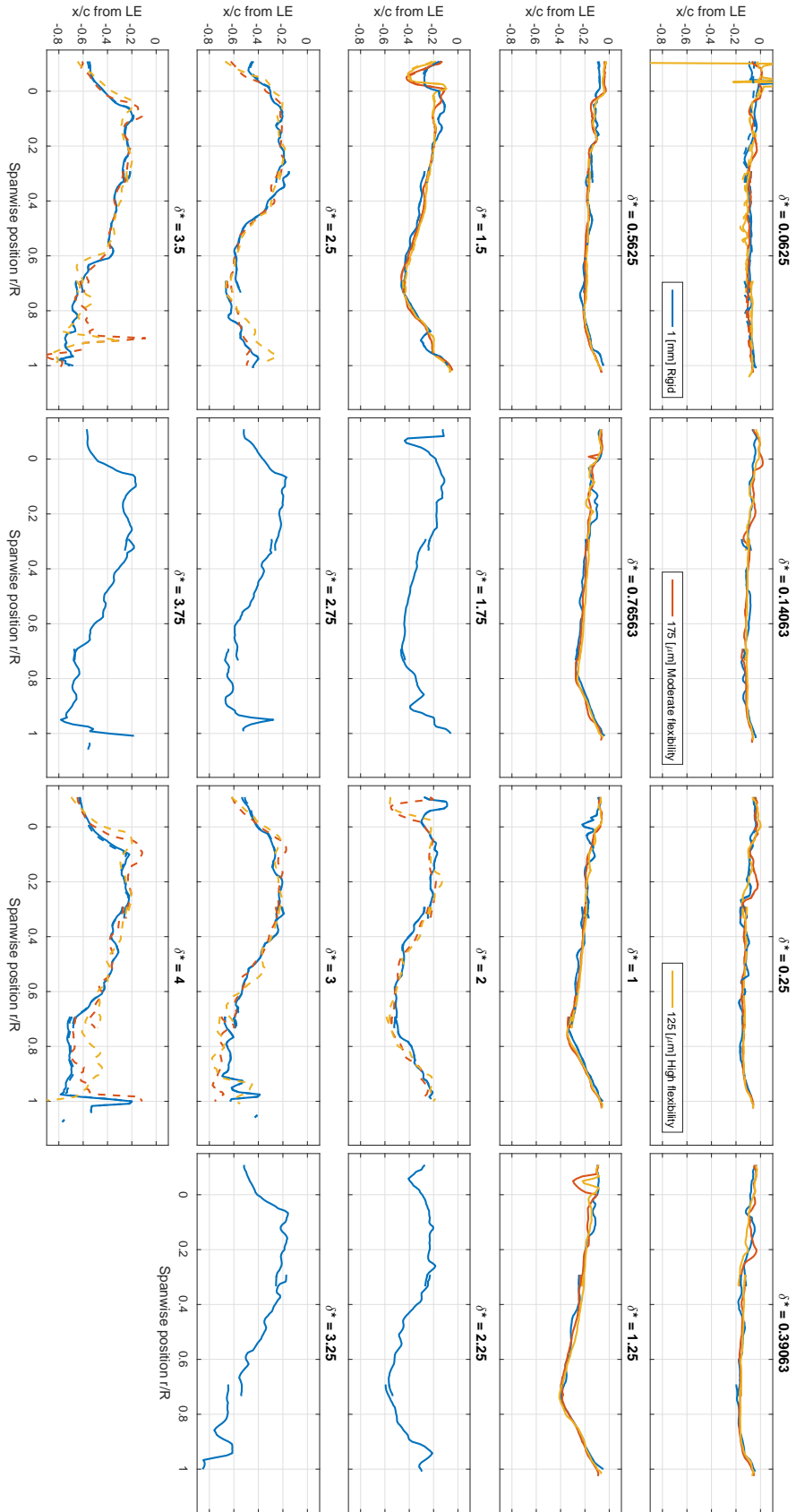


Figure 8.4: Temporal evolution of the spanwise distribution of the LEV pressure centroid chord distance in x -direction from the LE (x/c). Solid line depicts a high temporal resolution of $TR^*=0.25$ and the dashed line depicts a coarsened temporal resolution of $TR^*=0.5$.

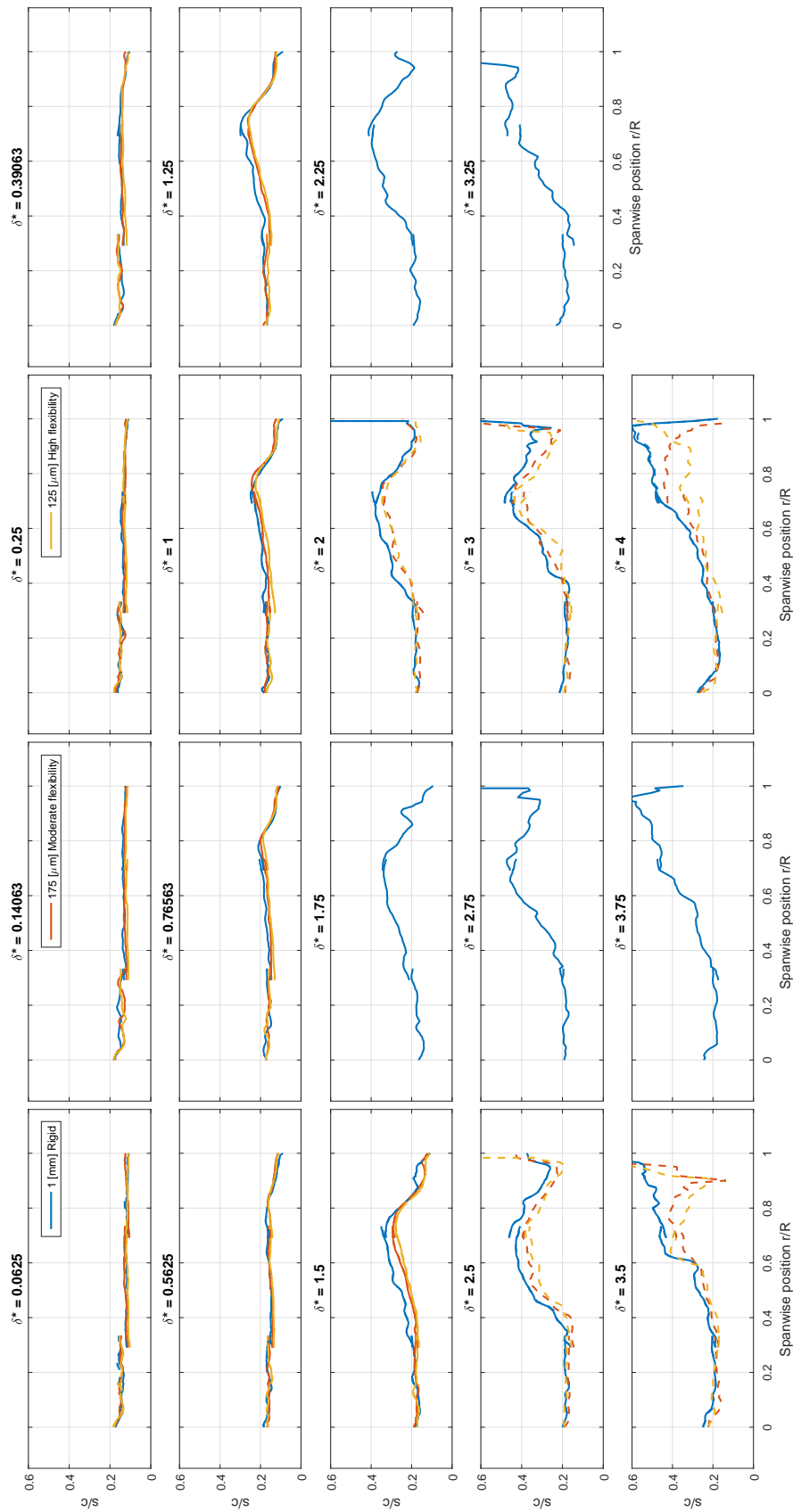


Figure 8.5: Temporal evolution of the spanwise distribution of the chord distance between the LEV pressure centroid and the wing surface (s/c). Solid line depicts a high temporal resolution of $TR^*=0.25$ and the dashed line depicts a coarsened temporal resolution of $TR^*=0.5$.

8.1.4 Pressure gradient

The pressure gradient is calculated as the numerical spatial gradient of the reconstructed pressure field. Since the pressure field is independent of reference frame, the spatial gradient of pressure can be related to the material acceleration in the inertial reference frame for an incompressible flow with negligible viscous effects as,

$$\frac{D\mathbf{u}}{Dt} = -\frac{1}{\rho}\nabla p \quad (8.2)$$

Spanwise pressure gradient A negative spanwise pressure gradient is associated with a positive spanwise acceleration (outboard) of a particle within the flow field. The process of vortex breakdown correlates well with the formation of a positive spanwise pressure gradient which is indicative for an inboard acceleration of a particle. As the outboard moving particles experience an adverse pressure gradient accompanied by an inboard acceleration, the spanwise advection of vorticity is decreased and vorticity is accumulated in a given plane, which can eventually lead to the burst of the vortical structure. In Figure 8.6 the spanwise pressure gradient is given for $\delta^* = 1.5$ and 4. In section A.8 a time-series animation of the spanwise pressure gradient regions is given.

Early in the revolving motion a region of negative pressure gradient is formed at the suction side of the wing that agrees well with the location of the LEV core and promotes the outboard spanwise advection of vorticity. This spanwise advection of vorticity balances the production of vorticity such that a stable LEV is created. The negative pressure gradient region that is formed on suction side of the wing at $\delta^* = 1.5$ correlates well with the location of the LEV core (see Figure 7.3 and Figure 7.5) and its strong levels of spanwise vorticity flux density (see Figure 7.8). However, also a region of positive pressure gradient is formed near midspan ($r/R = 0.5$) at the LE on the suction side of the wing which correlates well with the onset of the vortex breakdown. Also a region of positive pressure gradient is formed near the tip of the wing above the region of negative pressure gradient, (see the x, y -plane at $r/R = 0.75$). Subsequently, the region of positive pressure gradient around midspan starts expanding. Simultaneously, the region of positive pressure gradient near the tip connects with the region of positive pressure gradient that is formed around midspan. Both regions start merging until a coherent region of positive and negative pressure gradient is formed at respectively the outboard and inboard part of the wing for steady-state conditions ($\delta^* = 4$). For decreasing flexural stiffness, the relative region of negative pressure gradient at the suction side of the wing surface is extended more towards tip of the wing, and agrees well with the spanwise vorticity flux density (see Figure 7.8). This may account for the enhanced spanwise advection of vorticity, and the increased stability and retention of the LEV.

Garmann & Visbal (2014) numerically studied rigid revolvings wings in which vortex breakdown also occurred around midspan. Moreover, the vortex breakdown showed a strong dependence on the spanwise pressure gradient established between the root and the tip. It was found that the pressure gradient force is dominant within the core of the LEV and is

responsible in the formation of outboard spanwise flow. However, outside the vortex core, the centrifugal force was found to be equally important in the formation of spanwise flow. Due to this spanwise flow, vorticity is advected along the span which stabilizes the LEV (Ellington et al., 1996). These observations are in agreement with (Lentink & Dickinson, 2009) who concluded that the pressure gradient force can explain the spanwise flow in the LEV core, whereas centrifugal pumping can explain the spanwise flow outside the LEV core. The current experimental study supports these findings. In this study it was also found that the negative spanwise pressure gradient has a high correlation with the location of the LEV core and the strong levels of spanwise transport of vorticity which are driven by an outboard spanwise velocity. Downstream of the LEV core a relatively large region of spanwise velocity is observed (see Figure 7.7, $r/R = 0.5$), while the pressure gradient is negligible. These spanwise velocities are likely to stem from the centrifugal effects.

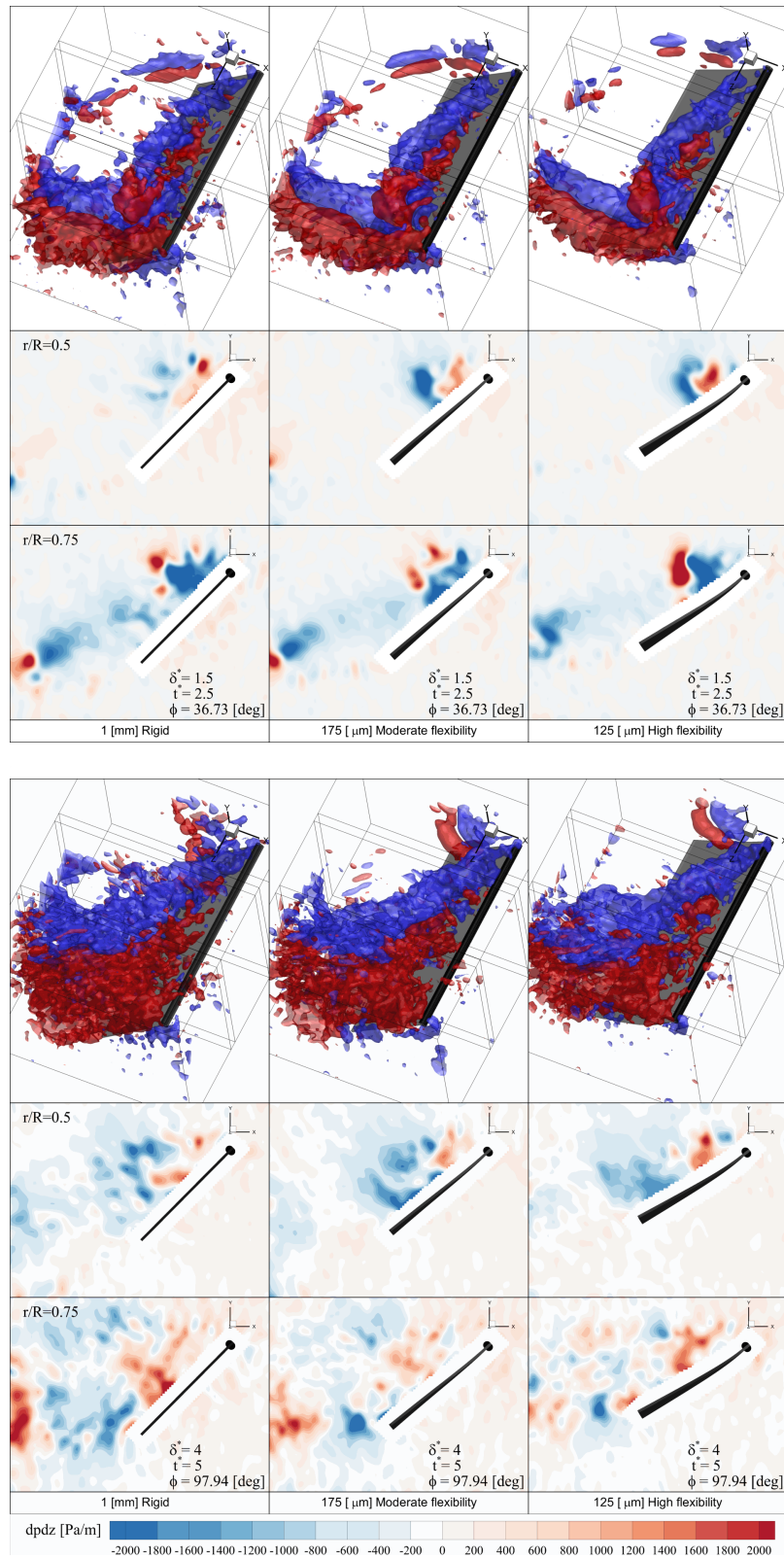


Figure 8.6: Spanwise pressure gradient contours and isosurfaces ($dpdz$) for $\delta^* = 1.5$ and 4 . *Top:* Isosurface of pressure gradient: Blue $dpdz = -1000$ Pa/m and Red $dpdz = 1000$ Pa/m. *Middle:* Spanwise pressure gradient contour at $r/R = 0.5$. *Bottom:* Spanwise pressure gradient contour at $r/R = 0.75$.

Comparison with Navier-Stokes momentum equation The numerical spanwise pressure gradient, based on the reconstructed pressure field, is compared with the pressure gradient given by the Navier-Stokes momentum equation, see Equation 5.2.

In Figure 8.6 the spanwise pressure gradient obtained from the Navier-Stokes momentum equation is given for $\delta^* = 1.5$.

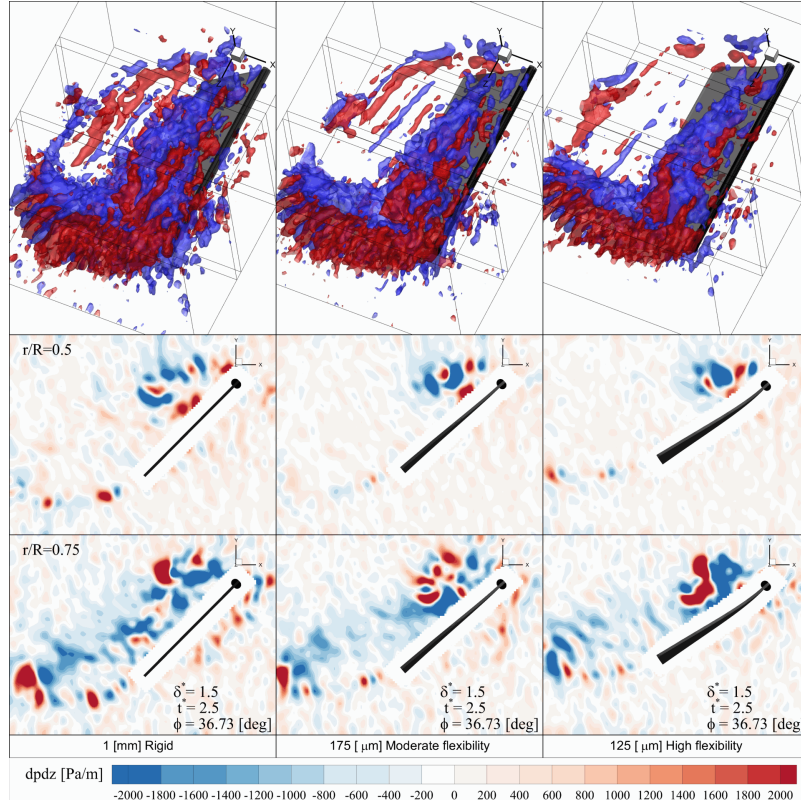


Figure 8.7: Spanwise pressure gradient contours and isosurfaces ($dpdz$) for $\delta^* = 1.5$, based on the Navier-Stokes momentum equation. *Top:* Isosurface of pressure gradient: Blue $dpdx = -1000$ and Red $dpdx = 1000$. *Middle:* Spanwise pressure gradient contour at $r/R = 0.5$. *Bottom:* Spanwise pressure gradient contour at $r/R = 0.75$.

Although the same global features are visible compared to Figure 8.6, some differences are observed. First of all the small scale features, such as those associated with the TEVs, are slightly better reconstructed with the pressure gradient directly obtained from the Navier-Stokes equation. However, the data also contains more noise. The pressure integration Poisson scheme has a smoothing nature which suppresses the small scale structures and noise. As a result the trends between the different wings are better captured by the numerical spanwise pressure gradient obtained from the reconstructed pressure field.

Pressure gradient in x -direction A negative pressure gradient in x -direction is associated with a positive acceleration in x -direction of a particle within the flow field. In Figure 8.8 the pressure gradient in x -direction is given for $\delta^* = 1.5$ and 4. In section A.9 a time-series animation of the pressure gradient in x -direction is given.

It can be observed that a region of positive and negative pressure gradient in x -direction is formed at the suction side of the wing. For $\delta^* = 1.5$, these regions correlate well with the location of the LEV core (see Figure 7.3 and Figure 7.5). A positive and negative region is formed at respectively the upstream and downstream location of the LEV due to its rotational motion in which the particles experience an acceleration in x -direction. However, the region of negative pressure gradient is larger than the region of positive pressure gradient. Near the starting-TEV these regions of positive and negative pressure gradient are also found. Also for $\delta^* = 4$, a large region of negative gradient is formed that has a high correlation with the LEV-TV (see Figure 8.3). Due to these significant regions of negative pressure gradient, the particles within the LEV will experience a net acceleration in the positive x -direction. This ensures that the LEV will stay close to the wing surface, such that the low pressure region associated with the LEV is located close to the wing surface resulting in a high resultant force acting on the wing. At the tip, vorticity is convected downstream by the TV. At these spanwise sections near the tip, a positive gradient is found, which is most pronounced for greater chord lengths (see $\delta^* = 4$). The positive gradient region at the LE of the wing is associated with a downstream (negative x -direction) acceleration of particles.

Lentink & Dickinson (2009) indicated that the Coriolis acceleration is an important condition for the stable attachment of the LEV, because this leads to a continuous acceleration in the revolving direction. Furthermore, (Jardin & David, 2015) found that the Coriolis effect stabilizes the rotational flow limiting global burst and concentrates the bursting near the tip. It was concluded that the Coriolis effect is the main mechanism for the enhanced lift generation for revolving wings. The current experimental study supports these findings. In this study a large region of negative pressure gradient in x -direction is found that has a high correlation with the location of the LEV which is likely to stem from the Coriolis effects. The associated accelerations in x -direction are likely to be responsible for the stability of the LEV and its close distance to the wing surface.

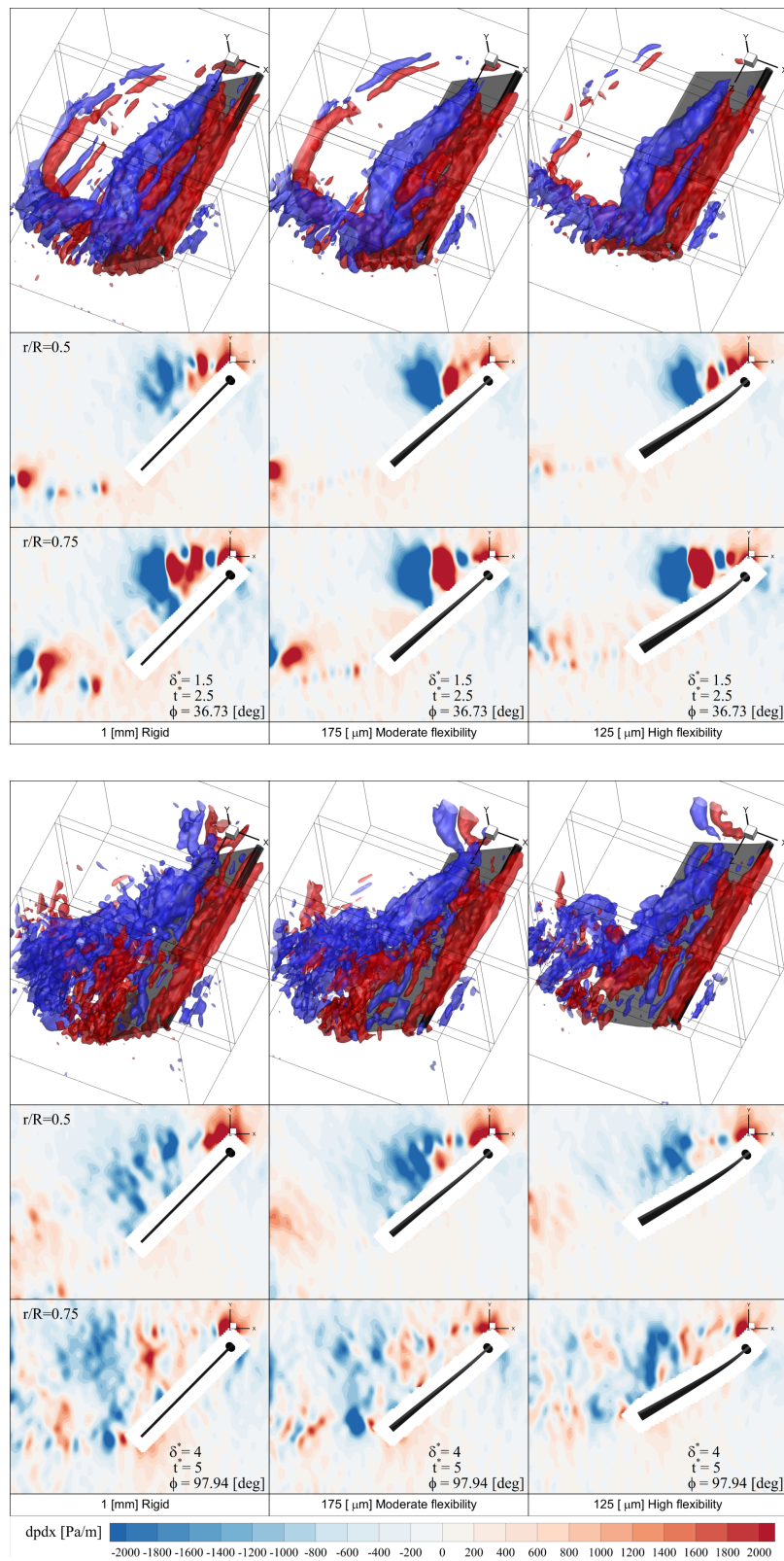


Figure 8.8: Pressure gradient in x -direction contours and isosurfaces ($dpdx$) for $\delta^* = 1.5$ and 4. *Top:* Isosurface of pressure gradient: Blue $dpdx = -1000$ Pa/m and Red $dpdx = 1000$ Pa/m. *Middle:* Pressure gradient in x -direction contour at $r/R = 0.5$. *Bottom:* Spanwise pressure gradient contour at $r/R = 0.75$.

8.2 Loads

8.2.1 Lift & drag coefficient

Comparison with balance data Figure 8.9 compares the forces obtained by means of balance measurements and the reconstructed loads by using the temporally coarsened data set for all the tested wings.

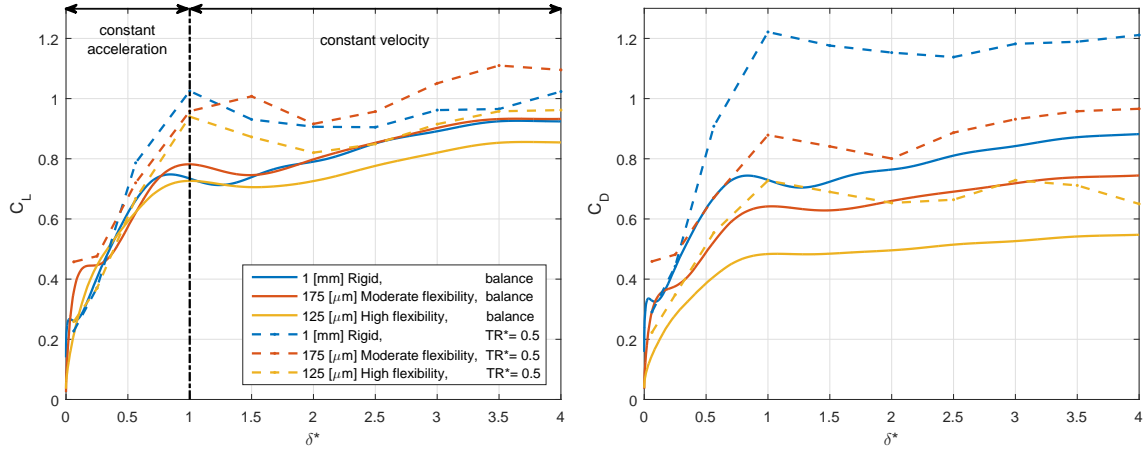


Figure 8.9: Temporal evolution of the lift (left column) and drag (right column). Solid line depicts the low pass filtered balance data and the dashed line depicts the reconstructed data with a coarsened temporal resolution of $TR^* = 0.5$. The reconstructed lift and drag coefficients are based on the summation of volume 1-3.

It can be observed that for both the lift and drag, the reconstructed loads are higher than the loads obtained by the balance measurements, which is most pronounced for the drag. The reconstructed lift and drag coefficient peak near the end of the acceleration ($\delta^* = 1$) is approximately equal to its steady-state value at $\delta^* = 4$, however, the balance measurements reach a significantly lower value than the steady-state lift and drag. Furthermore the reconstructed lift and drag coefficient peak at the start of the revolving motion show a discrepancy with the balance data. With the higher temporal resolution of $TR^* = 0.25$ these peaks are slightly better captured, see Figure 5.5.

To compare the relative differences of the loads between the wings, the reconstructed lift and drag coefficients are normalized to the steady-state balance data of the 1 [mm] Rigid wing. The normalization factor for the lift NF_{C_L} is calculated as,

$$NF_{C_L} = \frac{\frac{1}{2} \{C_{L_{\text{Balance}}}(\delta^* = 3.5) + C_{L_{\text{Balance}}}(\delta^* = 4)\}}{\frac{1}{2} \{C_{L_{\text{Reconstructed}}}(\delta^* = 3.5) + C_{L_{\text{Reconstructed}}}(\delta^* = 4)\}} \quad (8.3)$$

The normalization factor for the drag NF_{C_D} is written analogous in terms of the drag coefficient. In Figure 8.10 the normalized temporal evolution of the lift and drag coefficient is given.

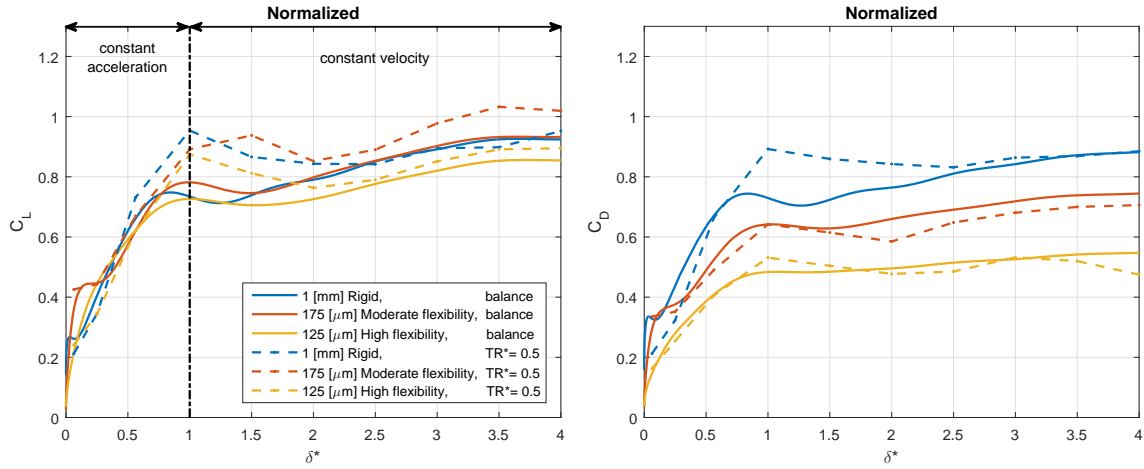


Figure 8.10: Normalized temporal evolution of the lift (left column) and drag (right column). Solid line depicts the low pass filtered balance data and the dashed line depicts the normalized reconstructed data with a coarsened temporal resolution of $TR^* = 0.5$. The reconstructed lift and drag coefficients are based on the summation of volume 1-3.

It can be observed that the relative differences in loads between the different wings are similar for both the reconstructed loads and the balance measurements. The reconstructed lift for the moderate flexible wing near steady-state conditions ($\delta^* = 4$) is slightly higher compared to the rigid wing, while the lift coefficient of the moderate flexible wing is approximately equal to the rigid wing for the balance measurements. The steady-state lift coefficient for both the reconstructed loads and balance measurements of the high flexible wing is lower than the rigid wing. However, the balance measurements display a relatively lower values than the reconstructed loads. The relative differences in the drag coefficient near steady-state conditions for the moderate and high flexible wings are similar for both the reconstructed loads and balance measurements, however, slightly lower values are found for the reconstructed loads. Furthermore, the relative differences of the global slope of the lift and drag between the wings in the acceleration phase ($\delta^* < 1$) is also similar for both the reconstructed loads and the balance measurements.

8.2.2 Lift & drag force contributions

The load contributions of the different wings within the evaluation of the control volume analysis are depicted in Figure 8.11.

Due to a positive contribution of the unsteady momentum term ($umdt$) and the pressure term (fp), the lift coefficient is not zero at $\delta^* = 0.0625$ for the moderate and high flexible wing. At steady-state conditions, the lift coefficient of the moderate and high flexible wing is relatively high due to the increased pressure term contribution (fp) compared to the rigid wing. The peak in lift coefficient at the end of the acceleration phase ($\delta^* = 1$) is caused by the large unsteady momentum contribution ($umdt$). During the start of the revolving motion the flow is deflected downwards which is associated with the build-up of the circulatory effects. As

a result, the unsteady momentum contribution causes an upward force component. When the flow starts settling to the steady-state conditions, the unsteady momentum contribution approaches zero.

It is found that for the steady-state drag coefficient, the pressure term contribution (fp) decreases for decreasing flexural stiffness, while the momentum flux contribution (fm) is comparable. Also it can be observed that the Coriolis momentum contribution ($mCor$) decreases (becomes more negative) with decreasing flexural stiffness. The Coriolis momentum contribution acts in the drag direction and relates to $\Omega_y U_z$. Since Ω_y is the same for each wing, the volume integral of U_z is more negative with decreasing flexural stiffness. This implies that the volume integral of the spanwise velocity in the inertial frame is decreased with decreasing flexural stiffness which is in accordance with Figure 7.7. At steady-state conditions the unsteady momentum contribution ($umdt$) approaches zero. At the start of the revolving motion, the unsteady momentum contribution is negative since the calculations are performed in a rotating reference frame ($U_{x_{rotating}} = U_{x_{inertial}} - \Omega_y z_{pv}$, see Equation 5.1). Due to the constant angular acceleration, Ω_y increases linearly during the acceleration phase. As a result, there is an approximate negative plateau until the end of the acceleration, after which the unsteady momentum contribution starts increasing. The trend of the unsteady momentum contribution is opposite to the Euler effect ($mEul$) in the acceleration phase.

Note that in this section the contributions of the different terms to evaluate the lift and drag are given by means of a control volume approach. However, it is rather difficult to comment on their influence on the formation of flow structures. For instance, although there is no contribution of the rotational effects in the evaluation of the lift based on the control volume approach, they still influence the flow field indirectly. These rotational effects are suggested to be responsible for the stability and enhancement of the LEV (Sane, 2003). The sustained LEV is accompanied by a low pressure region at the suction side of the wing. The suction forces that act normal to the wing surface are dominant for the resultant force acting on the model. Consequently these rotational effects are likely to have a positive influence in the generation of elevated lift.

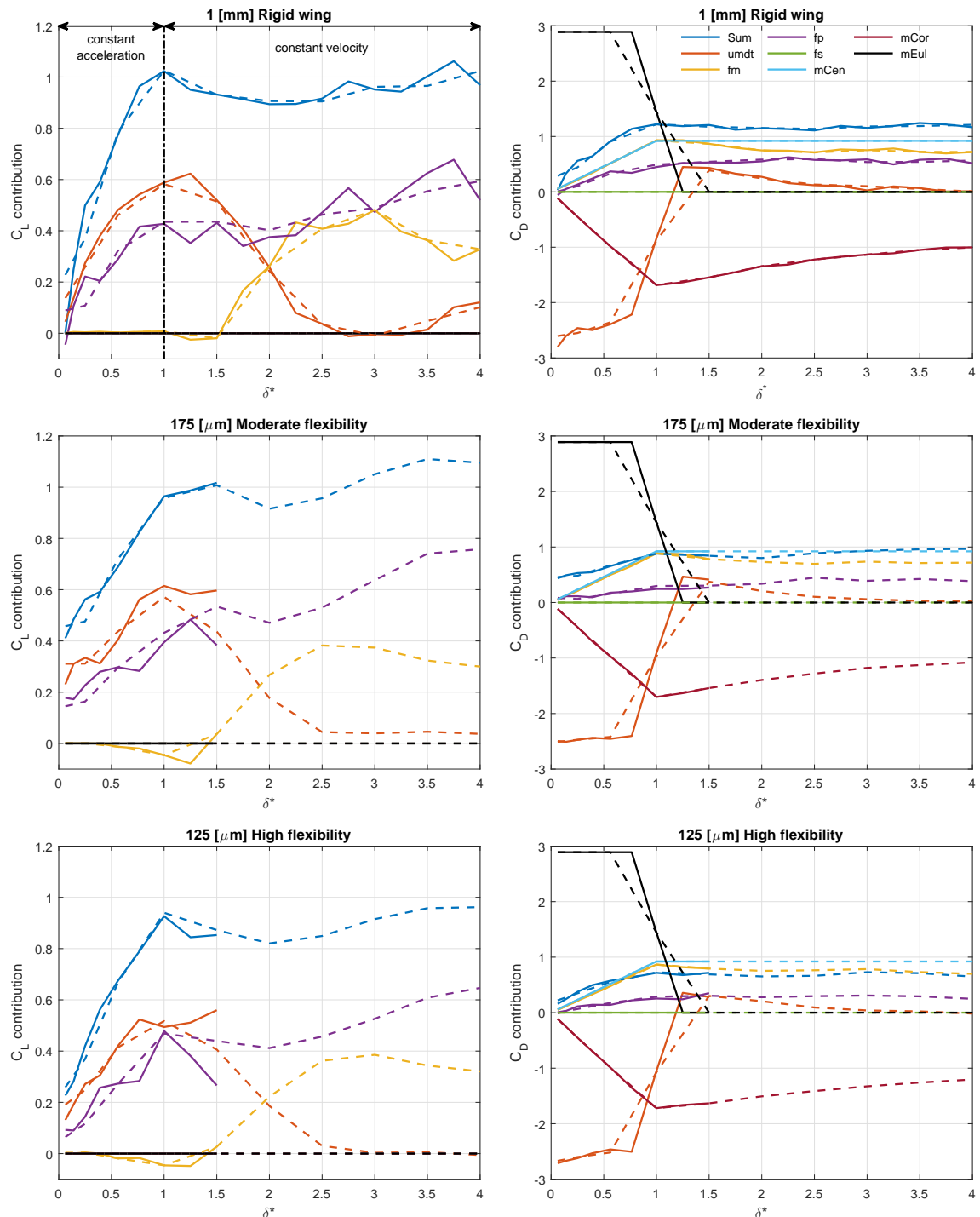


Figure 8.11: Temporal evolution of the reconstructed lift (left column) and drag (right column) coefficient components based on the summation of volume 1-3. Force contributions: unsteady momentum $umdt$ (I), momentum flux fm (II), pressure fp (III), viscous stress fs (III), centrifugal momentum $mCen$ (IV), Coriolis momentum $mCor$ (V) and Euler momentum $mEul$ (VI) contribution, see Equation 5.14. Solid line depicts a high temporal resolution of $TR^* = 0.25$ and the dashed line depicts a coarsened temporal resolution of $TR^* = 0.5$.

8.2.3 Sectional lift & drag coefficients

The sectional lift and drag are evaluated in control volumes placed side-by-side along the wing span with a spanwise thickness dz of 7 vectors ($0.12c$) (see Equation 5.18) and an overlap of 6 vectors. In Figure 8.12 the spanwise sectional lift coefficient distribution is given.

For $\delta^* > 0.14063$ the lift coefficients calculated from both high and coarsened temporal resolution data are in a good agreement for the different wings. At the root ($r/R = 0$) and tip ($r/R = 1$) the lift approaches zero. The trend in lift coefficient is comparable for the different wings. For $\delta^* < 1.25$ the sectional lift distribution shows a linear increase until approximately $r/R = 0.9$ which corresponds to the linear increase in rotational velocity. Subsequently, at about $\delta^* > 1.5$ a transition period is observed which correlates well with the onset of vortex breakdown after which steady-state conditions are reached at approximately $\delta^* = 4$. For the steady-state conditions the sectional lift distribution displays a smooth variation over the span with its maximum at approximately $r/R = 0.7$.

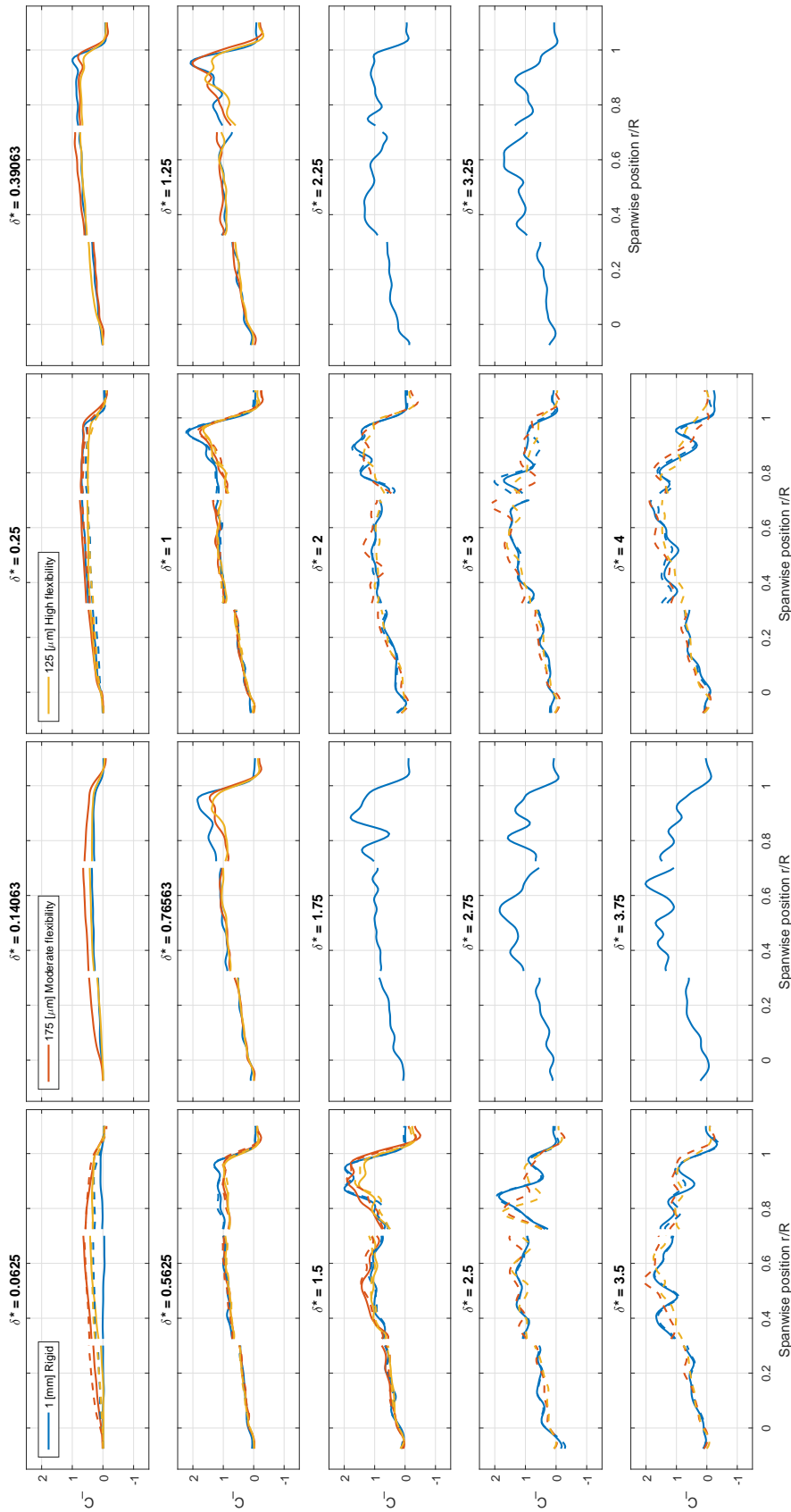


Figure 8.12: Temporal evolution of the spanwise sectional lift coefficient distribution (C_l). Solid line depicts a high temporal resolution of $\text{TR}^* = 0.25$ and the dashed line depicts a coarsened temporal resolution of $\text{TR}^* = 0.5$.

For a two-dimensional steady, incompressible and inviscid flow the sectional lift can be related to circulation using the Kutta-Joukowski theorem. However, within the framework of inviscid potential flow theory, the predicted sectional lift is expected to be relatively accurate for viscous flows as long as the flow is steady and unseparated (Anderson, 2011). The main advantage of the Kutta-Joukowski theorem is its simplicity. Also, for an incompressible flow, the Kutta-Joukowski theorem is solely related to flow fields, which can directly be obtained by PIV measurements. The Kutta-Joukowski theorem is given as,

$$l = \rho V_{\infty} \Gamma \quad (8.4)$$

where V_{∞} stands for the freestream velocity and Γ the total circulation around the wing. It should be noted in the calculation of sectional forces by use of the Kutta-Joukowski theorem (Equation 8.4), instantaneous sectional freestream velocity, which varies linearly over the span due to curvilinear motion, is used. Since the LEV carries majority of the circulation around the wing and the bound circulation is negligible, as discussed in section 7.3, it is expected that sectional lift prediction by use of the LEV circulation performs well.

In Figure 8.13 the sectional lift distribution that is based on a control volume approach, is compared with the Kutta-Joukowski theorem using the LEV circulation and total circulation in the limited domain of integration (see Figure 7.10) for $\delta^* = 0.5625, 1, 1.5$ and 4.

The sectional lift distributions that are based on the control volume approach and the Kutta-Joukowski theorem - LEV circulation show a similar trend for the different wings. However, substantially lower lift values are found for the high flexible wing using the Kutta-Joukowski theorem - total circulation, due to the decreased total circulation (see Figure 7.13). Until the end of the acceleration phase ($\delta^* < 1$) the sectional lift coefficient distribution, based on both the control volume analysis and the Kutta-Joukowski theorem, show a linear increase until approximately $r/R = 0.9$ which corresponds to the linear increase in rotational velocity. After $\delta^* = 1.5$, during the transition phase, significant differences are observed between the control volume analysis and the Kutta-Joukowski theorem. At steady-state conditions ($\delta^* = 4$), the control volume analysis shows a better match with the Kutta-Joukowski theorem - LEV circulation compared to the evaluation based on the total circulation because the control volume approach allows to capture the three-dimensional and unsteady effects. It is further noted that the control volume analysis predicts a more even lift distribution over the span with lower peak values near its maximum compared to the Kutta-Joukowski theorem.

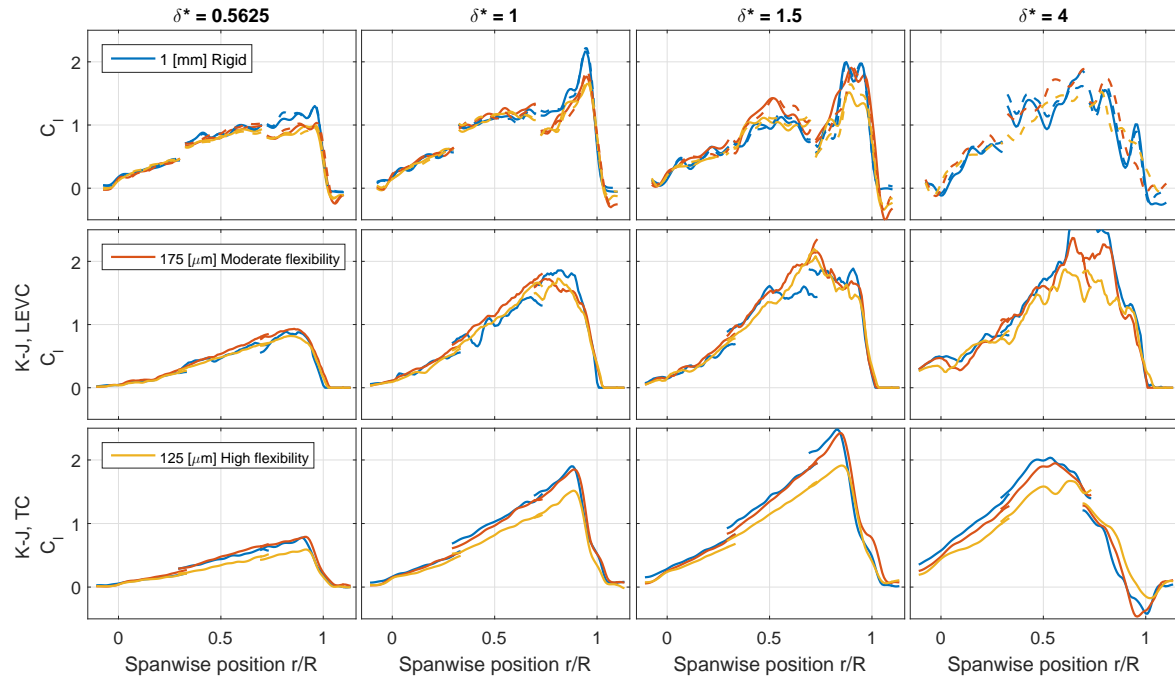


Figure 8.13: Sectional lift distribution for $\delta^* = 0.5625, 1, 1.5$ and 4 . *Top row:* Sectional lift coefficient based on control volume analysis. Solid line depicts a high temporal resolution of $TR^* = 0.25$ and the dashed line depicts a coarsened temporal resolution of $TR^* = 0.5$. *Middle row:* Sectional lift coefficient based on Kutta-Joukowski theorem using the LEV circulation (LEVC) evaluated in the complete flow field (see Figure 7.19). *Bottom row:* Sectional lift coefficient based on Kutta-Joukowski theorem using the total circulation (TC) evaluated in the limited integration region bounded by the TE of the wing (see Figure 7.13).

Subsequently, the sectional lift distribution is integrated along the span to obtain the lift coefficient of the complete wing. In Figure 8.14 the lift coefficient that is obtained from the balance data is compared with the control volume approach, and the Kutta-Joukowski theorem based on the LEV circulation and the total circulation. During the acceleration phase ($\delta^* < 1$) the Kutta-Joukowski theorem - LEV circulation shows a reasonable prediction of the lift when compared to the balance and control volume analysis. Also, the Kutta-Joukowski theorem - total circulation shows a reasonable prediction, however, significant lower values for the high flexible wing are found due to its lower predicted sectional lift distribution originating from the lower total circulation. At the start of the revolving motion the balance data shows a peak in the lift coefficient which are not observed with the Kutta-Joukowski theorem by evaluating the circulation that is created within the flow field. Also the build-up of lift is stronger compared to the Kutta-Joukowski theorem. These discrepancies can be explained by the additional non-circulatory added mass reaction force contribution in the acceleration phase which results into an additional force in the direction of lift. However, at the end of the acceleration ($\delta^* = 1$), the balance data predicts a lower lift value compared to the control volume analysis and the Kutta-Joukowski theorem. After the acceleration phase significant discrepancies are found between the predicted lift that is based on the Kutta-Joukowski theorem and the balance measurements, while the control volume approach shows a significant better agreement with the balance measurements.

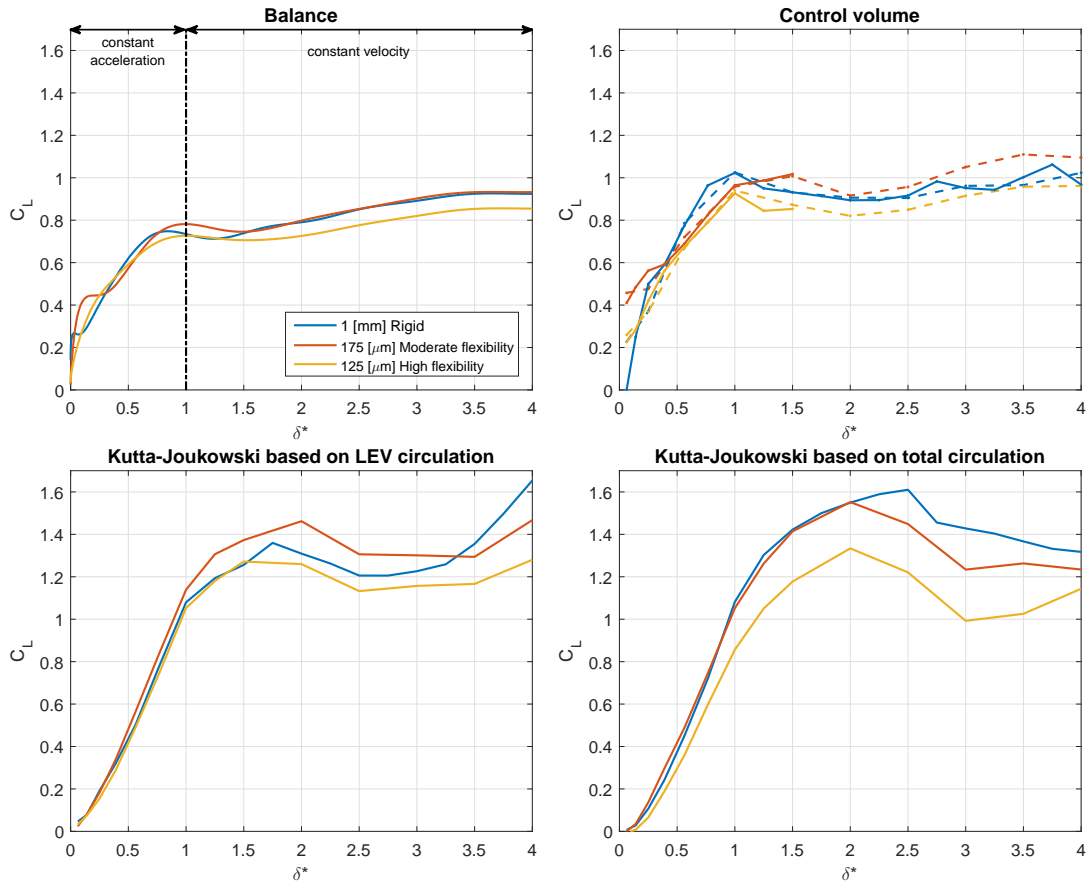


Figure 8.14: Comparison of temporal evolution of lift. *Balance*: Lift coefficient obtained from low-pass filtered balance data (see section 6.2). *Control volume*: Lift coefficient obtained from control volume analysis (see subsection 8.2.1). Solid line depicts a high temporal resolution of $TR^* = 0.25$ and the dashed line depicts a coarsened temporal resolution of $TR^* = 0.5$. *Kutta-Joukowski based on LEV circulation*: Lift coefficient obtained from the Kutta-Joukowski theorem using the LEV circulation evaluated in the complete flow field (see Figure 7.19). *Kutta-Joukowski based on total circulation*: Lift coefficient obtained from the Kutta-Joukowski theorem using the total circulation evaluated in the limited integration region bounded by the TE of the wing (see Figure 7.13).

It is concluded that the lift obtained from the circulation in the flow field by means of the Kutta-Joukowski theorem shows a reasonable agreement with the lift obtained with a control volume analysis during the early phases of the revolving motion in which the flow is rather two-dimensional (see chapter 7). The Kutta-Joukowski theorem - LEV circulation shows a better agreement with the total lift obtained from the balance data, and the sectional lift distribution obtained from the control volume analysis compared to the Kutta-Joukowski theorem - total circulation.

Birch et al. (2004) studied a steady revolving rigid wing that is based on a *Drosophila* wing planform at an angle of attack of 45 deg for the Reynolds numbers of 120 and 1,400. The Kutta-Joukowski theorem was evaluated to predict the sectional lift. It was concluded that the maximum sectional lift for the Reynolds number of 1,400 occurs at approximately $0.65r/R$ (see Figure 2.9), which is also observed in the current study. Inboard of the position of the maximum sectional lift coefficient, an approximate linear increase along the span was reported by Birch et al. (2004), which is also in agreement with the current observations. However, Birch et al. (2004) found a negative sectional lift of approximately half of the maximum positive sectional lift near the tip of the wing for the Reynolds number of 1,400, while in the current study the sectional lift is close to zero at the tip.

Garmann & Visbal (2014) numerically studied a rigid revolving rectangular wing at an angle of attack of 60 deg and a Reynolds number of 1,000 for an aspect ratio of 2. The spanwise distribution of the sectional lift coefficient for steady-state values (270 deg) is approximately similar to the sectional lift coefficient distribution found in this study. The maximum peak is also found at approximately the same spanwise location, at $r/R = 0.7$ (see Figure 2.9). However, differences are observed. Garmann & Visbal (2014) found that close to the root, at approximately $r/R = 0.05$, a peak in the lift coefficient followed by a dip, while in the current study a more continuous linear increase is observed along the span. Furthermore the sectional lift distribution reported by Garmann & Visbal (2014) displays a less-oscillatory behaviour. This may be due to the fact that the Reynolds number is lower, resulting into more coherent structures and less smaller fragmented scale structures. Also, this can be caused by the limited temporal resolution or the experimental uncertainties in the current study.

Although the Kutta-Joukowski theorem has been used to estimate the lift generation in the context of flapping-wing aerodynamics, it does not always give satisfactory results, as reviewed in (Wang et al., 2013). Wang et al. (2013) proposed a sectional lift formula to estimate the lift in highly unsteady and separated flows associated with flapping-wing flight. The lift formula was derived by neglecting the total pressure and viscous stress terms on the outer boundary from the integral momentum balance of the Navier-Stokes equation within a control volume. The presented lift formula is based on the vorticity and velocity information on a freestream (chordwise) orientated plane. In this respect the Kutta-Joukowski theorem is a reduced form of the derived lift formula which neglects the vortex force and unsteady inertial effect contribution. In this study two-dimensional DNS calculations for a flapping flat-plate pitching and heaving wing were performed. It was found that the application of the Kutta-Joukowski theorem as a quasi-steady model to unsteady low Reynolds number flows might cause errors in the prediction of the phase, amplitude and waveform of the unsteady lift of a flapping wing. In the current study the reconstructed sectional lift and drag was calculated means of a control volume analysis. Although the lift formula derived in (Wang et al., 2013) might

give a better estimate in the acceleration phase where the flow is rather two-dimensional, it is expected that the three-dimensional contributions within the control volume approach are required to accurately estimate the lift when the revolving motion further progresses. Moreover, due to the limited field of view in the current study, vortical structures are present near the upper and lower boundary of the domain such that steady-state conditions are less well defined. As a result, it is expected that the total pressure term cannot be neglected and the pressure term contribution needs to be taken into account for an accurate estimate of the lift when the field of view is limited.

In Figure 8.15 the spanwise sectional drag coefficient distribution is given. It can be seen that for $\delta^* > 0.14063$ the sectional drag coefficient calculated based on the temporally coarsened data matches the high temporal resolution well over the complete span for the different wings. In general it can be observed that the sectional drag decreases with decreasing flexural stiffness. Similar to the sectional lift distribution, the sectional drag increases approximately linearly with span until $r/R = 0.9$ for $\delta^* < 1,25$. Subsequently, a transition phase is observed, after which steady-state conditions are reached. For steady-state conditions the drag is distributed smoothly over the span with its maximum at approximately $r/R = 0.7$. The significant decrease in drag with decreasing flexural stiffness is most pronounced for $r/R > 0.3$. Consequently, within the significantly expanded LEV bubble-like structure outboard of midspan ($r/R > 0.5$), a significant decrease of sectional drag is found for decreasing flexural stiffness. This is caused due to the significantly reduced pressure drag (see Figure 8.16). Slightly outward of the tip a significant negative sectional drag coefficient peak is observed for both flexible wings.

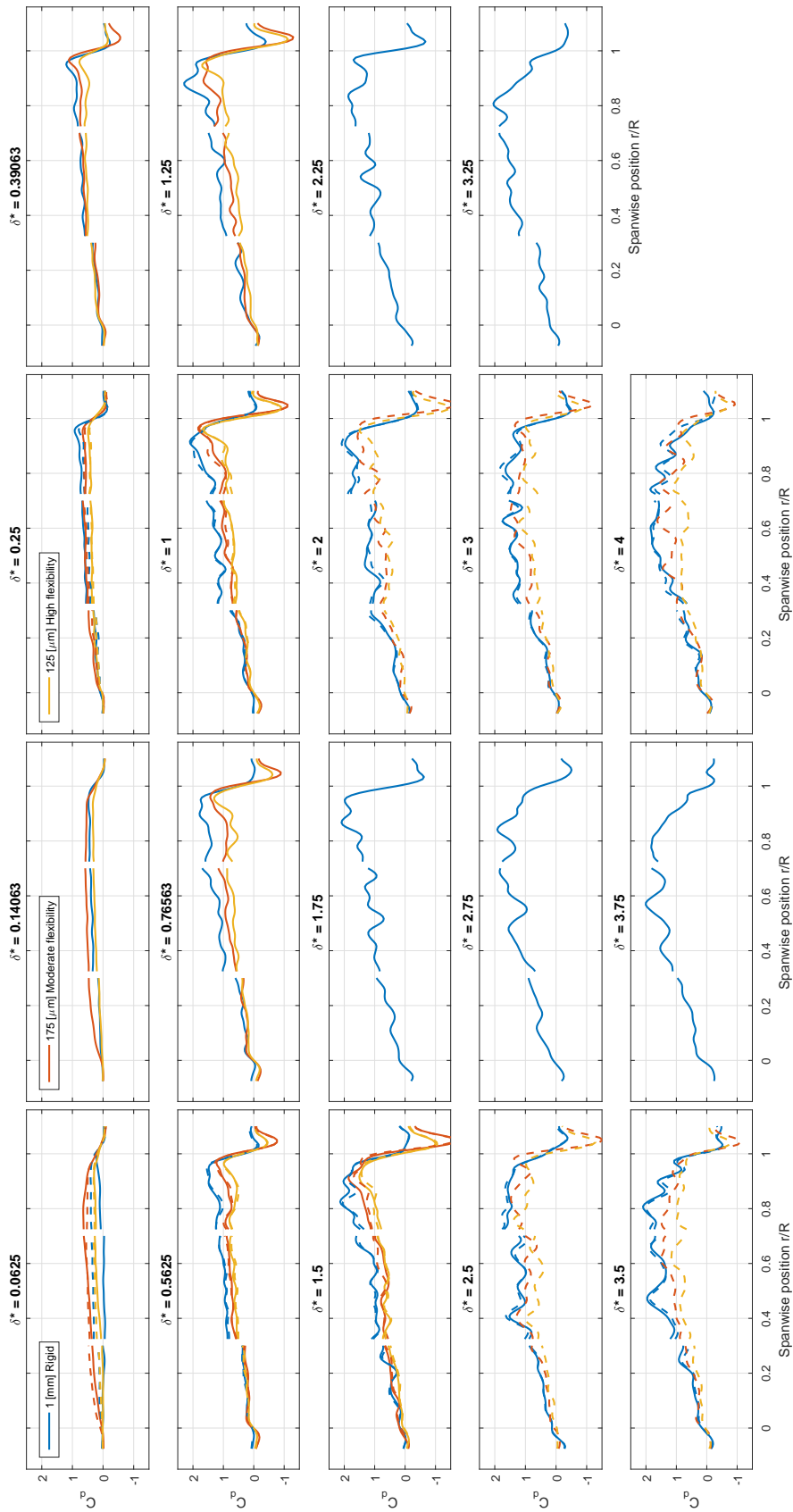


Figure 8.15: Temporal evolution of the spanwise sectional drag coefficient distribution (C_d). Solid line depicts a high temporal resolution of $TR^* = 0.25$ and the dashed line depicts a coarsened temporal resolution of $TR^* = 0.5$.

In Figure 8.16 the contributions of different terms in the calculation of the sectional lift and drag coefficients are shown for the steady-state conditions. The oscillatory behavior in the sectional lift and drag distribution mainly originate from the momentum flux contribution (fm). The pressure term contribution (fp) for the sectional lift increases with spanwise position until approximately $r/R = 0.7$ after which it decreases to zero at the tip. The corresponding magnitude of the pressure term contribution in the direction of lift is comparable for the different wings. The pressure term distribution for the sectional drag is approximately zero until $r/R=0.15, 0.225, 0.3$ for respectively the rigid, moderate flexible and high flexible wing. Subsequently, further outboard, the pressure term contribution increases and reaches a maximum at approximately $r/R = 0.6$. For decreasing flexural stiffness this pressure drag contribution is significantly attenuated at the spanwise locations which correspond to the spanwise locations of the significantly expanded LEV bubble-like structure. This agrees well with the reduced size of the wake for the flexible wings (see Figure 8.2). Moreover, these observations are in good agreement with the smaller size of low pressure region accompanying the LEV for decreasing flexural stiffness (see Figure 8.1). As a result, the total force acting on the wing is reduced, but also tilted more towards the direction of lift due to the wing deformation. Consequently, at the spanwise locations of the expanded LEV bubble-like structure, the pressure term contribution in the direction of lift remains relatively high, while its contribution in the direction of drag is significantly decreased. The Coriolis component ($mxCor$) has a more negative drag contribution with decreasing flexural stiffness over the complete span of the wing. This implies that the volume integral of spanwise velocities within these sectional control volumes is decreased over the complete wing span. Finally, the negative sectional drag coefficient peak that is found slightly outboard of the tip, is caused by the high negative momentum flux contribution.

The integrated sectional lift and drag values over all spanwise positions are comparable to the results given in Figure 8.11 when non-dimensionalized as given in Equation 5.18. The small discrepancies in absolute values mainly originate from the momentum flux contribution.

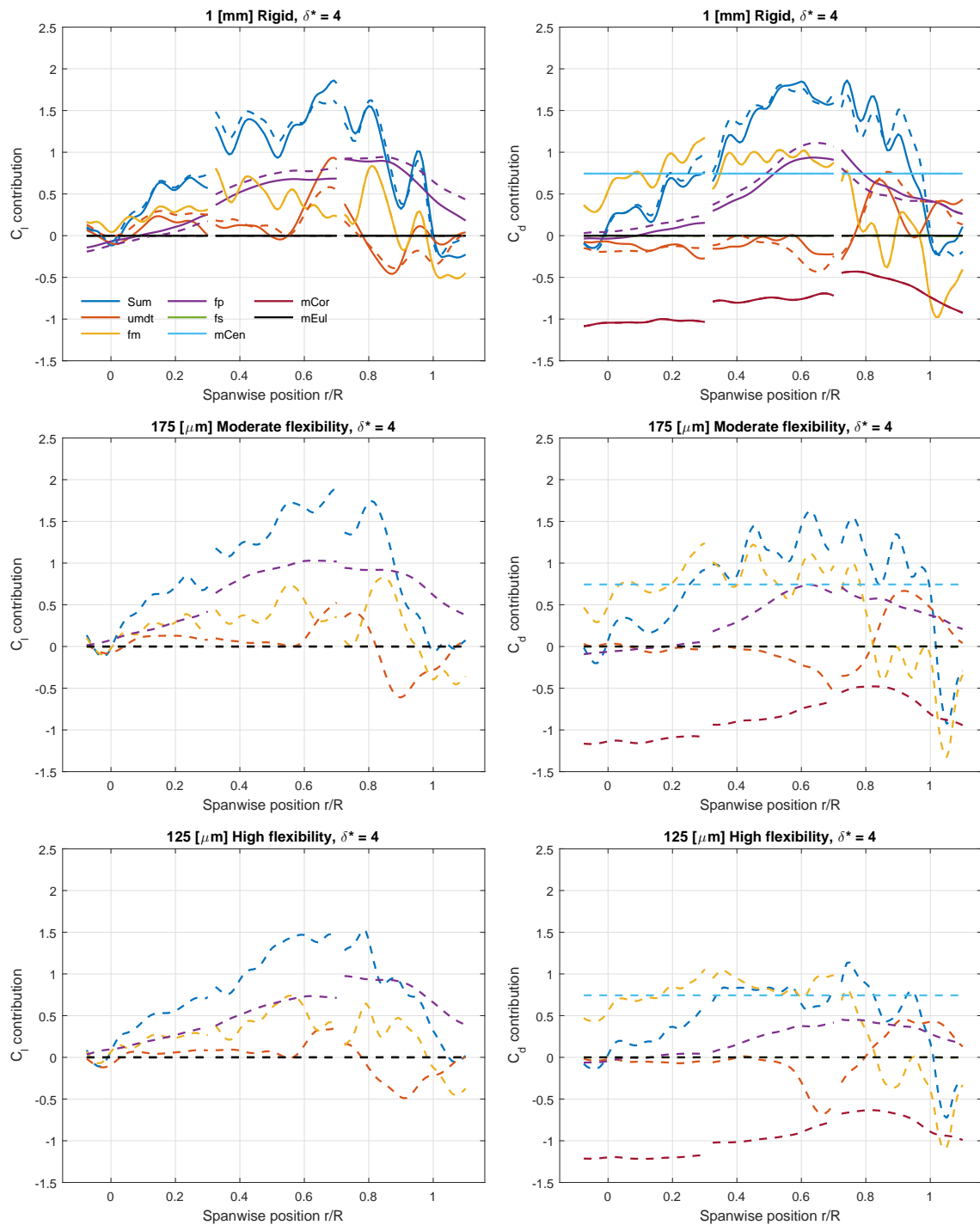


Figure 8.16: Temporal evolution of the spanwise sectional lift (left column) and drag (right column) coefficient distribution components at steady-state conditions ($\delta^* = 4$). Force contributions: unsteady momentum $umdt$ (I), momentum flux fm (II), pressure fp (III), viscous stress fs (III), centrifugal momentum $mCen$ (IV), Coriolis momentum $mCor$ (V) and Euler momentum $mEul$ (VI) contribution, see Equation 5.14. Solid line depicts a high temporal resolution of $TR^* = 0.25$ and the dashed line depicts a coarsened temporal resolution of $TR^* = 0.5$.

Spanwise centroid of lift & drag The spanwise centroid for lift and drag along the span is calculated as,

$$\text{Spanwise centroid of } C_l = \frac{\int r C_l dr}{\int C_l dr} \quad ; \quad \text{Spanwise centroid of } C_d = \frac{\int r C_d dr}{\int C_d dr} \quad (8.5)$$

The spanwise centroid of the lift and drag represent the spanwise locations at which the resultant lift and drag reproduce the same moment about the root of the wing. In Figure 8.17 the temporal evolutions of the spanwise centroid for lift and drag are given.

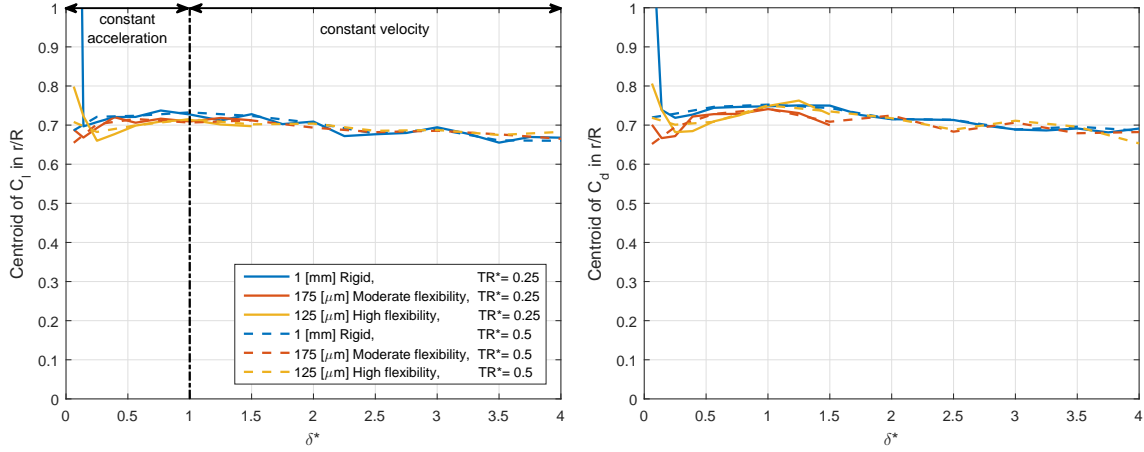


Figure 8.17: Temporal evolution of the spanwise centroid for the lift (left column) and drag (right column). Solid line depicts the low pass filtered balance data and the dashed line depicts the reconstructed data with a coarsened temporal resolution of $TR^*=0.5$.

It can be observed that the spanwise centroid for lift and drag is approximately equal to $r/R = 0.7$ for the different wings and for the full revolving motion. Until approximately the onset of vortex breakdown, for $\delta^* < 2$, the spanwise centroid for lift and drag are located a bit more towards the root for the flexible wings compared to the rigid wing. The spanwise centroid in this study may be interpreted as the spanwise center of pressure. This observations may simplify the modeling of revolving wings at relatively high angles of attack, since the spanwise centroid for lift and drag is approximately constant during the complete revolving motion for different chordwise flexible wings.

The steady-state spanwise centroid of lift and drag are similar to the spanwise pressure center obtained by the balance measurements at greater chord lengths of travel, see Figure 6.12. Contrary to the spanwise centroid of lift and drag, the spanwise pressure center obtained by the balance measurement is located significantly more outboard in the early phases of the revolving motion.

8.3 Summary of the spanwise characteristics in terms of the LEV properties and sectional force coefficients for $\delta^* = 1, 1.5$ and 4

In Figure 8.18 the spanwise distribution of the LEV circulation, LEV vorticity flux, LEV centroid, LEV pressure centroid and sectional lift & drag coefficients for $\delta^* = 1, 1.5$ and 4 are given.

Until the end of the acceleration period ($\delta^* = 1$) all wings display very similar characteristics in terms of the LEV properties and sectional force coefficients. Subsequently, at about $\delta^* > 1.5$ a transition period appears to occur which correlates with the onset of vortex breakdown. Finally, at approximately $\delta^* = 4$, the spanwise distribution is settled and approximate steady-state conditions are reached. The LEV circulation at ($\delta^* = 1$) is similar for the different wings and shows a linear increase of circulation with spanwise position until $r/R = 0.9$ which is associated with the increase in rotational velocity due to the curvilinear nature of the motion, after which it decreases to zero at the tip. At steady-state conditions ($\delta^* = 4$), the circulation inboard of midspan ($r/R < 0.5$) is similar for the different wings, while outboard of midspan the circulation is decreased significantly with decreasing flexural stiffness. For $\delta^* < 1$ there is little spanwise transport of vorticity within the LEV and the flow behaves two-dimensional. Subsequently, there is a very strong increase of positive spanwise vorticity flux, followed by a transition period after which a constant positive spanwise distribution of spanwise advection of vorticity within the LEV is reached at $\delta^* = 4$. Furthermore, it can be noted that the spanwise advection of vorticity within the LEV is stronger for the flexible wings compared to the rigid wing. The LEV centroid and the LEV pressure centroid have a high correlation for the different flexibilities with the most pronounced difference near the tip at $\delta^* = 4$. This agreement between the LEV and pressure centroid positions is in accordance with Figure 8.1 and Figure 8.3 in which the LEV structure correlates well with the low pressure region. It can be observed that the LEV pressure centroid is located significantly closer to the wing surface for decreasing flexural stiffness. This is most pronounced outboard of midspan ($r/R > 0.5$) at $\delta^* = 4$ and correlates with the observations of the spanwise pressure fields, as depicted in Figure 8.1. The aft tilt of the LEV is approximately similar for the different flexibilities, except near the tip ($r/R > 0.6$) at $\delta^* = 4$, which corresponds with the bubble-like structure, at which the LEV is tilted less aft with decreasing flexural stiffness. The sectional lift and drag at the end of the acceleration ($\delta^* = 1$) show a linear increase with spanwise position until approximately $r/R = 0.9$ which correlates with the increase in rotational velocity and LEV circulation. The spanwise oscillations in the sectional lift and drag mainly originate from the momentum flux contribution in the calculations based on the control volume approach. While the sectional lift for the different wings is comparable, a significant decrease in sectional drag can be observed with decreasing flexural stiffness. These observations are in accordance with the behavior of the total forces as determined by the balance measurements (see Figure 6.8). While the sectional drag inboard of $r/R = 0.3$ is approximately similar for the different wings, the sectional drag considerably decreases with the flexural stiffness at the outboard locations. The spanwise centroids of the lift and drag are located at approximately 70% of the span for all the cases throughout the complete motion.

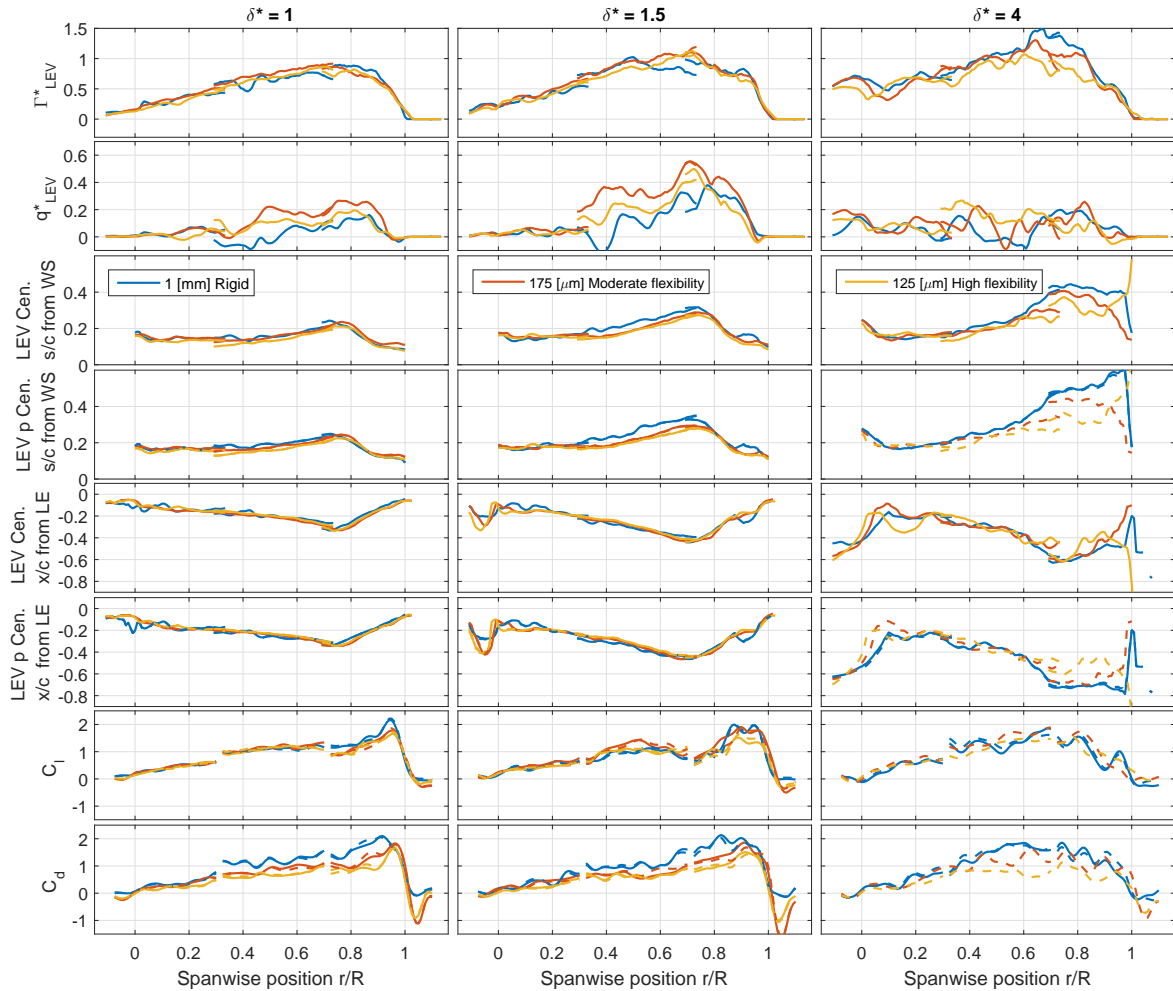


Figure 8.18: Spanwise characteristics for $\delta^* = 1, 1.5$ and 4 . From the top to bottom row respectively: LEV circulation (Γ_{LEV}^*), LEV vorticity flux (q_{LEV}^*), LEV centroid chord distance (s/c) normal to wing surface (WS), LEV pressure centroid chord distance (s/c) normal to wing surface (WS), LEV centroid chord distance in the x -direction (x/c) from leading edge (LE), LEV pressure centroid chord distance in the x -direction (x/c) from leading edge (LE), Sectional lift coefficient (C_l) and Sectional drag coefficient (C_d) as a function of spanwise position along the span (r) non-dimensionalized with the span length (R). The LEV region is considered as the region for which $\gamma_2 > 2/\pi$ (see section 7.1) evaluated in the complete flow field. The sectional control volumes have a spanwise thickness of $dz = 7$ vectors and an overlap of 6 vectors. For the LEV pressure centroid and the sectional lift & drag, the solid line depicts a temporal resolution of $TR^* = 0.25$ and the dashed line depicts a coarsened temporal resolution of $TR^* = 0.5$

8.4 Conclusion

At low Reynolds numbers the flow field is highly repeatable, notably for the initial development phase of the flow considered in the present experiments, which allows obtaining temporal information from phase-locked measurements. The pressure field and loads have been reconstructed successfully from ensemble averaged phase-locked tomographic PIV measurements for different flexible wings, employing the non-inertial moving reference frame of the rotating wing. Furthermore, the pressure field that covers a complete wing has been successfully reconstructed from three volumes that have been measured independently, which allowed a proper comparison of pressure fields between different wings.

Pressure field The vortex system structures encompass a low pressure region which has a high correlation with the vortical structures identified by the Q-criterion. As a result a comparative assessment between the different wings regarding the size of the low pressure zone associated to the LEV as well as the size of the wake can be made on the basis of the Q-criterion.

The LEV pressure centroid correlates well with the LEV centroid. Consequently, the center of the LEV suction peak can be approximated with the LEV center. The LEV pressure centroid location is similar for the different wings in absolute sense. However, due to the deflection of the flexible wings, the LEV pressure centroid is located closer to the wing surface. As the low pressure region accompanying the LEV becomes smaller with increasing flexibility, the total force acting on the wing is reduced, but it is also tilted more towards the lift direction due to the wing deformation. As a consequence, the lift component remains relatively high, also because the suction peak is located closer to the wing surface. Simultaneously, the drag is significantly suppressed for increasing flexibility, which is also reflected in the smaller size of the wake.

The process of vortex breakdown correlates well with the formation of a positive spanwise pressure gradient which is indicative of an inboard acceleration of a particle in the flow field. As the outboard moving particles experience an adverse pressure gradient accompanied by an inboard acceleration, the spanwise advection of vorticity is decreased and vorticity is accumulated in a given plane, which can eventually lead to the burst of the vortical structure. Early in the revolving motion a region of negative pressure gradient is formed at the suction side of the wing. At the onset of vortex breakdown, near midspan ($r/R = 0.5$), a region of positive pressure gradient is formed near the LE at the suction side of the wing. Also a region of positive pressure gradient is formed near the tip above the region of negative pressure gradient. Subsequently, the region of positive pressure gradient around midspan starts expanding. Simultaneously the region of positive pressure gradient near the tip connects with the region of positive pressure gradient that is formed at midspan. Both regions start merging until a region of positive and negative pressure gradient is formed at respectively the outboard and inboard part of the wing for steady-state conditions. For decreasing flexural stiffness the relative region of negative pressure gradient at the suction side of the wing surface is extended more towards tip of the wing, which may account for the enhanced spanwise advection of vorticity and the increased stability of the LEV.

The negative spanwise pressure gradient that is formed during the revolving motion has a high correlation with the location of the LEV core and the strong levels of spanwise transport of vorticity. This transport of vorticity is driven by an outboard spanwise velocity and stabilizes the LEV. The spanwise velocities outside the LEV core are likely to stem from the centrifugal effects. Also a region of negative pressure gradient in x -direction is formed which has a high correlation with the LEV, and is likely to be responsible for the stability of the LEV and its close distance to the wing surface.

Loads Although the absolute values for the reconstructed loads do not exactly match the balance measurements, the relative differences between the wings show a high agreement with the corresponding relative differences of the balance measurements. The most pronounced difference between the reconstructed loads and the balance measurements are the lift & drag coefficient peaks near the end of the acceleration which are approximately equal to the steady-state value for the reconstructed loads, while significantly lower for the balance measurements.

Based on a control volume analysis the lift is relatively high for decreasing flexural stiffness due to the relatively high pressure term contribution. The drag is significantly reduced with decreasing flexural stiffness due to the decreased pressure term and Coriolis term contributions. While the sectional lift distribution remains comparable for the different wings after the onset of vortex breakdown, a significant decrease of sectional drag is found for decreasing flexural stiffness at the outboard wing locations. These locations of reduced drag correspond to the spanwise locations in which the LEV is significantly expanded. For steady-state conditions the sectional lift and drag distribution varies smoothly over the span with its maximum at approximately $r/R = 0.7$. The pressure term contribution for the sectional lift increases with spanwise position until approximately $r/R = 0.7$, after which it decreases to zero at the tip. The pressure term distribution for the sectional drag is approximately zero until $r/R = 0.15, 0.225, 0.3$ for respectively the rigid, moderate flexible and high flexible wing. Subsequently, further outboard, the pressure term contribution increases and reaches a maximum at approximately $r/R = 0.6$. The decreased sectional drag at the outboard wing locations agree well with the significant decreased pressure term contributions.

The lift obtained from the Kutta-Joukowski theorem shows a reasonable agreement with the lift obtained with the control volume analysis during the early phases of the revolving motion in which the flow behaves two-dimensional (approximately until the end of the acceleration phase). The Kutta-Joukowski theorem that is based on the LEV circulation shows a better agreement with the total lift obtained from the balance data and the sectional lift distribution obtained from the control volume analysis compared to the Kutta-Joukowski theorem that is based on the total circulation.

The spanwise centroid for lift and drag is approximately equal to $r/R = 0.7$ for all wings and for the full revolving motion, which may simplify the modeling of revolving wings.

Conclusions & Recommendations

To improve the understanding of the effect of wing flexibility on the aerodynamic performance of biological flapping-wing flight, chordwise flexible revolving wings have been extensively studied. In the present chapter, conclusions of this thesis are given, after which recommendations for further studies in line with the present investigation are summarized.

9.1 Conclusions

The flow fields and fluid-dynamic loads generated by revolving low-aspect-ratio flat-plate wings with different degree of chordwise flexibility are experimentally studied using tomographic PIV and simultaneous force measurements. Three different wings were tested in the experiments in order to investigate the influence of wing flexibility: a rigid wing from 1 mm thick Plexiglas, a moderately flexible wing from 175 μm PET and a highly flexible wing from 125 μm PET.

The force measurements reveal that during the acceleration phase the build-up of lift is similar for the different wings, while the build-up of drag is significantly lower for decreasing flexural stiffness. At steady-state conditions the net resultant force generation is decreased significantly with decreasing flexural stiffness. However, this does not adversely affect the lift generation such that the lift coefficients for the rigid and the moderate wings are very similar, while it is only slightly (about 7%) smaller for the high flexible wing. On the other hand, the drag decreases monotonically with decreasing flexural stiffness, up to 36% for the most flexible wing. As a result the most flexible wing has an increased lift-to-drag ratio of approximately 45% and an increased power efficiency of 40%. It is further found that for the chordwise flexible wing configurations considered in this study, the lift-to-drag ratio at the steady-state conditions correlates well with the geometric angle of attack of the deformed structure near the wing tip. Moreover, it is shown that a rigid wing with a geometric angle of attack identical to that of the deformed wing generates similar lift and drag. This suggests

that the geometric angle of attack at steady-state conditions is dominant for the lift and drag generated by chordwise flexible wings considered in this study. This may significantly simplify the modeling of flexible revolving wings, since the aerodynamic forces can be approximated based on a rigid revolving wing model.

A similar vortex system, comprising LEV, TV, RV and starting TEV components, are observed in all cases. With increased wing deformation the TV is located more upwards while the spanwise position is maintained. Also, the TV and starting vortex are more elongated in the streamwise direction for the flexible cases. For decreasing flexural stiffness, the coherency of this vortex system is increased. At greater phases of the revolving motion vortex breakdown occurs for all wings. Near midspan, for $\delta^* = 1.5$, the core of the LEV structure is lifted off and expanded into a substantial bubble-like structure that grows in size along the span until about 75% of the span length which is indicative of vortex breakdown. For increased wing flexibility the TV and LEV are confined to a smaller region within the flow field, of which the reduced size of the LEV is especially pronounced in the significantly expanded LEV structure. Furthermore, the LEV structure of the flexible wings has an increased spanwise vorticity flux distribution compared to the rigid wing and shows higher helical density values that are indicative of an outboard spanwise vorticity flux along the axis of the LEV which are associated with the spanwise transport of vorticity contributing to the stability and retention of the LEV.

At low Reynolds numbers the flow field is highly repeatable, notably for the initial development phase of the flow considered in the present experiments, which allows obtaining temporal information from phase-locked measurements. The pressure field and loads have been reconstructed successfully from ensemble averaged phase-locked tomographic PIV measurements for different flexible wings, employing the non-inertial moving reference frame of the rotating wing. Furthermore, the pressure field that covers a complete wing has been successfully reconstructed from three volumes that have been measured independently, which allowed a proper comparison of pressure fields between different wings. With the increased dominance of rotation in the rotating reference frame compared to the inertial reference frame, the Eulerian based material derivative performed best to reconstruct the pressure fields and loads. The vortex system structures encompass a low pressure region which has a high correlation with the vortical structures identified by the Q-criterion. As a result a comparative assessment between the different wings regarding the size of the low pressure zone associated to the LEV as well as the size of the wake can be made on the basis of the Q-criterion. Although the absolute values for reconstructed loads do not exactly match the balance measurements, the relative differences between the wings show a high agreement with the corresponding relative differences of the balance measurements. Based on the control volume analysis, the lift is relatively high for decreasing flexural stiffness due to the relative high pressure contribution, while the significant decrease in drag is caused by the decreased pressure and Coriolis term contributions. During the early phases of the revolving motion, in which the flow behaves two-dimensional, the lift obtained from the Kutta-Joukowski theorem shows a reasonable agreement with the reconstructed loads.

The process of vortex breakdown correlates well with the formation of a positive spanwise pressure gradient which is indicative for an inboard acceleration of a particle in the flow field. As the outboard moving particles experience an adverse pressure gradient accompanied

by an inboard acceleration, the spanwise advection of vorticity is decreased and vorticity is accumulated in a given plane, which can eventually lead to the burst of the vortical structure. Early in the revolving motion a negative pressure gradient is formed at the suction side of the wing that agrees well with the location of the LEV core, and drives the high spanwise transport of vorticity of the LEV structure. At the onset of vortex breakdown, near midspan, a region of positive pressure gradient is formed near the LE at the suction side of the wing. Subsequently, this region starts expanding. At steady-state conditions a region of positive and negative pressure gradient is present at respectively the outboard and inboard part of the wing. For decreasing flexural stiffness the relative region of negative pressure gradient at the suction side of the wing surface is extended more towards tip of the wing, which may account for the enhanced spanwise advection of vorticity and the increased stability of the LEV.

Due to the same predefined local angle of attack of 45 deg at the leading edge for the different wings, the circulation of the flexible wings is relatively high and over a large extent of the span and revolving motion similar to that of the rigid wing. The LEV pressure centroid correlates well with the LEV centroid. Consequently, the center of the LEV suction peak can be approximated with the LEV center. The LEV pressure centroid location is similar for the different wings in absolute sense. However, due to the deflection of the flexible wings, the LEV pressure centroid is located closer to the wing surface. Additionally, it was found that the chordwise location of the center of pressure is located closer to the LE of the wing for decreasing flexural stiffness. As the low pressure region accompanying the LEV becomes smaller with increasing flexibility, the total force acting on the wing is reduced, but it is also tilted more towards the lift direction due to the wing deformation. As a consequence, the lift component remains relatively high, also because the suction peak is located closer to the wing surface. Simultaneously, the drag is significantly suppressed for increasing flexibility, which is also reflected in the smaller size of the wake. While the sectional lift along the full span is comparable for the different wings, the sectional drag is significantly reduced for increasing flexibility at the outboard wing locations. These locations of reduced drag correspond to the spanwise locations in which the LEV is significantly expanded. The corresponding spanwise centroids of lift and drag are located at approximately 70% of the span for all the cases throughout the complete revolving motion, which may simplify the modeling of revolving wings in the context of flapping-wing flight.

9.2 Recommendations for future work

This study shows that the lift-to-drag ratio of three wings with different degree of chordwise flexural stiffness at steady-state conditions correlates well with the geometric angle of attack of the deformed structures near the tip. To further investigate this relation an increased range of chordwise flexural stiffness should be tested. Moreover, this study suggests that the geometric angle of attack is dominant for the lift and drag of these chordwise flexible wings. Therefore, the lift and drag of a rigid revolving wing with the same kinematic parameters, planform, Rossby number and Reynolds number at steady-state conditions should be acquired over a range of angles of attack that match the range of geometric angle of attack of the chordwise flexible wings. Consequently, the lift and drag of the rigid wing that revolves at the identical

geometric angle of attack of a broad range of chordwise flexible wings can be investigated in more detail.

During the pressure reconstruction a mask is build around the airfoil to obtain converged lift and drag values. Subsequently, this pressure field can be used as a Dirichlet boundary condition to further reconstruct the pressure field towards the wing surface. Alternatively, the flow field can be divided into sub-domains based on the quality of the measurement data (Tronchin et al., 2015) to further reconstruct pressure information towards the wing surface. Consequently, the loads can be verified by integrating the pressure forces around the wing surface and comparing them with the balance data and reconstructed loads that are based on a control volume approach. Also, the loads can be verified by analytically eliminating the pressure from the Navier-Stokes momentum equations and expressing the loads in pure kinematic flow characteristics (Noca et al., 1999; DeVoria et al., 2014). Additionally, the loads can be validated using a numeral fluid-structure interaction simulation.

Within this experimental study the main focus was on the tomographic PIV measurements and to a lesser extent on the wing reconstruction. By performing dedicated measurements for the wing reconstruction, a more accurate representation of the wing can be obtained. As a result, the relation between the lift-to-drag ratio and the geometric angle of attack near the tip of the wing can be studied in more detail. Moreover, this allows to further investigate the dominance of the geometric angle of attack on the resultant lift and drag for chordwise flexible wings. Additionally, a smaller mask around the wing for the pressure reconstruction can be created because the location of the vectors with a relatively high uncertainty in proximity of the wing can be more accurately estimated.

The flow field in the current study is expected to be incompressible and divergence free. However, when reconstructing the pressure field under the assumption of divergence-free flow an incorrect pressure field is obtained. By means of a Helmholtz decomposition the divergence-free part of the velocity field can be extracted. Subsequently, the pressure field and loads can be reconstructed with the divergence free part of the velocity field. Consequently, the sensitivity of a divergence-free flow field assumption in the reconstruction of pressure fields and loads from PIV based measurements can be investigated in more detail.

Finally, the effect of wing flexibility can be extended to other inherent unsteady aerodynamic mechanisms in the context of biological flapping-wing flight such as the clap and fling effect, and the effect of wake capture. In these unsteady aerodynamic mechanisms, in which rapid stroke reversal mechanisms play an important role, wing flexibility is also thought to be important in the enhancement of the aerodynamic forces (Mountcastle & Daniel, 2009; Eldredge et al., 2010; Beals & Jones, 2015). By further studying the effect of chordwise flexibility more insights will be gained into biological flapping-wing flight which can lead to the design of more efficient MAVs.

Bibliography

- Anderson, J. (2011). *Fundamentals of Aerodynamics*. Anderson series. McGraw-Hill.
- Baur, T. & Kongeter, J. (1999). PIV with high temporal resolution for the determination of local pressure reductions from coherent turbulence phenomena. In *Proceedings of the Third International Workshop on PIV*. Hosted by the University of California, Santa-Barbara.
- Beals, N. & Jones, A. R. (2015). Lift Production by a Passively Flexible Rotating Wing. *AIAA Journal*, 53(10), 2995–3005.
- Birch, J. M. & Dickinson, M. H. (2001). Spanwise flow and the attachment of the leading-edge vortex on insect wings. *Nature*, 412(6848), 729–733.
- Birch, J. M., Dickson, W. B., & Dickinson, M. H. (2004). Force production and flow structure of the leading edge vortex on flapping wings at high and low reynolds numbers. *Journal of Experimental Biology*, 207(7), 1063–1072.
- Bross, M. & Rockwell, D. (2015). Three-dimensional flow structure along simultaneously pitching and rotating wings: effect of pitch rate. *Experiments in Fluids*, 56(4), 82.
- Carr, Z. R., Chen, C., & Ringuette, M. J. (2013). Finite-span rotating wings: three-dimensional vortex formation and variations with aspect ratio. *Experiments in Fluids*, 54(2), 1444.
- Carr, Z. R., DeVoria, A. C., & Ringuette, M. J. (2015). Aspect-ratio effects on rotating wings: circulation and forces. *Journal of Fluid Mechanics*, 767, 497–525.
- Charonko, J. J., King, C. V., Smith, B. L., & Vlachos, P. P. (2010). Assessment of pressure field calculations from particle image velocimetry measurements. *Measurement Science and Technology*, 21(10), 105401.
- Combes, S. a. (2003). Flexural stiffness in insect wings I. Scaling and the influence of wing venation. *Journal of Experimental Biology*, 206(17), 2979–2987.
- Dabiri, J. O., Bose, S., Gemmell, B. J., Colin, S. P., & Costello, J. H. (2014). An algorithm to estimate unsteady and quasi-steady pressure fields from velocity field measurements. *Journal of Experimental Biology*, 217(3), 331–336.

- Daniel, T. L. (2002). Flexible Wings and Fins: Bending by Inertial or Fluid-Dynamic Forces? *Integrative and Comparative Biology*, 42(5), 1044–1049.
- David, L., Jardin, T., & Farcy, a. (2009). On the non-intrusive evaluation of fluid forces with the momentum equation approach. *Measurement Science and Technology*, 20(9), 095401.
- de Kat, R. & van Oudheusden, B. W. (2012). Instantaneous planar pressure determination from PIV in turbulent flow. *Experiments in Fluids*, 52(5), 1089–1106.
- DeVoria, A. C., Carr, Z. R., & Ringuette, M. J. (2014). On calculating forces from the flow field with application to experimental volume data. *Journal of Fluid Mechanics*, 749, 297–319.
- Dickson, W. B. (2004). The effect of advance ratio on the aerodynamics of revolving wings. *Journal of Experimental Biology*, 207(24), 4269–4281.
- Eldredge, J. D., Toomey, J., & Medina, A. (2010). On the roles of chord-wise flexibility in a flapping wing with hovering kinematics. *Journal of Fluid Mechanics*, 659, 94–115.
- Ellington, C. P. (1984). The Aerodynamics of Hovering Insect Flight. II. Morphological Parameters. *Philosophical Transactions of the Royal Society B: Biological Sciences*, 305(1122), 17–40.
- Ellington, C. P., van den Berg, C., Willmott, A. P., & Thomas, A. L. R. (1996). Leading-edge vortices in insect flight. *Nature*, 384(6610), 626–630.
- Elsinga, G. E., Scarano, F., Wieneke, B., & van Oudheusden, B. W. (2006). Tomographic particle image velocimetry. *Experiments in Fluids*, 41(6), 933–947.
- Ethier, C. R. & Steinman, D. (1994). Exact fully 3d navier-stokes solution for benchmarking. *International Journal for Numerical Methods in Fluids*, 19(5), 369–376.
- Garmann, D. J. & Visbal, M. R. (2014). Dynamics of revolving wings for various aspect ratios. *Journal of Fluid Mechanics*, 748, 932–956.
- Garmann, D. J., Visbal, M. R., & Orkwis, P. D. (2013). Three-dimensional flow structure and aerodynamic loading on a revolving wing. *Physics of Fluids*, 25(3), 034101.
- Gharali, K. & Johnson, D. a. (2014). PIV-based load investigation in dynamic stall for different reduced frequencies. *Experiments in Fluids*, 55(8), 1–12.
- Graftieaux, L., Michard, M., & Grosjean, N. (2001). Combining PIV, POD and vortex identification algorithms for the study of unsteady turbulent swirling flows. *Measurement Science and Technology*, 12(9), 1422–1429.
- Green, A. & Taylor, G. (1937). Mechanism of the production of small eddies from larger ones. In *Proc. Royal Soc. A*, volume 158, (pp. 499–521).
- Gurka, R., Liberzon, a., & Hefetz, D. (1999). Computation of pressure distribution using PIV velocity data. *Workshop on Particle Image Velocimetry*, 106(2), 1–6.

- Harbig, R. R., Sheridan, J., & Thompson, M. C. (2013). Relationship between aerodynamic forces, flow structures and wing camber for rotating insect wing planforms. *Journal of Fluid Mechanics*, 730, 52–75.
- Hunt, J. C. R., Wray, A. A., & Moin, P. (1988). Eddies, stream, and convergence zones in turbulent flows. *Center for Turbulence Research Report CTR-S88*, 193–208.
- Jardin, T. & David, L. (2014). Spanwise gradients in flow speed help stabilize leading-edge vortices on revolving wings. *Physical Review E*, 90(1), 013011.
- Jardin, T. & David, L. (2015). Coriolis effects enhance lift on revolving wings. *Physical Review E*, 91(3), 031001.
- Jaw, S. Y., Chen, J. H., & Wu, P. C. (2009). Measurement of pressure distribution from PIV experiments. *Journal of Visualization*, 12(1), 27–35.
- Jeong, J. & Hussain, F. (1995). On the identification of a vortex. *Journal of fluid mechanics*, 285, 69–94.
- Jones, a. R. & Babinsky, H. (2010). Unsteady Lift Generation on Rotating Wings at Low Reynolds Numbers. *Journal of Aircraft*, 47(3), 1013–1021.
- Jones, a. R. & Babinsky, H. (2011). Reynolds number effects on leading edge vortex development on a waving wing. *Experiments in Fluids*, 51(1), 197–210.
- Jones, A. R., Medina, A., Spooner, H., & Mulleners, K. (2016). Characterizing a burst leading-edge vortex on a rotating flat plate wing. *Experiments in Fluids*, 57(4), 52.
- Kang, C.-K., Aono, H., Cesnik, C. E. S., & Shyy, W. (2011). Effects of flexibility on the aerodynamic performance of flapping wings. *Journal of Fluid Mechanics*, 689(June), 32–74.
- Kim, D. & Gharib, M. (2010). Experimental study of three-dimensional vortex structures in translating and rotating plates. *Experiments in Fluids*, 49(1), 329–339.
- Kruyt, J. W., van Heijst, G. F., Altshuler, D. L., & Lentink, D. (2015). Power reduction and the radial limit of stall delay in revolving wings of different aspect ratio. *Journal of The Royal Society Interface*, 12(105).
- Lehmann, F.-O. (2004). The mechanisms of lift enhancement in insect flight. *Naturwissenschaften*, 91(3), 101–122.
- Lentink, D. & Dickinson, M. H. (2009). Rotational accelerations stabilize leading edge vortices on revolving fly wings. *Journal of Experimental Biology*, 212(16), 2705–2719.
- Lentink, D., Dickson, W. B., van Leeuwen, J. L., & Dickinson, M. H. (2009). Leading-Edge Vortices Elevate Lift of Autorotating Plant Seeds. *Science*, 324(5933), 1438–1440.
- Liu, X. & Katz, J. (2006). Instantaneous pressure and material acceleration measurements using a four-exposure PIV system. *Experiments in Fluids*, 41(2), 227–240.
- McLean, D. (2012). *Understanding Aerodynamics: Arguing from the Real Physics*. Wiley.

- McMahon, T. (1973). Size and shape in biology elastic criteria impose limits on biological proportions, and consequently on metabolic rates. *Science*, 179(4079), 1201–1204.
- Moffatt, H. K. (1969). The degree of knottedness of tangled vortex lines. *J. Fluid Mech*, 35(1), 117–129.
- Mohebbian, A. & Rival, D. (2012). Assessment of the derivative-moment transformation method for unsteady-load estimation. *Experiments in Fluids*, 53(2), 319–330.
- Mountcastle, A. M. & Daniel, T. L. (2009). Aerodynamic and functional consequences of wing compliance. *Animal Locomotion*, 46(5), 873–882.
- Noca, F., Shiels, D., & Jeon, D. (1999). A comparison of methods for evaluating time-dependent fluid dynamic forces on bodies, using only velocity fields and their derivatives. *Journal of Fluids and Structures*, 13, 551–578.
- Ozen, C. a. & Rockwell, D. (2012). Flow structure on a rotating plate. *Experiments in Fluids*, 52(1), 207–223.
- Percin, M. & van Oudheusden, B. W. (2015a). Flow visualization and force measurements on accelerated revolving flat plates at low Reynolds numbers. In *45th AIAA Fluid Dynamics Conference*, number June, (pp. 1–12).
- Percin, M. & van Oudheusden, B. W. (2015b). Three-dimensional flow structures and unsteady forces on pitching and surging revolving flat plates'. *Experiments in Fluids*, 56(2), 1–19.
- Pines, D. J. & Bohorquez, F. (2006). Challenges Facing Future Micro-Air-Vehicle Development. *Journal of Aircraft*, 43(2), 290–305.
- Poelma, C., Dickson, W. B., & Dickinson, M. H. (2006). Time-resolved reconstruction of the full velocity field around a dynamically-scaled flapping wing. *Experiments in Fluids*, 41(2), 213–225.
- Ragni, D., van Oudheusden, B. W., & Scarano, F. (2011). Non-intrusive aerodynamic loads analysis of an aircraft propeller blade. *Experiments in Fluids*, 51(2), 361–371.
- Sane, S. P. (2003). The aerodynamics of insect flight. *Journal of Experimental Biology*, 206(23), 4191–4208.
- Scarano, F. (2013). Tomographic PIV: principles and practice. *Measurement Science and Technology*, 24(1), 012001.
- Shyy, W., Aono, H., Chimakurthi, S. K., Trizila, P., Kang, C. K., Cesnik, C. E. S., & Liu, H. (2010). Recent progress in flapping wing aerodynamics and aeroelasticity. *Progress in Aerospace Sciences*, 46(7), 284–327.
- Shyy, W., Aono, H., Kang, C., & Liu, H. (2013). *An Introduction to Flapping Wing Aerodynamics*. Cambridge Aerospace Series. Cambridge University Press.
- Tay, W. B., Percin, M., van Oudheusden, B., Bijl, H., Cetiner, O., & Unal, M. (2013). Numerical and experimental analysis of tandem flapping flight. In *43rd Fluid Dynamics Conference*, (pp. 1–24)., Reston, Virginia. American Institute of Aeronautics and Astronautics.

- Tronchin, T., David, L., & Farcy, A. (2015). Loads and pressure evaluation of the flow around a flapping wing from instantaneous 3D velocity measurements. *Experiments in Fluids*, *56*(1), 1–16.
- Usherwood, J. R. & Ellington, C. P. (2002). The aerodynamics of revolving wings i. model hawkmoth wings. *Journal of Experimental Biology*, *205*(11), 1547–1564.
- van de Meerendonk, R., Percin, M., & van Oudheusden, B. W. (2016). Three-dimensional flow and load characteristics of flexible revolving wings at low Reynolds number. In *International Symposia on Applications of Laser and Imaging Techniques to Fluid Mechanics*, number July, Lisbon.
- van Oudheusden, B. W. (2013). PIV-based pressure measurement. *Measurement Science and Technology*, *24*(3), 032001.
- van Oudheusden, B. W., Scarano, F., & Casimiri, E. W. F. (2006). Non-intrusive load characterization of an airfoil using PIV. *Experiments in Fluids*, *40*(6), 988–992.
- van Oudheusden, B. W., Scarano, F., Roosenboom, E. W. M., Casimiri, E. W. F., & Souverein, L. J. (2007). Evaluation of integral forces and pressure fields from planar velocimetry data for incompressible and compressible flows. *Experiments in Fluids*, *43*(2-3), 153–162.
- Vanyo, J. (2015). *Rotating Fluids in Engineering and Science*. Elsevier Science.
- Wang, S., Zhang, X., He, G., & Liu, T. (2013). A lift formula applied to low-Reynolds-number unsteady flows. *Physics of Fluids*, *25*(9), 093605.
- Wang, Z. J. (2007). Aerodynamic efficiency of flapping flight: analysis of a two-stroke model. *Journal of Experimental Biology*, *211*(2), 234–238.
- Westerweel, J. & Scarano, F. (2005). Universal outlier detection for PIV data. *Experiments in Fluids*, *39*(6), 1096–1100.
- White, F. (2006). *Viscous Fluid Flow*. McGraw-Hill international edition. McGraw-Hill Higher Education.
- Wolfinger, M. & Rockwell, D. (2014). Flow structure on a rotating wing: effect of radius of gyration. *Journal of Fluid Mechanics*, *755*(8), 83–110.
- Wu, J.-Z., Ma, H.-Y., & Zhou, M.-D. (2006). *Vorticity and Vortex Dynamics*. Berlin, Heidelberg: Springer Berlin Heidelberg.
- Wu, J. Z., Pan, Z. L., & Lu, X. Y. (2005). Unsteady fluid-dynamic force solely in terms of control-surface integral. *Physics of Fluids*, *17*(9).
- Zhao, L., Deng, X., & Sane, S. P. (2011). Modulation of leading edge vorticity and aerodynamic forces in flexible flapping wings. *Bioinspiration & Biomimetics*, *6*(3), 036007.
- Zhao, L., Huang, Q., Deng, X., & Sane, S. P. (2009). Aerodynamic effects of flexibility in flapping wings. *Journal of The Royal Society Interface*.

Appendix A

Time-series animation of flow structures

The time-series animations in this appendix can be accessed with the digital version of the manuscript which is available at <http://repository.tudelft.nl>

A.1 Q-criterion isosurfaces

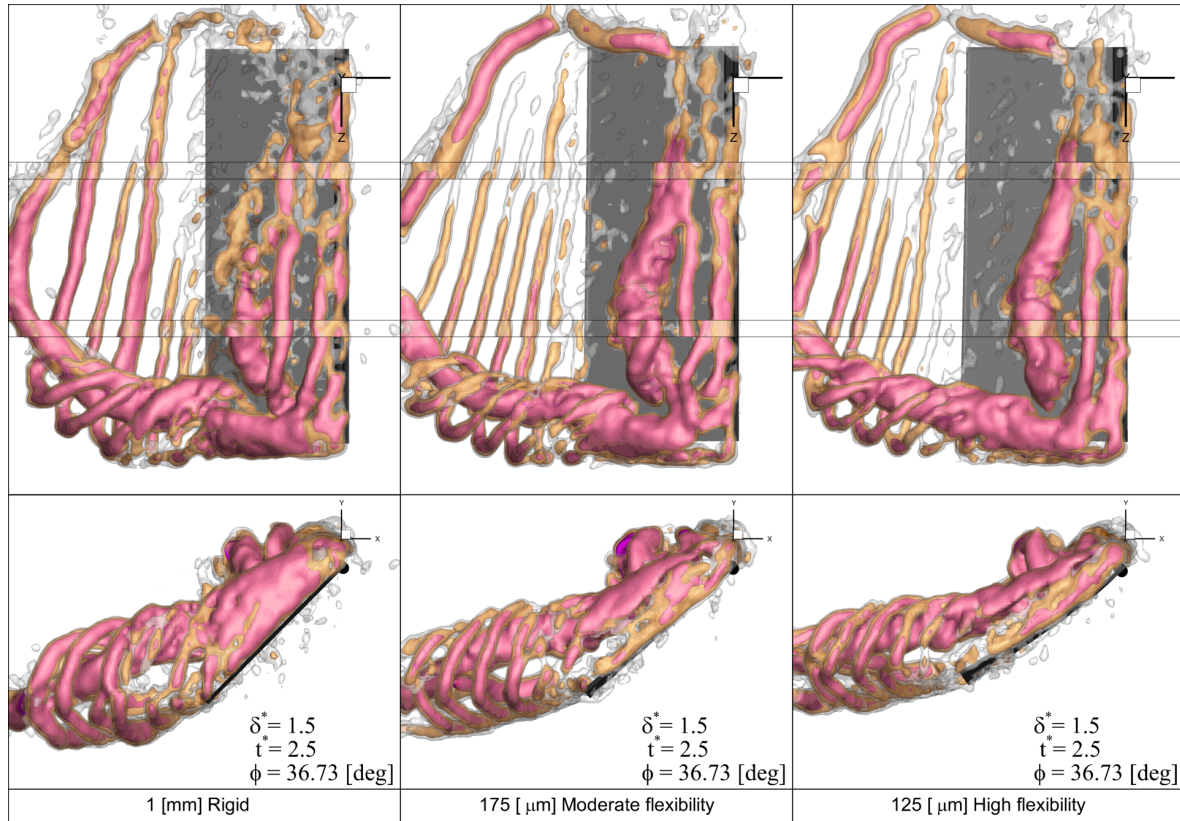


Figure A.1: Temporal evolution of vortical structures. Isosurfaces of Q-criterion: White $Q/(V_t/c)^2 = 3$, Orange $Q/(V_t/c)^2 = 10$ and Pink $Q/(V_t/c)^2 = 30$. *Left:* 1 [mm] Rigid wing. *Middle:* 175 [μm] Moderate flexible wing. *Right:* 125 [μm] High flexible wing.

A.2 Q-criterion colored with helical density

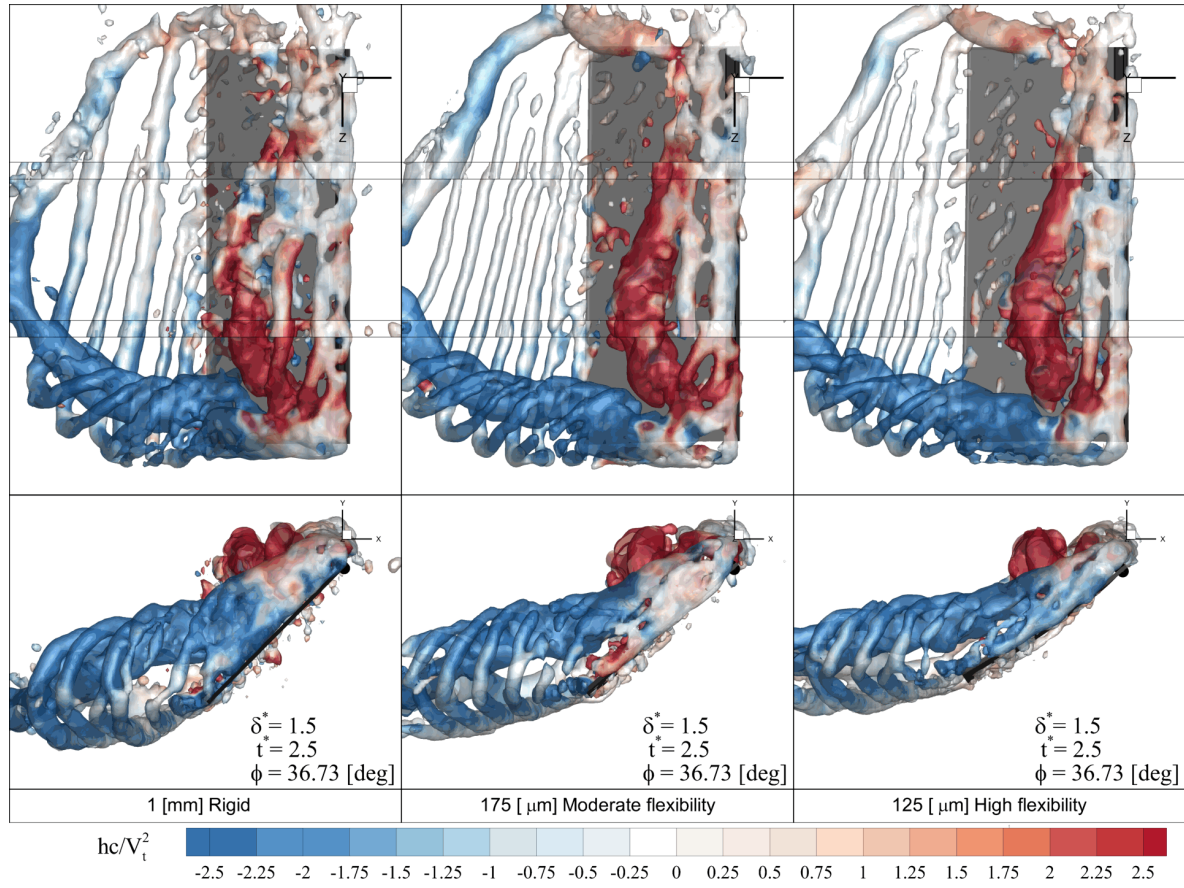


Figure A.2: Temporal evolution of vortical structures. Isosurfaces of Q-criterion ($Q/(V_t/c)^2=3$) colored by helical density (hc/V_t^2).

A.3 Spanwise vorticity

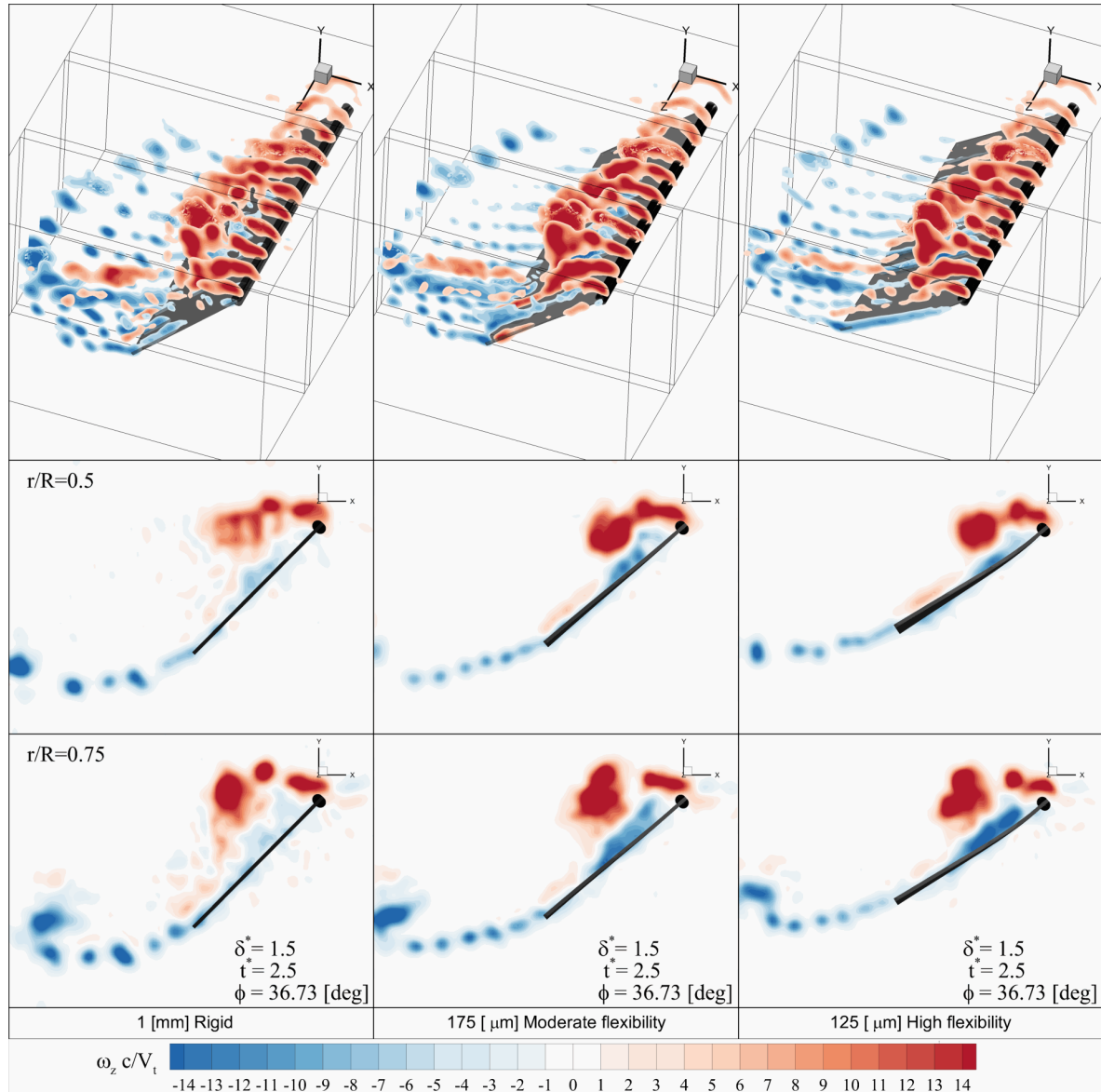


Figure A.3: Temporal evolution of spanwise vorticity contours ($\omega_z c/V_t$). *Top:* Vorticity contours along the span. *Middle:* Spanwise vorticity contour at $r/R = 0.5$. *Bottom:* Spanwise vorticity contour at $r/R = 0.75$.

A.4 Spanwise velocity

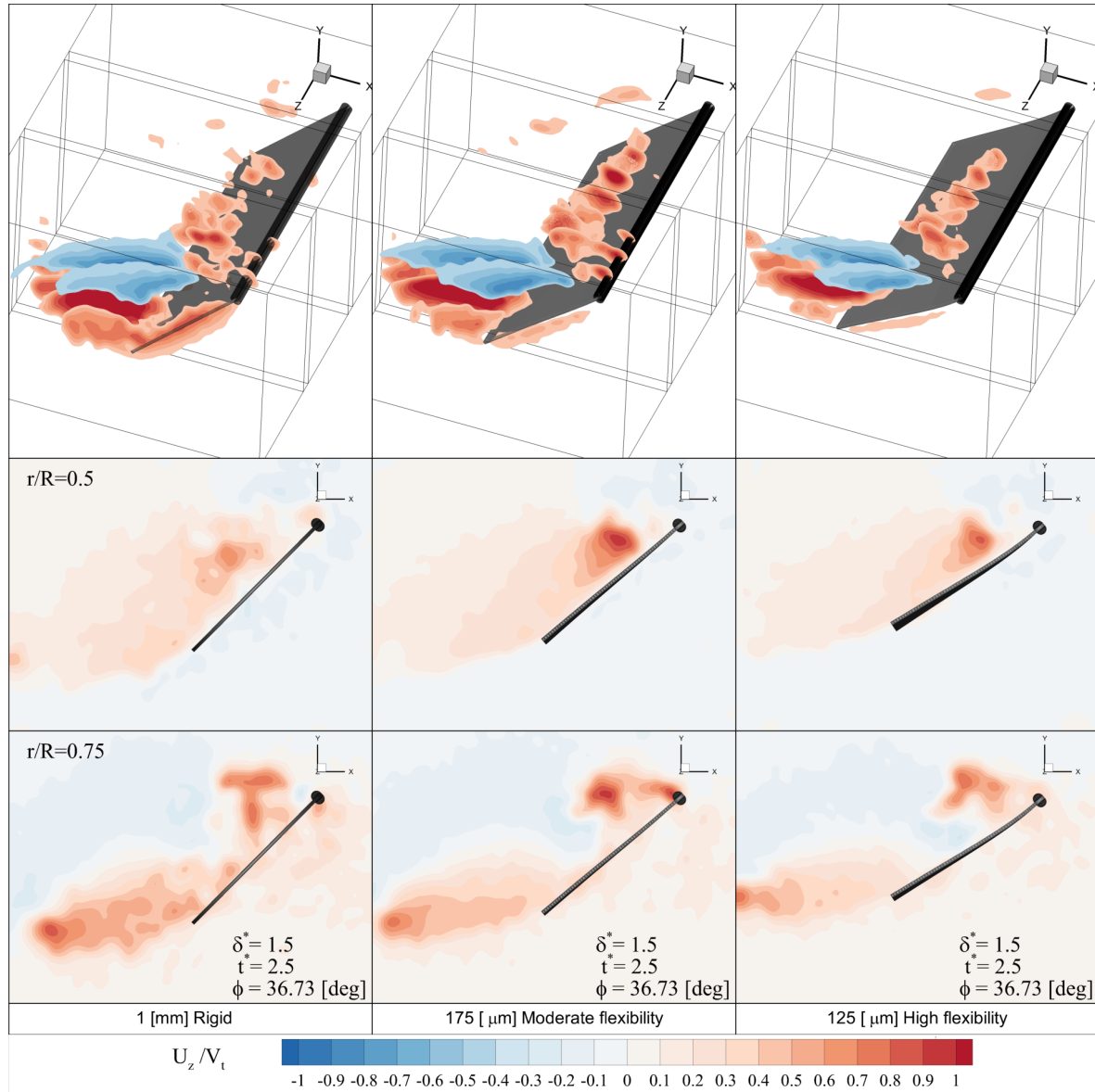


Figure A.4: Temporal evolution of spanwise velocity contours (U_z/V_t). *Top:* velocity contours along the span. *Middle:* Velocity contour at $r/R = 0.5$. *Bottom:* Velocity contour at $r/R = 0.75$.

A.5 Spanwise vorticity flux density

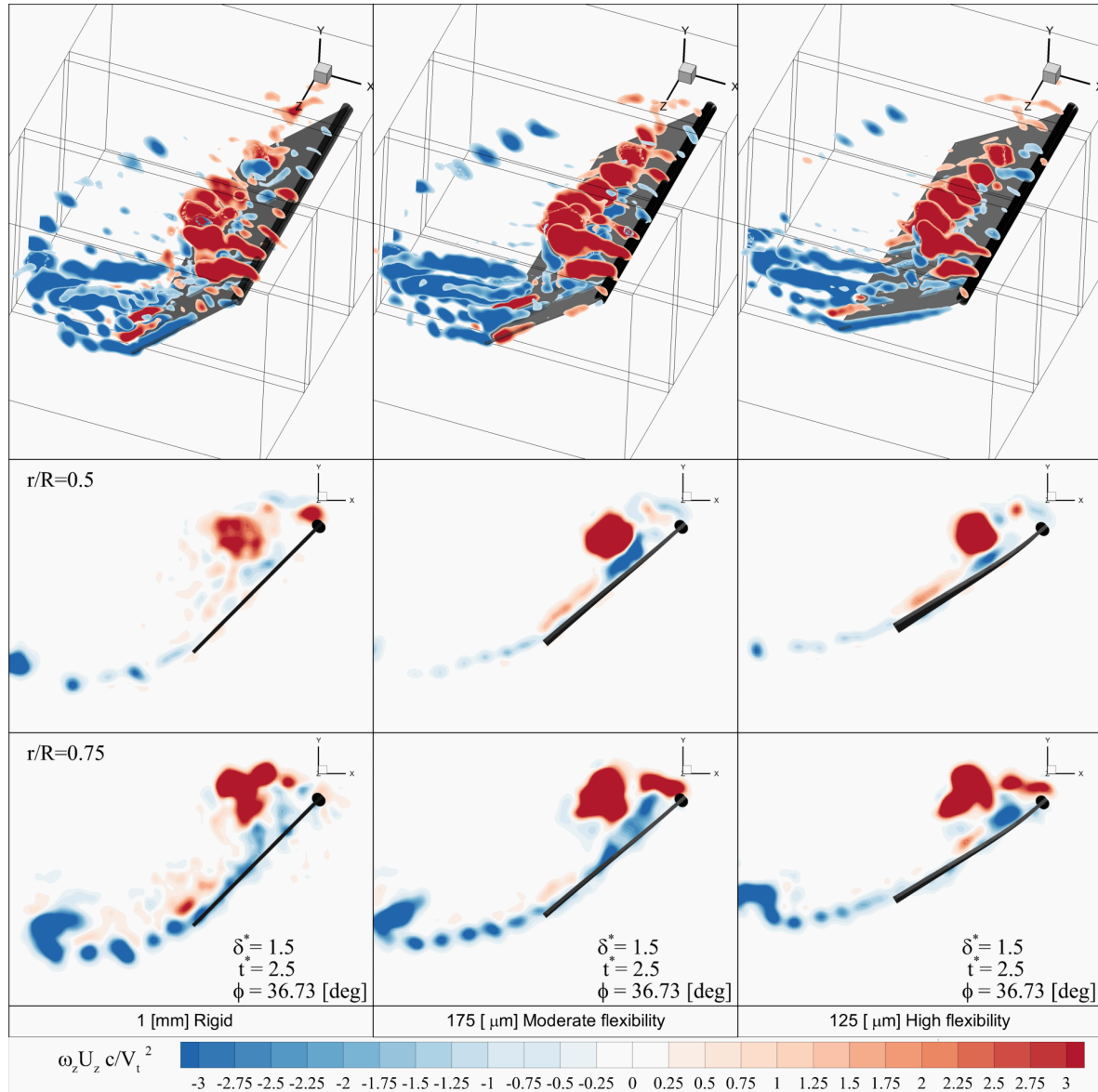


Figure A.5: Temporal evolution of spanwise vorticity flux density contours ($\omega_z U_z c / V_t^2$). *Top:* Vorticity contours along the span. *Middle:* Spanwise vorticity flux density contour at $r/R = 0.5$. *Bottom:* Spanwise vorticity flux density contour at $r/R = 0.75$.

A.6 Pressure distribution

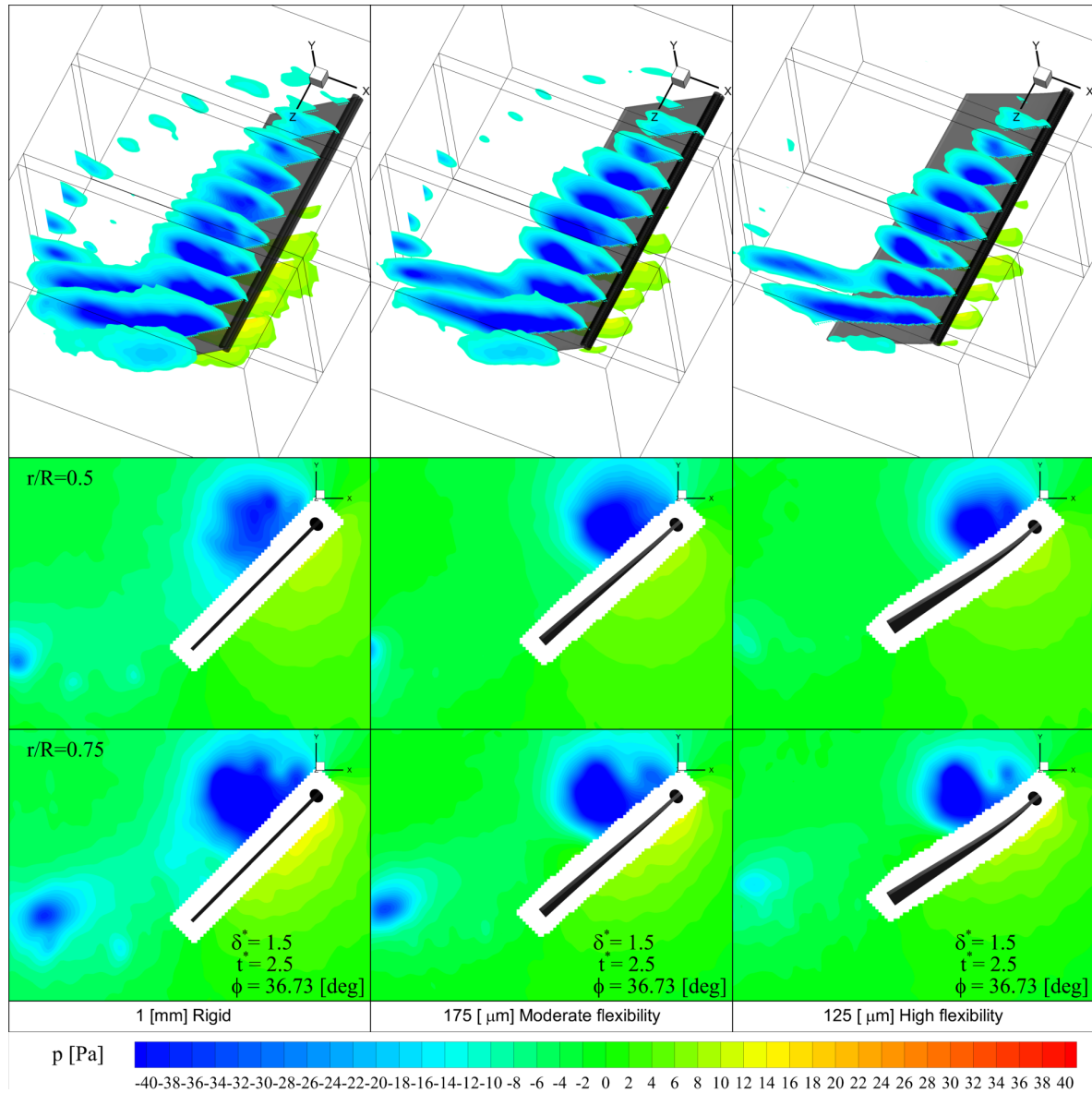


Figure A.6: Temporal evolution of pressure contours (p). *Top:* Pressure contours along the span. *Middle:* Pressure contour at $r/R = 0.5$. *Bottom:* Pressure contour at $r/R = 0.75$.

A.7 Vortical structures and pressure distribution

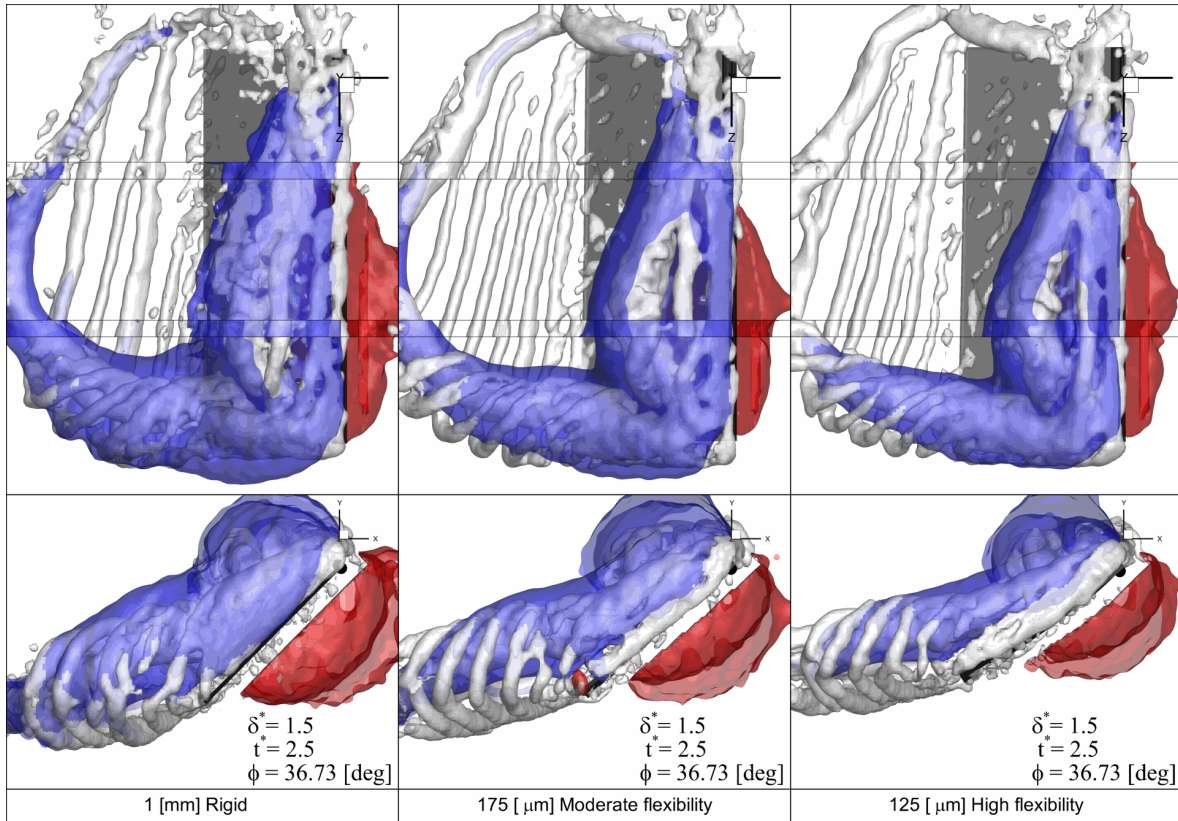


Figure A.7: Temporal evolution of vortical structures and reconstructed pressure fields. Isosurfaces of Q-criterion: White $Q/(V_t/c)^2 = 3$. Isosurfaces of reconstructed pressure field: Blue $p = -13$ Pa and Red $p = 6$ Pa.

A.8 Spanwise pressure gradient

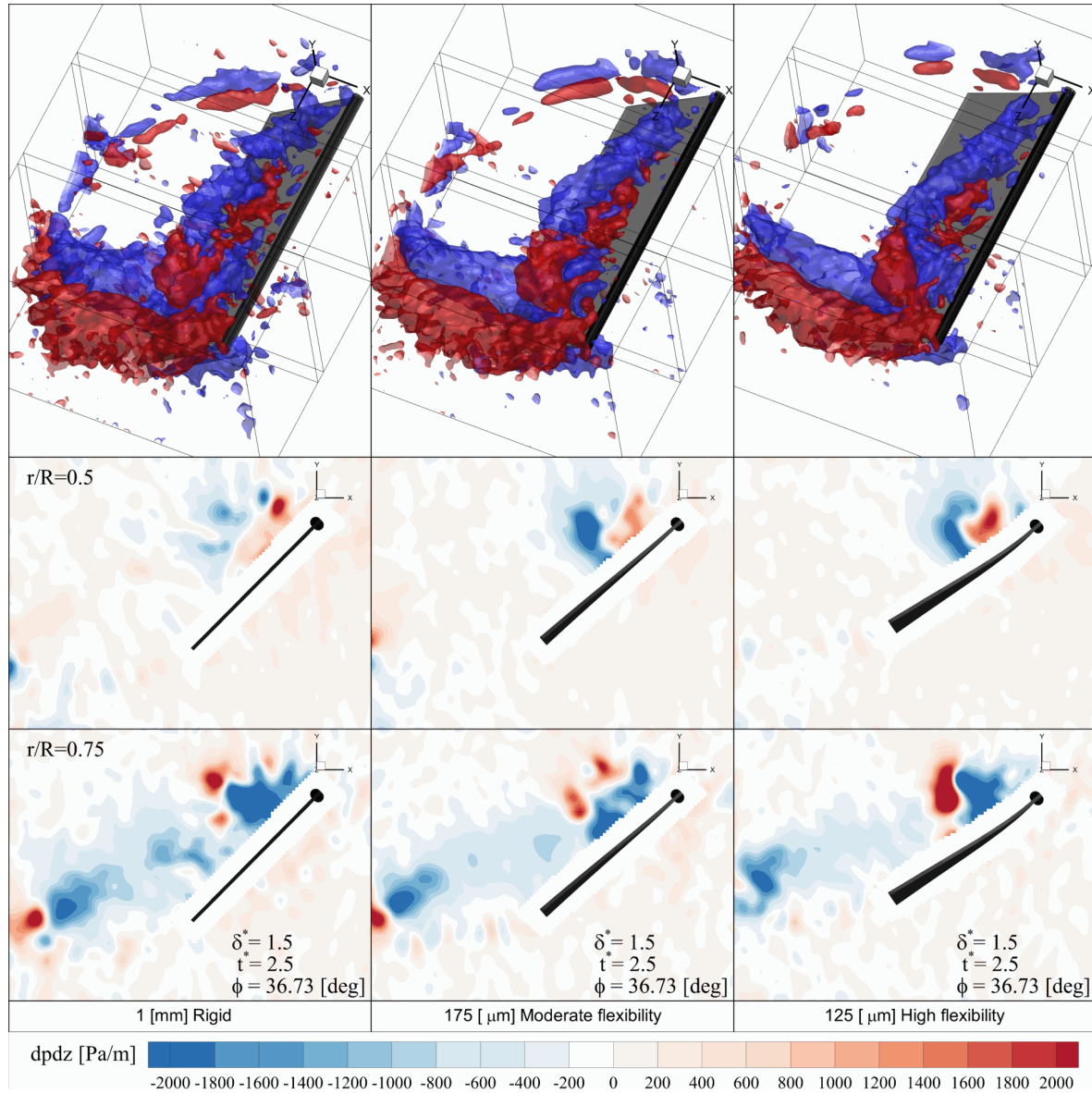


Figure A.8: Temporal evolution of spanwise pressure gradient contours and isosurfaces ($dpdz$).
 Top: Isosurface of $dpdz$: Blue $dpdz = -1000$ Pa/m and Red $dpdz = 1000$ Pa/m. Middle: Spanwise pressure gradient contour at $r/R = 0.5$. Bottom: Spanwise pressure gradient contour at $r/R = 0.75$.

A.9 Pressure gradient in x -direction

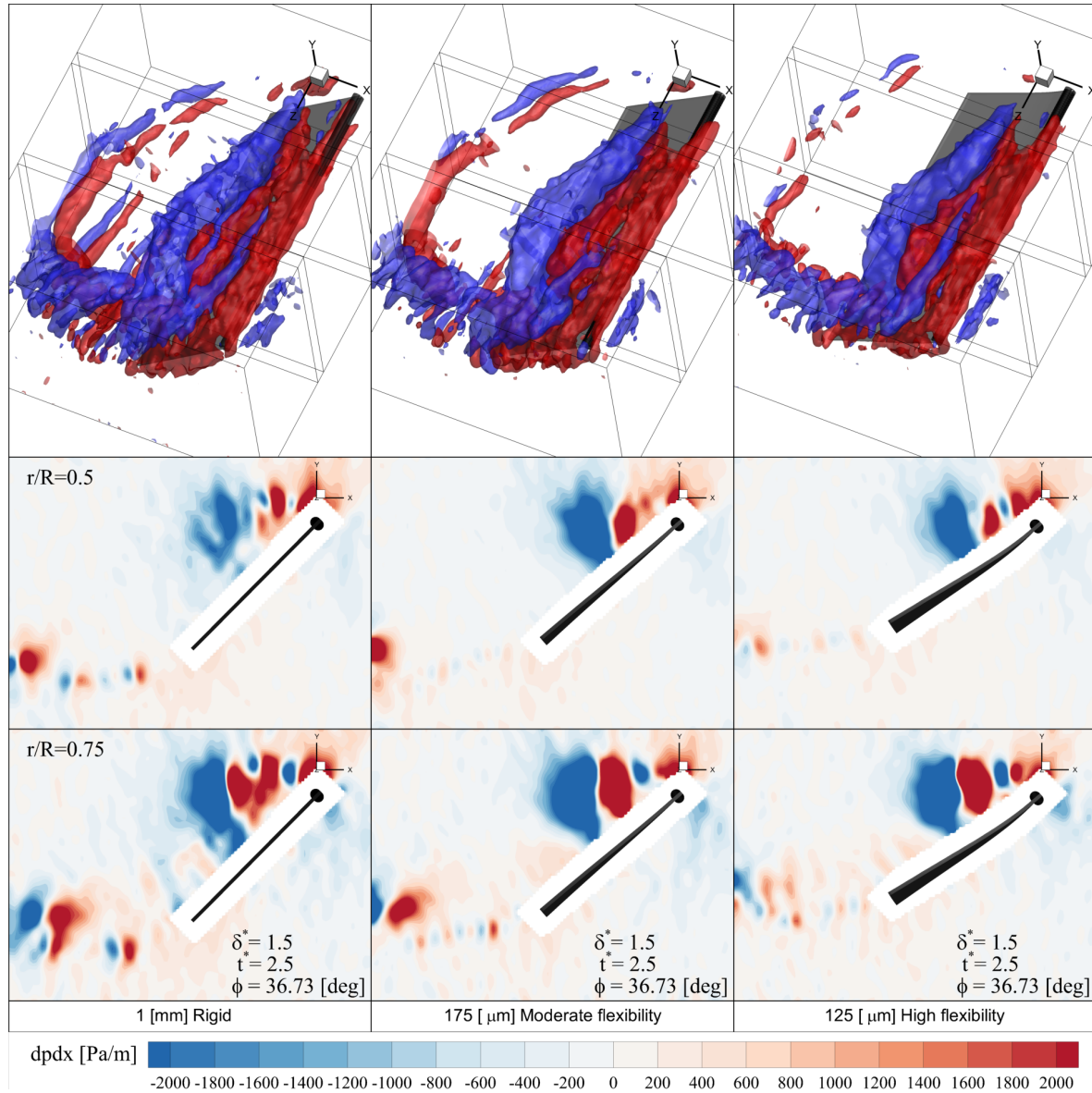


Figure A.9: Temporal evolution of pressure gradient in x -direction contours and isosurfaces ($dpdx$). *Top:* Isosurface of $dpdx$: Blue $dpdx = -1000$ Pa/m and Red $dpdx = 1000$ Pa/m. *Middle:* Pressure gradient in x -direction contour at $r/R = 0.5$. *Bottom:* Pressure gradient in x -direction contour at $r/R = 0.75$.

